Universitat Autònoma de Barcelona

MAGNETICALLY INDUCED FORCES DURING LISA PATHFINDER IN-FLIGHT OPERATIONS

JUAN PEDRO LÓPEZ-ZARAGOZA

MAGNETICALLY INDUCED FORCES DURING LISA PATHFINDER IN-FLIGHT OPERATIONS

THESIS SUBMITTED FOR THE DEGREE OF DOCTOR OF PHILOSOPHY

at

UNIVERSITAT AUTÒNOMA DE BARCELONA (UAB)

Departament de Física

Programa de Doctorat en Física

by

JUAN PEDRO LÓPEZ-ZARAGOZA

ADVISOR: DR. MIQUEL NOFRARIAS I SERRA

TUTOR: DR. JORDI MOMPART PENINA

October 2020

Dedicated to the loving memory of Lluís Gesa, without whose work this thesis would not have been possible

1976 – 2020

Science is a way of thinking much
more than it is a body of knowledge.

— Carl Sagan

AGRADECIMIENTOS

Si quisiera poner un inicio a toda esta aventura, podría decirse que todo comenzó cuando, allá por 2013 o 2014, como estudiante de física, contacté con el Institut de Ciències de l'Espai (ICE) para realizar mi trabajo de fin de carrera. Todavía no tenía clara la temática sobre la que hacerlo, pero sabía que iba a ser algo relacionado con el espacio, disciplina que me apasiona. Así fue como Alina respondió a mi correo y me hablo por primera vez de LISA Pathfinder y de Miquel Nofrarias. No pasó mucho tiempo hasta que conocí a Miquel y me explicó lo que era LISA Pathfinder, lo emocionante de las medidas que iba a realizar y que iba a lanzarse en los próximos años. Quién me iba a decir entonces que tantos años después estaría escribiendo estos agradecimientos al acabar mi tesis doctoral sobre LISA Pathfinder y con Miquel como director.

Pocos años después Miquel me ofreció la posibilidad de empezar mi doctorado dentro del grupo del ICE continuando con mi trabajo realizado los años anteriores. Nunca podré agradecerle lo suficiente la oportunidad que me brindó, y que me ha permitido vivir una de las etapas más bonitas de mi vida. Miquel ha sido un gran maestro y un gran amigo. Siempre ha estado ahí para ayudarme en todos y cada uno de los problemas que he tenido, y para guiarme y ofrecerme sus consejos en los momentos difíciles. ¡La de horas que hemos pasado hablando sobre magnetómetros, campos magnéticos, técnicas de análisis y similares! Pero no sólo eso, sino que también ha estado ahí para hablarme sobre el futuro y lo que podría hacer una vez acabado el doctorado. Sin ti esta tesis no hubiese sido posible, muchas gracias Miquel.

La siguiente persona sobre la que quisiera detenerme a hablar es Fran. Este doctorado no hubiese sido lo mismo sin él como compañero de viaje. Hemos compartido tantísimas horas y experiencias juntos... Hemos compartido innumerables charlas sobre deporte, política, historia, religión y filosofía. También hemos vivido innumerables viajes juntos. Como olvidar esos desayunos en el Commundo, en Darmstadt. Nuestro inolvidable road-trip por USA, o la final de la champions vivida en Benasque. La verdad que has sido el mejor amigo que he hecho en todos estos años. Sin ti este viaje no hubiese sido lo mismo, muchas gracias Fran.

Y ahora le toca el turno al grupo de ondas gravitacionales del ICE. He tenido la suerte de compartir todos estos años de trabajo con un grupo genial. Carlos, Miquel, Víctor, Lluís, Nacho, Ivan, Nikos, Ferran, Dani, Fran, Marius, David, Juan, Pep, Carles, Alberto e Iván. Quisiera destacar un poco a Víctor, que ha sido como un hermano mayor para mi durante todo este período. Siempre ha estado pendiente de como estábamos Fran y yo, siempre dispuesto a ayudarnos cuando teníamos problemas de programación y siempre haciéndonos reír con su forma directa (y porqué no decirlo, un poco malsonante) de decir las cosas. Muchas

gracias Víctor.

También quisiera aprovechar estas líneas para recordar a Lluís. Su pérdida nos rompió el corazón a todos. Además de un gran compañero era un gran amigo, y junto a Víctor, ese otro hermano mayor que siempre cuidó de nosotros. Sin tu trabajo en LISA Pathfinder, seguramente nuestro grupo no hubiese tenido un rol tan importante en la misión, y por lo tanto yo no hubiese estado aquí escribiendo esta tesis doctoral. Esta tesis va por ti. Gracias por todo Lluís, y hasta siempre, amigo.

He de agradecer también todos los buenos momentos pasados junto a los demás doctorand@s del instituto. Todas esas pausas para el café, todos esos días comiendo juntos en la cafetería de la ETSE, todas esas charlas interesantes en la cocina del instituto...sin duda habéis hecho de esta experiencia algo mucho más bonito.

Y también quisiera dedicar algunas líneas para las chicas de administración del IEEC: Eva, Anna y Pilar, que siempre están ahí para solucionarnos los problemas (y que no son pocos) que nos van surgiendo en este mundillo de la investigación, en el cual las cosas deberían ser mucho mas sencillas de lo que desgraciadamente son. Tampoco me podría olvidar de Josep Guerrero, que siempre ha estado ahí para solucionarme cualquier problema con el ordenador, para hacerme reír con esos chistes tan malos, y que siempre te arranca una sonrisa cuando te lo encuentras por el pasillo y te salta con una de sus bromas. ¡Gracias Josep!.

También quiero dedicaros unas líneas a vosotros, papá, mamá y Luisa, que tantos años lleváis siguiendo mi trayectoria, y que os alegráis por mis logros tanto como si fueran los vuestros propios. Lleváis apoyándome y siguiéndome desde que era un niño pequeño al que le gustaba ver las estrellas. Sin todos vuestros esfuerzos para que haya podido tener una gran educación, y sin toda vuestra dedicación y amor a la hora de criarme, seguramente no hubiese llegado hasta aquí. ¡Que sepáis que esto de estudiar y formarse no acaba aquí! Habéis criado a un hijo que, por suerte o por desgracia, esta loco por el conocimiento y por la ciencia, y a estas alturas creo que ya es algo que no tiene remedio. Gracias, papá, mamá y Luisa. Que sepáis que tampoco me olvido de vosotr@s: abuelas, tías, tíos, padrino, madrina, que siempre estáis ofreciéndome todo vuestro apoyo y preocupándoos por mi. Tengo la suerte de tener una gran familia, os quiero a tod@s.

Y como se diría en inglés, esa lengua que tan poco te gusta, *last but not least*, te ha llegado el turno, Irene. ¡Cuánto camino llevamos recorrido juntos, y cuánto nos queda! La verdad que no puedo ni llegarme a imaginar como hubiesen sido todos estos años sin ti. En mi cabeza no podría separar mis años de doctorado de todos nuestros viajes juntos durante estos años, o de todas esas tardes de fin de semana en nuestro pequeño piso de Vallcarca, que tantas cosas tiene a mejorar y que, no obstante, tantos momentos felices nos ha dado. Como olvidar tampoco todos nuestros viajes a Mallorca, dónde exprimimos cada verano al máximo visitando todas las playas posibles, quedando con nuestros amigos, y

comiendo todas las ensaimadas, cocas de trempó, panades y delicias varias que nos ofrece esta bonita isla. Como ya sabes, somos un equipo, y como en todo buen equipo, mis logros no hubiesen sido posibles sin tu ayuda. Nuestro futuro se encuentra lleno de nuevos proyectos y emocionantes retos, y estoy seguro de que conseguiremos realizarlos todos. Me alegro de haber encontrado a la mejor persona que pudiese imaginar con quien recorrer este largo camino que es la vida. Muchas gracias, Irene.

Barcelona, Octubre de 2020

CONTENTS

LIST OF FIGURES

LIST OF TABLES

ACRONYMS

AC	Alternating Current
ACE	Advanced Compton Explorer
AOM	Acousto-Optic Modulator
ASD	Amplitude Spectral Density
AU	Astronomical Unit
AURIGA	Antenna Ultracriogenica Risonante per l'Indagine Gravitazionale Astronomica
BH	Black Hole
BICEP	Background Imaging of Cosmic Extragalactic Polarization
CMB	Cosmological Microwave Background
CMNT	Colloidal Micro Newton Thruster
CPSD	Cross-Power Spectral Density
CVM	Caging and Venting Mechanism
DAL	Days After Launch
DAU	Data Acquisition Unit
DC	Direct Current
DDS	Data and Diagnostics Subsystem
DFACS	Drag-Free Attitude Control System
DMU	Data Management Unit
DoF	Degree of Freedom
DOY	Day Of the Year
DPS	Differential Power Sensing
DWS	Differential Wavefront Sensing
EH	Electrode Housing
eLISA	evolved LISA
ELITE	European LIsa Technology Experiment
EMRI	Extreme Mass Ratio Inspiral

EPTA European Pulsar Timing Array

ESA European Space Agency

ESOC European Science and Operations Centre

FEE Front End Electronics

GPRM Grabbing, Positioning and Release Mechanism

GR General Relativity

GRACE-FO Gravity Recovery and Climate Experiment Follow-On

GRS Gravitational Reference Sensor

GSE Geocentric Solar Ecliptic

GW Gravitational Wave

HCSC Heliospheric Current Sheet Crossing

HR High Resolution

IMF Interplanetary Magnetic Field

IndIGO Indian Initiative in Gravitational Wave Observations

IPTA International Pulsar Timing Array

IS Inertial Sensor

ISS-FEE Inertial Sensor Subsystem Front End Electronics

KAGRA Kamioka Gravitational Wave Detector

L1 Lagrange Point 1

LAGOS Laser Gravitational Observatory

LCA LISA Core Assembly

LIGO Laser Interferometer Gravitational Observatory

LISA Laser Interferometric Space Antenna

LPF LISA Pathfinder

LTP LISA Technology Package

LTPDA LISA Technology Package Data Analysis

MB Magnetic Barrier

MB Modulation Bench

MCMC Monte Carlo Markov Chain

MOC Mission Operations Centre

MOSA Moving Optical Assembly

NASA National Aeronautics and Space Agency

NGO New Gravitational Observatory

NS Neutron Star

NTC Negative Temperature Coefficient

OB Optical Bench

OBC On-board Computer

OMS Optical Metrology System

PD Photodiode

PPTA Australian Parker's Pulsar Timing Array

PSD Power Spectral Density

PTA Pulsar Timing Array

RIN Relative Intensity Noise

RMS Root Mean Squared

SKA Square Kilometre Array

SMART Small Missions for Advanced Research in Technology

SMBH Super Massive Black Hole

SMBHB Super Massive Black Hole Binary

SMBHM Supermassive Black Holes Merger

ST7-DRS Space Technology 7 Disturbance Reduction System

TDI Time-Delay Interferometry

TM Test Mass

USA United States of America

UV Ultraviolet

WR Wide Range

1 INTRODUCTION

The Laser Interferometric Space Antenna (LISA) [1] is a future European Space Agency (ESA) mission expected to be launched in 2034 with the main goal of detecting gravitational waves in the millihertz range. It will consist of three spacecrafts forming an equilateral triangle with a separation of 2.5 million kilometres between spacecrafts, building a three-arm gigantic interferometer. With this setup, LISA will be able to measure the passing by of gravitational waves in the millihertz range.

Constructing such a complex detector is a huge task. One of the main technological challenges is to be able to put two Test Masses (TMs) in a free-fall good enough that we can measure how the relative distance changes when a Gravitational Wave (GW) passes between them. In order to achieve this goal, ESA launched in December 2015 LISA Pathfinder (LPF) [2, 3], which was a technology demonstrator for LISA with the main goal of demonstrating that the level of free fall required to build a GW observatory in space like LISA is achievable. The idea behind LPF is to squeeze one of LISA arms into just one spacecraft and then measure the relative acceleration between two TMs. LPF was a complete success [4], achieving an unprecedented level of free-fall in space, and thus, gave green light to LISA.

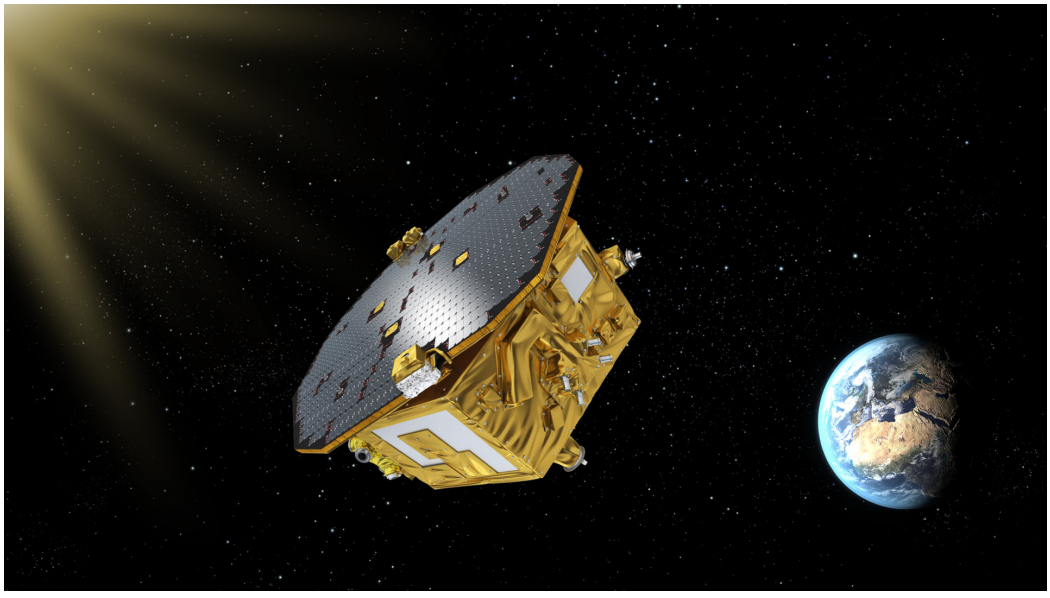

Figure 1: Artistic drawing of the LPF spacecraft with the Earth on the back (Credits: European Space Agency www.esa.int).

There are several physical effects that can disturb the TMs from its geodesic motion. Amongst them, magnetically originated forces can be of great importance below the millihertz. They originate from the coupling of the remanent

magnetisation and the magnetic susceptibility from the TMs with the surrounding magnetic field and magnetic field gradient.

The main aim of this thesis is to study the magnetic environment within the LPF mission and to determine the magnetic parameters from LPF TMs. With these contributions, we can quantify how this magnetically induced forces contribute to the main scientific product of LPF, which is the fluctuations of the relative acceleration between the two TMs.

1.1 INTRODUCTION

The world of physics underwent a great revolution when back in February 2016 Laser Interferometer Gravitational Observatory (LIGO) announced to the world that they have detected a GW signal coming from the merging of two black holes of a distant galaxy [5]. This signal was observed on September 9th, 2014, and was given the name 'GW150914'. The effect of GWs have already been observed by Hulse and Taylor [6] when they discovered that the decay in the period of their pulsar system matched perfectly to the loss of energy corresponding from GW emission, but the detection from LIGO was the first time in which the passing by of a GW has been directly measured.

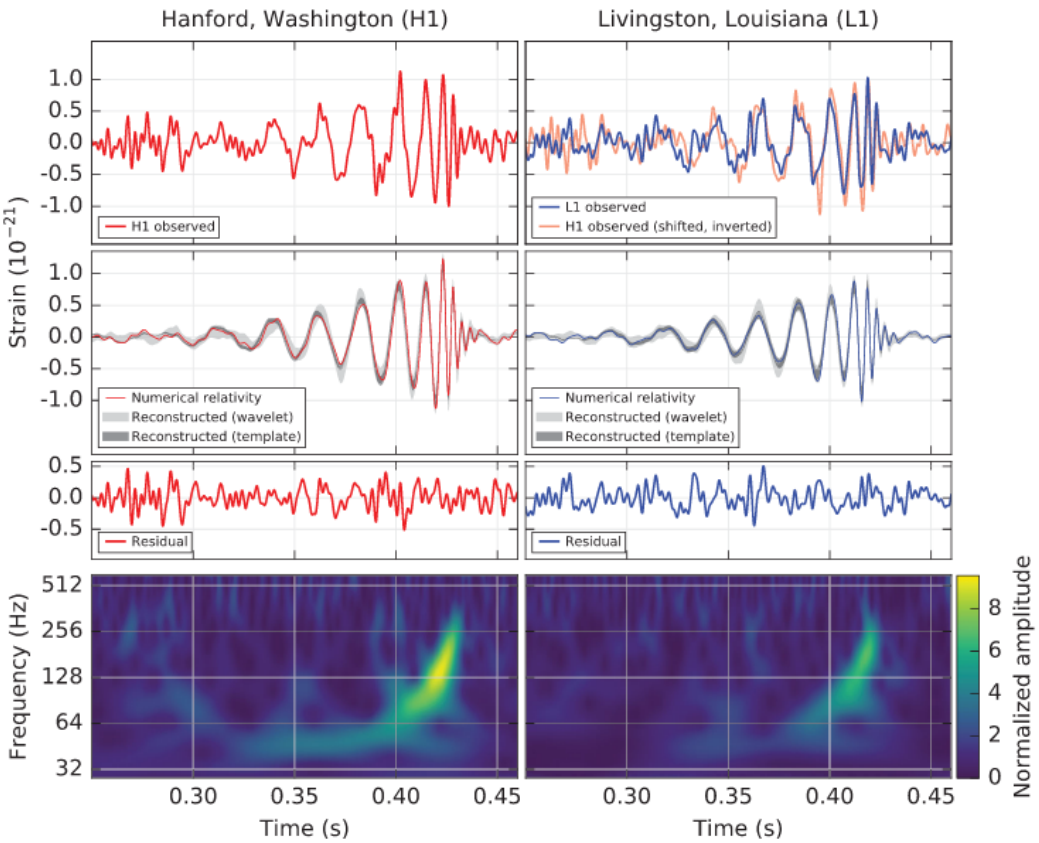

Figure 2: GW signal from 'GW150914' measured by the two LIGO detectors (Credits: [5]).

With the detection of LIGO, a new era has started in the study of the Universe. Now we can not only study the cosmos through the electromagnetic spectrum,

but also through GWs. A whole new spectrum have appeared to study the Universe and to try to unveil its secrets. A good example of how LIGO has opened a new field of study was the detection of the first Neutron Star (NS) merger [7] a few years later after the detection of 'GW150914', an event which was called 'GW170817'. This event did not just explain how some heavy metals can form on the universe [8], but was also the first GW detection in which an electromagnetic counterpart was detected. This detection opened a very interesting field, the so called Multimessenger Astronomy, in which we can study different events in the Universe through electromagnetic and GW radiation together.

All the GWs detected by LIGO so far (and other on-ground detectors, like Virgo) are around the killohertz, which is the instrument frequency band sensible to GW radiation. A case of particular interest is the study of GWs in the so called low-frequency-band of the spectrum, in the millihertz range. This region is expected to be populated by GWs from a wide range of interesting and different sources: Supermassive Black Holes Mergers (SMBHMs), Extreme Mass Ratio Inspirals (EMRIs), etc. LISA is expected to be able to detect all the previous events, and thus, detecting GWs in the millihertz range just like LIGO did above the hertz.

In this chapter, we will start introducing what GWs are and how they are produced. We will afterwards move on and make a short review about the different types of detectors for GWs and the different frequency regimes at which they work. Finally, we will enter into more detail about the future space-based GW detector: LISA.

1.2 GRAVITATIONAL WAVES

Back in 1916, Albert Einstein introduced to the world his theory of General Relativity (GR) [9]. In this theory, among other points, he introduced the concept of GWs. Just as in electromagnetism, where two accelerated charges produce electromagnetic waves, when we have a mass distribution in space-time that changes over time, it produces GWs. These waves can be interpreted as small ripples that stretch and compress space-time, travelling at the speed of light c and making the proper distance between two ideal proof masses in geodesic motion to slightly change periodically.

Despite its similarities with electromagnetic radiation, gravitational radiation has some differences with respect to the former. Just as the most basic source of electromagnetic radiation is the electric dipole, in the case of gravitational waves is the mass quadrupole. In general relativity, the rate of change of the mass dipole moment scales as the linear momentum of the system, which is a conserved quantity. The next strongest source of electromagnetic radiation is the magnetic dipole. In the case of gravity, the change of the magnetic dipole is proportional to the angular momentum of the system, which is again a conserved quantity. Therefore, mass dipole radiation does not exist in Einstein's relativity theory. Another difference with electromagnetic radiation is the tiny amplitude of the waves, which is a direct consequence of the gravitational force being much weaker than electromagnetic force. Typical astronomical sources detected by LIGO

emit GWs with amplitudes of the order of 10^{-22}, so detecting them is a huge technological challenge, as we will see through this chapter.

To start our description of GWs we will take the weak field field approximation, i.e., we will consider our space-time to be almost flat when it suffers a small perturbation, so that the second order terms of the perturbation are negligible. This approximation is correct if we are far enough from the GWs source. Therefore, we can describe our space-time metric as:

$$g_{\mu\nu} = \eta_{\mu\nu} - h_{\mu\nu} + O(h_{\mu\nu}^2) \tag{1.1}$$

where $\eta_{\mu\nu} = diag(-1111)$ is the Minkowski metric (corresponding to a flat space-time), $h_{\mu\nu}$ is the small perturbation caused by the GW and $O(h_{\mu\nu}^2)$ the second order terms of the perturbation that we can neglect. Since $|h_{\mu\nu}| << 1$, and thus, $O(h_{\mu\nu}^2)$ negligible, we can consider the linear equations of GR.

Let's now remember which are the Einstein equations of GR. According to Misner, Thorne, Wheeler, et al. [10] and Schutz [11], they are given by:

$$G_{\mu\nu} + \Lambda g_{\mu\nu} = \kappa T_{\mu\nu} \tag{1.2}$$

where $g_{\mu\nu}$ is the metric tensor, which for our case we have defined in Equation (1.1), $G_{\mu\nu} = R_{\mu\nu} - \frac{1}{2}Rg_{\mu\nu}$ is the Einstein Tensor, with $R_{\mu\nu}$ being the Ricci Tensor and R the scalar curvature, Λ the cosmological constant, $T_{\mu\nu}$ the energy-momentum tensor and κ a constant. If we consider that $\Lambda = 0$ and $k = 8\pi G/c^4$ (value derived from the movement of the inner planets of the Solar System), we can write Equation (1.2) as:

$$G_{\mu\nu} = \frac{8\pi G}{c^4} T_{\mu\nu} \tag{1.3}$$

with G being Newton's gravitational constant.

Since Einstein's tensor is given by:

$$G_{\mu\nu} = \frac{1}{2}\left(-\frac{1}{c^2}\frac{\partial^2}{\partial t^2} + \nabla^2\right)\bar{h}_{\mu\nu} \tag{1.4}$$

with $\bar{h}_{\mu\nu}$ being the trace-reverse perturbation, Einstein's equations for a weak field can be written as:

$$\left(-\frac{1}{c^2}\frac{\partial^2}{\partial t^2} + \nabla^2\right)\bar{h}_{\mu\nu} = -\frac{16\pi G}{c^4} T_{\mu\nu} \tag{1.5}$$

If we now write Equation (1.5) in the absence of matter ($T^{\mu\nu} = 0$), and sufficiently far away from the source, we can write it as:

$$\left(-\frac{1}{c^2}\frac{\partial^2}{\partial t^2} + \nabla^2\right)\bar{h}_{\mu\nu} = 0 \tag{1.6}$$

where we have used the *transverse-traceless* gauge conditions (TT). Equation (1.6) has a particular solution, which is the plane wave:

$$\overline{h}_{\mu\nu} = A_{\mu\nu} e^{ik_\lambda x^\lambda} \tag{1.7}$$

where $A_{\mu\nu}$ is a traceless, symmetric and constant tensor containing the wave polarisation, so we will call it polarisation tensor. The value of $\overline{h}_{\mu\nu}$ will be constant in a hypersurface in which the internal product $k_\lambda x^\lambda$ remains constant.

If we consider the wave vector $\overrightarrow{k} = (\omega, 0, 0, \omega)$ where ω if the frequency of the wave that is propagating in the z direction, we have the canonical representation, which corresponds to the *transverse-traceless* gauge mentioned before:

$$\overline{h}_{\mu\nu} = A_{\mu\nu} \cos[\omega(t-z)] = \begin{bmatrix} 0 & 0 & 0 & 0 \\ 0 & A_{xx} & A_{xy} & 0 \\ 0 & A_{xy} & -A_{xx} & 0 \\ 0 & 0 & 0 & 0 \end{bmatrix} \cos[\omega(t-z)] \tag{1.8}$$

where A_{xx} and A_{xy} are the plus and cross polarisation amplitudes of the GW. A graphical representation of them can be seen in Figure 3.

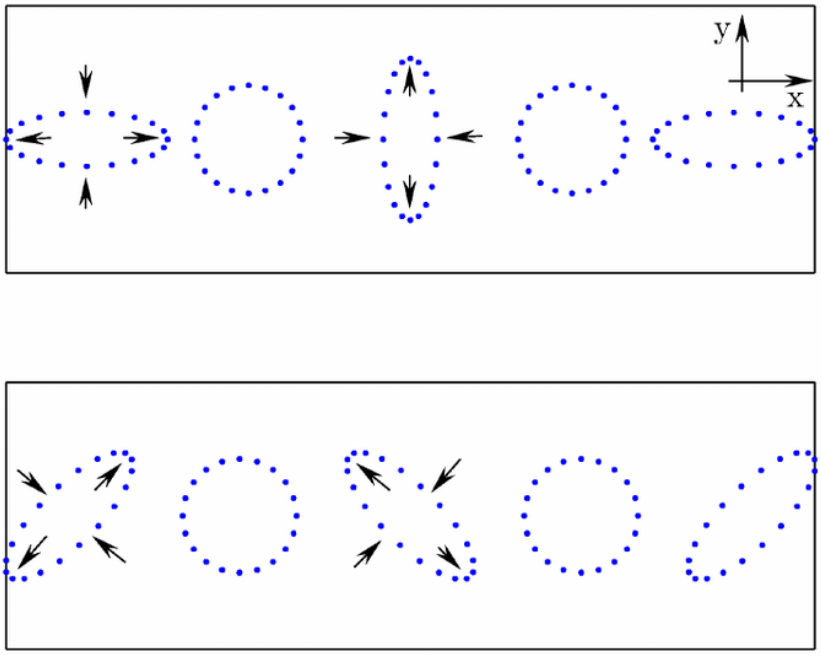

Figure 3: Plus '+' (top) and cross 'x' (bottom) polarisation modes of GWs. (Credits: [12]).

It can be proven [11] that far away from the source and when the motion is small compared to c, the dominant contribution to the strain h is:

$$h \simeq \frac{2G}{rc^4}\ddot{Q}_{\mu\nu} \tag{1.9}$$

where G is the gravitational constant, r the distance to the source and $\ddot{Q}_{\mu\nu}$ the second derivative of the reduced quadrupole moment, which is defined as:

$$Q_{\mu\nu} = \int \rho(\mathbf{r}) \left(x_\mu x_\nu - \frac{1}{3}\delta_{\mu\nu} r^2 \right) d^3r \tag{1.10}$$

where ρ is the matter density. Taking this into consideration, it can be seen how spherically symmetric perturbations of the metric do not produce GW radiation, like the spherically symmetric collapse of a massive star.

The first GW detection ever made by LIGO ('GW150914') measured a strain amplitude of about $h \simeq 10^{-21}$ in the final moments of the merger. This was for a Black Hole (BH) merger located at 430 Mpc and with a chirp mass of 28.6 $M_\odot$, where the Chirp Mass of a system of two bodies m_1 and m_2 is defined as:

$$M = \frac{(m_1 m_2)^{3/5}}{(m_1 + m_2)^{1/5}} \tag{1.11}$$

see Abbott et al. [5] for further details. In laser interferometric detectors, which we will study later on, the amplitude of the GW (or GW strain) is usually approximated as the change in the distance ΔL of two test bodies initially separated by a distance L:

$$h \simeq \frac{\Delta L}{L} \tag{1.12}$$

For a detector like LIGO, which has its test bodies separated by $L \sim$ 3-4 km, measuring a strain amplitude of about $h \simeq 10^{-21}$ would mean that the interferometer had to measure variations in the initial separation of the two test bodies ΔL of the order of $\Delta L \sim 10^{-18}$ m. In LIGO this is improved (apart from other upgrades) by the fact that the laser is sent back and forth, making the effective length of the detector of $\sim$ 300 km. This reduces the previous demanding in measuring ΔL by two orders of magnitude.

That is the major problem with GW detection, the effect produced by GWs is extremely tiny, and we can only aim to detect GW radiation coming from enormous masses which change their mass distribution very rapidly, like BH or NS mergers. That is the reason why they have not been detected before, even though Einstein predicted their existence a century ago, because the technology needed to measure the small perturbations they produce in space-time has only been reached in recent years.

1.3 GRAVITATIONAL WAVES SPECTRUM

As it happens with the electromagnetic spectrum, GWs are originated in the cosmos in a wide range of frequencies, and so, we have a rich spectrum of GWs, as we show in Figure 4. Depending on the physical event from which they are originated, they will be emitted at different frequencies, and so, different type of detectors are needed in order to measure their effects. Usually in the field, the GW spectrum comes divided in four different areas depending on the type of detector that is used in the corresponding bandwidth:

HIGH-FREQUENCY BAND: This band typically goes from 1 to 10^4 Hz, and is the bandwidth where terrestrial interferometric detectors like LIGO [13] and Virgo [14] work. In this band we can find GWs emitted by merging systems in the last moments of their inspiral, like BH-BH, BH-NS and NS-NS mergers. Asymmetric stellar core collapses that cause supernovae, as well as deformed spinning NS are also expected to emit GWs in this bandwidth. At the moment of writing this thesis, from all the previous sources, terrestrial interferometers have detected BH-BH and NS-NS mergers, and there are several solid candidates for BH-NS mergers pending to be confirmed. Beyond this frequency band, there are currently proposals for very-high frequency detectors in the MHz-GHz region based in different technologies [15].

LOW-FREQUENCY BAND: It comprises the band going from 10^{-5} to 1 Hz. Since gravity gradients and seismic noise makes almost near impossible for interferometric ground based detectors to measure GWs below the Hz, the proposed scheme is to build an interferometric detector in space, like the future LISA [1]. In this bandwidth we expect to find the coalescence of Supermassive Black Holes (SMBHs), as well as the BH-BH mergers we detect in the high-frequency band but during an earlier phase of their merger. This is the bandwidth where we also expect to find compact objects captured by SMBHs, the so called EMRIs. Finally, in this frequency band we also expect to find galactic binaries and white dwarf binaries. Current estimates for detectable galactic binary systems are in the order of 10^4, together with a confusion background of unresolved sources from our own Galaxy.

VERY-LOW FREQUENCY BAND: This band comprises the range going from 10^{-9} to 10^{-5} Hz and is the bandwidth where pulsar timing detectors work, like the International Pulsar Timing Array (IPTA) [16] and the Square Kilometre Array (SKA) [17]. In this case, the mechanism of detection consists in measuring small deviations in known pulsar periods, which would be caused by a GW passing between them and the Earth [18]. In this bandwidth we mainly expect to find the imprint of GW radiation coming from SMBH binaries in the centre of galaxies.

EXTREMELY-LOW FREQUENCY BAND: This bandwidth goes from 10^{-18} to 10^{-13} Hz. Since in this bandwidth we are on scales of the order of the age of the Universe, the aim is to try to study the physics of the very first moments of the Universe. In this region we expect to find the signatures of the GW background emitted during the cosmic inflation period, which should produce a po-

larisation in the anisotropies of the Cosmological Microwave Background (CMB) [19]. Experiments that study this region are the Background Imaging of Cosmic Extragalactic Polarization (BICEP) [20, 21] experiment series or the Keck Array [22].

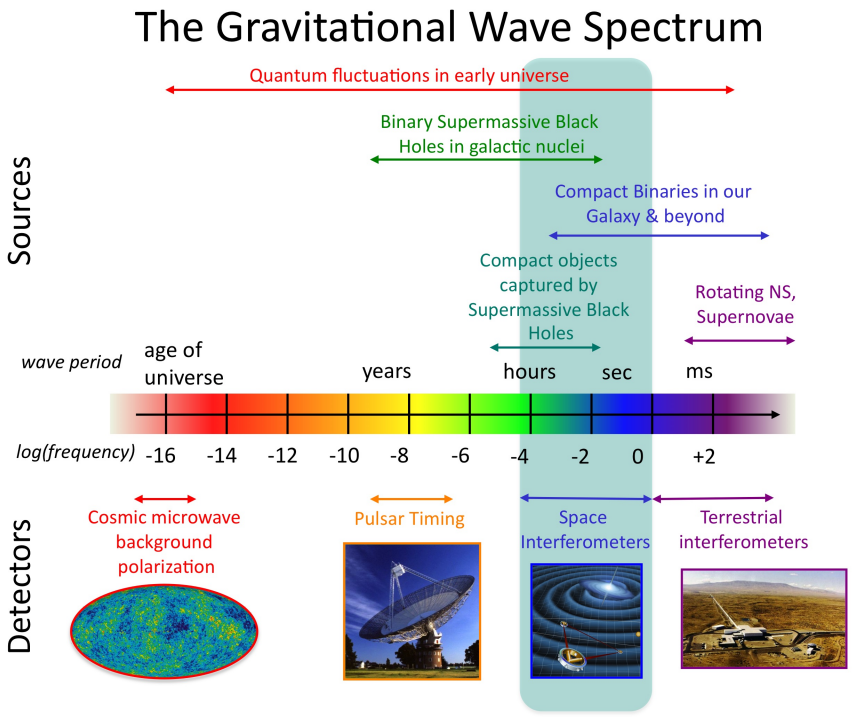

Figure 4: GWs Spectrum. On the top side, different astrophysical and cosmological events can be observed as well as the frequencies at which they happen. On the bottom side, the frequency range at which the different type of detectors work (Credits: NASA Goddard Space Flight Center www.nasa.gov).

1.4 GRAVITATIONAL WAVE DETECTORS

So far, we have explained the mechanisms behind GW emission, and briefly described their sources and the frequency ranges at which they are emitted. As previously explained, GWs are emitted at different frequencies and we need different kind of detectors for each frequency range. Moreover, GW detection is quite a technological challenge due to the precision with which we have to perform measurements. In this section we will explain which are the efforts to detect GWs at each frequency, and we will review a bit of the history of how GW detection first appeared and which were the first efforts towards detecting GWs.

1.4.1 *Resonant mass detectors*

The first efforts towards GW detection were performed by J. Weber in the 1960s [23] with his resonant mass detectors. The principle of detection behind resonant mass detectors lies in considering that a GW passing by perpendicular to a certain

material could excite the natural vibration modes of the material, and by means of an array of sensors, we could measure its deformation. The principal idea is to build a solid with a high mechanical quality factor Q, which means a low dissipation of energy when it oscillates at a specific frequency.

Weber's first design was built in 1966 and consisted in an aluminium cylindrical bar two meters long and half a meter in diameter, held at room temperature and isolated from vibrations in a vacuum chamber, working at a resonance frequency of around 1.6 kHz. Although Weber claimed that he detected GW radiation [24], it was later demonstrated that with his detector it was not possible to detect GWs [25, 26]. Nevertheless, it is widely recognised that his efforts opened the field of GW detection, allowing us nowadays to do research in such a challenging field.

Figure 5: Professor Joseph Weber with a GW detector (Credits: Special Collections and University Archives, University of Maryland Libraries www.umdrightnow.umd.edu).

Over the next decades major improvements were constantly performed in such detectors, applying cryogenic techniques to reduce thermal vibrations and many other enhancements like in the detectors Allegro [27], Antenna Ultracriogenica Risonante per l'Indagine Gravitazionale Astronomica (AURIGA) [28], Explorer [29], Niobe [30] and Nautilus [31].

In general, resonant-mass detectors are cheaper and easier to build than interferometers and potentially have a high sensitivity, but their main drawback is that they are narrow band detectors, as opposed to laser interferometer detectors, which are broad band detectors. Resonant mass detectors could only detect GWs in a very narrow frequency range, which is the frequency at which the bar has its resonance peak.

1.4.2 *Laser Interferometry detectors*

The development of laser interferometry techniques soon emerged as an interesting alternative to GW detection in order to replace resonant mass detectors. Replacing a single vibrating mass by two TMs with an interferometer measuring their relative distance brings several advantages, like the the widening of the operational bandwidth and the improvement of the sensitivity.

In laser interferometry detectors, we measure the distance fluctuation between two test bodies caused by a passing GW by means of an interferometer. A typical detector consists in at least two arms, as illustrated in Figure 6. If we consider that a GW travels perpendicular to our detector, it will squeeze one of the arms while stretching the other, causing a phaseshift when we recombine the light coming from the two arms. According to Lobo [32], in the case of a GW travelling perpendicular to our detector, the phase variation will be given by:

$$\delta\phi = 2\frac{\omega_L}{\Omega_{GW}} h_+ \sin\frac{\Omega_{GW}\,\tau}{2} \tag{1.13}$$

where ω_L is the laser angular frequency, Ω_{GW} the angular frequency of the GW which induces a polarised strain h_+ in the direction of the interferometer's arms, and τ the proper time it takes the laser beam to go back and forth in a single arm of distance L ($\tau = 2L/c$).

On-ground interferometric detectors are limited in different parts of their sensing bandwidth by different noise sources:

- SEISMIC NOISE AND GRAVITY GRADIENTS: they start to dominate at frequencies below 10 Hz. Seismic noise is produced by Earth's natural seismic activity, wind, ocean activities an even human vehicle traffic. In GW detectors, this noise is filtered or attenuated by mounting the different elements of the optic system in complex pendulum suspensions, and using different materials as isolators. Gravity gradients are caused by changes in the local newtonian field, like fluctuations in atmospheric pressure, variations in seismic density waves, and basically any

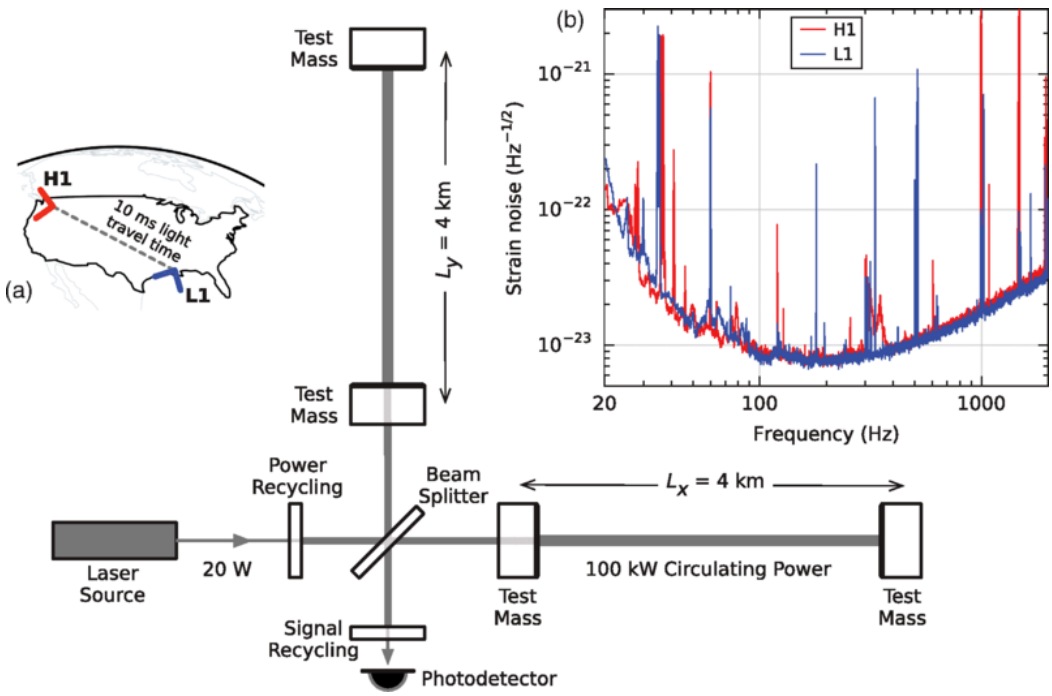

Figure 6: (a) Simplified schematics of the LIGO interferometer, with the position of both detectors in the USA. (b) Sensitivity curve for LIGO detector (Credits: [5] www.ligo.caltech.edu).

big change in the distribution of mass near the mirrors.

- THERMAL NOISE AND GAS NOISE: they are dominant in the middle band of the detector, between 10 and 200 Hz. On the one hand, thermal noise is caused due to the small fluctuations of the atoms of the mirrors and their suspensions. On the other hand, gas noise is caused by the interactions of the residual gas particles in the vacuum chambers with the mirrors and the laser light.

- QUANTUM NOISE: it limits the sensitivity of the detector for frequencies above 200 Hz. This noise is composed by a combination of shot noise (acting at higher frequencies) and photon radiation pressure (acting at lower frequencies). Shot noise is caused by the random distribution of the arrival of photons at the detector as we increase the frequency. This effect can be mitigated increasing the laser power, but at the cost of increasing the radiation pressure, which becomes a dominant noise source when using a powerful enough laser. The solution to increase the sensitivity keeping a compromise between the two previous effects is to inject squeezed states of light taking advantage of Heisenberg's uncertainty principle [33].

Some of the on-ground interferometric detectors are LIGO [13] in the United States of America (USA), with his two detectors in Hanford, Washington State (one operational and the other for testing and prototyping) and another operational one in Livingston, Louisiana. Virgo [14], located in Pisa, Italy, and GEO600 [34] in Hannover, Germany, are the other interferometric detectors currently operating. LIGO and GEO600 have performed science runs together in the past, al-

though the current sensitivity in GEO600 makes it difficult to detect a GW. On the other hand, LIGO and Virgo have performed science runs together, and during the last science run they were emitting live alerts for possible GW candidates, allowing for the possible detection of electromagnetic counterparts. Kamioka Gravitational Wave Detector (KAGRA) [35] is another detector in Japan which was recently completed, and is about to start observations by the time of the writing of this thesis. It is expected to join LIGO and Virgo in joint observations in 2021-2022. Besides, LIGO has planned to add another detector in India, called Indian Initiative in Gravitational Wave Observations (IndIGO) [36] in the following years.

All this big network of detectors will allow for a better sky localisation of the different GW events. Although the first GW detected did not have a good sky localisation due to only having two detectors available at that time (the two from LIGO), this has improved since Virgo started joint runs together with LIGO, and the situation will improve even further in the future when KAGRA and IndIGO become operative too, building a worldwide network of GW detectors.

The Einstein Telescope [37] and Cosmic Explorer [38] are future detectors in the so called 3rd generation of on-ground interferometric detectors. They will bring several improvements in sensitivity and reach, thanks to the use of new techniques, like cryogenics, to reduce the mirrors thermal noise and underground facilities, to reduce the seismic noise. Nevertheless, this generation of detectors are expected for the decade of 2030.

1.4.3 *Pulsar Timing Array detectors*

The idea behind Pulsar Timing Arrays (PTAs) is to use the highly accurate emission of the pulses emitted by millisecond pulsars to detect GWs. A GW passing between the Earth and a millisecond pulsar could in principle affect the arrival time of the pulses to the Earth in the order of nanoseconds over periods of time going from weeks to decades, so the frequency range at which PTAs work can go from 10^{-6} to 10^{-9} Hz.

The current PTA projects are the Australian Parker's Pulsar Timing Array (PPTA) [39], the European Pulsar Timing Array (EPTA) [40] and the American NANOGrav [41]. Since approximately 2010, all of them started sharing data and working together to create the IPTA [16]. In the future, the SKA [42] is also expected to greatly contribute in the detection of GWs in this frequency range, due to the high improvement in sensitivity it will bring to radio detection.

Since the timescales are so large, the detection of GWs using PTAs require long sets of data, of the order of years. Actually, there is open discussion about the probabilities of detecting GWs using PTAs anytime soon [43].

1.4.4 *Cosmic Microwave background detectors*

If we want to study GWs emitted at even lower frequencies, in timescales of the order of the age of the universe, the way to go is to study the polarisation of the CMB. The idea is trying to observe the B-mode polarisation of the CMB that would have its origin in the GWs originated during early stages of the Universe evolution. If that is the case, this B-mode polarisation map would have a quadrupole signature imprinted by primordial GWs originated during the early stages of the Universe.

BICEP [20, 21], with its different generations, and the Keck array [22] have been some of the experiments aiming to find the imprint of inflationary GWs in the CMB. In March 2014, BICEP-2 claimed they had found the imprint of GWs from the very early universe [44], but a posterior analysis using data from Planck [45] assigned the origin of the observed signal to interstellar dust in the region [46].

The actual generation of observations are being carried out by BICEP-3 [47] and the Keck Array [22], and they have already put some constraints on primordial GWs [48]. The future for this kind of observations is the BICEP array [49], which is expected to be fully installed for the 2020 observing season.

1.5 SPACE-BASED DETECTORS:LISA

With the detectors presented so far, the bandwidth around the millihertz remains veiled. This bandwidth is of particular interest because many astrophysical and cosmological sources are expected to emit GWs in this region. This is the region where we expect to find the coalescing of Supermassive Black Hole Binaries (SMBHBs), the capture of compact objects by SMBHBs, and many more. In Figure 7 we show an example of different GW sources emitting around the millihertz, together with their characteristic strain amplitude and the sensitivity of a space-based observatory like the future LISA.

Taking into account that going below the hertz is very difficult for on-ground GW observatories due to seismic noise and gravity gradients limitations, a concept for a space-based GW observatory started to flourish in the 1980s. The advantage of going into space is not only to be able to go below the barrier of the hertz, but also to be able to build much larger detectors. In space the arms of the detector can be orders of magnitude larger, therefore improving the sensitivity of the detection as explained in Section 1.2. After some years, the concept about a GW observatory in space converged into the project Laser Gravitational Observatory (LAGOS) [50, 51], and consisted in three spacecrafts directly orbiting the Sun in near one year orbits, using laser interferometry and drag-free techniques to maintain a free-fall motion between the TMs. Some years later, in the 1990s, the concept evolved into an early design of what we nowadays know as LISA. It emerged as a joint proposal [52] between ESA and NASA to ESA's "Call for Mission Proposals" for a third medium-size project (M3).

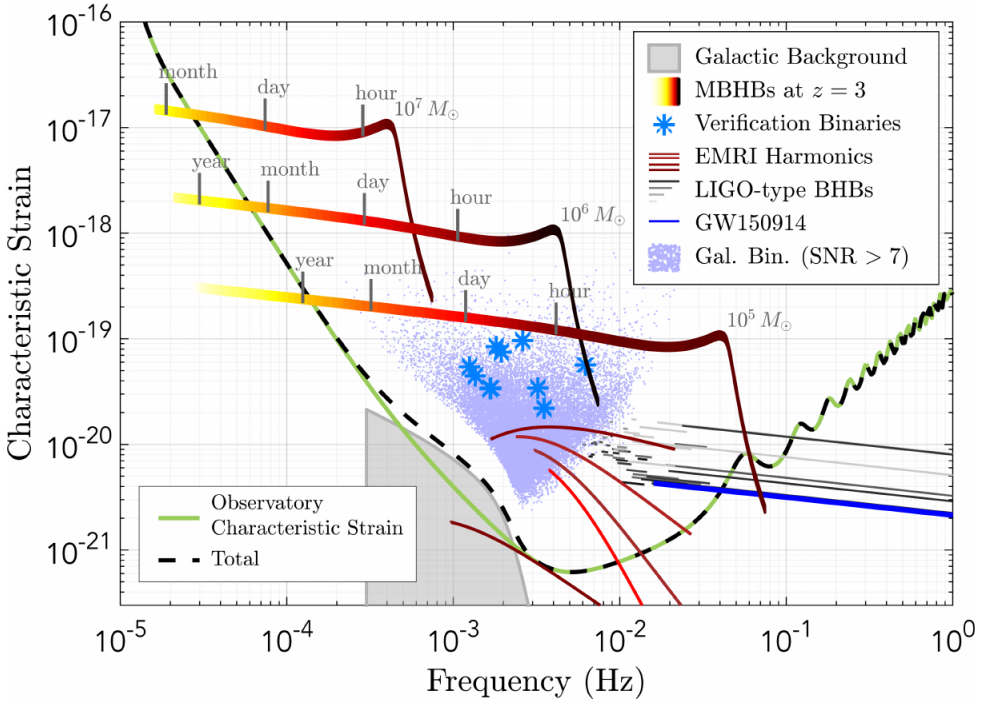

Figure 7: Possible GW sources for LISA (Credits: [1] www.elisascience.org).

ESA and NASA followed a joint schedule during the next years, but in 2012 NASA announced they could not follow on the project due to budget problems, and ESA was forced to continue with a reduced version called New Gravitational Observatory (NGO) [53], which only had two arms separated by one million kilometres. Later, in 2013, a new proposal was submitted for ESA's L2 call for missions called evolved LISA (eLISA) [54] that fitted in the concept of NGO, and although it was not selected, ESA decided that the science theme for the following L3 mission would be *The Gravitational Universe*. It was finally in January 2017, after the GW detection of LIGO [5] and the great success of LPF [4] when LISA was selected as ESA's L3 mission as a project led by ESA with contributions from NASA.

LISA will be a GW observatory in space. It will consist of three spacecrafts separated by 2.5 million kilometres each and forming a triangular constellation, as we show in Figure 8. The LISA constellation will trace the Earth with an angle of around 20° with respect to the Sun, a declination of 60° with respect to the ecliptic and orbiting the Sun at one Astronomical Unit (AU). The satellites will have laser links joining each of the sides of the triangle, and so, performing interferometry in three different arms. This three-arm configuration, as opposed to typical two-arm configurations for on-ground detectors, allows for better sky localisation, provides information about the wave polarisation and also gives some system redundancy. It is worth pointing that the beam divergence over several million kilometres limits severely the received laser light power, to the point that each spacecraft is expected to receive just some hundreds of pW from the original 2 W emitted, which rules out passive reflection for the return path. Instead, each spacecraft acts as an active transponder, transmitting a fresh high-power beam that is phase-locked to the incoming weak beam, with a fixed offset frequency.

The constellation is fully symmetric, with similar measurements taking place in both directions along each of the three arms.

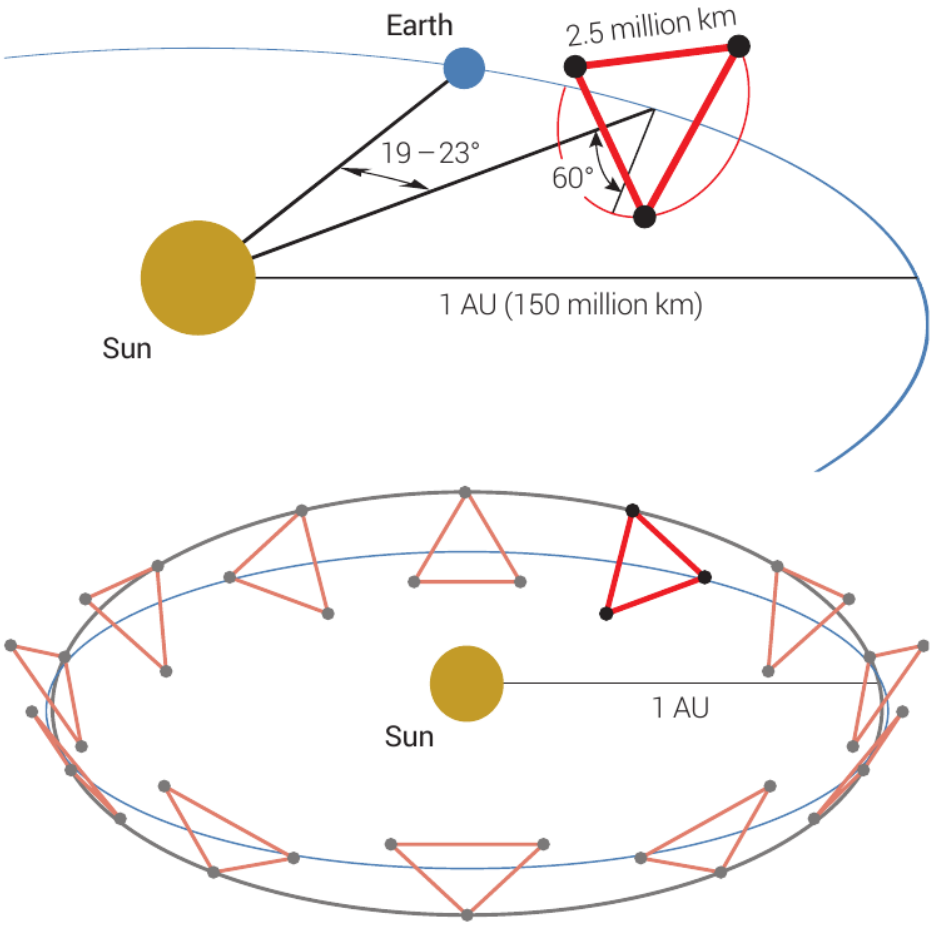

Figure 8: View of the proposed LISA orbit (Credits: [1] www.elisascience.org).

Each spacecraft will contain two Moving Optical Assemblies (MOSAs), which will consist in a telescope to gather the light coming from the other spacecrafts, two Optical Benches (OBs), where the interferometry is performed and two Gravitational Reference Sensor (GRS), which hold the TMs inside their respective Electrode Housings (EHs), which in turn are placed inside two vacuum enclosures. These TMs will be platinum-gold cubes of 46 mm each edge which actuate as end mirrors for the interferometric system and are released in the vacuum chamber in near free-fall conditions. The TMs will be kept in free-fall inside the spacecraft using a precision attitude control system called drag-free control loop [55]. Both MOSAs can rotate in order to point accurately to the other spacecrafts, and will be joined by an optical fibre cable. The principle of detection is that if a GW passes trough the constellation, it will vary the optical path between the TMs of one arm relative to the other arms, therefore triggering a GW detection.

Around the millihertz, LISA strain sensitivity should be around 10^{-21} $Hz^{-1/2}$. Therefore, this interferometric system is expected to be accurate enough to measure differences of around 10 pm $Hz^{-1/2}$ in the round trip path length between arms. This is not a simple task, since the spacecrafts are exposed to external perturbations like the solar radiation pressure or the solar wind, that induce net forces and fluctuations to the spacecrafts that can perturb the TMs geodesic motion. Therefore, one of the main goals of the spacecrafts is to isolate the TMs from these kind of environmental perturbations in order to keep the TMs in free-fall. The spacecraft position does not then translate into a GW signal. Nevertheless, the spacecraft needs to keep centred around the TMs to reduce local noises and to avoid the TMs to touch the inner walls of the EH in the worst case, but also to prevent that the spacecraft motion or any associated control force is transferred to the TMs. To achieve this goal, the motion of the spacecraft with respect to the TMs is measured by a capacitive sensor that measures the change in electrical capacitance between the TMs and the set of electrodes that surround them. If this system detects that the spacecraft has moved with respect to the TMs, a command is sent to a set of thrusters that exert forces of the order of μN to keep the spacecraft centred around the TMs. This technique is called drag-free control [55].

In a typical Michelson interferometer, a single light source is split and recombined after travelling an identical optical path length. The laser frequency noise is therefore cancelled when measured by the photodetector, since it is common to both laser beams. This is not the case for LISA, where there will be six different laser sources, one per TM. Thus, in LISA the frequency noise originated from the lasers is uncorrelated and not cancelled and will dominate the measurement of the distance between TMs. The technique used to deal with this problem is a post-processing technique known as Time-Delay Interferometry (TDI), which consists on forming combinations of different phasemeter outputs from different OBs with different time delays in order to create correlated signals to cancel the noise [56]. This technique must also deal with the fact that the absolute distance between satellites is not fixed, and can oscillate around 1% of the nominal distance between them (2.5 million kilometres).

The sensitivity of LISA is determined in the different frequency regions by:

- Antenna frequency response: in the higher frequency part of the LISA sensitivity band ($> 10^{-2} - 10^{-1}$ Hz), noise is dominated by the roll-off of the antenna transfer function. The longer the arms, the more sensitive the detector is to long-period GWs, but its sensitivity to wavelengths shorter than the arms is reduced. The noise in the antenna goes as τf^{-1} for frequencies above the inverse of the round-trip time τ, that for LISA would be around 8-9 seconds.

- Shot noise: in the middle of LISA sensitivity band, around $10^{-3} - 10^{-2}$ Hz, noise is dominated by the photon rate fluctuations in the laser beam. This noise causes a noisy path difference δL inversely proportional to the square root of the received laser power. This noise can be reduced by increasing the rate of photons arriving to the photoreceiver, which can be achieved, amongst other ways, by

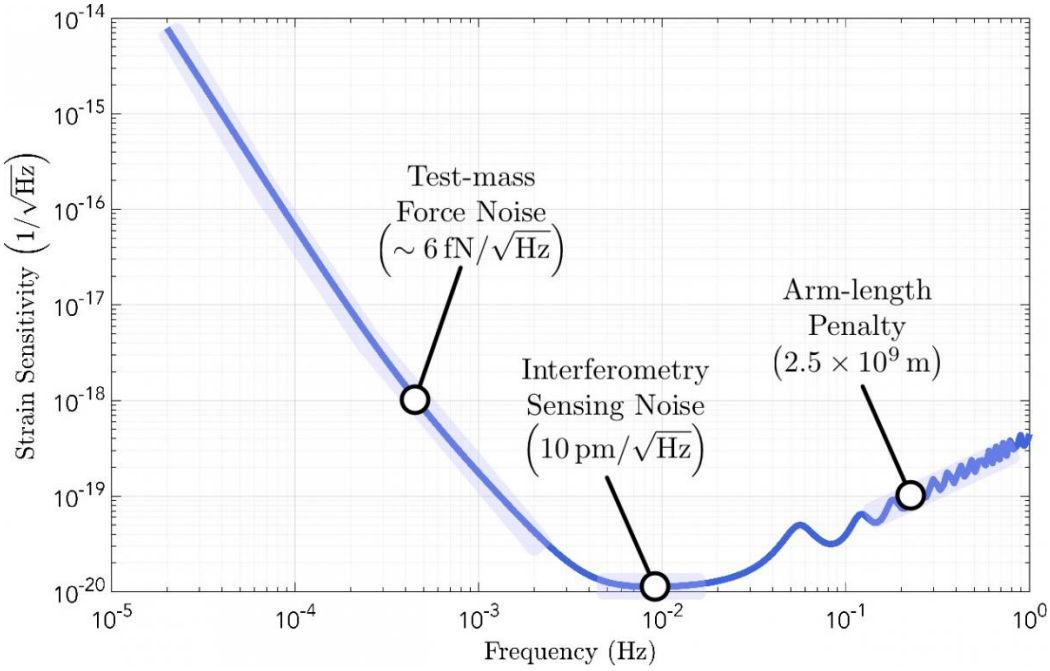

Figure 9: Expected strain sensitivity curve for LISA (Credits: www.lisamission.org).

increasing the laser power or by using a larger telescope.

- ACCELERATION NOISE: in the lower part of LISA sensitivity band, below 10^{-3} Hz, noise is dominated by local forces on the TMs that can not be shielded by the drag-free control system. This phenomena have been widely studied in LPF and will be studied in more depth in Chapter 2. Some of these forces are caused by: temperature fluctuations, magnetic forces, residual gravity effects, cross-talks from electrostatic actuation noise, charging of the TMs due to cosmic and solar radiation, etc.

If we consider all these different noise sources and their implications in the different frequency bands, the expected LISA strain sensitivity curve is shown in Figure 9.

As previously mentioned, LPF has tested a lot of the necessary technology to carry out GW measurements in space, but not only LPF has been relevant for the future LISA. Gravity Recovery and Climate Experiment Follow-On (GRACE-FO) [57] was launched in 2018 and has been the first space mission to successfully perform long distance inter-spacecraft laser interferometry. It consisted in two satellites orbiting the Earth and separated by about 220 km with the goal of monitoring Earth's water movements. Unfortunately, TDI technology has not been tested on it, since GRACE-FO Follow-On has only one arm and at least two are needed to perform TDI.

2 THE LISA PATHFINDER MISSION

As seen in the previous chapter, a space mission like LISA brings up several technological challenges that need to be addressed before it becomes operational. Some of these aspects can not be proven on-ground, like for example achieving a high level of free-fall for frequencies around the millihertz. Because of this, ESA and NASA decided to launch a technology demonstrator for LISA: LPF. Some aspects of LISA can be proven on-ground (like the local interferometer noise) and some haven already been proved in space – like performing interferometry between spacecrafts, as in GRACE-FO [57]. Nevertheless, although some experiments with torsion pendulums [58, 59] can characterise some of the noise sources that produce forces on the TMs, not all the sources can be studied on-ground this way, and some of these contributions may change when going to space. The acceleration noise in the TMs is responsible for limiting the instrument sensitivity for frequencies around the mHz and down to 20 μHz, until which LISA will be able to measure [1]. Spurious forces on the TMs appear due to a wide variety of effects, ranging from: temperature stability, electric charging of the TMs, interaction of the TMs with the local magnetic field, etc. These effects are localised, meaning that the interaction between spacecrafts does not play any role in these kind of forces, they are all produced within each spacecraft. Therefore, it was decided to squeeze one of LISA arms into one single spacecraft, putting both TMs inside it in order to study and reduce the spurious forces on them. While this prevents the detection of GWs, it perfectly allows the study of the forces on the TMs. That is the birth of the idea behind LPF.

This chapter is organised as follows. First, we start with a brief historical description of the project until we arrive to its launch and mission operations, to end this introduction explaining in a simplified way in what LPF consists and which were its goals. Then, we move into explaining in depth the LISA Technology Package (LTP), which is the main scientific instrument on the satellite. We perform an exhaustive analysis of all its systems and explain how they contribute to the satellite scientific performance. Once we have described the satellite and its components, we move into explaining how the main scientific output of LPF, Δg, was computed. Afterwards, we review which are the known forces that affect the geodesic motion of the TMs and briefly describe each of them. We end this chapter doing a review of how were LPF mission operations, and which were the results obtained during them.

2.1 INTRODUCTION

LPF was proposed for the first time in 1998 as European LIsa Technology Experiment (ELITE). It consisted of a single spacecraft in geostationary orbit with a goal in differential acceleration between its two TMs of 10^{-14} fm s^{-2} Hz$^{-1/2}$ over the frequency range of 1-100 mHz. The original proposal was refined and proposed

to ESA in 2000 to fit into the Small Missions for Advanced Research in Technology (SMART)-2 announcement. The proposal consisted in a joint LISA and Darwin pathfinder mission, consisting in two free-falling spacecrafts and three payloads: LTP [60], Darwin Technology Package and a NASA provided LISA technology package. The goals of the mission were to demonstrate drag-free control (for LISA) and formation flying (for Darwin). The mission was approved in November 2000.

After the initial industrial studies, the mission was reduced to a single spacecraft, cancelling Darwin Pathfinder and renaming it to LPF. At the beggining, LPF carried two payloads, the European LTP and NASA's Space Technology 7 Disturbance Reduction System (ST7-DRS) [61]. Both payloads were completely functional on their own, consisting in two inertial sensors, a laser metrology system, micro-Newton thrusters and drag-free control software. However, after the initial development phase, the ST7-DRS was descoped and finally consisted on micro-Newton thrusters and a dedicated processor running the Drag-Free Attitude Control System (DFACS), relying on LTP for the inertial sensing.

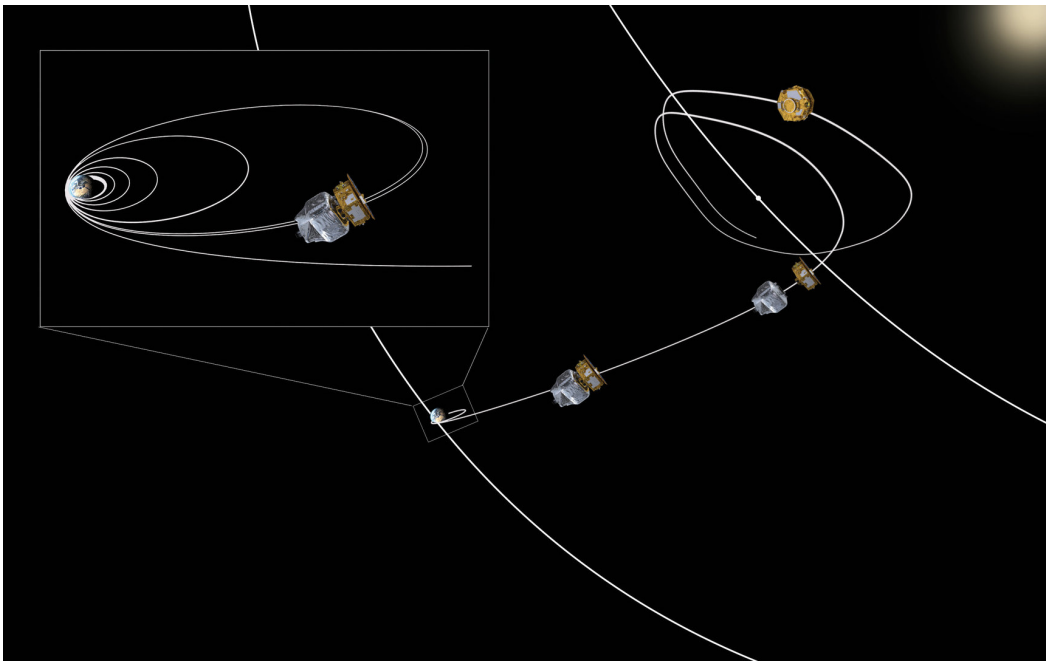

Figure 10: LPF's trip to L1 (Credits: www.esa.int).

LPF was launched from Kourou, French Guiana on December 3rd, 2015. After some orbit elevation maneuvers, it started its journey to L1 – see Figure 10 for a schematic view. This location is 1.5 million kilometers away from Earth towards the Sun and has the particularity that, at this location, Earth counters the gravitational pull coming from the Sun to the point that the orbital period of any object at this location will be the same as Earth's orbital period. Apart from some minor setbacks, it operated continuously until July 17th, 2017, when it was passivated by ESA.

LPF consisted in a simplified version of LISA, where one of LISA arms is squeezed into a single spacecraft to test the free-fall performance of the TMs. The distance between the TMs is thus reduced to 38 cm to fit into a single spacecraft – in com-

parison with the 2.5 million kilometers in the case of LISA's TMs. Therefore, the main goal of the mission was not to detect gravitational waves, but to validate the different subsystems and technologies necessary for the future LISA, such as to achieve picometer resolution interferometer in space, prove drag-free control, and many others. The satellite hosted two payloads. First, the LTP [60], ESA's contribution, and second, the ST7-DRS [62], NASA's contribution. Both will be explained more extensively during the chapter.

LPF's main goal was to achieve a level of residual differential acceleration noise between the TMs of:

$$S_a^{1/2}(f) \leqslant 3 \times 10^{-14} \sqrt{1 + \left(\frac{f}{3\ \text{Hz}}\right)^2}\ \text{m s}^2\ \text{Hz}^{-1/2} \tag{2.1}$$

in the frequency band between $1 < f < 30$ mHz. As we will see later in the section about LPF results, this goal was achieved far beyond this requirement, making LPF a complete success.

LPF TMs are cubes of a gold-platinum alloy. This alloy is used because of its high density, making the TMs more massive and thus reducing the acceleration noise the different physical effects produce on them. Its also used in order to reduce the magnetic forces acting on the TMs due to the local magnetic field and magnetic field gradient, as well as for reflecting the laser beam of the interferometer, acting as the end mirrors of the system. The masses have an edge of 46 mm and weight 1.96 kg. Each TM is located inside an EH, which is in charge of sensing the relative position of the TM with respect to the satellite by means of a series of electrodes along its walls and control their movement. Each of the two TM-EH system composes the main part of each of the two GRS, which will be explained later on. The requirement shown by Equation (2.1) was only needed to be achieved along the axis joining the two TMs, i.e. the x-axis. The instrument responsible for achieving this differential measurement was an interferometer able to measure picometer displacements, and which monitored the motion between both TMs and between one TM and the spacecraft. If a large enough displacement between this TM and the spacecraft was measured, a micronewton propulsion system corrected the position of the spacecraft to keep this TM centred inside its EH.

The two main payloads on-board the satellite were the LTP and the ST7-DRS.

- LTP: the LTP [60] was the European payload for LPF, and contained all the necessary systems for the correct functioning of the spacecraft scientific operations. This payload will be explained in detail in Section 2.2.
- ST7-DRS: the ST7-DRS was NASA's scientific payload to the mission. ST7-DRS contained two main elements: an alternative set of drag-free control laws implemented on a separate computer, and an alternative micropropulsion system based on a novel colloidal microthruster technology. During mission operations, the propulsion and actuation systems were switched and similar results were achieved between LTP and ST7-DRS [62].

2.2 THE LISA TECHNOLOGY PACKAGE

The LTP was the main scientific instrument carried on-board LPF. It consisted on two GRS, the Optical Metrology System (OMS) and the different subsystems which were needed to perform the different experiments. The central part of the LTP consists on the two GRS with the OB of the OMS located in between and some additional subsystems, like sensors from the Data and Diagnostics Subsystem (DDS). This formed the LISA Core Assembly (LCA). All the other equipment like the different control units, power management units, batteries, etc. were located in different compartments around. See Figure 11 for a more clear view. The LCA was in turn attached to the rest of the satellite by means of eight suspension struts, as seen in Figure 12.

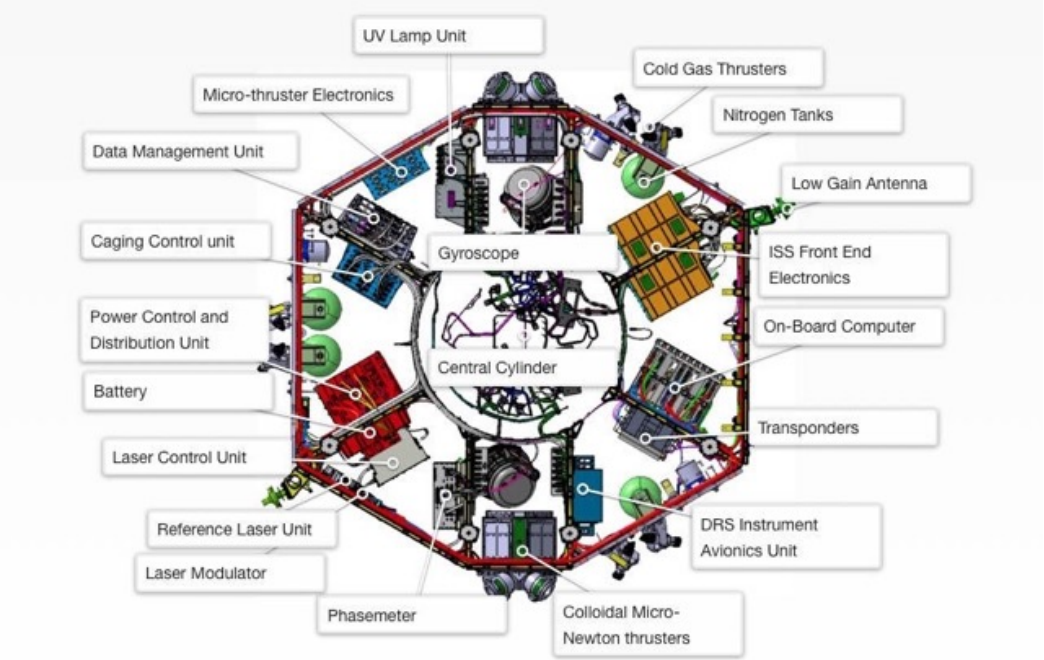

Figure 11: x-y plane view and distribution of the different systems inside LPF, with the LCA in the middle (Credits: www.esa.int).

The core components of the LTP were the two GRS, whose main mission was to keep the TMs isolated and in geodesic motion and the OMS, which was in charge of measuring the relative distance between the two TMs. It was also composed by other subsystems needed to keep the experiment running, like the DFACS, which controlled the motion of the spacecraft in order to keep TM1 centred in its EH, or the DDS, which incorporated several sensors to help studying the environment within the satellite and the payload computer to control all the data and LTP systems.

2.2.1 *The Gravitational Reference Sensor (GRS)*

There were two GRS inside the spacecraft, each one holding one of the TMs. The GRS consisted of several systems, which were aimed to: sense and control the TMs position, to keep them isolated from the environment and to allow for a a free-

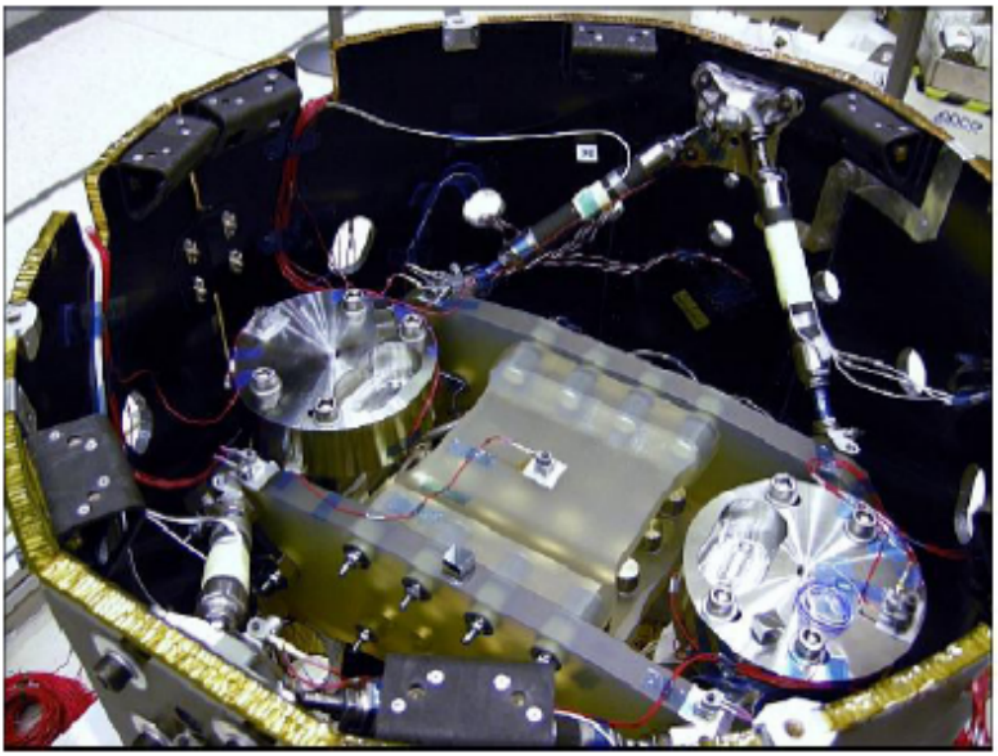

Figure 12: View of the LCA, which was attached to the external thermal shield by a series of struts (Credits: Airbus Space and Defence).

fall movement along the axis joining both TMs. Each GRS consisted in an Inertial Sensor (IS), which held an EH which was in charge of sensing and controlling the position of the TM, a vacuum system, the Front End Electronics (FEE), a caging mechanism and the charge management system. See Figure 13 for an schematic view.

The measurements of the system were provided by an accurate capacitive system that constantly monitored the variation of electrical capacitance between pairs of electrodes and the TMs. There were a total of eighteen electrodes, with the layout shown in Figure 14. Not all of them had the same purpose: twelve were for capacitive sensing and actuation on the different Degrees of Freedom (DoFs) and the other six were used for inducing bias voltage signals on their corresponding TM. The distance between these electrodes and the external faces of their corresponding TM was of 4 mm.

The read-out electronics, the Inertial Sensor Subsystem Front End Electronics (ISS-FEE), was arranged in such a way that the electrodes of opposite faces were combined via capacitive sensing. That meant that a change in the position of a TM induced a bipolar differential signal that was introduced as input data in the DFACS – which we will explain in the following. Then, the ISS-FEE could correct the TM displacement applying a different combination of forces and torques using these electrodes [63].

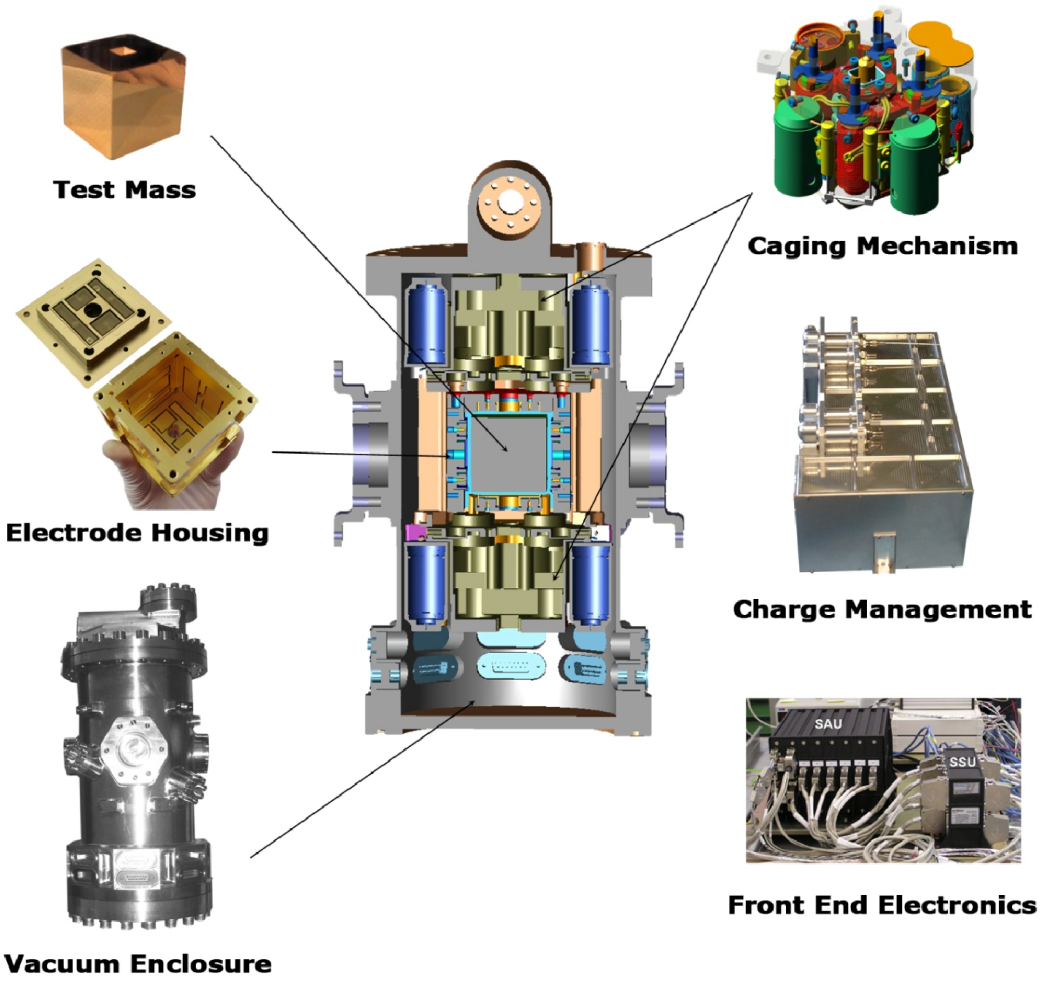

Figure 13: Lateral view of the GRS and its different components.

The ISS-FEE operated in two different modes: High Resolution (HR) and Wide Range (WR). On the one hand, the HR provided less noisy measurements, and therefore was the preferred option during mission operations. It provided a sensitivity of 1.8 nm $Hz^{-1/2}$ at 1 mHz per pair of electrodes (which implied measurements of 1.5 aF $Hz^{-1/2}$) in a range of ± 200 µm and an actuation authority of 5 nN. On the other hand, the WR provided a greater sensing range, approximately up to 4 mm, the size of the gap between the electrodes and the faces of the TM. This came with a cost, since its sensing noise was a few orders of magnitude worse than the one from HR [64].

The vacuum system allowed to keep the TMs inside the EHs reaching pressure values as low as 1µPa [65, 66]. This was achieved thanks to the fact that after arriving at L1 and successfully releasing the TMs, a venting system opened to space, slowly releasing gas particles from inside the EHs to space.

Due to the charge associated with collisions from cosmic rays and solar charged particles, a discharge system was installed inside each GRS. Since the TMs were isolated and not in contact with any surface, the discharging was performed taking advantage of the photoelectric effect using a system of Ultraviolet (UV) light

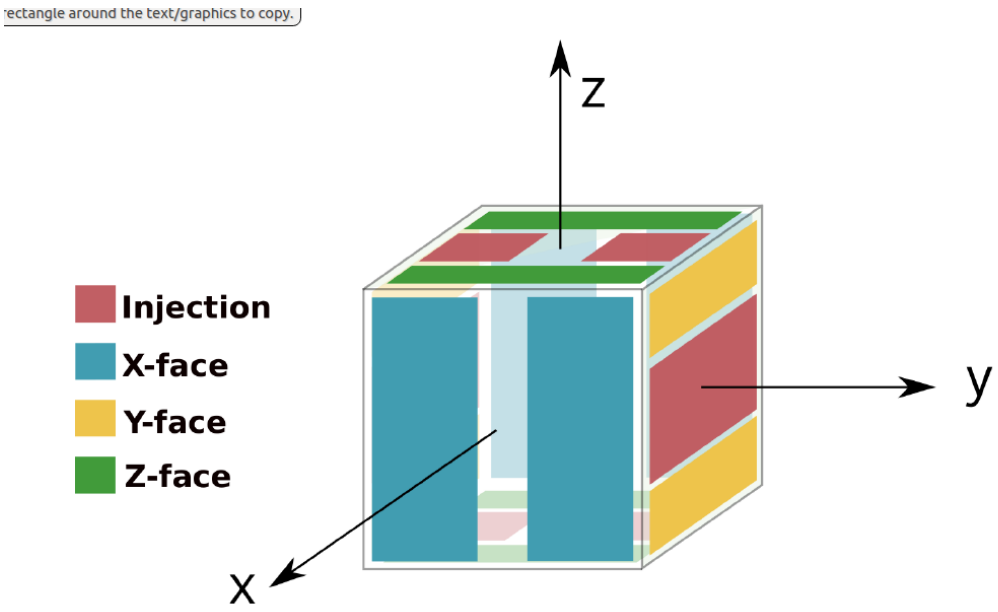

Figure 14: Distribution of the different electrodes that surrounded each of the TMs.

coming from mercury vapour lamps. Depending if the TMs were positively or negatively charged (this was measured via the electrodes), the lamps shone over the TM or over the electrodes in order to discharge the TMs. The results of the experiments which measured the charging of the TMs and their contribution to the noise measurement can be checked at [67, 68].

Finally, the caging and grabbing mechanism was in charge of keeping the TMs in place during the launch and transfer and to release them once the satellite arrived to L1 [69]. Two different mechanisms were installed on the spacecraft to achieve these goals. First, the Caging and Venting Mechanism (CVM) grabbed the TMs with eight fingers to withstand the high forces experienced during the launch on the rocket. And second, the Grabbing, Positioning and Release Mechanism (GPRM), which held the TMs in place with a less constraining system, only holding them centred in their respective EHs by means of two fingers in the $\pm$ z faces. These two fingers were slowly retracted once LPF arrived to L1, but also actuated as a fail-safe mechanism, being able to grab again the TMs if needed [70]. This system released the TMs with velocities smaller than 5 μm/s and 100 mrad/s [69].

2.2.2 *The Optical Metrology System (OMS)*

The unprecedented level of geodesic motion achieved by the TMs thanks to the GRS and the other spacecraft systems was measured thanks to the nice performance of the OMS, which was able to measure displacements of $\sim$ 10 pm $\mathrm{Hz}^{-1/2}$ in most of the LPF bandwidth of interest thanks to laser interferometry. The laser used on LPF consisted in a Nd:YAG laser with a wavelength of 1064 nm and a power of 25 mW [71, 72]. The interferometry was split mainly between two benches:

- Modulation Bench (MB): It was composed of the optical fibers, Acousto-Optic Modulators (AOMs) and the first beam splitter (BS_0). The initial beam was divided in two paths, with each of them shifted in frequency with the AOMs for a different amount, one at 80 mHz and the other at 80 mHz + 1.2 kHz, and therefore, with a heterodyne frequency of 1.2 kHz. After this, by means of the optical fibers, the two beams continue their path on the OB.

- OB: The OB was composed of a block of Zerodur base plate with mirrors of fused silica [71, 73] which was placed between the two GRS. In this bench, the beams were recombined and carried to the Photodiodes (PDs).

When the two beams with their shifted frequencies arrived to the OB, the different beam splitters formed a system of four Mach-Zender interferometers [74] that performed the following measurements:

- x_{12} *interferometer*: This was the main measurement of the system, which measured the relative motion between both TMs along the x-axis, namely called x_1-x_2. This interferometer readout also provided measurements of the relative angles between the TMs in the y-axis (η) and z-axis (θ). The measurement of x_{12} drove the electrostatic system of TM2, which applied the necessary forces on its different faces in order to follow the movement of TM1.

- x_1 *interferometer*: This interferometer provided the measurements of the relative motion between TM1 and the OB. As in the previous case, it was also sensitive to the relative rotations around η and θ between TM1 and the OB. The measurement provided by this system drove the drag-free control loop, which commanded the thruster systems to exert the neccesary forces to keep TM1 centred inside his EH.

- *Reference interferometer*: This interferometer measured environment perturbations and path-length noise originated outside the OB. Its measurement was subtracted to the readout of the other interferometers to remove common-mode noise disturbances and increase their sensitivity.

- *Frequency interferometer*: This interferometer had an intended 38 cm path-length mismatch, which made it specially sensitive to laser frequency fluctuations. Its phase was used to stabilise the frequency [75].

After receiving the signal from the PDs, they were sent to the phasemeter. The phasemeter extracted the data at the heterodyne frequency and performed a single discrete Fourier Transform to measure the phase of the signals at the heterodyne frequency. The PDs used on LPF were quadrant PDs, which are sensitive to displacements and angular fluctuations of the beams. Two different approaches were used to measure these angles [71, 76]:

- *Differential Power Sensing (DPS)*: In this approach, beam displacements were measured on the PD quadrants and the TM angles inferred from it. Basically, the mean laser power arriving at one half of the photodiode was subtracted to the mean laser power arriving at the other half, normalised by the total power collected.

- *Differential Wavefront Sensing (DWS)*: With this other approach, the TM angles were obtained through the measurement of the relative phases between the two beams on each PD quadrant using the phasemeter. Although the DPS technique provided a wider dynamical range, the DWS was used in the different control loops because it provided better sensitivity.

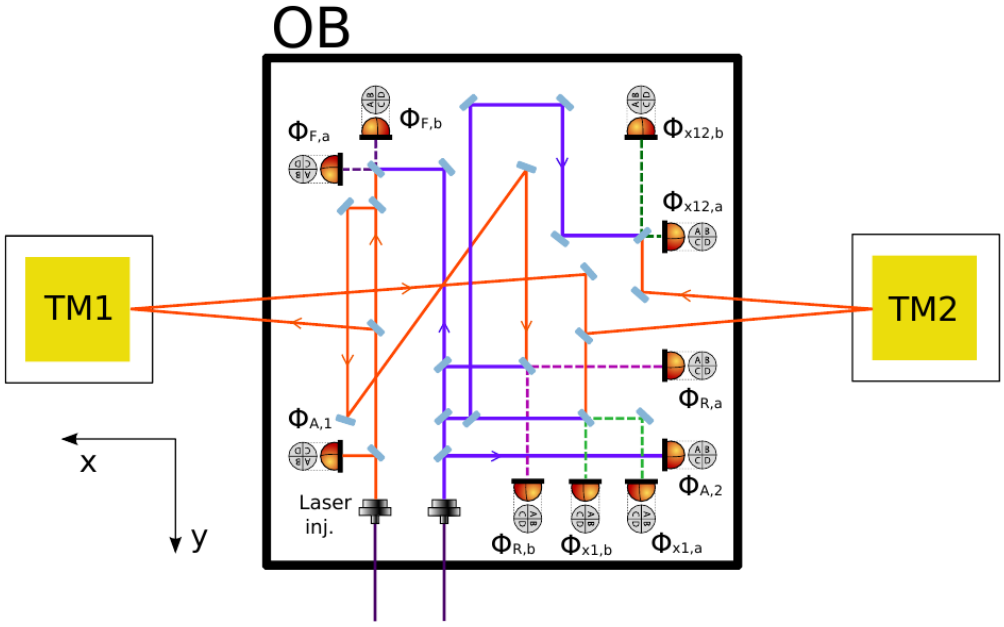

Figure 15: Schematics of the OB on-board LPF and its main measurements. On the one hand, the ϕ_{12} quadrant photodiodes measured the relative displacement of TM1 with respect to TM2, and the angular relative position around y and z axis between them. On the other hand, ϕ_1 quadrant photodiodes measured the same displacement and angles on TM1 but with respect to the spacecraft. The final relative displacements x_{12} and x_1 were obtained by subtracting the reference measurement ϕ_R to both, ϕ_{12} and ϕ_1. The suffixes a and b refer to each of the redundant photodiodes of each interferometer measurement, while the dashed lines represent the recombined beams for each measurement.

Each interferometer measurement was actually made by two quadrant PDs for redundancy. Considering that there were two additional PDs to control the amplitude stability of each injected laser beam, a total of ten quadrant PDs were placed on the LTP's OB, as can be seen in Figure 15. Summarising, LPF's OMS was composed by the two benches, the MB and the OB, plus the Reference Laser Unit, the Laser modulator and the Phasemeter. The whole system was controlled in turn by the Data Management Unit (DMU) [77].

2.2.3 *Drag-Free Attitude Control System (DFACS)*

The DFACS [78] was the control system in charge of keeping a free-fall environment for the TMs in order to be able to achieve the mission goals. This system worked using a series of sensors and actuators with which was possible to detect and measure disturbances on TM1, around which the satellite was centred, and to correct deviations from its geodesic trajectory using a capacitive suspension

control and a set of μN thrusters. The thrusters used in the LTP were a set of 12 μN cold gas thusters grouped in three different clusters [79]. These thrusters controlled the position and motion of the spacecraft above the bandwidth of 1 to 30 mHz, whereas below this bandwith, TM2 followed the movement of TM1 using the capacitive suspension control. Therefore, strictly speaking TM2 was not in geodesic motion, but its deviations were out of the instrument measuring band.

The DFACS controlled a total of 15 out of the 18 DoFs of the system: 6 for each TM and 3 for the spacecraft motion. These different DoF along with the LTP reference frame can be better visualised in Figure 16. Apart from maintaining the free fall environment for the two TMs, the DFACS was also in charge of keeping the solar array pointing to the Sun and the communication antenna pointing to Earth. This was achieved thanks to the star tracker (there were two of them for redundancy) which helped in controlling the attitude of the spacecraft, dealing with the rotation of the satellite, which was of about 2 degrees per day. During nominal performance, the spacecraft attitude was not subordinated to the star tracker sensing, but it was kept active in order to put the spacecraft in safe mode in the case it turned away more than 5 degrees from the Sun direction.

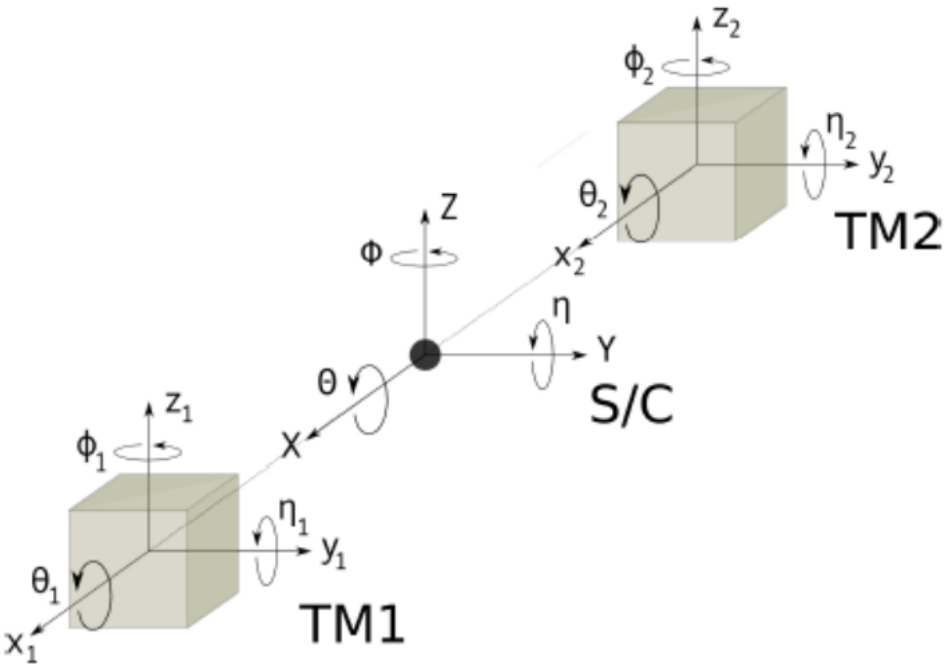

Figure 16: Different DoFs for the satellite motion and its reference frame centred between the two TMs.

Different modes of operation were available for the DFACS (or if we extrapolate it to the whole package, for the LTP), each one for different purposes:

- Attitude Mode: its purpose was to only control the attittude of the spacecraft, while the TMs remained mechanically caged.

- Accelerometer Mode: in this mode the TMs are electrostatically caged with a high gain and bandwidth. The motion of the two TMs is subjugated to the spacecraft motion in this mode.
- Normal Mode: the spacecraft is set to follow the drift on the x-axis of TM1, while the second TM is set to follow the spacecraft motion using high bandwidth controllers and capacitive sensors.
- Science Mode: in this mode both, the spacecraft and TM2 follow the x-axis drift of TM1. There are two submodes of interest within this mode:
  - Science Mode 1.1: in this submode the TMs motion is only measured using the capactive readouts of the GRS.
  - Science Mode 1.2: in this other submode, OMS readouts are used for the redundant measurements (x_1 , x_2, η_1, η_2, ϕ_1 and ϕ_2) together with capacitive measurements for the remaining DoF.

Science mode 1.2 was the relevant one for LTP scientific operations. The satellite spent most of its operating time in this mode, performing experiments and measurements. The main results obtained of the characterisation of the LTP propulsion system through these experiments and measurements can be checked at [80]. There were two important control loops to secure the correct performance of the system in science mode:

- The High-Gain Loop: this loop consisted in a high bandwidth controller that actuated in any required DoF of the spacecraft or the TMs. Its primary responsibility was to keep the spacecraft well centred around TM1.
- The Low-Frequency Suspension Loop: this other controller operated with a very low gain to minimise frequency components in the mHz band. This control loop was used for controlling over some critical DoFs whose actuation would interfere in the measurement of the relative acceleration between the TMs, like for example the x-motion of TM2, which was the one following TM1.

2.2.4 *The Data and Diagnostics Subsystem (DDS)*

The DDS [81] was a part of the LTP which was composed by a series of sensors and actuators intended to study different noise sources that could affect the TMs motion, like cosmic and solar charged particles, magnetic fields or thermal gradients around the TMs. The DMU, which coordinated and controlled most of the scientific instrumentation on-board the satellite also formed part of this system. We describe the different components of this system in the following:

RADIATION MONITOR: Variations in the electric charge of the TMs directly affected the sensing and actuation system of the GRS. These variations in the charging of the TMs could come from the exposure of the spacecraft to cosmic and solar charged particles – which were mainly photons. To study this radiation and their effect on the TMs, a radiation monitor was installed on-board LPF. The radiation monitor design was based in two PIN silicon diodes, and it was

capable of detecting particles above a threshold of 70 MeV – which were the approximate shielding the spacecraft offered to the TMs [82]. Besides, if a charged particle appeared traversing the two diodes (a coinciding event) the radiation monitor was able to classify the deposited energy in 1024 different bins up to 5 MeV. The results coming from the radiation monitor data and the experiments associated to it can be can be found in [67, 83, 84].

THERMAL DIAGNOSTICS: The LTP was equipped with a total of 24 thermal sensors and 14 heaters, whose locations can be checked in Figure 17. Heaters were used to inject thermal signals in different points of the satellite to study the reaction of the system. Therefore, apart from measuring the temperature in different points of the satellite, the heaters installed on-board allowed to perform different experiments where the disturbances created by these injections were studied. Results coming from the thermal sensors and heaters and the experiments related to them can be found in [85, 86].

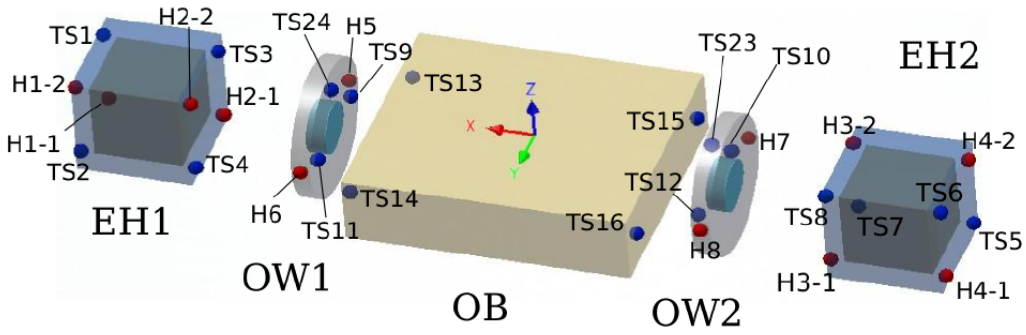

Figure 17: Location of the different thermal sensors and heaters inside the LCA. Another 6 sensors and 6 heaters, which are not shown in this image, were located in the struts that connected the LCA with the rest of the satellite. (Credits: [85]).

MAGNETIC DIAGNOSTICS: The magnetic susceptibility and remanent magnetic moment of the TMs could couple with their surrounding magnetic field and magnetic field gradient, creating disturbances in the geodesic motion of the TMs. The magnetic diagnostics subsystem [87] on-board LPF was aimed to study these effects. It consisted in four fluxgate magnetometers, to measure the magnetic field, and two magnetic coils, to inject controlled magnetic fields in the position of the TMs. The study of these effects is the main aim of this thesis, and they will be deeply studied in the following chapters. Results about the magnetic field in the satellite using the magnetometers measurements have been published in [88].

DATA MANAGEMENT UNIT: The DMU [77] was the computer that managed most of the scientific instrumentation on the spacecraft. Apart from controlling the different DDS components, it also handled the acquisition of data from different scientific units on-board by means of two Data Acquisition Unit (DAUs). It

played an important role in the OMS measurements, since it received the interferometer readout from the phasemeter, time-stamped the samples with its own clock, generated the feedback control signals to the laser control system and sent the OMS data to the DFACS to apply the needed corrections to the position of the spacecraft. The other big managing computer on the spacecraft, the On-board Computer (OBC), controlled systems more related to the platform itself, like the thrusters, solar array, star trackers, etc.

2.3 DELTA G

The main scientific output from LPF was to achieve a very low differential acceleration between the two free-falling TMs in the desired frequency range. This acceleration was called Δg, and was computed using the interferometer readouts, modelling the spacecraft motion and subtracting several known forces that were affecting the TMs. If we assume a situation like the one shown in Figure 18, we can define Δg as:

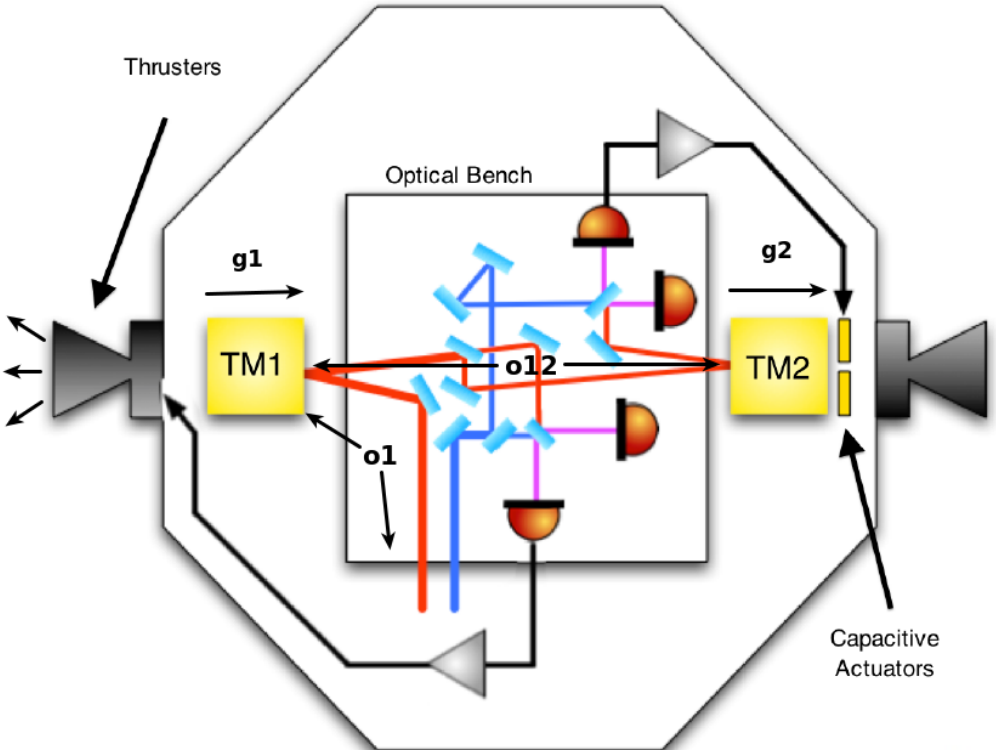

Figure 18: Scheme representing the different forces acting on each TM and the spacecraft. TM1 suffers an acceleration g_1 and moves. The movement is sensed thanks to the inteferometer measurement o_1, which monitors the distance between the OB and TM1. The DFACS automatically commands the thrusters to exert a force such that the spacecraft follows TM1. The actuators exert a force causing an acceleration g_2 on TM2 so it follows TM1. The relative distance between both masses is constantly monitored by the interferometer readout o_{12}.

$$\Delta g \equiv g_2 - g_1 \tag{2.2}$$

where $g_1 = F_1/m$ and $g_2 = F_2/m$ are the forces per unit of mass on TMs 1 & 2, respectively (each TM has a mass of $m = 1.928 \pm 0.001$ kg). If we consider Newton's equation for the motion of each TM:

$$g_1(t) \equiv m \cdot \ddot{x}_1(t) = F_1(t) - m \cdot \omega_1^2 \cdot (x_1(t) - x_{SC}(t)) \tag{2.3}$$
$$g_2(t) \equiv m \cdot \ddot{x}_2(t) = F_2(t) - m \cdot \omega_2^2 \cdot ((x_2(t) - x_{SC}(t)) + F_{ES}(t)) \tag{2.4}$$

where $x_1(t)$ & $x_2(t)$ are the displacements of TMs 1 & 2, respectively, with respect to the inertial frame along the x-axis, and $\ddot{x}_1(t)$ & $\ddot{x}_2(t)$ their second derivatives. $x_{SC}(t)$ is the displacement of the spacecraft, while $F_{ES}(t)$ are all the different forces acting on the spacecraft. Finally, ω_1 & ω_2 are the total stiffness per unit of mass between each TM and the spacecraft, since the movement between both can be modelled as a mass (the TM) attached to a spring (which would be the role of the drag-free and electrostatic suspension systems) which in turn attaches to the rest of the spacecraft.

Now, let's consider the interferometers readouts:

$$o_{12}(t) = x_2(t) - x_1(t) + n_{12}(t) \tag{2.5}$$
$$o_1(t) = x_1(t) - x_{SC}(t) + n_1(t) \tag{2.6}$$

where $o_{12}(t)$ is the readout corresponding to the differential position between both TMs, $o_1(t)$ the readout corresponding to the differential position between TM1 and the spacecraft, $n_{12}(t)$ the noise associated to the interferometer $o_{12}(t)$ and $n_1(t)$ the noise associated to the interferometer $o_1(t)$. If we substitute Equations (2.5) & (2.6) into Equations (2.3) & (2.4) and build the difference, we can write Δg as:

$$\Delta g \equiv \ddot{o}_{12}(t) - \frac{F_{ES}(t)}{m} + \Delta\omega_{12}^2 \cdot o_1(t) + \omega_2^2 \cdot o_{12}(t) - \Delta g_{IFO}(t) \tag{2.7}$$

where $\omega_{12}^2 = \omega_2^2 - \omega_1^2$ couples spacecraft motion into Δg and $\Delta g_{IFO}(t) = n_{12}(t) + \omega_{12}^2 \cdot n_1(t) + \omega_2^2 \cdot n_{12}(t)$ is the noise associated to the interferometer.

Several experiments were designed to extract the calibration parameters, where signals were injected into the electrostatic suspension control loop and the drag-free loop. On the one hand, the signals injected into the electrostatic suspension control loop modulated the relative displacements of TM2 relative to TM1 and to the spacecraft, calibrating the parameter ω_2^2, by introducing large commanded commanded forces $F_{ES}(t)$. On the other hand, the signals injected into the drag-free loop modulated the relative displacements between TM1 and the spacecraft, calibrating $\Delta\omega_{12}^2$ [89]. To obtain these parameters, a fit to $\Delta\omega_{12}^2$ was performed using the following model [4]:

$$\Delta\ddot{o}_{12}(t) = (1+\lambda)\frac{F_{ES}(t)}{m} - \omega_2^2 \cdot o_{12}(t) + \Delta\omega_{12}^2 \cdot o_1(t) \tag{2.8}$$

where λ, ω_2^2 and ω_{12}^2 are the parameters to fit.

Another effect that we have to take into account for the computation of Δg are cross-coupling effects. Any misalignment between the TMs, the sensors-actuators and the spacecraft could produce them, which in turn would produce cross-talk signals in the interferometer readouts – the interferometer noise $\Delta g_{IFO}(t)$ seen in Equation (2.7). This cross-talk generated a small bump in the Δg spectrum from 20 to 200 mHz [4], which can be appreciated in Figure (20). The effect of the cross-talk can be subtracted using the following model [89]:

$$\delta g_{\text{cross-talk}} = C_1 \ddot{\overline{\phi}}(t) + C_2 \ddot{\overline{\eta}}(t) + C_3 \ddot{\overline{y}}(t) + C_4 \ddot{\overline{z}}(t) + C_5 \overline{y}(t) + C_6 \overline{z}(t) \tag{2.9}$$

where $\delta g_{\text{cross-talk}} = \Delta g_{IFO}(t)$, $(\,\overline{\ }\,)$ indicates the mean displacement or rotation of both TMs along the given coordinate (see Figure (16) for which are the different DoFs), and $(\ddot{})$ denotes the second derivative of the given coordinate with respect to time. Although this model effectively subtracts the bump, the coefficients C_i do not give us much information about the underlying mechanisms that produced this cross-coupling effect. A deeper understanding of this system is still a work in progress [90].

A final effect that had to be taken into account for computing Δg are rotational effects Δg_{rot}, which are introduced due to the fact that LPF was a rotating reference frame which introduced inertial forces along the x-axis. Two type of forces appeared due this fact: centrifugal forces due to the spacecraft angular velocity Ω with respect to the LTP reference frame (see Figure (16) for a clearer picture) and Euler forces due to a spacecraft rotational acceleration $\dot{\Omega}$ different from zero [89].

Taking all the previous effects and corrections into account, we can finally write the main LPF observable, the differential acceleration between both TMs or Δg as [66, 89]:

$$\begin{aligned}\Delta g \equiv \ddot{o}_{12}(t) - \frac{F_{ES}(t)}{m} + \Delta\omega_{12}^2 \cdot o_1(t) + \omega_2^2 \cdot o_{12}(t) \\ - \delta g_{\text{cross-talk}}(t) - g_{\text{rot}}\end{aligned} \tag{2.10}$$

2.4 FORCES ON THE TEST MASSES

Different stray forces could affect the main goal of LPF, which was to achieve a low level of differential acceleration between the two free-falling TMs. These forces could originate from a wide set of physical effects. LPF was set to study and characterise these forces, to create a noise model for the future LISA by means of a full projection of the differential acceleration noise into its components. To this end, the mission was not only set up to perform measurements of acceleration, but carried on-board a list of devices to perform injections and designed specially to characterise these forces. The main idea behind all these experiments was to deliberately create a signal related to the physical effect we want to study (thermal, magnetic, etc) to analyse the coupling it produced with the system. This

made LPF a laboratory in space.

Many disturbances were analysed on-ground, to later on be checked during the satellite operations. For forces that were not feasible to test on-ground, simulation models predicted their contribution, and this contributions were also checked on-flight. Here there is a brief description of the different contributions to the Δg noise budget [91]:

- *Brownian noise*: residual gas particles inside the vacuum chamber interacted with the TMs to produce a noisy force. This force was proportional to the pressure p at which the gas were, and to the temperature inside the EH. This noise source dominated the mid-band of LPF spectrum, between 1 to 10 mHz. For the best achieved results of LPF, this contribution was computed to be $S_{\Delta g}^{1/2} = (1.74 \pm 0.05)$ fm s^{-2} $/\sqrt{\text{Hz}}$ [66].

- *Random TM charging*: the arrival of cosmic rays and solar energetic particles could electrically charge the TMs if they penetrate the spacecraft. In order to discharge them, 2 mercury vapor UV lamps were installed to discharge them via the photoelectric effect. The light produced by them was channelled either to the EH or the TM, depending on the sign of the charge of the TM. In Section 2.5, the results from the charging experiments carried on-board are further explained.

- *Stray voltages*: an important electrostatic disturbance for the TMs is the coupling between the TM charge and the residual stray electrostatic field inside the EH. A fluctuating stray field will produce a force noise on the TM by multiplying a non-zero average TM charge.

- *Laser radiation pressure*: because of amplitude fluctuations on the laser, laser radiation pressure exerts a fluctuating force on the TMs. The Power Spectral Density (PSD) of this noise source is important at low frequencies and follows a f^{-2} power law.

- *Cross-talk*: since the TMs were only free along the x-axis and controlled via electrostatic forces in the other DoFs, the dynamics in these other DoFs could induce some cross-talk effects due to missalignments between the electrodes of the EHs and their respective TMs. This effect could induce a noisy force along the x-axis. The experiments carried on-board to characterise this effect are further discussed in Section 2.5.

- x/ϕ *actuation*: fluctuations in the applied voltages induced in turn a fluctuation in the commanded forces on TM2. This noise source was dominant at low frequencies, but could be limited by increasing the voltage stability levels and improving the gravitational balancing of the satellite, in order to reduce the needed force to apply to TM2. In Section 2.5, the results from the actuation experiments carried on-board are further explained.

- *Interferometric noise*: any noise in the differential interferometry readout would be converted into effective force noise. At high frequencies, above 3 mHz, this noise contribution dominates the noise power spectrum. This

noise could arise from different sources, and it was characterised in on-ground campaigns and also with some experiments carried out on orbit. Experiments carried on-board to characterise this effect are further discussed in Section 2.5.

- *Thermal gradient effects*: any thermal gradient across the EH was expected to create a noisy force on its TM via the radiometric and radiation pressure effects [86, 92]. In Section 2.5, the results from thermal experiments carried on-board are further explained.

- *Thermo-optical and thermo-elastic effects*: variations in the temperature of the optical window of the GRS could create variations in the optical path of the laser and noisy forces. In a similar manner, variations in the temperature of the struts that connected the LTP to the rest of the satellite could create, as well, forces that affected the geodesic motion of the TMs [86]. Different experiments were carried out to study these effects, and more details can be seen in Section 2.5.

- *Magnetic effects*: the remanent magnetic moment and magnetic susceptibility of the TMs coupled to the fluctuations of the magnetic field and its gradient produced a force on the TMs. This contribution is expected to be important at low frequencies. The magnetic effects are the main focus of study of this thesis, and the forces they produce and the mechanisms behind them will be deeply studied in the next chapters.

- *Unmodeled noise sources*: closing this recopilation of forces acting on the geodesic motion of the TMs, it is worth considering that some noise sources that are not considered here could have played an important role in the results obtained for LPF. In fact, as discussed in [66], a portion of the noise at low frequencies is not yet explained by our modelisation, and some effects that are not being considered should be playing an important role there.

2.5 LPF OPERATIONS

Soon after LPF's launch, on December 3rd 2015, the satellite initiated a short trip to L1. After a commissioning phase that started on January 11th 2016, the scientific operations started on March 1st, 2016. The communication with the satellite was performed trough ESA's Estrack ground station network. Afterwards, the data was sent to ESA's Mission Operations Centre (MOC) located at the European Science and Operations Centre (ESOC) in Darmstadt, Germany. There, data retrieval and conversion were carried out to store it in repositories afterwards [93]. Each day had two deliverables: the instrument configuration and evaluation data early in the morning, and the full data set in the afternoon [94].

During mission operations phase, there was always at least one scientific team on duty at ESOC, while most of the time there were two of them. Each team consisted in three persons, one team leader and two data analysts. As previously explained, each day there were experiments planned to carry on-board. Due to the down-link and conversion of the data, the data from those experiments was

only ready to be analysed two days after carrying out the experiments. Therefore, the team responsible of analysing the experiments performed two days before, started their work shift two days after the experiments were actually performed, while they actually travel the day before. This working scheme is summarised in Table 1. Usually, the teams had some extra time the days they were travelling: to prepare for their upcoming work shift the day they travel to ESOC, and to consolidate and finish any on-going analysis the day they were travelling from ESOC. Actually, the time each team spent on-duty also depended on how long each experiment lasted, varying from one to several days. After their working shift, each team had the responsibility to write a logbook analysing everything that happened in the previous day.

Day	1	2	3	4	5	6
Experiment #	#1	#2	#2	#3	#3	#3
Team 1		Travel	On-duty	Travel		
Team 2			Travel	On-duty	On-duty	Travel
Team 3					Travel	On-duty

Table 1: Example of LPF working scheme during mission operations.

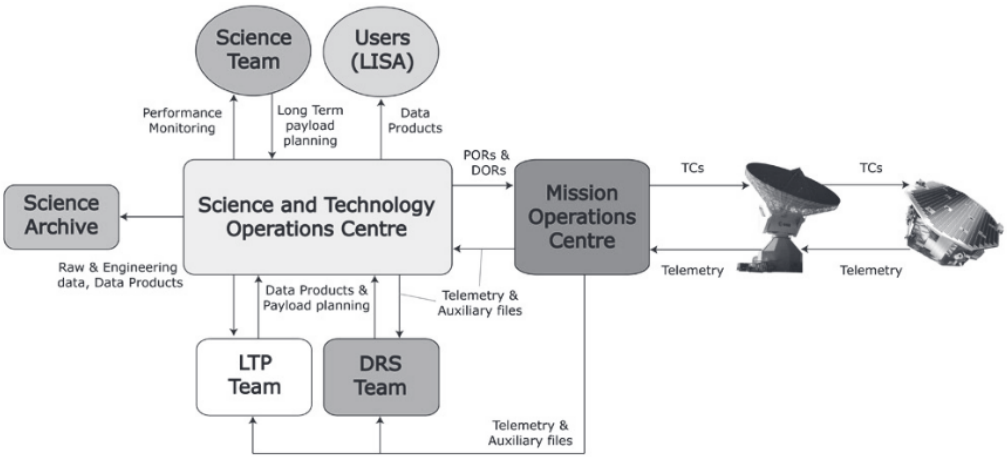

Figure 19: Operations scheme (Credits: [95]).

Data was analysed with the LISA Technology Package Data Analysis (LTPDA) toolbox [96], a dedicated MATLAB toolbox developed by the LPF data analysis team. This toolbox allowed for object-oriented data analysis and allowed transporting the history of the objects with themselves, easily tracking them. Daily data from LPF mission operations were analysed with this toolbox, providing a common and easy to use environment to all data analysts.

As previously explained in the chapter, the main objective of the mission was to reach a certain level of noise in Δg – see Equation (2.10). In order to achieve this goal, several experiments were carried out during mission operations to try to understand or remove all the possible noise contributions that disturbed the two TMs from their geodesic motion. This, in some sense, made LPF different. It

was not just an observatory in space, it was a laboratory in space.

The performed experiments ranged quite a lot in their purpose. In each of them, a different subsystem was stimulated to try to study/cancel different non-gravitational effects. Some of the experiments carried out during mission operations to study the different disturbances on the relative acceleration between the two TMs were:

ACCELERATION NOISE MEASUREMENTS: During these runs is when the main objective of LPF was carried out. In these runs, the system was kept as stable as possible in order to achieve the lowest acceleration noise between the masses. These runs were performed in different control modes, different stiffness conditions, different temperatures, etc. They contain the main results from LPF [4, 66].

DYNAMIC SYSTEM IDENTIFICATION EXPERIMENTS: In these experiments the main goal was to calibrate the dynamics of LPF. As seen in Equation (2.10), the Δg computation depends on several parameters that need to be calibrated. Because of this, several experiments were performed during the mission lifetime where sinusoidal signals where injected into the control loop in order to study how the system behaves, and therefore, be able to estimate these parameters. The results of these experiments have already been published [89].

CROSS-TALK EXPERIMENTS: The TMs could move freely along the x-axis, but in the other DoFs they were commanded via the actuators of the EH to prevent it from crashing into its walls. The electrical forces applied to achieve this goal could induce some cross-talk effects that could appear as noise along the x-axis. Therefore, several experiments were performed where sinusoidal signals were applied in order to calibrate the parameters that describe these couplings. The results of these experiments are being analysed during the writing of this thesis.

FREE-FALL EXPERIMENTS: The action of the actuators to cage the TMs in other DoFs other than on the x-direction limit the sensitivity of the system in normal performance. Long periods without the actuation of the electrodes would make the TMs to slowly drift due to residual forces until they crash with the EH walls. However, if these forces are properly characterised, a series of short electrostatic kicks could induce a parabolic trajectory on one TM allowing it to free-fall for several minutes without the disturbance of the actuators. Results about these experiments have been published in [97].

CHARGE EXPERIMENTS: The arrival of random cosmic rays and solar energetic particles could penetrate the spacecraft and electrically charge the TMs. This was a major problem, since they were caged via electrostatical forces and any change in their electrical charge could perturbate their motion. Also, since they were isolated from the rest of the spacecraft, they could not be grounded to anything to get rid of this excess charge. The solution was to discharge them through the photoelectric effect using UV light from mercury vapour lamps installed within the LTP. The charge in the TMs could be measured injecting sinu-

soidal voltages on the x-axis electrodes and controlled via the UV lamps if needed. The results of these experiments have already been published [67, 68].

LASER FREQUENCY NOISE EXPERIMENTS: Laser frequency noise could translate into a phase shift of the interferometric distance between both TMs. The dedicated frequency reference interferometer measured it, being its signal used by a nested control loop to stabilise the frequency [75, 98].

LASER AMPLITUDE NOISE EXPERIMENTS: Laser amplitude also needed to be stabilised in two different frequency ranges. In the range going from 1 mHz to 30 mHz, laser power fluctuations produced radiation pressure on the TMs, creating direct forces on them, which were suppressed by the phasemeter. On the heterodyne frequency, around 1 kHz, the Relative Intensity Noise (RIN) takes place, coupling into the phase. This noise contribution was suppressed by balance detection [75].

THERMAL EXPERIMENTS: Thermal fluctuations in different locations of the satellite could create direct forces on the TM or couple with the phase of the interferometric signal. In order to characterise those, heaters and temperature sensors were placed in different locations of the spacecraft. The experiments consisted in injecting thermal signals through the heaters, and by analysing the temperature changes and the interferometer response, these effects could be studied in detail [86, 92].

MAGNETIC EXPERIMENTS: The coupling between the environmental magnetic field and the magnetic properties of the TMs created forces that could disturb the TMs from their geodesic motion. In order to study them, magnetic fields were injected with a pair of coils to analyse the TMs response. These experiments are one of the main areas of study within this thesis, and will be deeply studied on Chapter 5.

2.6 LPF RESULTS

Some months after the start of LPF operations, on June 2016, the first results about LPF were published [4]. In this publication, the results of a "noise run" of 6.5 days were presented. During LPF operations, a "noise run" was a configuration of the spacecraft were the TMs and the satellite were on the quietest possible configuration, and the interferometer system gathered data during days to compute a Δg spectrum where a low level of acceleration between the TMs was achieved. In Figure 20, the results of the Amplitude Spectral Density (ASD) of Δg during this noise run are presented. This ASD was computed averaging 26 periodograms of 40000 s each, using a 50% overlapping data and a Blackmann-Harris window (with the Welch averaged periodogram method [99]), with the four first frequency bins of the averaged periodogram discarded. This produces a relative error of 1σ of 10% in $S_{\Delta g}^{1/2}$, with an effective spectral resolution of ± 50 μHz. See Section B.1 for more details about the calculation of the spectrum.

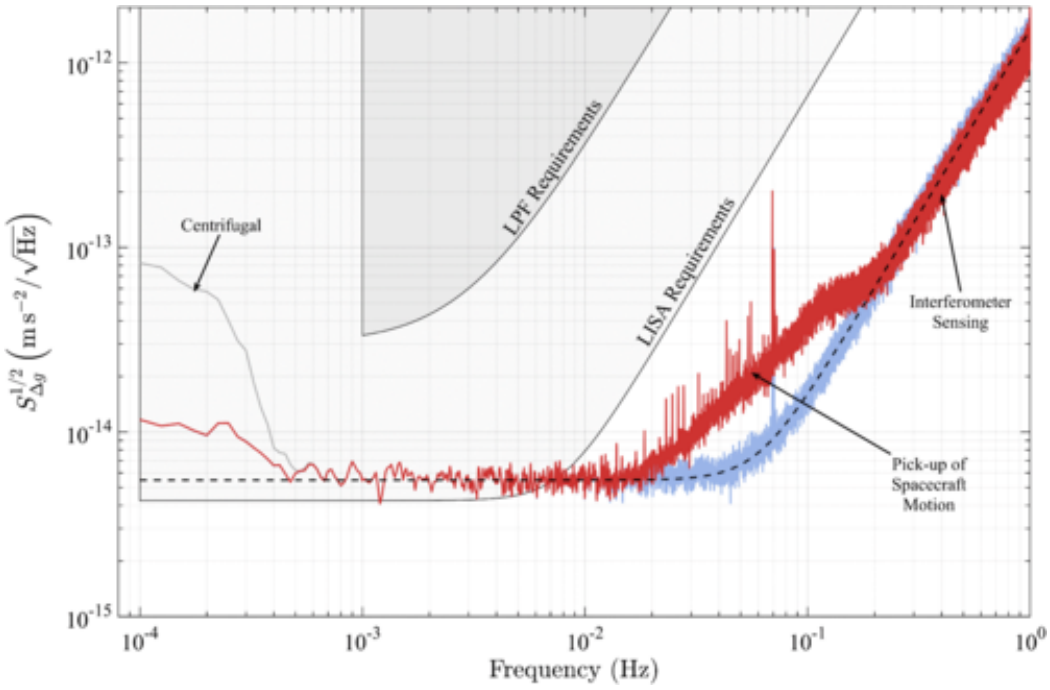

Figure 20: *Shaded areas:* LISA and LPF requirements. *Gray curve:* ASD for Δg. *Red curve:* ASD of the same time-series from the red curve, but with the correction of the centrigugal force applied. *Blue curve:* ASD of the same time-series from the red curve after the correction of the pickup of spacecraft motion by the interferometer. *Dashed black line:* $S_{\Delta g}(f) = S_0 + S_{IFO}(2\pi f^4)(f)$, being $S_0^{1/2} = (5.57 \pm 0.04)$ fm s^{-2} Hz$^{-1/2}$ and $S_{IFO}^{1/2} = (34.8 \pm 0.3)$ fm s^{-2} Hz$^{-1/2}$. (Credits: [4]).

As seen in Figure 20, the first results of $S_{\Delta g}^{1/2}$ were a complete success. Between 0.7 and 10 mHz the level of noise achieved was of $S_{\Delta g}^{1/2} = (5.57 \pm 0.04)$ fm s^{-2} $/\sqrt{\mathrm{Hz}}$, a factor 5 below the mission requirements. It also improved the LISA requirements below 10 mHz, and between 0.5 and 10 mHz was just below them by a tiny factor.

Equation (2.10) was used to compute the ASD of Δg (the grey line shown in Figure 20). Two effects are corrected and shown in this Figure. First, the cross-talk coming from spacecraft motion and misalignments that produced the bump observed between 20 and 200 mHz, which was explained in Section 2.3. And second, the centrifugal force produced by the spacecraft rotation, which uppers the low frequency tail in frequencies below 0.5 mHz and which was also described in Section 2.3. Both effects are corrected in the blue line shown in Figure 20.

The spectrum of LPF's Δg can be divided in three different parts, depending on which kind of noise limits the sensitivity of the system:

HIGH-FREQUENCY: around 60 mHz, the sensitivity of the system starts to ramp up due to the noise in the differential interferometry readout. This frequency-independent interferometer noise, limited by noise in the phasemeter [71, 100],

results in a displacement noise ASD of (34.8 ± 0.3) fm$/\sqrt{\text{Hz}}$ and dominates Δg above 60 mHz.

MID FREQUENCY: between 0.7 and 20 mHz, the sensitivity of the instrument is limited by brownian noise associated with viscous gas damping. This noise is proportional to p/m_0 [65] with p being the pressure of residual a gas of molecular weight m_0. This noise provides a contribution of (5.57 ± 0.04) fm$/\sqrt{\text{Hz}}$ at all frequencies. As we will see later on, this noise source was reduced during the mission due to the decreasing p caused by the venting of the vacuum system to space.

LOW-FREQUENCY: below 0.5 mHz, several stray forces contribute to increase the power in the Δg spectrum. Some of these contributions are [4, 66]: TM charge fluctuations, thermal gradient effects, laser radiation pressure fluctuations and magnetic force effects, which are the object of study of this work. This low frequency tail stays below 12 fm$/\sqrt{\text{Hz}}$ down to 0.1 mHz. Even when considering all the known force contributions, there is an excess noise at low frequencies which is not explained yet, and is still under study.

As the mission operations continued, the results on the noise acceleration between the two TMs kept improving, and new results were published in February 2018 [66]. In Figure 21 we can see the best results achieved during LPF mission operations. The figure shows the ASD of Δg for a noise run of 13 days during February 2017 (red curve) and compares it to the noise run previously published (blue curve), which also corresponds to the blue curve in Figure 20. This new ASD was obtained averaging 10 periodograms of 2×10^5 s each, using a 50% overlapping data and a Blackmann-Harris spectral window (Welchs averaged periodogram method [99]), with the first four bins of the periodogram discarded. The black dots over both spectra were estimated using a Bayesian inference method that modifies the length of the periodograms for each of the selected frequencies, allowing to achieve better precision at a specific frequency, which in this case was useful to give values for different force contributions at some key frequencies [66]. Check Section B.1 for more details about their calculation.

As seen in Figure 21, in the mid-band of the spectrum, between 1 mHz to 10 mHz, there was a factor improvement of around 3. This improvement was achieved by two reasons. First, during January 2017, the temperature within the LTP was lowered from the nominal 22-23 °C to 11-12 °C. Second, the evacuation of residual gas, that continued to lower the pressure around the TMs since the beginning of mission operations by roughly a factor 10. These two factors combined made the Brownian noise to decrease to a value of $S_{\Delta g}^{1/2} = (1.74 \pm 0.05)$ fm s^{-2} $/\sqrt{\text{Hz}}$.

At high frequencies, though, there was an increase of the interferometer readout for the February 2017 noise run – not visible in Figure 21. The value obtained corresponds roughly to 100 fm s^{-2} $/\sqrt{\text{Hz}}$, an increase with respect to the 35 fm

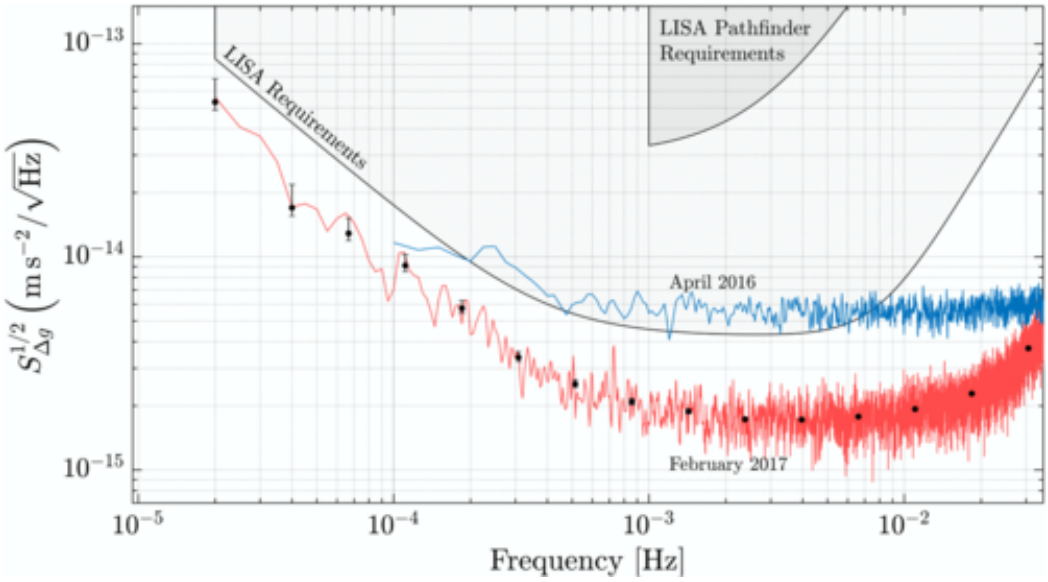

Figure 21: *Shaded areas:* LISA and LPF requirements. *Blue curve:* ASD of Δg, which corresponds to the blue line shown in Figure 20. *Red curve:* ASD for Δg obtained during the noise measurements in February 2017. (Credits: [66]).

$s^{-2}/\sqrt{Hz}$ obtained during April 2016 noise run. This increase is not attributed to any worsening in the interferometer noise itself, but to the change in the TM position and attitude control points. This effect increases the noise associated with correcting the cross-talk forces due to the satellite motion, using noisier capacitive sensing measurements [66].

Finally, at frequencies below 1 mHz, in the February 2017 noise run we can see an improvement too with respect to the April 2016 noise run. Also, due to the fact that we increased the duration of the noise run, we were able to reach lower frequencies in the spectrum, down to 20 μHz. Like in the April 2016 noise run, beginning at around 1 mHz, the noise starts to ramp up down to the 20 μHz roughly following a f^{-2} dependence. Nevertheless, there was an improvement thanks to two reasons. First, a more accurate calculation of the actuation force, and second, the identification and subtraction of another inertial force due to the spacecraft rotation – Euler forces, see Equation 2.10.

Despite of the improvement at low frequencies, a portion of the noise budget remains unmodeled and is not yet explained. Magnetically originated forces, which are the main focus of this thesis, may explain a part of this excess noise at low frequencies. In the following chapters we will introduce which is the origin of these forces, we will quantify them, and in Chapter 6, give a contribution to this low frequency tail coming from magnetic effects.

3

MAGNETIC FORCES IN LISA PATHFINDER

Magnetic noise is expected to have an important contribution in the low-frequency tail of LPF noise budget, which is the region where there is an excess noise not explained by our models [66]. Magnetic noise appears because the residual magnetisation and magnetic susceptibility of the TMs couple with the surrounding magnetic field and its gradient, inducing a force. Even though the TMs were designed to show a very tiny magnetic susceptibility, and they were baked around their Curie temperature to reduce as much as possible their residual magnetisation, the acceleration noise in LPF is so low (we were able to measure force fluctuations of the order of fN) that even the small magnetic forces generated by this effect will play a role in the total acceleration noise budget. It is therefore important to understand the different magnetic mechanisms that can produce a disturbance in the geodesic motion of the TMs.

In this chapter we will start with a brief introduction, explaining which are the forces and torques that appear on the TMs, together with a brief explanation of magnetism in materials. Next, we will move to explain which are the fluctuations of the previously explained forces, and how they affect the TMs geodesic motion. Following this explanation, we will introduce what happens if we have an oscillating magnetic field, not a fixed one. We will see how the magnetic susceptibility changes with the frequency, and afterwards, how the forces and torques also behave in the presence of an Alternating Current (AC) magnetic field.

3.1 MAGNETIC FORCES ON THE TEST MASSES

To compute the magnetic noise contribution, we will consider that our TMs are dipoles inside a magnetic field. From Ampere's law, the elementary force on a current element $I\mathbf{dl}$ inside a magnetic field $\mathbf{B}$ is computed as $\mathbf{dF} = I(\mathbf{dl} \times \mathbf{B})$. From now on, a bold letter will mean a vectorial quantity, like $\mathbf{B} = (B_x, B_y, B_z)$. We can further calculate the total force $\mathbf{F}$ on the current distribution $\mathbf{J}(\mathbf{x})$ in an external field $\mathbf{B}$ as [101]:

$$\mathbf{F} = \int \mathbf{J}(\mathbf{x}) \times \mathbf{B} dV \tag{3.1}$$

We can further manipulate equation (3.1) to obtain [102]:

$$\mathbf{F} = \langle \langle \mathbf{M} \cdot \boldsymbol{\nabla} \rangle \mathbf{B} \rangle V \tag{3.2}$$

where $\mathbf{M}$ refers to the magnetic moment density of the TM, $\mathbf{B}$ is the magnetic field at the TM position and $\boldsymbol{\nabla}$ the nabla operator. In Equation (3.2) and further on, $\langle ... \rangle$ refers to the TM volume average of the enclosed quantity, therefore $\mathbf{M}$ and $\mathbf{B}$ are expressed at each TM differential volume dV, where V is the volume

of the TM.

The magnetic moment density **M** can be divided into two terms. The first one is the remanent magnetic moment $\mathbf{M_r}$, which will depend on the orientation of magnetic dipoles inside the material in the absence of any magnetic field, being close to zero if the orientation of the dipoles inside the material does not have any preferred orientation. The second term is the induced magnetic moment $\mathbf{M_i}$. This term describes how the magnetic dipoles inside the material behave when an external magnetic field is applied. The induced magnetic moment $\mathbf{M_i}$ can be expressed as a linear function of the external magnetic field **B**, multiplied by the magnetic susceptibility:

$$\mathbf{M_i} = \frac{\chi}{\mu_0}\mathbf{B} \tag{3.3}$$

where χ is the magnetic susceptibility of the test mass, μ_0 the magnetic permeability constant in vacuum, which has a value of $4\pi \times 10^{-7}$ m kg $s^{-2}A^{-2}$ and **B** the external magnetic field.

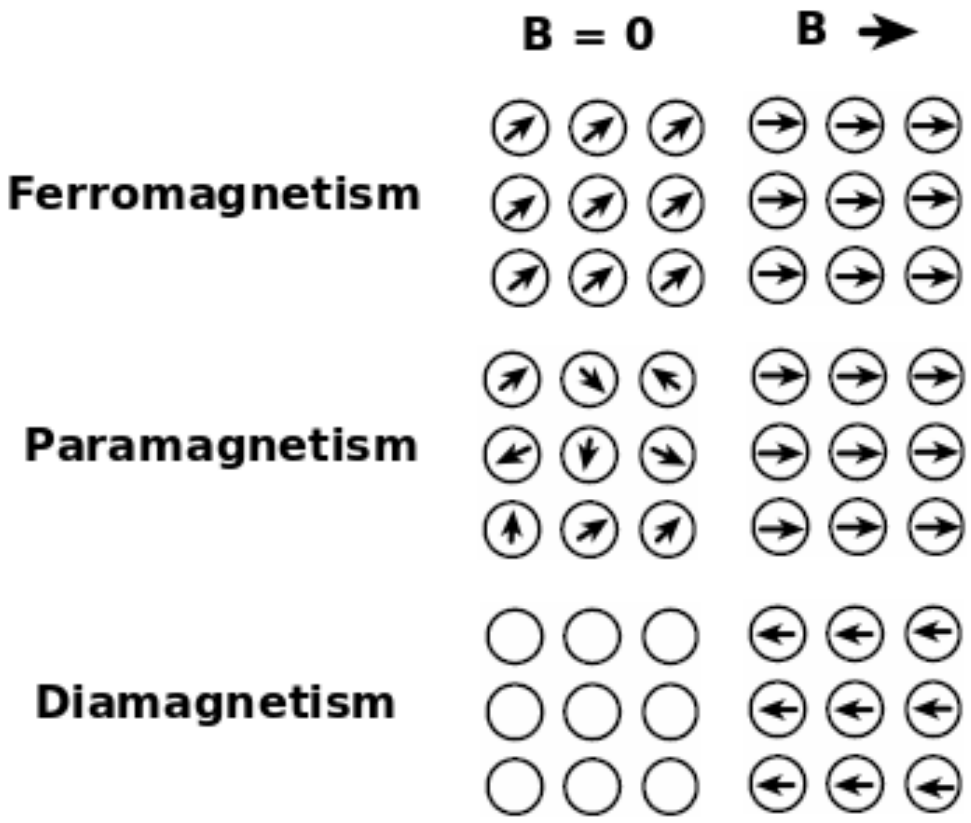

Figure 22: Principal types of magnetic behaviour on materials depending on the alignment of the magnetic dipoles within it in the presence and absence of an external magnetic field. (Credits: This work.)

The parameters χ and $\mathbf{M_r}$ describe the magnetic behaviour of a material, and they will depend on how the material behaves in the presence and absence of a magnetic field. In Figure 22 we can see a visual representation of the main types of magnetic behaviour on materials:

- FERROMAGNETISM: ferromagnetism is the mechanism by which certain materials form permanent magnets or are attracted to them, and is the strongest effect of the three described in Figure 22. In ferromagnets, the magnetic dipoles within the material have a preferred orientation in the absence of magnetic field, thus having a high remanent magnetic moment ($|\mathbf{M_r}| >> 0$). Moreover, if we apply an external magnetic field, the magnetic dipoles within the material will respond aligning with it, therefore showing a positive and big magnetic susceptibility ($\chi >> 0$).

- PARAMAGNETISM: paramagnetism is a form of magnetism by which some materials are weakly attracted to an external magnetic field. This effect happens due to the material having unpaired electrons and is usually much weaker than the one that ferromagnetism produces, but greater than diamagnetism. In paramagnets, the magnetic dipoles within the material have no preferred orientation in the absence of magnetic field, thus showing a net close to zero remanent magnetic moment ($|\mathbf{M_r}| \simeq 0$). When we apply an external magnetic field, the magnetic dipoles within the material align with it, enhancing the magnetic field within the material, and therefore showing a positive magnetic susceptibility ($\chi > 0$).

- DIAMAGNETISM: diamagnetism is an effect that all materials show at some degree, and by which they repel external magnetic fields. When it is the only contribution to the magnetism, the material is called diamagnetic. In paramagnetic and ferromagnetic substances, the weak diamagnetic force is overcomed by the attractive force of magnetic dipoles in the material. This effect appears when the material have no unpaired electrons, and is usually much weaker than the previous two effects described, ferromagnetism and paramagnetism. In diamagnets, the atoms inside the material show little to zero magnetic moment, thus being the remanent magnetic moment negligible ($|\mathbf{M_r}| = 0$). When we apply an external magnetic field, the magnetic dipoles within the material align opposite to it, partially cancelling the magnetic field within the material, and therefore showing a negative magnetic susceptibility ($\chi < 0$). When the material completely cancels the external magnetic field within it ($\chi = -1$), we call it a perfect diamagnet. This is the case of superconductors.

Given that the dominant material in the TM composition (73% Au-27% Pt) is gold, and gold shows a diamagnetic behaviour while Platinum is paramagnetic, we will assume the response of the induced magnetic moment to be dominated by its diamagnetic behaviour ($\chi < 0$), and therefore be inversely proportional to the applied magnetic field $\mathbf{B}$. Nevertheless, notice that we left the sign undetermined in Equation (3.3), and we will do so for the rest of the following analysis. Also, we have implicitly assumed here an isotropic TM which allows a scalar susceptibility in the previous equation.

If we now rewrite Equation (3.2) dividing the magnetisation $\mathbf{M}$ into its two contributions, we get the following expression:

$$\begin{aligned}\mathbf{F} &= \left\langle \left[\left(\mathbf{M_r} + \frac{\chi}{\mu_0}\mathbf{B} \right) \cdot \boldsymbol{\nabla} \right] \mathbf{B} \right\rangle V \\ &= \left\langle (\mathbf{M_r} \cdot \boldsymbol{\nabla}\mathbf{B}) + \frac{\chi}{\mu_0} [\mathbf{B} \cdot \boldsymbol{\nabla}\mathbf{B}] \right\rangle V \end{aligned} \tag{3.4}$$

And the force acting along the x-axis, i. e., the axis joining the two TMs will be:

$$F_x = \left\langle (\mathbf{M_r} \cdot \boldsymbol{\nabla}B_x) + \frac{\chi}{\mu_0} [\mathbf{B} \cdot \boldsymbol{\nabla}B_x] \right\rangle V \tag{3.5}$$

In the presence of a magnetic field, the TMs will not only experience a force like the one we just explained, but also a torque, which according to [101] is given by:

$$\mathbf{N} = \langle \mathbf{M} \times \mathbf{B} + \mathbf{r} \times [(\mathbf{M} \cdot \boldsymbol{\nabla})\, \mathbf{B}] \rangle\, V \tag{3.6}$$

where $\mathbf{r}$ denotes the distance to the centre of the TM, and all the other parameters have previously been defined. If we substitute the magnetisation $\mathbf{M}$ for its two components, the remanent magnetic moment $\mathbf{M_r}$ and the induced magnetic moment $\mathbf{M_i} = \chi \mathbf{B} \mu_0^{-1}$, we will have:

$$\mathbf{N} = \left\langle \mathbf{M_r} \times \mathbf{B} + \mathbf{r} \times \left[(\mathbf{M} \cdot \boldsymbol{\nabla}\mathbf{B}) + \frac{\chi}{\mu_0} (\mathbf{B} \cdot \boldsymbol{\nabla}\mathbf{B}) \right] \right\rangle V \tag{3.7}$$

3.2 MAGNETIC FORCE FLUCTUATIONS

In order to assess the contribution of the magnetic force fluctuations to Δg, we have to consider the time varying components of Equation (3.4). For the following analysis, the fluctuations of the remanent magnetic moment $\mathbf{M_r}$ and magnetic susceptibility χ can be considered negligible – although in Section 3.3 we will see how the magnetic susceptibility varies in the presence of an oscillating magnetic field. However, we have to take into account the fluctuations of the magnetic field and its gradient. They are the main responsible of a magnetic fluctuating force appearing in Δg, i.e., in the acceleration noise between the two TMs.

We can divide the magnetic field $\mathbf{B}$ and magnetic field gradient $\boldsymbol{\nabla}\mathbf{B}$ in the TM position as a sum of two components, one coming from the interplanetary magnetic field $\mathbf{B}_{ip}$, which will be the same at any point of the spacecraft, and another one which is originated within the spacecraft $\mathbf{B}_{sp}$. The latter is caused due to the different units inside the spacecraft. These units generate small magnetic fields, and since this component is very inhomogeneus within the spacecraft, the magnetic field produced by it will be different depending on which point of the spacecraft we are. Considering this, the magnetic field can be expressed as:

$$\mathbf{B} = \mathbf{B}_{sp} + \mathbf{B}_{ip} \tag{3.8}$$

We can further express each of this components as the sum of a constant part $\mathbf{B}^{DC}$ and a time varying component $\delta\mathbf{B}$:

$$\mathbf{B}_{sp} = \mathbf{B}_{sp}^{DC} + \delta\mathbf{B}_{sp} \qquad \mathbf{B}_{ip} = \mathbf{B}_{ip}^{DC} + \delta\mathbf{B}_{ip} \tag{3.9}$$

The same can be done for the magnetic field gradient, it can be divided into a constant part $\nabla\mathbf{B}^{DC}$ and a fluctuating part $\delta\nabla\mathbf{B}$. However, in this case, we can consider negligible the magnetic field gradient of the interplanetary component (both, Direct Current (DC) and fluctuations), taking into account the small dimensions of the spacecraft with respect to the interplanetary medium.

$$\nabla\mathbf{B}_{sp} = \nabla\mathbf{B}_{sp}^{DC} + \delta\nabla\mathbf{B}_{sp} \qquad \nabla\mathbf{B}_{ip} \simeq 0 \tag{3.10}$$

We can now rewrite Equation (3.4) taking into account these changes as:

$$\begin{aligned}\mathbf{F} &= \mathbf{F}^{DC} + \delta\mathbf{F} = \\ &= \left\langle \left(\mathbf{M}_r \cdot \nabla\mathbf{B}_{sp}^{DC}\right) + \frac{\chi}{\mu_0}\left[\left(\mathbf{B}_{sp}^{DC} + \mathbf{B}_{ip}^{DC}\right) \cdot \nabla\mathbf{B}_{sp}^{DC}\right] \right\rangle V \\ &+ \delta\mathbf{F}\end{aligned} \tag{3.11}$$

with the fluctuation of the force $\delta\mathbf{F}$ being:

$$\begin{aligned}\delta\mathbf{F} &= \left\langle \left[\left(\mathbf{M}_r + \frac{\chi}{\mu_0}\delta\mathbf{B}\right) \cdot \nabla\right] \delta\mathbf{B} \right\rangle V \\ &= \left\langle (\mathbf{M}_r \cdot \delta\nabla\mathbf{B}) + \frac{\chi}{\mu_0}\left[\delta\mathbf{B} \cdot \nabla\mathbf{B}^{DC} + \mathbf{B}^{DC} \cdot \delta\nabla\mathbf{B}\right] \right\rangle V\end{aligned} \tag{3.12}$$

if we expand the different terms and distinguish between spacecraft and interplanetary contribution we end up having:

$$\begin{aligned}\delta\mathbf{F} &= \left\langle \left(\mathbf{M}_r + \frac{\chi}{\mu_0}\left[\mathbf{B}_{sp} + \mathbf{B}_{ip}\right]\right) \delta\nabla\mathbf{B}_{sp} \right\rangle V \\ &+ \left\langle \frac{\chi}{\mu_0}\left[\delta\mathbf{B}_{sp} \cdot \nabla\mathbf{B}_{sp}^{DC} + \delta\mathbf{B}_{ip} \cdot \nabla\mathbf{B}_{sp}^{DC}\right] \right\rangle V \\ &+ \left\langle \frac{\chi}{\mu_0}\left[\delta\mathbf{B}_{sp} \cdot \delta\nabla\mathbf{B}_{sp} + \delta\mathbf{B}_{ip} \cdot \delta\nabla\mathbf{B}_{sp}\right] \right\rangle V\end{aligned} \tag{3.13}$$

Therefore, we can finally express our force as a sum of a constant term and a fluctuating part:

$$\mathbf{F} = \mathbf{F}^{DC} + \delta\mathbf{F} = \tag{3.14a}$$

$$= \left\langle \left(\mathbf{M_r} \cdot \boldsymbol{\nabla}\mathbf{B}_{sp}^{DC}\right) + \frac{\chi}{\mu_0}\left[\left(\mathbf{B}_{sp}^{DC} + \mathbf{B}_{ip}^{DC}\right) \cdot \boldsymbol{\nabla}\mathbf{B}_{sp}^{DC}\right]\right\rangle V \tag{3.14b}$$

$$+ \left\langle \left(\mathbf{M_r} + \frac{\chi}{\mu_0}\left[\mathbf{B}_{sp} + \mathbf{B}_{ip}\right]\right) \delta\boldsymbol{\nabla}\mathbf{B}_{sp}\right\rangle V \tag{3.14c}$$

$$+ \left\langle \frac{\chi}{\mu_0}\left[\delta\mathbf{B}_{sp} \cdot \boldsymbol{\nabla}\mathbf{B}_{sp}^{DC} + \delta\mathbf{B}_{ip} \cdot \boldsymbol{\nabla}\mathbf{B}_{sp}^{DC}\right]\right\rangle V \tag{3.14d}$$

$$+ \left\langle \frac{\chi}{\mu_0}\left[\delta\mathbf{B}_{sp} \cdot \delta\boldsymbol{\nabla}\mathbf{B}_{sp} + \delta\mathbf{B}_{ip} \cdot \delta\boldsymbol{\nabla}\mathbf{B}_{sp}\right]\right\rangle V \tag{3.14e}$$

In the previous equation we can see the different kind of effects that the magnetic environment will induce on the TMs. These effects range from:

- Constant force contributions, as shown by Eq. (3.14b), that appear due to the coupling of the magnetic field generated by the spacecraft $\mathbf{B}_{sp}^{DC}$, its gradient $\boldsymbol{\nabla}\mathbf{B}_{sp}$ and the Interplanetary Magnetic Field (IMF) $\mathbf{B}_{ip}^{DC}$ with the TMs remanent magnetic moment $\mathbf{M_r}$ and magnetic susceptibility χ.
- The fluctuations of the spacecraft magnetic field gradient $\delta\boldsymbol{\nabla}\mathbf{B}_{sp}$ coupling with the remanent magnetic moment $\mathbf{M_r}$ and magnetic susceptibility χ, together with the spacecraft magnetic field $\mathbf{B}_{sp}^{DC}$ and IMF $\mathbf{B}_{ip}^{DC}$, as shown by Eq. (3.14c).
- The fluctuations of both, the spacecraft $\delta\mathbf{B}_{sp}$ and IMF $\delta\mathbf{B}_{ip}$ coupling with the magnetic susceptibility χ and the spacecraft magnetic field gradient $\boldsymbol{\nabla}\mathbf{B}_{sp}^{DC}$, as indicated in Eq. (3.14d).
- The coupling of the fluctuations of the spacecraft magnetic field gradient $\delta\boldsymbol{\nabla}\mathbf{B}_{sp}$ with the fluctuations of both, the spacecraft $\delta\mathbf{B}_{sp}$ and IMF $\delta\mathbf{B}_{ip}$, together with the magnetic susceptibility χ, as shown in Eq. (3.14e). Notice these are second order terms, since the coupling is between fluctuations, and not fluctuations with a constant term.

In Chapter 6, once we have estimated the values of the different terms, we will check how each of these contributions affect to the total magnetic acceleration noise, along with some other terms like the Lorentz Force or the down-converted AC magnetic fields.

3.3 MAGNETIC SUSCEPTIBILITY IN THE PRESENCE OF AN AC FIELD

Up to this point, we have not considered the time dependence of the magnetic field. If the TM is magnetised by a low alternating magnetic field:

$$\mathbf{B}(t) = \mathbf{B}_i^{AC}\,\sin(\omega\, t) \tag{3.15}$$

where $\mathbf{B}_i^{AC}$ is the AC amplitude and ω the frequency of the applied magnetic field. Therefore, we obtain a magnetisation that varies with time accordingly, $\mathbf{B}(t)$.

In diamagnetic, paramagnetic and many ferromagnetic materials, the magnetisation also varies sinusoidally and in phase with the applied magnetic field with a constant ratio given by the magnetic susceptibility. However, some ferromagnetic materials show a delayed response that is not in phase with the applied field. This phenomena is typically described by considering the in-phase χ_r and out-of-phase χ_i components of the magnetic susceptibility that allows the temporal dependence of the magnetisation to be written as

$$\mathbf{M}(t) = \chi_r \, \mathbf{B}_i^{AC} \, \sin(\omega \, t) + \chi_i \, \mathbf{B}_i^{AC} \cos(\omega \, t), \tag{3.16}$$

which, according to Néel [103], is equivalent to the usual convention of describing the magnetic susceptibility as composed by a real and an imaginary part which are related by:

$$\begin{aligned} \chi_r = \chi \sin\varphi \qquad & \chi_i = \chi \cos\varphi \\ \chi = \sqrt{{\chi_r}^2 + {\chi_i}^2} \quad & \varphi = \arctan(\chi_i/\chi_r) \end{aligned}$$

The out-of-phase component is not usually considered although it finds important applications for instance in geophysics and material science since it can be advantageously used for characterisation and identification of materials [104–107].

There are three major physical mechanisms that can produce the out-of phase response [108]: i) viscous relaxation, ii) electrical eddy currents (induced by AC fields in conductive materials), iii) weak-field (so-called Rayleigh) hysteresis, involving a non-linear and irreversible dependence of the magnetisation on the applied magnetic field. Among these, the most relevant for the experiments in LPF will be eddy currents, since this contribution becomes increasingly important with the increasing conductivity of the material. In comparison, viscous relaxation is typical of ultrafine magnetic particles that may experience state transitions in their magnetic domains, while weak-field hysteresis appears in materials with a wide hysteresis loop.

According to Vitale [109], at low frequencies the AC magnetic susceptibility of LPF TMs can be approximated as:

$$\chi(\omega) \simeq \chi_{\text{off.}} + \frac{i\omega\tau_e}{1 + i\omega\tau_e} \tag{3.17}$$

with $\chi_{\text{off.}}$ being the DC magnetic susceptibility and τ_e being the magnetic susceptibility cut-off, i.e., the frequency at which the real and imaginary parts of the magnetic susceptibility have the same value. For LPF, this value was measured on-ground to be [110] $\tau_e = (2\pi \, 630)^{-1} \text{Hz}^{-1}$.

In Figure 23 we show the frequency dependence of both components of magnetic susceptibility for LPF TMs. According to the model described by Equation (3.17), the imaginary component of the magnetic susceptibility is very weak compared

to the real component for frequencies below the Hz. Therefore, in the range of frequencies LPF studies (around the mHz and below), the real component of magnetic susceptibility will completely dominate over the imaginary. As we go above the Hz, the imaginary part starts to grow reaching its maximum at the susceptibility frequency cut, starting to diminish afterwards. On the other hand, the real component only grows as we increase frequency, tending exponentially to -1 for very high frequencies, which means that the TM behaves like a perfect diamagnet at very high frequencies, repelling all magnetic fields that oscillate very rapidly.

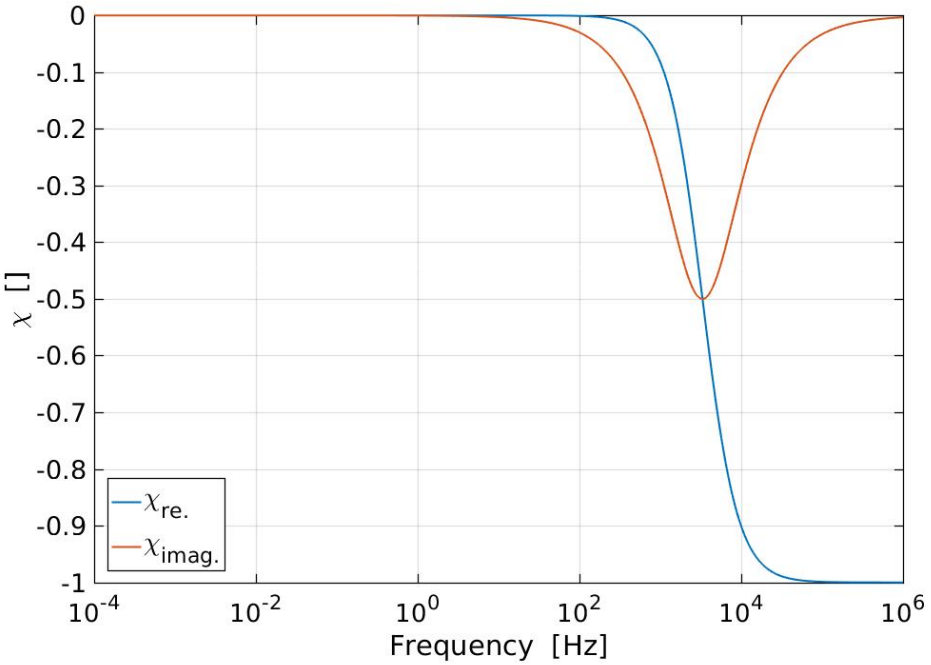

Figure 23: Magnetic susceptibility dependence on frequency for LPF TMs.

3.4 MAGNETIC FORCE IN THE PRESENCE OF AN APPLIED AC MAGNETIC FIELD

During LPF operations we carried a series of injections with the magnetic coils to generate a controlled magnetic field at the TMs position. The goal was to produce a force to move the TMs. Analysing the movement through the interferometer readout, we can extract the magnetic properties of the TMs and the surrounding environment. In this section we will study the different forces and torques generated at the TMs during the coils injections. This is a specific case, but the expressions obtained here are quite general and would apply when analysing the movement of a magnetic dipole in the presence of an oscillating magnetic field with a certain offset.

Let's start considering that we now do not have a constant magnetic field **B**. Instead, our magnetic field at the TM position will be composed by the sum of a

background magnetic field $\mathbf{B}_{\text{back.}}$ and the field generated by the coil $\mathbf{B}_i$, which in turn will be composed by an oscillating signal $\mathbf{B}_i^{AC}\sin(\omega t)$ plus an offset $\mathbf{B}_i^{DC}$:

$$\mathbf{B} = \mathbf{B}_{\text{back.}} + \mathbf{B}_i = \mathbf{B}_{\text{back.}} + \mathbf{B}_i^{DC} + \mathbf{B}_i^{AC}\sin(\omega t) \tag{3.18}$$

$$= \mathbf{B}_o + \mathbf{B}_i^{AC}\sin(\omega t) \tag{3.19}$$

where ω is the frequency of the injected signal with the coil and $\mathbf{B}_i^{AC}$ its amplitude. In Equation (3.19) we have included the two non-oscillating terms, the corresponding to the magnetic field background $\mathbf{B}_{\text{back.}}$ and coil injected offset $\mathbf{B}_i^{DC}$ into a single term $\mathbf{B}_o$. Exactly the same can be applied for the magnetic field gradient:

$$\nabla\mathbf{B} = \nabla\mathbf{B}_{\text{back.}} + \nabla\mathbf{B}_i = \nabla\mathbf{B}_{\text{back.}} + \nabla\mathbf{B}_i^{DC} + \nabla\mathbf{B}_i^{AC}\sin(\omega t) \tag{3.20}$$

$$= \nabla\mathbf{B}_o + \nabla\mathbf{B}_i^{AC}\sin(\omega t) \tag{3.21}$$

where $\nabla\mathbf{B}_o$ is approximately equal to $\nabla\mathbf{B}_i^{DC}$, since the gradient of the interplanetary magnetic field $\nabla\mathbf{B}_{\text{back.}}$ is negligible, as stated before. If we substitute Equations (3.19) and (3.21) into Equation (3.4) and rearrange the terms, using the trigonometric identity:

$$\sin^2(\omega t) = \frac{1}{2} - \frac{\cos(2\omega t)}{2} \tag{3.22}$$

we can separate the terms into three different contributions:

$$\mathbf{F} = \mathbf{F}_{DC} + \mathbf{F}_{1\omega} + \mathbf{F}_{2\omega} = \tag{3.23a}$$

$$= V\left[\langle \mathbf{M_r}\cdot\nabla\mathbf{B}_o\rangle + \frac{\chi}{\mu_0}\left(\langle \mathbf{B}_o\cdot\nabla\mathbf{B}_o\rangle + \frac{1}{2}\langle \mathbf{B}_i^{AC}\cdot\nabla\mathbf{B}_i^{AC}\rangle\right)\right] \tag{3.23b}$$

$$+ V\sin(\omega t)\left[\langle \mathbf{M_r}\cdot\nabla\mathbf{B}_i^{AC}\rangle + \frac{\chi}{\mu_0}\left(\langle \mathbf{B}_o\cdot\nabla\mathbf{B}_i^{AC}\rangle + \frac{1}{2}\langle \mathbf{B}_i^{AC}\cdot\nabla\mathbf{B}_o\rangle\right)\right] \tag{3.23c}$$

$$- \frac{V\cos(2\omega t)}{2}\left[\frac{\chi}{\mu_0}\langle \mathbf{B}_i^{AC}\cdot\nabla\mathbf{B}_i^{AC}\rangle\right] \tag{3.23d}$$

where we can distinguish three different contributions. A DC term, as indicated in Eq. (3.23b), which is independent of the frequency ω of the injected magnetic field. A term that oscillates at the same frequency ω of the injected signal, as seen in Eq. (3.23c). And finally, a term that oscillates at two times the frequency ω of the injected signal, as stated in Eq. (3.23d).

With all the above considerations, we can compute which will be the force acting along the axis joining the two TMs F_x:

$$F_x = F_{DC,x} + F_{1\omega,x} + F_{2\omega,x} = \tag{3.24a}$$

$$= V\left[\langle \mathbf{M_r}\cdot\nabla B_{o,x}\rangle + \frac{\chi}{\mu_0}\left(\langle \mathbf{B}_o\cdot\nabla B_{o,x}\rangle + \frac{1}{2}\langle \mathbf{B}_i^{AC}\cdot\nabla B_{i,x}^{AC}\rangle\right)\right] \tag{3.24b}$$

$$+ V\sin(\omega t)\left[\langle \mathbf{M_r}\cdot\nabla B_{i,x}^{AC}\rangle + \frac{\chi}{\mu_0}\left(\langle \mathbf{B}_o\cdot\nabla B_{i,x}^{AC}\rangle + \frac{1}{2}\langle \mathbf{B}_i^{AC}\cdot\nabla B_{o,x}\rangle\right)\right] \tag{3.24c}$$

$$- \frac{V\cos(2\omega t)}{2}\left[\frac{\chi}{\mu_0}\langle \mathbf{B}_i^{AC}\cdot\nabla B_{i,x}^{AC}\rangle\right] \tag{3.24d}$$

3.5 MAGNETIC TORQUES IN THE PRESENCE OF AN APPLIED AC MAGNETIC FIELD

If we manipulate the equations regarding the torque, we will observe a similar behaviour like the one described in the previous section, with DC, 1ω and 2ω terms. However, as we will see later when we observe the data series of the magnetic injections, we will only be able to measure the 1ω term. The reason comes from the fact that our instrument is not as sensitive measuring rotations as it is measuring displacements along the axis joining the test masses (the x-axis). That, along with the fact that the 1ω term will be the strongest one during an injection will make us neglect the terms $\mathbf{N}_{DC}$ and $\mathbf{N}_{2\omega}$ from now on. Taking that into account, if we apply an oscillating magnetic field $\mathbf{B}(t) = \mathbf{B}_i^{AC}\sin(\omega t)$ we will have the following expression:

$$\mathbf{N} = V\sin(\omega t)\left\langle \mathbf{M_r}\times\mathbf{B}_i^{AC} + \mathbf{r}\times\left[(\mathbf{M}\cdot\boldsymbol{\nabla})\mathbf{B}_i^{AC}\right]\right\rangle \tag{3.25}$$

if we further expand the expression into its different components we will have, first the torque around the x-axis, $N_{1\omega,\theta}$:

$$\begin{aligned} N_{1\omega,\theta} =& V\sin(\omega t)\Bigg[\left\langle M_{r,y}B_{i,z}^{AC} - M_{r,z}B_{i,y}^{AC}\right\rangle && (3.26a)\\ &+y\left\langle M_{r,x}\frac{\partial B_{i,z}^{AC}}{\partial x} + M_{r,y}\frac{\partial B_{i,z}^{AC}}{\partial y} + M_{r,y}\frac{\partial B_{i,z}^{AC}}{\partial z}\right\rangle && (3.26b)\\ &-z\left\langle M_{r,x}\frac{\partial B_{i,y}^{AC}}{\partial x} + M_{r,y}\frac{\partial B_{i,y}^{AC}}{\partial y} + M_{r,y}\frac{\partial B_{i,y}^{AC}}{\partial z}\right\rangle\Bigg] && (3.26c)\end{aligned}$$

the torque around the y-axis, $N_{1\omega,\eta}$:

$$\begin{aligned} N_{1\omega,\eta} =& V\sin(\omega t)\Bigg[\left\langle M_{r,z}B_{i,x}^{AC} - M_{r,x}B_{i,z}^{AC}\right\rangle && (3.27a)\\ &+x\left\langle M_{r,x}\frac{\partial B_{i,z}^{AC}}{\partial x} + M_{r,y}\frac{\partial B_{i,z}^{AC}}{\partial y} + M_{r,y}\frac{\partial B_{i,z}^{AC}}{\partial z}\right\rangle && (3.27b)\\ &-z\left\langle M_{r,x}\frac{\partial B_{i,x}^{AC}}{\partial x} + M_{r,y}\frac{\partial B_{i,x}^{AC}}{\partial y} + M_{r,y}\frac{\partial B_{i,x}^{AC}}{\partial z}\right\rangle\Bigg] && (3.27c)\end{aligned}$$

and the torque around the z-axis, $N_{1\omega,\phi}$:

$$\begin{aligned} N_{1\omega,\phi} =& V\sin(\omega t)\Bigg[\left\langle M_{r,x}B_{i,y}^{AC} - M_{r,y}B_{i,x}^{AC}\right\rangle && (3.28a)\\ &+x\left\langle M_{r,x}\frac{\partial B_{i,y}^{AC}}{\partial x} + M_{r,y}\frac{\partial B_{i,y}^{AC}}{\partial y} + M_{r,y}\frac{\partial B_{i,y}^{AC}}{\partial z}\right\rangle && (3.28b)\\ &-y\left\langle M_{r,x}\frac{\partial B_{i,x}^{AC}}{\partial x} + M_{r,y}\frac{\partial B_{i,x}^{AC}}{\partial y} + M_{r,y}\frac{\partial B_{i,x}^{AC}}{\partial z}\right\rangle\Bigg] && (3.28c)\end{aligned}$$

We can simplify a lot these expressions. First of all, our interferometric system is not sensitive to rotations around the x-axis since this axis is aligned with the laser beam – and those rotations would not affect the distance x between the TMs. Hence, we can completely forget about the term $N_{1\omega,\theta}$. Second, the terms containing y, like in (3.28c) and z, like in (3.27c) will be negligible, since the coil centre and the TM are aligned along the x-axis. This alignment has a precision below the µm [111, 112]. Hence, the terms containing x, like (3.28b) and (3.27b) will be orders of magnitude bigger, and we can safely neglect the terms with y and z. Regarding the terms containing x, (3.28b) and (3.27b), we can neglect them too since the magnetic field in the y and z direction is zero along the axis joining the coil and TM centres (there is only component in the x-axis), and both $\boldsymbol{\nabla} B^{AC}_{i,y}$ and $\boldsymbol{\nabla} B^{AC}_{i,z}$ will be zero. For the same reason, the term containing $B^{AC}_{i,z}$ (3.27a) and $B^{AC}_{i,y}$ in (3.28a) can be neglected too.

After all these simplifications, we will have that during an applied sinusoidal signal with the coils during LPF magnetic experiments, the torque measured around the y-axis will be:

$$N_{1\omega,\eta} = V \sin(\omega t) \left\langle M_{r,z} B^{AC}_{i,x} \right\rangle \tag{3.29}$$

and the torque around the z-axis will be:

$$N_{1\omega,\phi} = V \sin(\omega t) \left\langle -M_{r,y} B^{AC}_{i,x} \right\rangle \tag{3.30}$$

Notice that, apart from the applied magnetic field, $N_{1\omega,\eta}$ only depends on $M_{r,z}$ and $N_{1\omega,\phi}$ only depends on $M_{r,y}$. Hence, analysing the torques during the magnetic experiments will be a good way of obtaining the y and z component of the remanent magnetic moment $\mathbf{M_r}$.

4

MAGNETIC ENVIRONMENT ON-BOARD LISA PATHFINDER

As we have seen in Chapter 3, the magnetic field surrounding the TMs couples with the remanent magnetic moment and magnetic susceptibility to produce a force on the TMs. It is therefore of the uttermost importance to have a complete understanding of the magnetic field for both, its DC and fluctuations. That is what we will do in this chapter. By using the magnetometers inside the spacecraft, we will study how the magnetic field behaves. Furthermore, we will disentangle which part is generated due to the spacecraft and which part is coming from the interplanetary medium.

The chapter is organized as follows. We will start it with a brief introduction of how are the magnetometers inside the spacecraft and where they are located. In the next section, we will study the DC magnetic field during the mission lifetime and its evolution. We will follow by studying which are the fluctuations of the magnetic field within the spacecraft, and will differentiate between the part coming from the spacecraft and the part coming from the interplanetary medium. Finally, we will see how the fluctuations of the magnetic field are not stationary, and how they vary depending on several parameters from the interplanetary medium.

4.1 INTRODUCTION

After a one-month cruise phase, LPF reached the L1 orbit in January 2016. The magnetometers on-board started collecting data on January 11th, at the start of the LTP commissioning phase and, apart from some short outages events, they acquired data uninterruptedly until the end of the scientific operations in July 2017.

Contrary to many other missions that carry their magnetometers at the end of a long boom to isolate the measurement from spacecraft interferences, magnetometers on-board LPF are located inside the spacecraft with the main objective of monitoring the magnetic field as close as possible to the TM position. At the same time, the magnetometers have to be sufficiently far away from the TMs since the fluxgate magnetometer head contains a magnetically active component that could induce spurious forces on the TM, therefore disturbing the main scientific measurement of the mission. The trade-off between these two conditions results in the locations shown in Figure 24.

All magnetometers are located in the plane defined by the TMs and the OB. This configuration allows for an approximate estimate of the magnetic field gradient, a key factor in the magnetic noise contribution to the TMs free-fall, across two axes but it leaves the third one, z in the spacecraft frame, unmeasured. It is worth stressing that the gradients estimated that way are unlikely to be representative of the magnetic field gradient at the TMs position, the reason being that local sources,

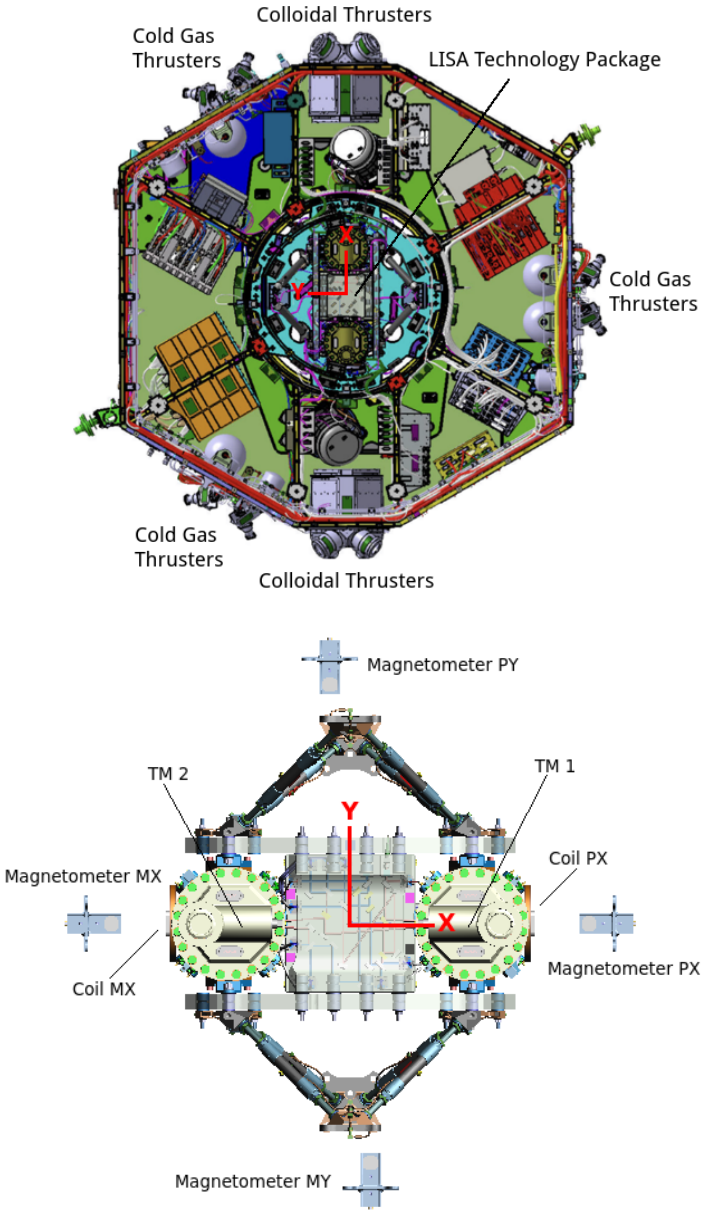

Figure 24: *Top:* x-y plane view of the LPF spacecraft with the solar panel removed. The positions of the three sets of Cold Gas thrusters and the two sets of Colloidal Thrusters are indicated, as well as the LTP in the centre of the spacecraft. The LPF reference frame is shown in red, with its origin in the middle of the LTP. *Bottom:* Zoom of the LTP from the upper figure. Here we show the position of several items from the DDS, consisting in two coils and four tri-axial fluxgate magnetometers. In this notation 'P' stands for 'plus' and 'M' for 'minus', being each element named according to their position within the satellite reference frame. The position of both TMs is also indicated, as well as the LPF reference frame, like in the upper figure.

as for instance the temperature sensors surrounding the TMs in the electrode housing, could be a potential source of local magnetic gradient [113]. For instance, for the worst case layout of these sensors, the magnetic field gradient across x between the two faces of the TMs could reach values around 10 μT m^{-1}, which

would be orders of magnitude above the values we report in Table 2 for the gradients computed across magnetometers. We will study this more in depth in Section 6.3. As we will show in the following, the DC value measured by each magnetometer is completely dominated by the spacecraft units while the fluctuations have both a spacecraft and an interplanetary contribution.

4.2 EVOLUTION OF THE MEASURED ON-BOARD MAGNETIC FIELD

In the top panel of Figure 25 we show the time series for the read-out of the four magnetometers on-board LPF since the magnetometers switch-on and until the end of the mission, in July 2017. We provide the magnetic field measurements in the x, y and z axes in the LTP reference frame, although the x-component contains most of the interesting features that we will discuss in the following.

The absolute value of the magnetic field at each magnetometer location is dominated by the spacecraft contribution reaching values up to 1 μT, far from typical IMF values which would be of the order of $5-10\,$nT. Most of the magnetic field measured by the magnetometers corresponds to the contribution of the cold gas micro-propulsion system, in particular to the magnets on the high-pressure latch valves. With an on-ground measured moment of 950 mA m^2, they contribute up to 80% of the magnetic field measured by some of the magnetometers [114].

The time series can be divided in six different segments which correspond to the different phases of the mission, namely comissioning, LTP operations, ST7-DRS operations, the associated mission extension for both experiments, and decomissioning. The most prominent features in the magnetic field timeline are experiments with the coils to characterise the magnetic contribution to the TMs free-fall. These experiments are listed in Table 3. Other features that affected the magnetic environment and can be identified in Figure 25 are listed in Table 4. In the latter case, these are not associated to the activation of the coils on-board (except for event 'a', which was a check of the correct functioning of coil 2) but to the operation of the spacecraft itself, i.e., from changes in configuration to identified anomalies during operations.

In order to provide a more quantitative description, we summarise in Table 2 the mean values of the three components of the magnetic field measured on-board for the four magnetometers. We repeated the same analysis for the four different phases that we already distinguished during our analysis, i.e. LTP and ST7-DRS nominal and extended operations. For each segment we also provide an estimate of the gradient of the magnetic field across each couple of magnetometers in the x and y directions. The dates for each subset were selected trying to maximise the amount of data for that segment and trying to avoid any major changes (no experiments, glitches, etc). LTP nominal goes from March 1st, 2016, to April 27th, 2016. LTP extended goes from December 07th, 2016, to January 13th, 2017 and from January 15th, 2017, to March 14th, 2017. The 2 days gap is to get rid of the short ST7-DRS period in between. ST7-DRS nominal goes from June 27th, 2016, to December 7th, 2016. ST7-DRS extended goes from March 19th, 2017, to April 28th, 2017.

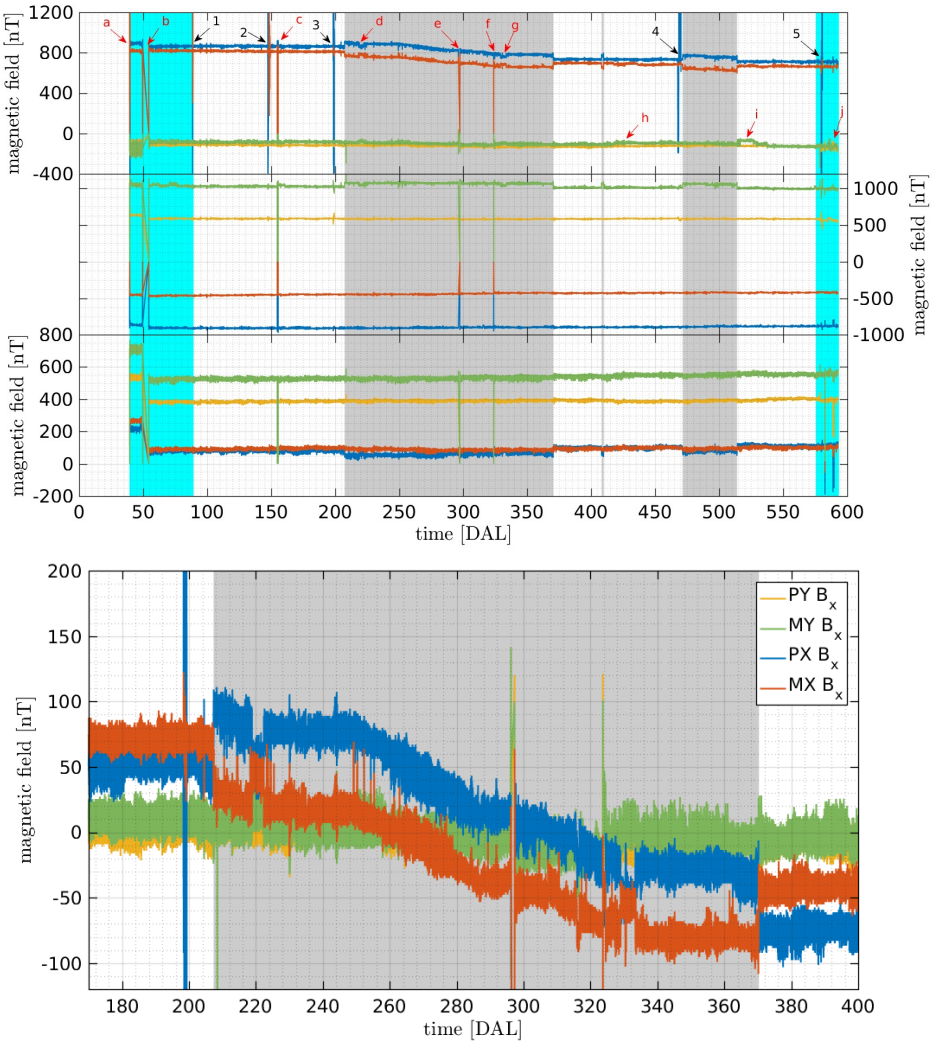

Figure 25: *Top:* Magnetic field measurements on-board LPF from launch date until the satellite passivation. The time axis is indicated in DAL. The two cyan areas (DAL 40-90 and DAL 575-593) correspond to the commissioning and decommissioning periods, respectively. The three grey shadowed areas (DAL 210-370, DAL 414-415 and DAL 470-510) correspond to the ST7-DRS operations, and the rest correspond to LTP operations. From top to bottom pannel: the x, y and z components of the magnetic field, for magnetometers PX (blue), MX (red), PY (yellow) and MY (green). In this notation, 'M' stands for minus and 'P' for plus. 'X' and 'Y' refer to axes on-board in which the magnetometers are aligned, so PX and MX are the two closest magnetometers to the TMs. The arrows correspond to events related to important changes in magnetic field. These events are reported in Tables 3 & 4. *Bottom:* Zoom of the x-component measurements for the four magnetometers during the first ST7-DRS operations period (Aug. - Nov. 2016). In this case, we removed the DC level from each channel to show all measurements in the same scale. See the text for more detail.

In terms of the magnetic environment, we notice that ST7-DRS operations had an impact in the spacecraft magnetic environment. As seen in the bottom panel of Figure 25, the mean value of the x component shows a steady decrease of around 150 nT starting around Aug. 8th and ending around Nov. 13th. for the two mag-

Magnetometer	LTP Nominal	
	(B_x, B_y, B_z) [nT]	$\lvert\vec{B}\rvert$ [nT]
PX	$(866.880 \pm 0.005, -908.001 \pm 0.005, 82.053 \pm 0.005)$	1258.046 ± 0.009
MX	$(816.303 \pm 0.005, -457.364 \pm 0.006, 91.730 \pm 0.005)$	940.184 ± 0.009
PY	$(-111.894 \pm 0.005, 585.993 \pm 0.005, 384.374 \pm 0.005)$	709.684 ± 0.009
MY	$(-86.583 \pm 0.006, 1023.586 \pm 0.006, 527.776 \pm 0.005)$	1154.890 ± 0.010
	$(\partial_x B_x, \partial_x B_y, \partial_x B_z)$ [nT/m]	$\lvert\partial_x\vec{B}\rvert$ [nT/m]
PX- MX	$(62.717 \pm 0.006, -611.033 \pm 0.007, -12.544 \pm 0.005)$	614.371 ± 0.010
	$(\partial_y B_x, \partial_y B_y, \partial_y B_z)$ [nT/m]	$\lvert\partial_y\vec{B}\rvert$ [nT/m]
PY- MY	$(-34.318 \pm 0.006, -542.507 \pm 0.005, -185.989 \pm 0.005)$	574.529 ± 0.009
	DRS Nominal	
	(B_x, B_y, B_z) [nT]	$\lvert\vec{B}\rvert$ [nT]
PX	$833.375 \pm 0.026, -901.685 \pm 0.004, 60.990 \pm 0.005)$	1229.337 ± 0.026
MX	$(710.415 \pm 0.024, -437.246 \pm 0.006, 87.603 \pm 0.003)$	838.778 ± 0.025
PY	$(-124.643 \pm 0.005, 581.454 \pm 0.003, 390.371 \pm 0.003)$	711.347 ± 0.007
MY	$(-102.913 \pm 0.006, 1064.324 \pm 0.006, 531.317 \pm 0.004)$	1194.016 ± 0.008
	$(\partial_x B_x, \partial_x B_y, \partial_x B_z)$ [nT/m]	$\lvert\partial_x\vec{B}\rvert$ [nT/m]
PX- MX	$(151.504 \pm 0.011, -627.590 \pm 0.018, -34.241 \pm 0.007)$	646.5250 ± 0.022
	$(\partial_y B_x, \partial_y B_y, \partial_y B_z)$ [nT/m]	$\lvert\partial_y\vec{B}\rvert$ [nT/m]
PY- MY	$(-29.619 \pm 0.005, -596.135 \pm 0.020, -182.260 \pm 0.006)$	624.078 ± 0.021
	LTP extended	
	(B_x, B_y, B_z) [nT]	$\lvert\vec{B}\rvert$ [nT]
PX	$(736.202 \pm 0.006, -896.577 \pm 0.005, 100.497 \pm 0.006)$	1164.450 ± 0.010
MX	$(696.128 \pm 0.005, -428.666 \pm 0.005, 94.944 \pm 0.006)$	823.021 ± 0.009
PY	$(-131.575 \pm 0.005, 582.902 \pm 0.005, 394.238 \pm 0.005)$	715.898 ± 0.009
MY	$(-109.538 \pm 0.006, 1006.245 \pm 0.006, 541.992 \pm 0.006)$	1148.165 ± 0.010
	$(\partial_x B_x, \partial_x B_y, \partial_x B_z)$ [nT/m]	$\lvert\partial_x\vec{B}\rvert$ [nT/m]
PX- MX	$(49.694 \pm 0.006, -634.456 \pm 0.006, 7.024 \pm 0.006)$	636.438 ± 0.010
	$(\partial_y B_x, \partial_y B_y, \partial_y B_z)$ [nT/m]	$\lvert\partial_y\vec{B}\rvert$ [nT/m]
PY- MY	$(-29.880 \pm 0.006, -524.843 \pm 0.006, -191.632 \pm 0.006)$	559.532 ± 0.010
	DRS extended	
	(B_x, B_y, B_z) [nT]	$\lvert\vec{B}\rvert$ [nT]
PX	$(762.165 \pm 0.011, -886.156 \pm 0.007, 79.828 \pm 0.009)$	1171.555 ± 0.016
MX	$(634.580 \pm 0.010, -421.112 \pm 0.005, 94.165 \pm 0.006)$	767.394 ± 0.013
PY	$(-118.939 \pm 0.005, 583.369 \pm 0.005, 391.387 \pm 0.006)$	712.495 ± 0.009
MY	$(-102.051 \pm 0.008, 1052.539 \pm 0.011, 551.385 \pm 0.008)$	1192.593 ± 0.016
	$(\partial_x B_x, \partial_x B_y, \partial_x B_z)$ [nT/m]	$\lvert\partial_x\vec{B}\rvert$ [nT/m]
PX- MX	$(158.210 \pm 0.015, -630.569 \pm 0.006, -18.599 \pm 0.008)$	650.380 ± 0.018
	$(\partial_y B_x, \partial_y B_y, \partial_y B_z)$ [nT/m]	$\lvert\partial_y\vec{B}\rvert$ [nT/m]
PY- MY	$(-22.898 \pm 0.010, -581.655 \pm 0.013, -207.513 \pm 0.006)$	617.987 ± 0.017

Table 2: Mean values of the DC magnetic field for different spacecraft configurations. Dates corresponding to each period are indicated on the text. Errors are computed as $\sigma/\sqrt{N}$.

netometers located near the test masses, i.e. magnetometers PX and MX in the bottom panel of Figure 24. This period is coincident with the start of operations of the ST7-DRS instrument. Apart from this long drift, in magnetometers PX and MX we also observe a DC increase of about 40 nT when we turn on the ST7-DRS

system and the same decrease when we turn it off. This DC change should be related to some units being switched on and off when we change the control system of the satellite. The reason of this long term trend observed in the magnetic field on-board can be explained by the differences between LTP and ST7-DRS micro-propulsion systems.

The LTP micro-propulsion system consists of three clusters each featuring four cold gas thrusters [80]. The thruster system uses high-pressure Nitrogen propellant to provide very small impulses with a thrust range of 1–500μN. Four Nitrogen tanks store the gas at 310 bar with a maximum capacity of 9.6 kilograms of Nitrogen. The ST7-DRS micropropulsion system is composed by two Colloidal Micro Newton Thruster (CMNT) clusters [115]. Each cluster includes four complete and independent thruster units. For the CMNT subsystem, thrust is adjustable from 5–30μN by changing the beam voltage and/or propellant flow rate that determines the beam current. In this case, the propellant is stored in four electrically isolated stainless steel bellows compressed by four constant force springs set to supply four micro-valves with propellant at approximately 1 atm of pressure. In terms of the spacecraft magnetic field, this sets a relevant difference between both thrust subsystems since the continuous operation of the CMNT subsystem leads to a steady displacement of the bellows inside the storage tank. Although not having a direct impact on the mission operations in terms of gravitational pull, it is precisely this displacement of the stainless steel bellows occurring during the depletion of the fuel tanks the one that originates the observed magnetic field change. Indeed, given the known geometry and measured magnetic properties of the CMNT we can estimate the impact of the operation of these thrusters on the magnetic environment. The CMNT are aligned in the direction joining both test masses (x direction) as can be seen in the top panel of Figure 24. They are located at a distance of 28 cm with respect to the two magnetometers that are located along this same axis, the PX and MX magnetometer in the notation of the bottom panel of Figure 24. The measurement on-ground reported a magnetic moment for these units of 209 mA m² (in modulus) which would produce a magnetic field of 1.1 μT on the position of the closest magnetometer to each CMNT according to the equation of the magnetic field produced by a magnetic dipole:

$$\mathbf{B}(\mathbf{r}) = \frac{\mu_0}{4\pi}\left(\frac{3\mathbf{r}(\mathbf{m}\cdot\mathbf{r})}{\mathbf{r}^5} - \frac{\mathbf{m}}{\mathbf{r}^3}\right) \tag{4.1}$$

with $\mathbf{m}$ being the magnetic moment of the source and $\mathbf{r}$ a vector going from the center of the magnetic dipole to the position where the magnetic field is being measured. If we now assume that the overall variation in the magnetic field measured in the x direction during ST7-DRS operations is due to the displacement of the bellow inside the CMNT valves, this would imply a 1 cm displacement which is compatible with the geometry of the valve and the amount of propellant being expelled during this period.

Event	Date (DAL)
(1) Comissioning injec. in TMs 1 & 2	28 Feb'16 (87)
(2) Mag. exps. in TMs 1 & 2	27 April'16 (146)
(3) Mag. exps. in TM 1	18 Jun'16 (198)
(4) Mag. exps. in TM 1	14 Mar'17 (467)
(5) Decomissioning injections	04 Jul'17 (579)

Table 3: Dates associated with magnetic experiments on-board LPF. In parenthesis we include the DAL.

Event	Date (DAL)
(a) Coils check	11 Jan'16 (39)
(b) Propulsion module released	22 Jan'16 (50)
(c) DMU software crash	5 May'16 (154)
(d) Cluster-2 DCIU anomaly	9 Jul'16 (219)
(e) LTP safe mode	24 Sep'16 (296)
(f) DMU software crash and reboot	21 Oct'16 (296)
(g) Thruster-4 anomaly	27 Oct'16 (329)
(h) Cooling down	23 Jan'17 (417)
(i) Cooling down	29 Apr'17 (513)
(j) High pressure latch valves switch	13 Jul'17 (588)

Table 4: Dates associated with events that impacted the magnetic environment on-board LPF. In parenthesis we include the DAL.

4.3 FLUCTUATIONS OF THE ON-BOARD MAGNETIC FIELD

Given that any varying magnetic field or magnetic field gradient will couple into the motion of the TMs, understanding the origin of the fluctuations of the magnetic field measured on-board is an important output of LPF for future gravitational-wave detectors in space. In the previous section we have seen how the electronic units on-board the satellite are the dominant contribution to the magnetometers DC measurement since the interplanetary contribution (typically of the order of $5-10\,\mathrm{nT}$) is at least one order of magnitude below the values reported, for instance, in Table 2. The situation is different when we study the variations of the magnetic field. A wide variety of phenomena can produce a varying magnetic field and, as we show in the following, both fluctuations originated by the spacecraft and by the IMF are relevant to understand the magnetic field spectra measured by LPF.

We divide the three sections below as follows. First, we provide a characterisation of the different magnitudes describing the fluctuations of the magnetic field on-board to then focus on the physical mechanisms describing these fluctuations for two different frequency regimes that we distinguish in our data.

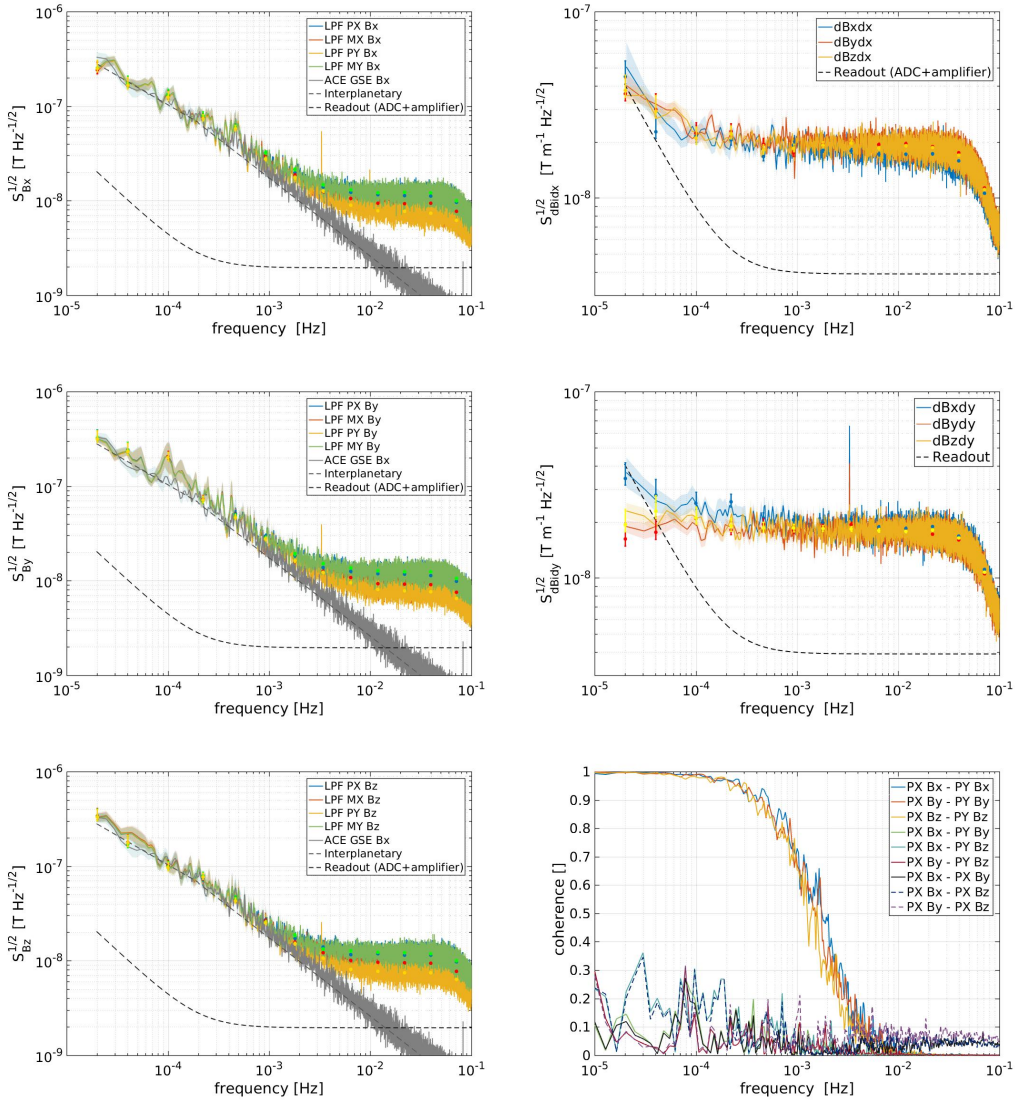

Figure 26: Characterisation of the magnetic field environment on-board for the period from 13 Feb'17 to 2 Mar'17. *Left:* Spectrum of the, from top to bottom, x, y and z components of the magnetic field from the four LPF magnetometers and from the ACE magnetometer. Dashed lines correspond to the contribution to LPF magnetometers coming from IMF and electronics. *Right:* Spectrum of the gradient of the magnetic field along the x-axis (uppermost panel) and y-axis (middle panel) on-board LPF. The dashed lines correspond to the contribution coming from electronics to LPF magnetometers. The bottom panel corresponds to the coherence function between the three axes magnetic field as measured in independent magnetometers on-board the satellite.

4.3.1 *Characterisation of magnetic field fluctuations on-board*

The fact that the four magnetometers of the magnetic diagnostics subsystem enclose the main instrument enables the direct comparison between different readouts to disentangle spacecraft from interplanetary contributions. In order to do so, we will use the coherence function which statistically quantifies common

fluctuations between two time series – see Section B.3. In the bottom right panel of Figure 26 we show the coherence function between the different channels of the magnetometers pair PX and PY, although the results shown are equivalent for each couple of magnetometers analysed. As shown in the figure, coherence between orthogonal axes is suppressed in the whole band while correlation between measurements on the same axes show a steep increase below 5 mHz. Given the low frequency of the coherent magnetic field fluctuations and the location of the magnetometers, these results points towards the IMF fluctuations as the leading contribution in the sub-mHz frequency regime. On the other hand, fluctuations above the mHz region would be dominated by read-out electronics. This is further confirmed by the following analysis.

To evaluate the magnetic field and magnetic field gradient fluctuations we compute the ASD (the square root of the PSD) by means of the Welch averaged periodogram [116]. We use data segments of 56 h and apply a Blackman-Harris window to prevent spectral leakage. To make sure that the window is not biasing our estimate we remove the lowest four frequency bins of the spectra. To compute the dots in the spectra we performed an averaging in the frequency domain. See Section B.1 and the method described in [117] for a deeper explanation. All the analysis and data post-processing were performed with LTPDA [118], a MATLAB toolbox designed for the analysis of the LPF data.

The spectra of magnetic field fluctuations are shown in the left panel of Figure 26, from top to bottom, for the x, y and z components of the magnetic field, respectively. In this case, we notice that the two frequency regimes previously observed in the coherence function also appear with differentiated spectral behaviour above and below 5 mHz. Indeed, while the sub-mHz fluctuations show an almost constant spectral index, fluctuations above the mHz are flat and uncorrelated. Moreover, the magnitude of sub-mHz fluctuations is equal for all four magnetometers whereas in the high frequency regime different magnetometers show a different noise plateau. In the different panels of Figure 26 we show some fits to the data (the small dots). We will describe them in detail in Section 4.4, where we will show how changes in some parameters of the interplanetary media affect the spectrum of the magnetic field.

As we described in Chapter 3, not only the gradient of the magnetic field but also the fluctuations of this gradient can contribute as a force exerted on the TMs. Thus, we took advantage of the configuration of the magnetometers on-board to estimate the magnetic field gradient from the difference between magnetic field measurements on opposing sides of the LTP. Opposing magnetometers are separated by 0.65 m in the PX-MX case, and 0.54 m in the PY-MY case. Check bottom panel of Figure 24 for a clear view of the setup. All magnetometers in the spacecraft are placed in the same x-y plane and, therefore, no estimates of the z gradients were possible. In the right top and right middle panels of Figure 26 we show the ASD of the fluctuations of the magnetic field gradient across the x and y axis, respectively, of LPF for the three components of the magnetic field. The spectra of the magnetic field gradient are flat at $20\,\mathrm{nT\ m^{-1}Hz^{-1/2}}$ down to about 0.1 mHz, to even smaller frequencies than in the case of the magnetic field

fluctuations. In this case, the noise measured seems to be in accordance with our electronics noise (see Section 4.3.1.2 for more details), and thus, we are limited by our instrument to measure any fluctuation smaller than this value. It should be reminded than this value is not likely to be representative of the magnetic field gradient at the TMs position, since any local source of magnetic field close to the TM could be a potential source of magnetic field gradient that would not be measured by our pair of magnetometers if they are too far away from the mentioned source.

Although we have previously described the smooth shape of the magnetic field spectra, there are also some spectra lines appearing in the panels in Figure 26. In some of them a line at 3.3 mHz appears in the PY magnetometer channels, with corresponding harmonics at 6.6 and 10 mHz. Moreover, the signal appears to be stronger in the x component of the magnetic field. We can not confirm the physical origin of these lines. However, since it is clearly visible in the magnetic field gradient across the y-axis, this points out to a local origin and excludes any source coming from the interplanetary media, which would be sensed equally by all our magnetometers. The distribution of the units and the magnetometers on-board points towards the OBC as the probable source of this magnetic field tone.

4.3.1.1 *Fluctuations in the sub-millihertz: interplanetary magnetic field contribution*

The IMF measured by our magnetometers is imprinted on the solar wind plasma that surrounds the spacecraft and travels through the interplanetary media. Plasma fluctuations in interplanetary space have been successfully described in the framework of the classical Kolmogorov turbulence [119]. In this framework, energy injected into the interplanetary plasma at large scales is transferred by non-linear interactions to microscales where it is finally dissipated, thus heating the plasma. The low-frequency part of the magnetic field and plasma-velocity power spectra often exhibits a clear f^{-1} scaling, from DC up to frequencies of about 10^{-4} Hz in the fast Alfvénic wind [120], where the turbulent energy cascade becomes active. It is worth noting that, contrary to the fast solar wind, in the low-speed streams the injection range may cover a smaller range of frequencies and sometimes not to be present at all [121]. At frequencies higher than 10^{-4} Hz but below the ionic break that occurs around 0.1–1 Hz, we find what we call the inertial range. In this range, the solar wind is in a state of fully developed turbulence, where the magnetic energy spectrum has a well defined Kolmogorov $f^{-5/3}$ spectrum [122]. At frequencies higher than the ionic break the Kolmogorov spectrum breaks down and the magnetic fluctuations display a steeper $f^{-7/3}$ power-law spectrum, up to frequencies of about 100 Hz [123], where dissipation processes at proton scales take place. At even higher frequencies sometimes the spectrum steepens even more, roughly described by a further power law [123] with a scaling exponent between $f^{-3.5}$ and $f^{-5.5}$, or perhaps by an exponential decay [124]. Since these scales suffer for a lack of spacecraft measurements, a clear indication cannot be provided. This region of frequencies has been indicated as a range where collisionless dissipative mechanisms are efficiently at work at electron scales [123–125]. All these different regimes can be seen at Figure 27, where we can see the

IMF spectrum for a wide range of frequencies.

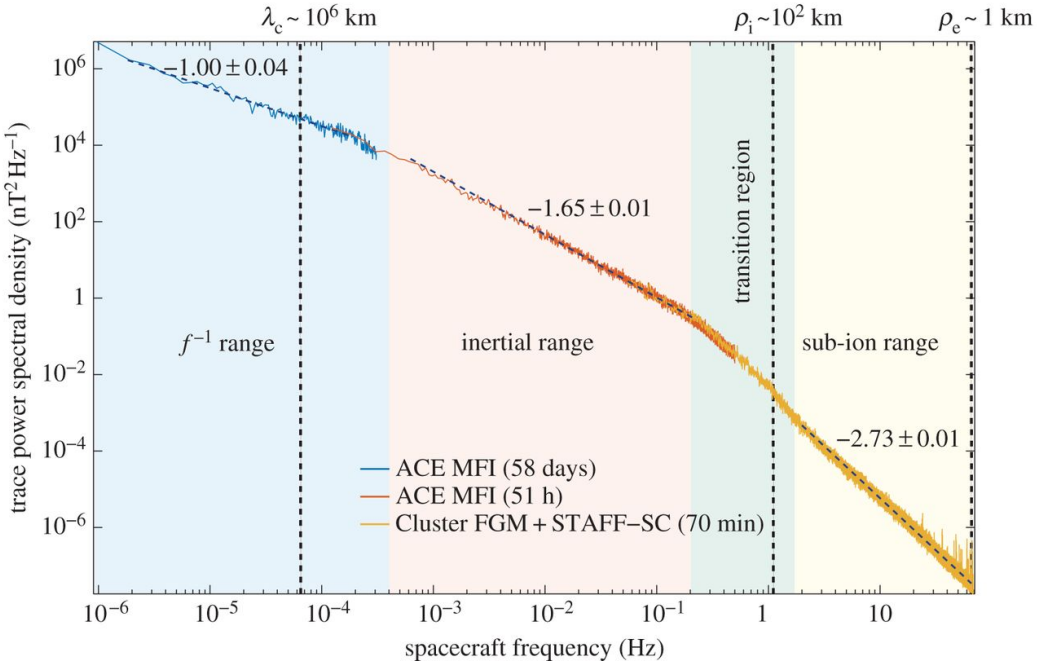

Figure 27: IMF fluctuations for a wide range of frequencies. In the figure we can observe the different frequency regimes which are explained on the text. (Credits: [126]).

In order to check our measurements with previous characterisation of the solar wind, in the left panels of Figure 26 we compare the ASD of the magnetic field obtained during a LPF noise run to a set of data obtained from ACE [127] in the same period of time. The ACE mission monitors different parameters of the solar wind by means of a suite of instruments on-board and, as LPF, follows a Lissajous orbit around L1. It is therefore a useful dataset with which to compare our measurements. ACE data is shown in Geocentric Solar Ecliptic (GSE) coordinate system, which has its x-axis pointing from Earth towards the Sun and its y-axis is chosen to be in the ecliptic plane pointing towards dusk. It is worth mentioning that even though both satellites are orbiting around L1, the distance separating them can be of the order of 10^5–10^6 kilometers. However, we can safely compare the fluctuations of the magnetic field between both satellites at frequencies around the 20–50 µHz, which is the band in which we will focus our analysis. As we will discuss in more detail, the typical velocity of around 200–500 km s^{-1} of the solar wind guarantees that fluctuations in this frequency range have a coherence length greater than the distance between both spacecrafts.

Our results show that, for frequencies below 3 mHz, the amplitude of fluctuations measured in LPF are in agreement with those measured by ACE during the same period of time. The spectral index obtained by both instruments is in agreement with previous characterisations of the spectra of IMF fluctuations corresponding to the inertial range, as we will see in detail in Section 4.4. From our analysis we confirm that whilst the absolute value of the magnetic field on-board is dominated by the units inside the spacecraft, the fluctuations of the magnetic

field are instead dominated by the fluctuations of the IMF. At the same time, this corroborates the results obtained in the bottom right panel of Figure 26. Since all magnetometers are measuring the interplanetary contribution, fluctuations of the magnetic field are completely correlated in the low frequency range for those channels measuring the magnetic field in a given direction. This correlation decays if we compare measurements of the magnetic field in transverse directions. As expected, the correlation between fluctuations of the magnetic field disappears for frequencies above 3 mHz. As we show in the following, this frequency range is dominated by the electronic noise of the sensing system, i.e. with no common correlation between channels.

4.3.1.2 *Fluctuations above the millihertz: fluxgate read-out electronics*

The noise analysis for the magnetometers shows that the amplifier and the analog-to-digital converter will limit the performance of our sensor at low and high frequencies, respectively. If we take into account the different components in the read-out chain and the noise figures in the data sheet values, we obtain the contribution shown in the different panels of Figure 26. On the one hand, in the low-frequency region, the noise follows a f^{-1} spectrum produced by the instrumentation amplifier. On the other hand, in the high-frequecy region, the spectrum is flat due to the analog-to-digital converter which sets a limit of $S_{ADC}^{1/2} \simeq 2\,\mathrm{nT\,Hz^{-1/2}}$ at the high frequency band.

In the left panels of Figure 26 we show, for the three different axes, the noise floor measured by the four magnetometers on-board during the period. On-board magnetometers measured a noise level above 3 mHz that differs for each magnetometer in a range that goes from $7\,\mathrm{nT\,Hz^{-1/2}}$ in the PY magnetometer to $11\,\mathrm{nT\,Hz^{-1/2}}$ in the MY magnetometer, all of them above the expected $2\,\mathrm{nT\,Hz^{-1/2}}$. Considering that the amplitude of the interplanetary fluctuations decay as $f^{-1.65}$ and taking into account that the observed noise is not correlated between the four magnetometers (see bottom right panel of Figure 26), we conclude that the read-out electronics must be the source of this excess noise. We have investigated this by focusing on the electronics design of the magnetometer read-out.

Our analysis shows that this noise contribution could be assigned to a common-mode noise at the input of the instrumentation amplifier which can be originated due to the lack of common ground between magnetometer and electronics read-out. We have experimentally tested this hypothesis by means of an engineering model of the LPF DMU [77] which included the DAU together with a flight model fluxgate magnetometer. With this setup we have verified that the measured noise plateau can vary from the design $2\,\mathrm{nT\,Hz^{-1/2}}$ if both units are not commonly grounded.

Hence, we conclude that the observed excess noise above 3 mHz could be assigned to this issue. Although it is not possible to assess the exact contribution to the noise budget due to this effect, a worst case estimate sets a value of 90 mV $\mathrm{Hz^{-1/2}}$ for the required fluctuations at the input of the instrumentation ampli-

fier in order to explain the excess observed by our magnetometers. This value is relatively high compared to our read-out voltage noise. Since it is not possible to measure the common-mode noise at the spacecraft, we are only establishing an upper bound without discarding other possible contributions to the excess noise in the high-frequency band. It is important to stress here that the main objective of the magnetometers on-board LPF was to track slowly varying magnetic fields that are the ones that can have an impact in the dynamics of the free falling TMs. Hence, an excess noise in the high frequency range, though unexpected, does not have an impact on the scientific objectives of the magnetic diagnostic subsystem, but if needed, could be corrected for a future space-based gravitational wave mission.

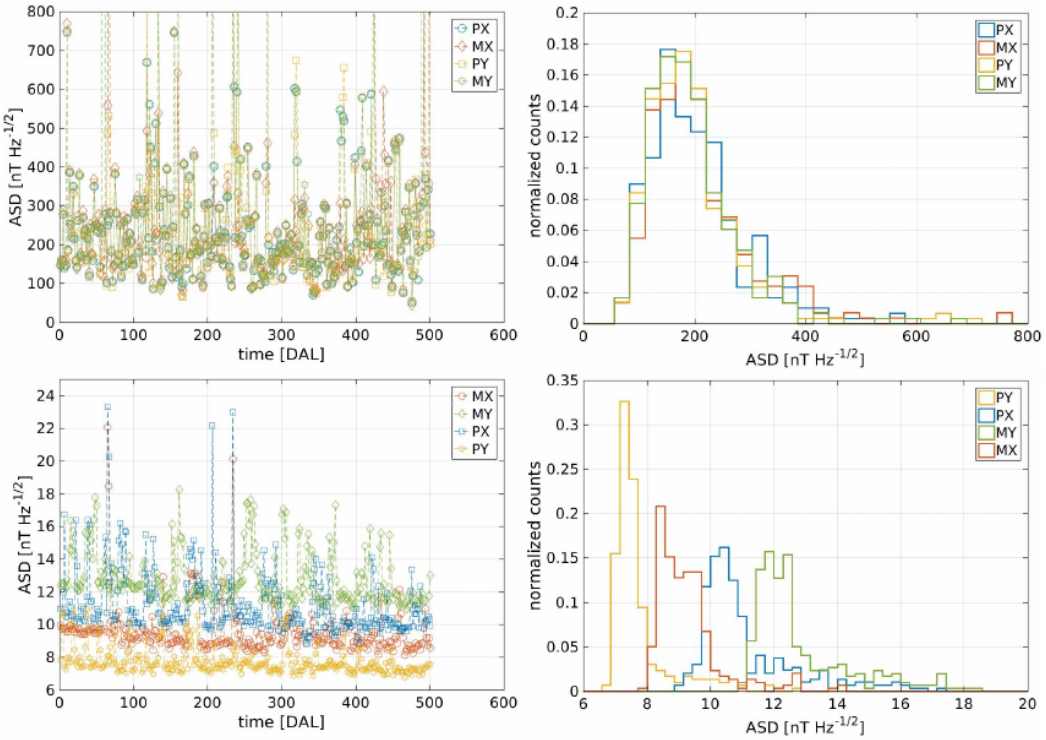

Figure 28: Time evolution and statistical distribution of the x-component of the magnetic field fluctuations as measured on-board, for two different frequency regimes. Colours correspond to magnetometers: PX (blue), MX (red), PY (yellow) and MY (green). Time is indicated in DAL. *Top:* Fluctuations in the frequency range $20 < f < 50$ μHz. *Bottom:* Fluctuations in the frequency range $20 < f < 40$ mHz.

4.4 NON-STATIONARITIES IN THE MAGNETIC FIELD FLUCTUATIONS

Until now we have based our analysis on the ASD, which entails the information of the magnetic field in the frequency span of interest. The ASD effectively describes the fluctuations during a fixed period of time. Hence, it would only be a complete statistical description if the environment on-board LPF were stationary. This is obviously not the case. On the contrary, several situations can induce abrupt changes in the measured magnetic field. In Table 4 we provided a series of

events that we identified in the magnetic field time-line. Since these were associated to satellite operations these events are both easily identified and, eventually, removed from the dataset through post-processing. A second, more complex, class of non-stationarity is the one associated to the IMF. In Section 4.3.1.1 we described the origin of the spectral index of the observed magnetic field fluctuations in the low frequency range and its relation with the solar wind speed. A rich variety of interplanetary structures is superposed to the unperturbed solar wind plasma [128, 129]. Structures such as corotating interaction regions, interplanetary shocks, magnetic clouds or heliospheric current sheet crossings will induce variations in the measured magnetic field on-board the spacecraft.

Since our DC magnetic field is completely dominated by the spacecraft components: around $\sim 1\mu$T, compared with the ~ 1 nT coming from the interplanetary media, we can not measure the absolute value of the IMF in these cases. Nevertheless, if the variations are strong enough (of the order of ~ 10 nT, for example) and especially if we see them in all four magnetometers, we could indeed assign an interplanetary origin to them. Accurate detection of the magnetic imprint of these events requires the magnetometers to be isolated from spacecraft contributions. This is the case for dedicated space weather missions which place the magnetometers at the end of a deployable boom, such as in the case of ACE [127] or Wind [130] missions. Moreover, these missions contain a suite of instruments that allow a complete characterisation of the plasma, tracking parameters such as the solar wind speed or the number density of the plasma that we will refer in the following. Nonetheless, it is worth noticing that, although not designed for that, the radiation monitor on-board LPF [77, 83] allowed for the detection of the passage of large scale interplanetary structures such as high-speed solar wind streams and interplanetary counterparts of coronal mass ejections generating recurrent and non recurrent depressions of the galactic cosmic-ray flux [83, 84].

As we have previously discussed, in LPF the effect of the IMF structures can not be easily distinguished in the absolute value of the measured magnetic field because the local magnetic field is largely dominated by the contribution of the spacecraft units. However, as we show in the following, the effect of these structures can have an impact in the spectra of fluctuations in the low-frequency band, i.e. below the Hz.

In order to trace the variability of the spectrum we took a closer look at the ASD in two different frequency regions, namely $20 < f < 50$ μHz and $20 < f < 40$ mHz. We selected these two frequency regions because, as discussed above, magnetic field fluctuations come from a different physical origin, i.e. IMF and magnetometer read-out electronics, respectively. For each of these frequency windows we compute the PSD. We selected windows of 16 hours to compute each bin. In order to avoid segments containing magnetic experiments or events as the ones reported in Tables 4 & 3, we apply a mask to the data. To do so we take as a figure of merit the ASD in the range $1 < f < 10$ mHz. Those segments where this figure of merit is exceed by five sigma are discarded from our analysis. Following this criterion, we exclude 9 segments out of 300. This analysis allows a generic description of the statistical behavior of the fluctuations without

any previous assumption on its stationarity. Figure 28 shows the results for both frequency ranges. In agreement with our previous analysis, the amplitude of the fluctuations for the low-frequency bin is coherent and follows the same statistical distribution for all four magnetometers. Bins are statistically distributed with similar median values, namely:

$$\begin{aligned}
\widetilde{S}^{1/2}_{B_z,PY}\Big|_{f_{LF}} &= 177^{+80}_{-53}\,\mathrm{nT\ Hz^{-1/2}},\\
\widetilde{S}^{1/2}_{B_z,MY}\Big|_{f_{LF}} &= 182^{+81}_{-60}\,\mathrm{nT\ Hz^{-1/2}},\\
\widetilde{S}^{1/2}_{B_z,PX}\Big|_{f_{LF}} &= 191^{+101}_{-62}\,\mathrm{nT\ Hz^{-1/2}},\\
\widetilde{S}^{1/2}_{B_z,MX}\Big|_{f_{LF}} &= 189^{+102}_{-64}\,\mathrm{nT\ Hz^{-1/2}}.
\end{aligned}$$

These values are based on the 16th, 50th and 84th percentiles of the histogram. Also, in this case we can derive a common mean value for the fluctuations in this frequency range of $207 \pm 6\ \mathrm{nT\ Hz^{-1/2}}$. On the other hand, the noise power in the higher frequency bins show a different ASD for each magnetometer. The median values in this case are:

$$\begin{aligned}
\widetilde{S}^{1/2}_{B_z,PY}\Big|_{f_{HF}} &= 7.4^{+0.8}_{-0.3}\,\mathrm{nT\ Hz^{-1/2}},\\
\widetilde{S}^{1/2}_{B_z,MY}\Big|_{f_{HF}} &= 12.3^{+2}_{-0.7}\,\mathrm{nT\ Hz^{-1/2}},\\
\widetilde{S}^{1/2}_{B_z,PX}\Big|_{f_{HF}} &= 10.6^{+2}_{-0.6}\,\mathrm{nT\ Hz^{-1/2}},\\
\widetilde{S}^{1/2}_{B_z,MX}\Big|_{f_{HF}} &= 9.0^{+0.8}_{-0.6}\,\mathrm{nT\ Hz^{-1/2}}.
\end{aligned}$$

In the latter we observe that the distribution of the median values are narrower and not overlapping between them. Both behaviors are clearly distinguished in the histograms of Figure 28, which characterises the variability of the magnetic field fluctuations on-board for the two frequency regimes that we have previously identified.

In the framework of future gravitational wave detectors in space, the variability in the spectra of magnetic field fluctuations is particularly relevant in the low-frequency regime. There are two main reasons for that: first, the mHz band is the main objective of a gravitational wave detector in space, since these observatories are designed to study the gravitational universe in this frequency band. Second, at the same time, the low frequency fluctuations will be precisely the main contribution to the magnetic induced force noise in the free falling TMs. According to [4], magnetic induced forces could contribute to a maximum of 3 fm s^{-2} $Hz^{-1/2}$ of the measured 12 fm s^{-2} $Hz^{-1/2}$ at 0.1 mHz of the differential acceleration measured on LPF TMs. For that reason it is worth characterising further the variability in this frequency regime to provide information for future space-borne observatories. As we show in the following, the fluctuations of the magnetic field in the sub-mHz band are deeply connected to the dynamics of the

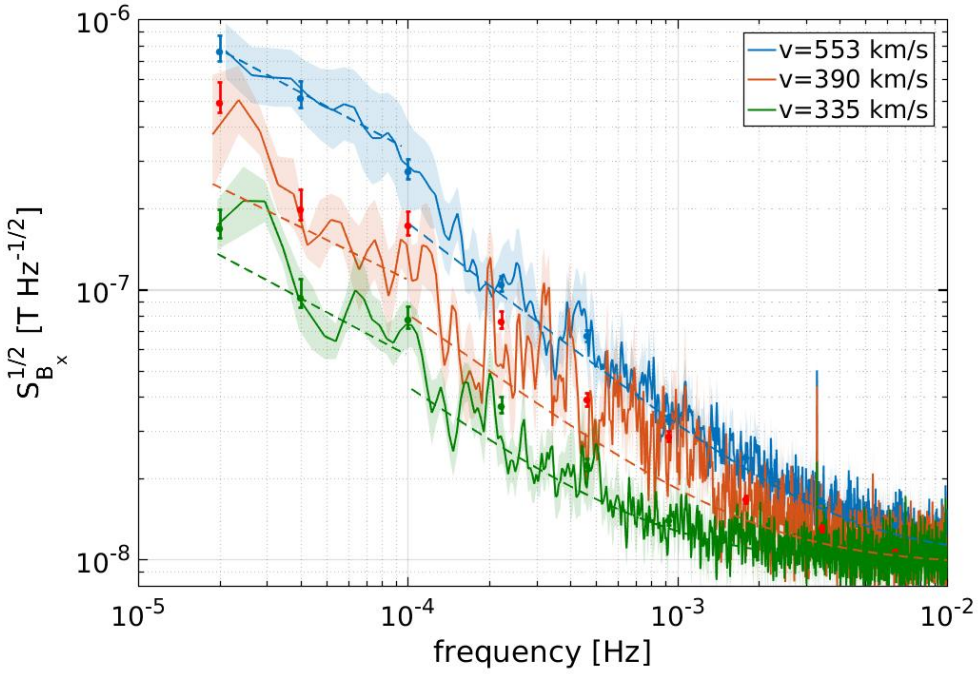

Figure 29: ASD of the x-component of the magnetic field for 3 periods of different solar wind speed. The data to compute each spectrum has been obtained combining the data from the four magnetometers. The values of the fits to the data (dashed lines) are reported in Table 5.

interplanetary plasma.

Fluctuations in the intensity of the IMF can be associated with a wide variety of phenomena [122]. However, particularly in the inertial range, the amplitude of the magnetic fluctuations is strictly related to the their Alfvénic nature. The solar wind is highly structured in high and low-speed streams, which carry different types of fluctuations. While fast wind is characterised by large-amplitude Alfvénic fluctuations, the slow wind generally advects less Alfvénic fluctuations characterised by a smaller amplitude – with the important exception of the Alfvénic slow wind, see D'Amicis and Bruno [131]. This means that, moving from high- to low-speed regions, the power level of the magnetic fluctuations within the inertial range progressively decreases, though keeping the typical $f^{-5/3}$ Kolmogorov scaling. As a matter of fact, solar wind turbulence may be thought as superposition of a magnetic field background spectrum, common to both fast and slow flows [132], and a turbulent large-amplitude Alfvénic spectrum, characteristic of the fast solar wind.

In order to study the impact of the solar wind speed in our measurements, we selected three segments representing stable periods of solar wind speed. These periods had to be long enough to allow an estimate of ASD down to 20 μHz. The selected time spans correspond to Jul. 7th-14th, 2016, May 28th-Jun. 1st ,

2017, and Feb. 11th-16th, 2017, when according to measurements recorded by ACE, the solar wind had a mean velocity of 553 ± 47 km s^{-1}, 390 ± 53 km s^{-1} and 335 ± 35 km s^{-1}, respectively. For each of these segments we evaluated the ASD of the magnetic field as measured by LPF magnetometers. Although other authors have already studied this phenomena [132], we extended the characterisation to the sub-mHz regime, which is the region of greatest interest for LISA and future gravitational wave detectors.

We show the results in Figure 29, where we can distinguish an increase in the power of the low-frequency fluctuations that correlates with the increase of solar wind velocity. Indeed, we observe that fluctuations at 20 μHz vary from 170^{+30}_{-10} nT Hz$^{-1/2}$ for a slow wind situation (typical velocities $v \simeq 300$ km s^{-1}) to 750^{+100}_{-50} nT Hz$^{-1/2}$ when we consider a situation of high speed wind (typical velocities $v \simeq 500$ km s^{-1}). These two scenarios represent a deviation of 18% and 362%, respectively, with respect to the mean value that we have previously derived for the complete time series, 207 ± 6 nT Hz$^{-1/2}$. Although other phenomena may also contribute to the variability of the sub-mHz fluctuations of the spectra, we consider this correlation with the solar wind as one of the physical mechanisms behind the statistical distribution of the fluctuations in the sub-mHz band that we obtained in Figure 28. It is thus a dependence that future space-borne gravitational-wave detectors will need to take into account, since as we mentioned in Chapter 3, the coupling of the magnetic field fluctuations with the magnetic moment of the TMs could produce spurious forces that a gravitational wave detector would sense as a change in the acceleration noise, and therefore, possibly confusing it with a gravitational wave signal.

In Table 5 we characterise the variation of the shape of the magnetic field fluctuations in terms of the solar wind speed. We fitted the spectra of the magnetic field fluctuations to two power laws, one between 20–100 μHz and another one from 100 μHz to 10 mHz. We have made this differentiation because, as previously explained, different mechanisms act at different time scales, resulting in different spectral indexes for these power laws. The fits were performed by means of a chi-square minimisation, non-linear fit using derivative-free method. For the sake of completeness, in Table 5 we also show the results of the analysis for the y and z axis, which are not shown in Figure 28.

It is interesting to notice that, according to our parametrisation, the main impact of the wind speed is in the parameter 'B' which accounts for the power of the fluctuations in the frequency band described by the power law. The values for the spectral index 'C' are around 1.5, smaller than the value expected, which is 1.65, for the inertial range of IMF fluctuations. This small difference may come from the fact that in the LPF case, the read-out noise of the magnetometers starts to flatten the spectrum around 1 mHz, and this may result in a slightly less steep curve when we perform the fit. Moreover, the inertial range of interplanetary magnetic field fluctuations starts between 0.1–1 mHz, while the magnetometers read-out noise starts to be dominant around 1 mHz. Therefore, we can not see a large and clear portion of the inertial range part of the IMF spectrum. With regard to the parameter 'A', the comparison between the different wind velocity regimes

	Solar wind speed [km/s]		
Parameter	553 ± 47	390 ± 53	335 ± 35
	B_x		
A ($10^{-16} \times [T^2/Hz]$)	1.02 ± 0.03	0.90 ± 0.02	0.91 ± 0.02
B ($10^{-19} \times [T^2/Hz]$)	3.8 ± 0.6	1.8 ± 0.4	0.6 ± 0.2
C [ ]	1.53 ± 0.03	1.42 ± 0.04	1.41 ± 0.06
D ($10^{-17} \times [T^2/Hz]$)	4 ± 10	1 ± 30	0.1 ± 0.4
E [ ]	1.1 ± 0.3	1.0 ± 0.5	1.0 ± 0.4
	B_y		
A ($10^{-16} \times [T^2/Hz]$)	1.11 ± 0.03	0.86 ± 0.02	0.94 ± 0.02
B ($10^{-19} \times [T^2/Hz]$)	2.8 ± 0.4	1.9 ± 0.6	0.3 ± 0.1
C [ ]	1.58 ± 0.03	1.34 ± 0.06	1.53 ± 0.07
D ($10^{-17} \times [T^2/Hz]$)	6 ± 20	0.001 ± 0.006	2 ± 10
E [ ]	1.0 ± 0.3	1.7 ± 0.4	0.8 ± 0.5
	B_z		
A ($10^{-16} \times [T^2/Hz]$)	1.09 ± 0.02	0.91 ± 0.02	0.96 ± 0.01
B ($10^{-19} \times [T^2/Hz]$)	1.2 ± 0.2	1.0 ± 0.3	0.22 ± 0.08
C [ ]	1.62 ± 0.03	1.46 ± 0.05	1.60 ± 0.06
D ($10^{-17} \times [T^2/Hz]$)	0.3 ± 0.9	10 ± 20	0.000 ± 0.001
E [ ]	1.3 ± 0.3	0.6 ± 0.1	1.8 ± 0.4

Table 5: Values of the fits of the dashed lines shown in Figure 29 to a function $A + B\,2\pi f^{-C}$ in the range between 100 μHz–10mHz and to a function $D\,2\pi f^{-E}$ in the range between 20 μHz–100 μHz.

do not show any significant variation, as we expected given that this parameter describes the noise floor of the instrument, which is dominated by the electronics read-out contribution. When we analyse the parameters corresponding to the slower frequency part, we find that the spectral index 'E' values are around 1, which are in good agreement with the f^{-1} behaviour of the interplanetary magnetic field fluctuations at this frequency range – even though the errors are high because we do not have many points for the fit. Finally, the values obtained for the parameter 'D' are not very well fitted, probably because of the small amount of data points available in this frequency range.

To finalise the study of the non-stationarity of the magnetic field fluctuations, we took a closer look at the impact of this contribution during the noise performance runs. Analogously as it is done with on-ground gravitational wave detectors during science runs, in LPF these runs were periods where the instrument was configured in its more sensitive configuration and kept in data acquisition mode without introducing any calibration signal. For LPF, these noise performance runs took typically 5 to 10 days although it is worth stressing that future space-borne gravitational wave detectors, such as LISA, aim to spend weeks or

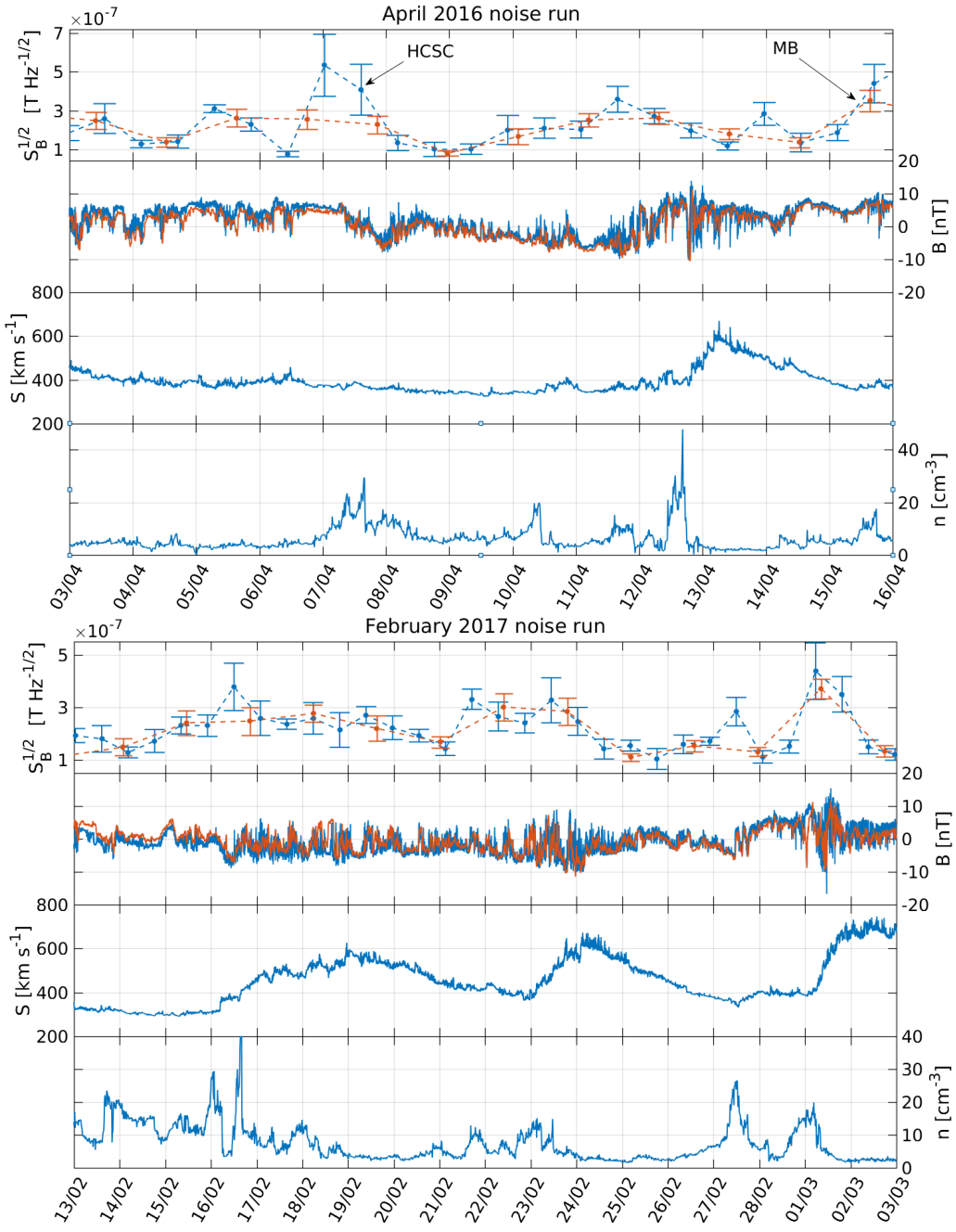

Figure 30: *Top:* Evolution during April 2016 noise run in LPF (dates indicated in figure) from (top to bottom): -*Upper Top:* Noise power in the 20–50 μHz frequency bin for an average of the three components of LPF PY magnetometer (red) and ACE magnetometer (blue). The events listed are taken from Armano et al. [84] and noted in the text. -*Middle top:* Magnetic field B_x component in GSE coordinates measured by ACE (blue), and LPF PY magnetometer B_z component (red) with a lowpass at 1 mHz and with its mean value subtracted. -*Middle bottom:* Solar wind speed in GSE coordinates as measured by ACE. -*Lower bottom:* Proton density as measured by ACE. *Bottom:* Same as top figure but for the February 2017 noise run performed in LPF (dates indicated in figure.)

months in this scientific acquisition mode.

In Figure 30 we analysed the non-stationarities of the low-frequency part of the magnetic field spectrum during the two LPF noise runs that were published in Armano et al. [4] (April 2016 noise run) and Armano et al. [66] (February 2017 noise run). Following the same approach as we have previously shown, we computed the ASD of the magnetic field in the frequency span that goes from 20–50 μHz. In the top panels of Figure 30 we show the evolution of this value over the duration of each LPF noise run for LPF and ACE satellites. We compare this with the evolution of the time series of the magnetic field itself B_x component in GSE coordinates (second panel) for ACE. In the same panel, we also show the magnetic field B_z component as measured in LPF during the same period. The reason to compare LPF's B_z in LPF reference frame with ACE's B_x in GSE coordinates is that LPF's z-axis points always towards the solar panel, which is always pointing towards the Sun. Thus, LPF positive z-axis is roughly equivalent to positive x-axis in GSE coordinates.

To do this comparison, LPF data has been low-pass filtered at 1 mHz in order remove the higher frequency noise coming from electronics and the mean subtracted in order to exclude the DC magnetic field coming from the spacecraft components. As we previously showed when analysing the components in the spectra, the main features of the long term evolution are driven by the interplanetary component. As we saw, the phenomena associated with the solar wind requires several parameters that detail the characteristics of the interplanetary plasma. In order to provide a comprehensive view of this phenomena during these two particular noise runs we show as well the solar wind speed (third panel) and the proton density (fourth panel), as measured by ACE.

The results show that, during the February 2017 noise run, there are roughly three clear increases in the ASD of the low frequency bin of the magnetic field. These three peaks seem to be caused by high-speed streams in the solar wind speed, i.e, sudden increases in the solar wind speed, a type of event that also carries a decrease in the proton density, as we can also clearly observe in the lowest panel. Regarding the April 2016 noise run, we can see another high-speed stream around April 13th that causes another small peak in the ASD of the low frequency bin of the magnetic field, associated with the corresponding decrease in proton density. Apart from that, there are two events that cause another increase in the time-series of the first panel. According to Armano et al. [84], these events would be associated to a Heliospheric Current Sheet Crossing (HCSC) and a MB. We refer the reader to the aforementioned references for more details on these events.

4.5 CONCLUSIONS

In this chapter we have provided a complete description of the magnetic field onboard LPF during its lifetime. We have seen how even though the magnetometers inside the spacecraft had to be placed far enough from the TMs to prevent their active magnetic core to induce magnetic forces on the free-falling TMs, they have provided valuable measurements in order to provide a good description of the

on-board magnetic field. Nevertheless, we have also seen how the magnetometers configuration had some drawbacks, being the most important one the lack of resolution to measure the magnetic field or the magnetic field gradient at the location of the TMs. The last is a major problem, since magnetic field gradients can highly contribute to the magnetic force fluctuations, and with our current configuration we have no way of measuring which are the local magnetic field gradients across the TMs. The best we can do is to compute the gradient across x and y using pairs of opposite magnetometers, but this gradient across the whole instrument is not necessary representative of the local gradient across the TMs faces. Moreover, we have no possibility of computing any gradient in the z direction since all our magnetometers are in the same x-y plane. Considering all this, an alternative setup should be considered for the future gravitational wave detector LISA [1].

Regarding the shown measurements, the DC magnetic field measured on-board is completely dominated by the contribution from the electronics of the spacecraft units. Amongst them, the thruster systems were a major contributor, both the cold gas high pressure latch valves (the ones used by ESA) and the colloidal thrusters (the ones operated by NASA). Cold gas thrusters or, more precisely, some permanent magnets in the cold gas thruster subsystem, contribute with roughly the 80% of the measured magnetic field. Although a strong contribution, this one remains constant throughout the mission (partially thanks to the high thermal stability reached on-board [85]), which is key for a mission as LISA with strong requirements on any potential source of fluctuations. This is not the case for the colloidal thrusters, where we observed a persistent slow drift of around 150 nT for the measurement of the two closest magnetometers to the TMs. This 150 nT drift took place over around 150 days, which corresponds to the first period of ST7-DRS operations – see Figure 25 to check the different periods. We attribute this effect to the displacement of a stainless steel bellow inside the thruster that keeps the propellant at a constant pressure. Although not a desirable effect for future gravitational wave detectors in space, this slow change in the local magnetic field should not be present in future missions, since it could impact the main measurement of a mission like LISA.

We took special care on the analysis of the fluctuations of the magnetic field on-board since these are a key component of the TM force noise apportioning. We reported how, on the one hand, the fluctuations of the magnetic field on-board are dominated at frequencies above the mHz by the contribution of the read-out electronics. In this frequency regime we identified and characterised an excess noise when compared to the design curve of our electronics. Although unexpected, this does not represent a major problem since the frequencies in which the magnetic noise may have an important impact are below the mHz. On the other hand, below the mHz, the fluctuations are dominated by the contribution from the IMF. Several indications point toward an interplanetary origin of the low-frequency fluctuations of the magnetic field. First, all magnetometers show coherent fluctuations in this frequency regime and, second, the densities of the magnetic field components measured by our four magnetometers match those measured by dedicated space weather missions ACE and Wind, which are also

orbiting around L1.

Finally, we evaluated the non-stationary component affecting the very low-frequency regime of the magnetic field fluctuations. Due to its dependence with the solar wind, the low-frequency fluctuations show a large variability associated with changes in the interplanetary plasma. We tracked the ASD in the low end of the LISA measuring band, i.e. at 20 μHz, during the whole duration of the mission. In this frequency regime, the magnetic field fluctuation on-board has a typical mean value of 207 ± 6 nT $\mathrm{Hz}^{-1/2}$, although it shows an important variability with a wide statistical distribution of its values. Following previous studies, we showed how this variability is tightly associated with a variety of phenomena associated with the dynamics of the interplanetary plasma. We have described and characterised how quantities describing the solar wind, as for example the plasma velocity, can be used to parametrise the variability of the low-frequency fluctuations. In the case of the solar wind speed, we saw how variations in the range of $300 - 500$ km s^{-1} are related to variations in the ASD of the magnetic field measured in LPF in the range $20 - 50$ μHz of around $170 - 750$ nT $\mathrm{Hz}^{-1/2}$.

5 MAGNETIC EXPERIMENTS ON-BOARD LISA PATHFINDER

LPF was on scientific operations during almost 600 days. During all that time, several experiments were performed in order to completely understand the different noise sources that play a role in the LPF acceleration noise curve that was obtained in [4] and [66]. Amongst these experiments, some of them were related to the magnetic noise force that can affect the geodesic motion of the TMs. Several injections with the magnetic coils were performed during different days in order to study the dynamics of the TMs. Analysing their movement, we are able to extract the magnetic parameters that rule their dynamics.

This chapter is organised as follows. First, we will introduce which is the aim of the magnetic experiments and how they are performed. Next, we will proceed to explain all the different magnetic injections we performed with magnetic coils onboard the satellite during mission operations. The next section will describe how we can manipulate the different forces explained in Chapter 3 for the specific case of the injections we performed in order to extract the different magnetic parameters from the TMs and the environment. We will then proceed to explain how we calibrate our coils with the magnetometers to finally show the results we obtain for the different parameters and the conclusions we can take from them.

5.1 INTRODUCTION

Soon after LPF started scientific operations, on March 1st, 2016, magnetic experiments were scheduled to try to extract the magnetic parameters related to the TMs. The experiments consisted in applying an electric current through the coils to induce a magnetic field in the position of the TMs. The applied current in the coils was a sinusoidal signal of the type:

$$I(t) = I^{DC} + I^{AC}\sin(\omega t) \tag{5.1}$$

where I^{DC} is a constant offset, I^{AC} the amplitude of the sinusoidal signal and ω its frequency. As explained in Appendix A this will produce a magnetic field at the centre of the TM of the type:

$$B_x(t) = B^{DC}_{i,x} + B^{AC}_{i,x}\sin(\omega t) \tag{5.2}$$

During the commissioning period, the coils were tested in order to check that everything was working correctly. Sadly, although coil number 1 worked perfectly, coil number 2, which was the one closer to TM2, showed a malfunctioning during those checks. Due to this fact, the injections performed during the operations period were done mostly on coil 1, and the only set of injections performed in coil 2 were done with low currents to prevent any possible current leak to other

systems, which resulted in noisy signals. This implies that most of the results that will be shown in this chapter will be for TM1 if not specified otherwise.

5.2 EXPERIMENTS DESCRIPTION

The 1st set of injections with the magnetic coils were performed on April 28th and 29th, 2016. The details of these two sets of injections can be checked on Tables 6 & 7 and Figures 31 & 32. This first set of injections were performed in order to try to understand the system, varying as many parameters as possible (offset and amplitude of the oscillations, its frequencies, etc). Is important to take into account that the injections on April 29th were the only ones performed in coil 2 (and therefore, on TM2) during the whole operations period due to the malfunctioning of this coil.

#	f [mHz]	I_{DC} [mA]	I_{AC} [mA]	duration [s]
1	5	-0.2	1.0	1000
2	5	-0.1	1.0	1000
3	5	0.00	1.0	1000
4	5	+0.1	1.0	1000
5	5	+0.2	1.0	1000
6	3	-0.2	0.5	1000
7	3	-0.1	0.5	1000
8	3	0.00	0.5	1000
9	3	+0.1	0.5	1000
10	3	+0.2	0.5	1000
11	1	0.00	0.1	20000

Table 6: Injections in coil 1 on April 28, 2016 (DOY 119). Each injection is a sinusoid with the values specified above. In the table are indicated the label of the injection #, its frequency f, the DC of the injected signal I^{DC}, the amplitude of the signal I^{AC} and its duration in seconds. See Figure 31 to check the relative acceleration produced between the test masses Δg for each injection.

After other different experiments were performed on the spacecraft, some months later we proceeded to perform a second set of injections in June 18, 2016 (DOY 170). Those experiments were carried out only in coil 1, since for these injections we were injecting high currents and coil 2 had shown a malfunctioning as explained before. Also, this time the injections lasted longer in order to obtain more cycles to do better statistics. This implied that, since many different experiments were also scheduled on the satellite, this 2nd set of injections could not last more than one day. For this second set of injections we were not varying the frequency of the injected signal, but instead, we focused more in changing constantly the offset and the amplitude of the injected signal. This will be very useful for the analysis we will show later on in Section 5.3.2 & Section 5.3.4. This second set of injections and the Δg they produced can be checked in detail on Table 8 and Figure 33, respectively. Since this 2nd set of injections are the most energetic

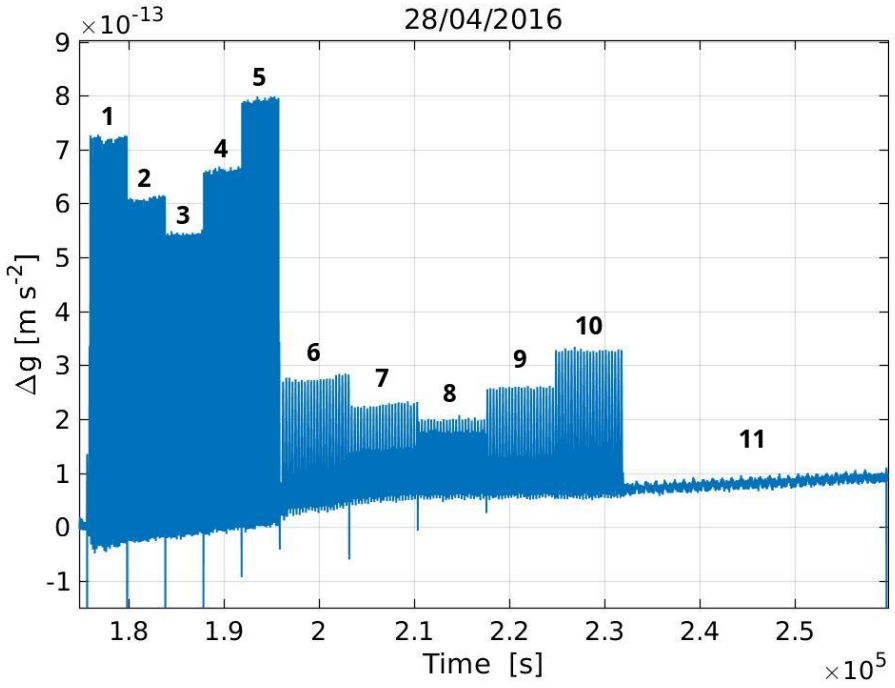

Figure 31: Δg produced between LPF TMs during the injections in coil 1 on April 28, 2016 (DOY 119), with the labelling of each injection. See Table 6 to check the exact values of each injection.

#	f [mHz]	I_{DC} [mA]	I_{AC} [mA]	duration [s]
1	5	-0.2	1.0	1000
2	5	-0.1	1.0	1000
3	5	0.00	1.0	1000
4	5	+0.1	1.0	1000
5	5	+0.2	1.0	1000
6	3	-0.2	0.5	1000
7	3	-0.1	0.5	1000
8	3	0.00	0.5	1000
9	3	+0.1	0.5	1000
10	3	+0.2	0.5	1000
11	1	0.00	0.1	20000

Table 7: Injections in coil 2 on April 29, 2016 (DOY 120). Each injection is a sinusoid with the values specified above. In the table are indicated the label of the injection #, its frequency f, the DC of the injected signal I^{DC}, the amplitude of the signal I^{AC} and its duration in seconds. See Figure 32 to check the relative acceleration produced between the TMs Δg for each injection.

ones in terms of applied current, we will also analyse the torques produced by them on TM1. These torques can be seen in Figure 33 too for each of the injections.

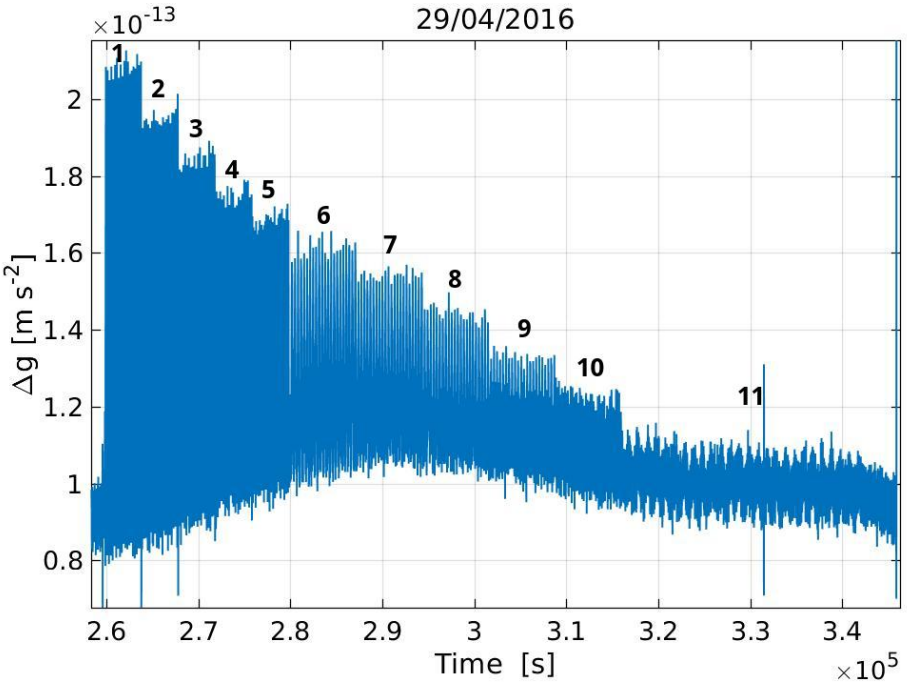

Figure 32: Δg produced between LPF TMs during the injections in coil 2 on April 29, 2016 (DOY 120), with the labelling of each injection. See Table 7 to check the exact values of each injection.

#	I_{DC} [mA]	I_{AC} [mA]	#	I_{DC} [mA]	I_{AC} [mA]
1	+1.5	1.5	11	0.00	0.8
2	+1.5	1.0	12	0.00	0.5
3	+1.5	0.8	13	-0.75	1.5
4	+1.5	0.5	14	-0.75	1.0
5	+0.75	1.5	15	-0.75	0.8
6	+0.75	1.0	16	-0.75	0.5
7	+0.75	0.8	17	-1.5	1.5
8	+0.75	0.5	18	-1.5	1.0
9	0.00	1.5	19	-1.5	0.8
10	0.00	1.0	20	-1.5	0.5

Table 8: Injections in coil 1 on June 18 2016 (DOY 170). Each injection is a sinusoid with a frequency of 5 mHz and a duration of 4000 seconds. In the table are indicated the label of the injection #, the DC of the injected signal I^{DC} and the amplitude of the signal I^{AC}. See Figure 33 to check the relative acceleration produced between the TMs (Δg) for each injection and Figure 33 to check the torques produced around θ and ϕ.

Finally, a 3rd set of injections were performed from March 14 to March 16 of 2017 (DOYs 73-75). These last injections were scheduled during the mission extension and during the last months of operations of LPF. They were performed

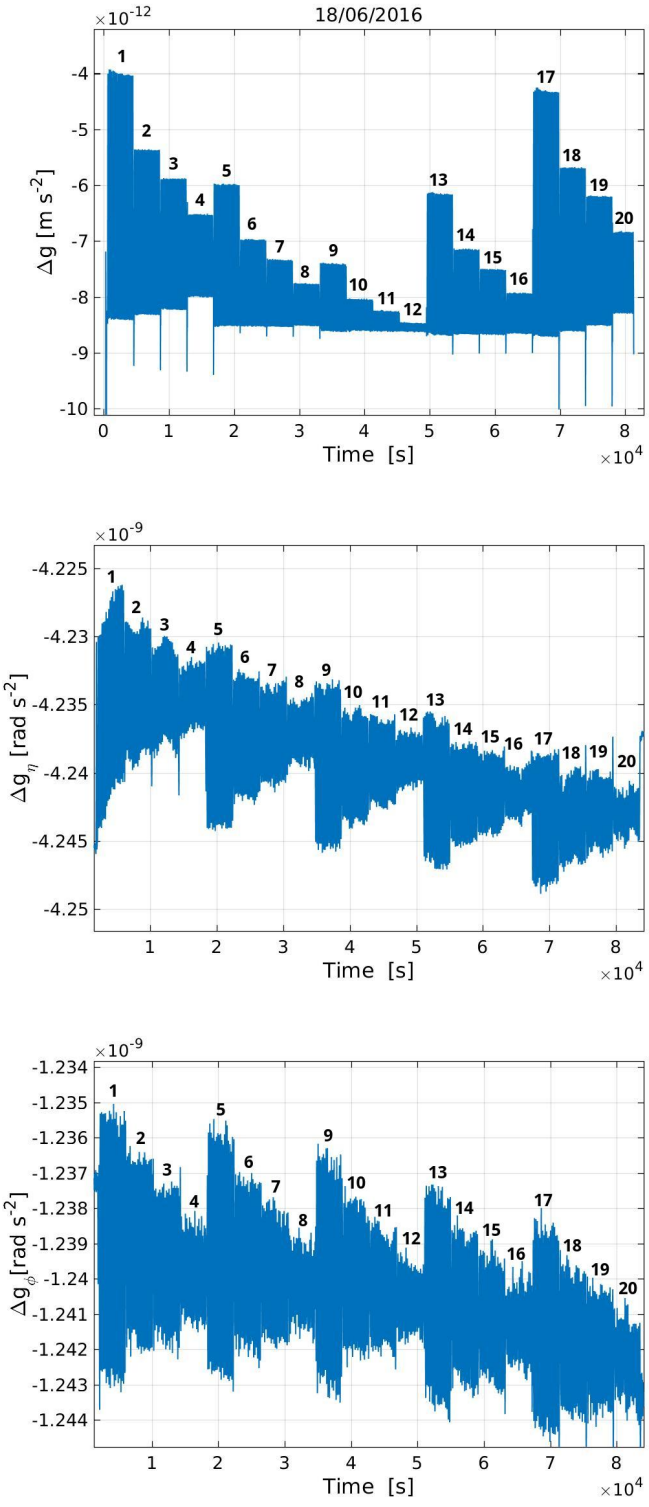

Figure 33: Δg along x (top), Δg around θ (mid) and around ϕ (bottom) produced between LPF TMs during the injections in coil 1 on June 18, 2016 (DOY 170), with the labelling of each injection. See Table 8 to check the exact values of each injection.

in the spacecraft configuration with the smallest authority for the electrodes of the electrode housing, and with which the best results for Δg were obtained.

The aim of this last experiment was to inject the highest offset possible on the coil injection during a long period of time in order to see if we can observe a magnetically-dominated Δg in the low frequencies, and to alternate it between positive and negative to disentangle the small difference that would be given by the environmental magnetic field and its gradient.

#	I_{DC} [mA]	I_{AC} [mA]
1	-0.5	0.07
2	+0.5	0.07
3	+1.0	0.07

Table 9: Injections in coil 1 between March 14 and March 16 of 2017 (DOYs 73-75). Each injection is a sinusoid with a frequency of 15 mHz and a duration of 75000 seconds. We indicate in the table the label of the injection #, the DC of the injected signal I^{DC} and the amplitude of the signal I^{AC}. See Figure 34 to check the relative acceleration produced between the TMs Δg for each injection.

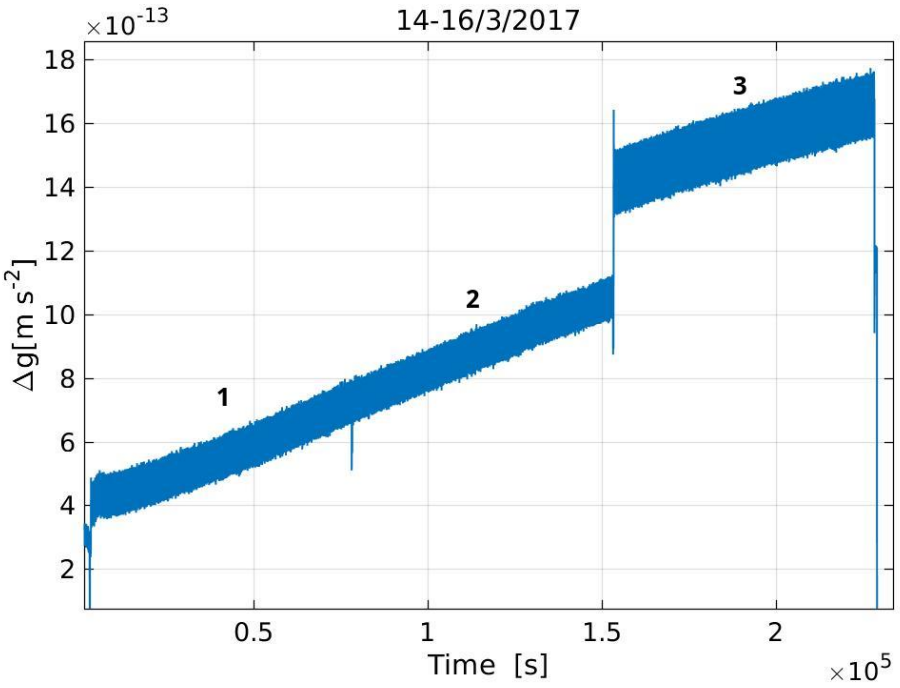

Figure 34: Δg produced between LPF TMs during the injections in coil 1 between March 14 and March 16 of 2017 (DOYs 73-75) with the labelling of each injection. See Table 9 to check the exact values of each injection.

5.3 EXTRACTION OF MAGNETIC PARAMETERS

In Chapter 3 we showed the equations that describe the force produced in our TMs due to the coupling of the TMs remanent magnetic moment and magnetic susceptibility with the surrounding magnetic field and magnetic field gradient. A bit more specifically, we introduced the forces and torques produced in the case that the magnetic field has an oscillating, AC component apart from a fixed, DC component. We saw how, in the latter case, we differentiated three different components in the force, a DC force F_{DC}, a force oscillating at the frequency of the magnetic field $F_{1\omega}$ and a force oscillating at two times the frequency of the magnetic field $F_{2\omega}$.

Although we applied those equations for the LPF case, they were very general, and would be valid for any case of a magnetic dipole inside a magnetic field. In this section we will go a step further, and manipulate the equations from Chapter 3 for the specific case of the injections we performed in our experiments with the coils. Furthermore, we will manipulate the equations to extract the specific parameters we are interested in, using the knowledge we have of the system.

5.3.1 *The $F_{2\omega}$ term: magnetic susceptibility*

As we saw in Equation (3.23d), the coupling between and induced magnetic field and its gradient with the magnetic susceptibility is responsible of a force at two times the frequency of the oscillating magnetic field. In this specific case, the oscillating magnetic field will correspond to the injection performed with the magnetic coils. Let's write again the corresponding force acting on the x-axis for $\mathbf{F}_{2\omega}$:

$$F_{2\omega,x} = -\frac{V\cos(2\omega t)}{2}\left[\frac{\chi}{\mu_0}\left\langle \mathbf{B}_i^{AC}\cdot\boldsymbol{\nabla}B_{i,x}^{AC}\right\rangle\right] \tag{5.3}$$

since the coil and TM centres are aligned, on the axis joining them we are only producing a magnetic field in this specific axis, i.e., the x-axis of our system – check Appendix A for more details about the magnetic field produced by the coils. That implies that in Equation (5.3) the product $\mathbf{B}_i^{AC}\cdot\boldsymbol{\nabla}$ will simply be $B_{i,x}^{AC}\cdot\nabla_x$. Therefore, Equation (5.3) ends up being:

$$F_{2\omega,x} = -\frac{V\cos(2\omega t)}{2}\left[\frac{\chi}{\mu_0}\left\langle B_{i,x}^{AC}\cdot\nabla_x B_{i,x}^{AC}\right\rangle\right] \tag{5.4}$$

Notice than in Equation (5.4) we can measure each of the terms directly except for the magnetic susceptibility χ. We can measure $F_{2\omega,x}$ very precisely demodulating the signal from Δg – in Section B.2 we explain in detail the method and tools used to demodulate the signals from LPF. The same goes for $B_{i,x}^{AC}$ and $\nabla_x B_{i,x}^{AC}$, where we can measure very precisely the amplitude of the applied magnetic field demodulating the signal from the current intensity in the coils and applying Equation (A.6) from Appendix A. Hence, if we isolate χ, we are obtaining a

measurement of the magnetic susceptibility at two times the frequency of the injected magnetic field with the coils:

$$\chi_r|_{2\omega} = -\frac{2\,\mu_0}{V}\,\frac{F_{2\omega,x}}{\left\langle B^{AC}_{i,x}\cdot\nabla_x B^{AC}_{i,x}\right\rangle} \tag{5.5}$$

With the previously explained equation, we are able to measure the real part of the magnetic susceptibility χ_r by demodulating the force that goes in phase with the injected field. More than that, we can take advantage of several more factors to differentiate the real χ_r and imaginary χ_i part of the magnetic susceptibility in Equation (5.4):

- The signal at 2ω only contains the magnetic susceptibility as an unknown parameter. Therefore, is a useful contribution to study in detail this parameter.
- The signal only depends on the amplitude of the injected oscillating signal $B^{AC}_{i,x}$, but not its offset $B^{DC}_{i,x}$. This is useful because we are able to obtain the amplitude of the oscillating signal with much more precision than its offset.
- The heterodyne demodulating method, explained in Section B.2, is a very powerful tool with which we can obtain the frequency of the signal ω, its amplitude $B^{AC}_{i,x}$ and its phase ϕ with very high precision.

Taking all these factors into account, we can differentiate its two contributions as we will explain in the following.

In Figure 35 we have generated an example of the force $F_{2\omega,x}$ we are measuring due to our magnetic injections. We have generated an example and not used real data in this explanation because, as we will now see, we have exaggerated the effect of the force produced by the imaginary susceptibility χ_i and diminished the effect of the force produced by the real susceptibility χ_r to better understand the method used.

If we take a look at Figure 35, the yellow signal $F_{2\omega,x}$ total is what we measure when we perform the magnetic experiments with the coils. On top of that, we show the real ($F_{2\omega,x}$ real) and imaginary ($F_{2\omega,x}$ imag.) contributions of the force generated by the magnetic susceptibility, which in the real data we can not differentiate unless we perform some analysis.

To obtain the real susceptibility, when doing the heterodyne demodulation we multiplied the force ($F_{2\omega,x}$ total) by a signal in-phase with the force produced by the real susceptibility χ_r. This way, we obtain the value of the signal ($F_{2\omega,x}$ total) at its maximum, i.e. the amplitude of the signal corresponding to the real part of the susceptibility with high precision. If instead, when we heterodyne we multiply the force with a signal out-of-phase by $\pi/2$, (which in the example would be a 50 seconds delay) we should obtain the value of the force ($F_{2\omega,x}$ total) at its minimum, which should be zero if no imaginary component appears. However, it appears that the measured value is not exactly zero because at a delay of $\pi/2$

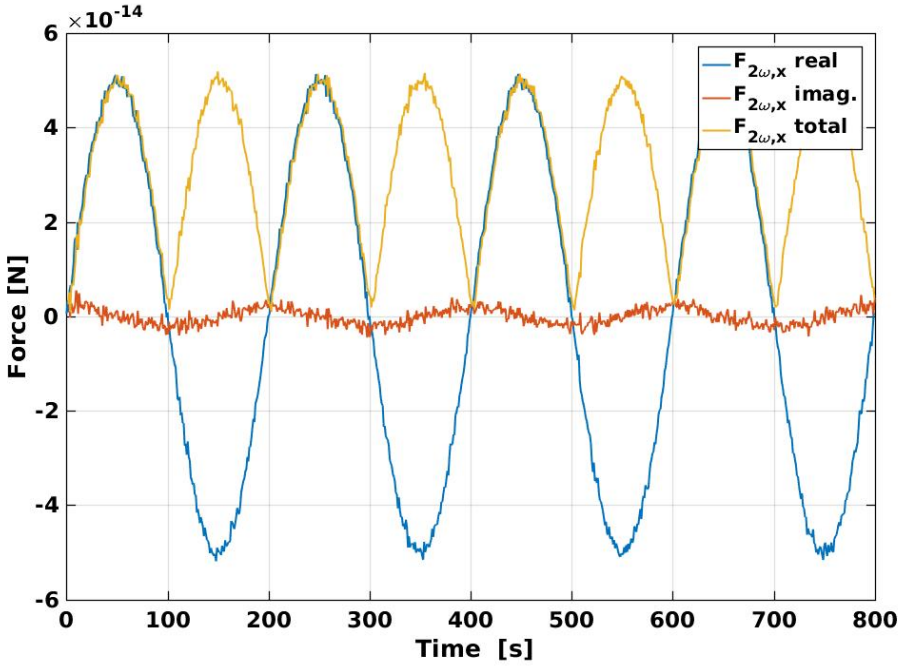

Figure 35: Not to scale example of the force $F_{2\omega,x}$ produced by the real and imaginary parts of the magnetic susceptibility, where we can differentiate the contributions of the real and imaginary parts. The simulated signal has a frequency of 5 mHz and a noise of 1 fN. $F_{2\omega,x}$ real has an amplitude of 50 fN and $F_{2\omega,x}$ imag. an amplitude of 2 fN.

the component of the force produced by the imaginary susceptibility reaches its maximum positive value. The same would happen at a delay of $3\pi/2$, where the imaginary susceptibility reaches its maximum negative value.

In the real data the signal coming from the imaginary susceptibility is smaller than the noise level (which at the frequencies we will work is at (1.74 ± 0.05) fm s^{-2} $Hz^{-1/2}$ [66]) and largely masked by the contribution of the real part of the magnetic susceptibility. Even so, thanks to the fact that our injections have a large number of cycles (which means more statistics to reduce the errors) and the heterodyne method allows us to measure frequencies, amplitudes and phases with a very high precision, in Section 5.5.3.2 we will see how this method allows us to obtain a value for χ_i analysing the most powerful injections performed:

$$\chi_i|_{2\omega} = -\frac{2\,\mu_0}{V}\,\frac{F_{2\omega,x(+\pi/2)}}{\left\langle B^{AC}_{i,x}\cdot\nabla_x B^{AC}_{i,x}\right\rangle} \tag{5.6}$$

or

$$\chi_i|_{2\omega} = -\frac{2\,\mu_0}{V}\,\frac{F_{2\omega,x(+3\pi/2)}}{\left\langle B^{AC}_{i,x}\cdot\nabla_x B^{AC}_{i,x}\right\rangle} \tag{5.7}$$

5.3.2 *The $F_{1\omega}$ term: magnetic moment in x and magnetic susceptibility*

As seen in Equation (3.23c), at the frequency of the signal we are injecting we have many terms mixed. Let's write again the force acting on the x-axis for the term $\mathbf{F}_{1\omega,x}$:

$$F_{1\omega,x} = V \sin(\omega t) \left[\left\langle \mathbf{M_r} \cdot \boldsymbol{\nabla} B_{i,x}^{AC} \right\rangle + \frac{\chi}{\mu_0} \left(\left\langle \mathbf{B}_o \cdot \boldsymbol{\nabla} B_{i,x}^{AC} \right\rangle + \frac{1}{2} \left\langle \mathbf{B}_i^{AC} \cdot \boldsymbol{\nabla} B_{o,x} \right\rangle \right) \right] \tag{5.8}$$

Following the same reasoning as when developing the term $F_{2\omega,x}$, due to axial symmetry all the terms containing magnetic field in the y and z direction will be zero in a first approximation. Therefore, we can rewrite the force in the x-direction as:

$$F_{1\omega,x} = V \sin(\omega t) \left[\left\langle M_{r,x} \cdot \nabla_x B_{i,x}^{AC} \right\rangle + \frac{\chi}{\mu_0} \left(\left\langle B_{o,x} \cdot \nabla_x B_{i,x}^{AC} \right\rangle + \frac{1}{2} \left\langle B_{i,x}^{AC} \cdot \nabla_x B_{o,x} \right\rangle \right) \right] \tag{5.9}$$

Now notice that each term in Equation (5.9) depends on $B_{i,x}^{AC}$ or $\nabla_x B_{i,x}^{AC}$. Since we are inducing the magnetic field with a single coil, and we are measuring at the same position (the distance between the coil and the TM centre), both magnetic field and magnetic field gradient will be proportional into each other, i.e. $B_{i,x}^{AC} = \kappa \nabla_x B_{i,x}^{AC}$. Therefore, we can rewrite Equation (5.9) as:

$$F_{1\omega,x} = V \sin(\omega t) \left[M_{r,x} + \frac{\chi}{\mu_0} \left(B_{o,x} + \kappa \nabla_x B_{o,x} \right) \right] B_{i,x}^{AC} \tag{5.10}$$

if we perform different injections in which we maintain the offset of the magnetic field constant and only variate the amplitude of the oscillations $B_{i,x}^{AC}$ (or equivalently, its gradient $\nabla_x B_{i,x}^{AC}$), the forces we measure will form a straight line in which the slope will correspond to the term between brackets in Equation (5.10). We will call this term the "effective" magnetic moment, since it has units of magnetic moment [A m^2] and plays the same role that the magnetic moment would have in a simple magnetic dipole. If we expand the term corresponding to the offset $B_{o,x}$ into its contribution coming from the DC of the background magnetic field $B_{back.,x}$ and the DC coming from the injection in the coil $BDC_{i,x}$ we can write the effective magnetic moment as:

$$M_{ef.,x} = \left(M_{r,x} + \frac{\chi}{\mu_0} \left[(B_{back.,x} + BDC_{i,x}) + \kappa \nabla_x (B_{back.,x} + BDC_{i,x}) \right] \right) \tag{5.11}$$

In Section 4.2 we have seen how the values of $B_{back.,x}$ are of the order of 1μT in the magnetometers, and we expect them to be around one order of magnitude smaller in the TM position. Now, the offset we injected in the experiments with the coils is quite high, generating a DC field in the position of the TM between 1-10 μT

depending on the injection. To simplify Equation (5.11), we will approximate that $B_{back.,x}$ is negligible in front of $BDC_{i,x}$. For the case of the gradient we will do the same, and it will be a even safer approximation since the difference between the background and applied gradient is even higher than in the case of the magnetic field. Therefore, we end up with:

$$M_{eff,x} \simeq M_{r,x} + \frac{2\chi V}{\mu_0} B_{i,x}^{DC} \tag{5.12}$$

since $B_{i,x}^{DC}$ is also proportional to $\nabla_x B_{i,x}^{DC}$ ($B_{i,x}^{DC} = \kappa \nabla_x B_{i,x}^{DC}$).

When doing the magnetic experiments, if we maintain constant $B_{i,x}^{AC}$ and the only varying parameter is $B_{i,x}^{DC}$, we can create a straight line following Equation (5.12), whose offset will be the remanent magnetic moment in the x-direction $M_{r,x}$ and with a slope proportional to the magnetic susceptibility χ at the frequency of the injection. Since we have also measured the effective magnetic moment $M_{eff,x}$ through the slope of Equation (5.10), we will have all the ingredients to finally obtain a measurement of the remanent magnetic moment.

5.3.3 $N_{1\omega}$ *terms: magnetic moments in* y *and* z *directions*

As we studied in Section 3.5, the TMs do not suffer just a force in the x-direction, but also some torques when we apply an oscillating magnetic field. We saw how, due to the symmetry of our system, a lot of the terms cancel in Equation (3.25). Also, we saw how our system is not sensitive to rotations around the x-axis, i.e., rotations in the angle θ. If we recapitulate all the cancellations we did, we ended up having:

$$N_{1\omega,\eta} = V \sin(\omega t) \left\langle M_{r,z} B_{i,x}^{AC} \right\rangle \tag{5.13}$$

and:

$$N_{1\omega,\phi} = V \sin(\omega t) \left\langle -M_{r,y} B_{i,x}^{AC} \right\rangle \tag{5.14}$$

Thus, the 1ω oscillation of the torque around the z-axis (in ϕ) is directly related to the remanent magnetic moment along y $M_{r,y}$, and the 1ω oscillation of the torque around the y-axis (in η) is directly related to the remanent magnetic moment along z $M_{r,z}$. Therefore, heterodyning the torque at 1ω for η and ϕ, as well as the injected magnetic field $B_{i,x}^{AC}$, is a straightforward way to obtain $M_{r,y}$ and $M_{r,z}$.

5.3.4 *The* F_{DC} *term: background estimates*

Let's remember which was the DC force produced in the TM when we perform a magnetic injection:

$$F_{DC,x} = V \left[\langle \mathbf{M_r} \cdot \boldsymbol{\nabla} B_{o,x} \rangle + \frac{\chi}{\mu_0} \left(\langle \mathbf{B}_o \cdot \boldsymbol{\nabla} B_{o,x} \rangle + \frac{1}{2} \left\langle \mathbf{B}_i^{AC} \cdot \boldsymbol{\nabla} B_{i,x}^{AC} \right\rangle \right) \right] \tag{5.15}$$

If we consider, like in the previous cases, the axial symmetry of our system, we can simplify some of the terms in Equation (5.15):

$$F_{DC,x} = V\Bigg[\langle M_{r,x}\cdot\nabla_x B_{o,x}\rangle + \frac{\chi}{\mu_0}\left(\langle B_{o,x}\cdot\nabla_x B_{o,x}\rangle + \frac{1}{2}\left\langle B^{AC}_{i,x}\cdot\nabla_x B^{AC}_{i,x}\right\rangle\right)\Bigg] \tag{5.16}$$

Similarly with what happened with the 1ω term, in Equation (5.16) we have many unknown parameters mixed. This time, though, we can take advantage of having analysed the 1ω term first. Thanks to this previous analysis, we will have an estimate of the remanent magnetic moment $M_{r,x}$, which is independent of the applied magnetic field, and therefore, of the frequency of the injections.

Now we will expand the DC magnetic field into its two contributions $B_{o,x} = B^{DC}_{i,x} + B_{back.,x}$. This time, we will rearrange Equation (5.16) writing all the terms as a function of $B^{DC}_{i,x}$. Remember that we can do this because the applied magnetic field and its gradient are related through a constant due to the geometry of the system ($B^{DC}_{i,x} = \kappa\nabla_x B^{DC}_{i,x}$):

$$F_{DC,x} = \underbrace{\left(\frac{\chi V}{\mu_0\kappa}\right)}_{a}(B^{DC}_{i,x})^2 + \underbrace{\left(\frac{M_{r,x}}{\kappa} + \frac{\chi V}{\mu_0}\left[\nabla_x B_{back.,x} + \frac{B_{back.,x}}{\kappa}\right]\right)}_{b} B^{DC}_{i,x} + \underbrace{\left(\langle M_{r,x}\cdot\nabla_x B_{back.,x}\rangle + \frac{\chi V}{\mu_0}\left[\langle B_{back.,x}\cdot\nabla_x B_{back.,x}\rangle + \frac{1}{2}\langle B^{AC}_{i,x}\cdot\nabla_x B^{AC}_{i,x}\rangle\right]\right)}_{c} \tag{5.17}$$

Notice that Equation (5.17) forms a 2nd order equation depending on the offset of the injected magnetic field $B^{DC}_{i,x}$. Hence, if we perform injections with different $B^{DC}_{i,x}$ and measure which is the DC force $F_{DC,x}$, we can obtain several parabolas which, if we fit them, can give us information about different terms:

- The constant a accompanying the 2nd order term, will give us a DC estimate of the magnetic susceptibility χ, since this force does not depend on the frequency of the injections.
- In terms b and c we have 4 unknown parameters: χ, $M_{r,x}$, $B_{back.,x}$ and $\nabla_x B_{back.,x}$. Nevertheless, we can obtain the DC part of χ through the value of the constant a, and we can obtain $M_{r,x}$ through the 1ω injections, and $M_{r,x}$ is independent of the frequency of the injections.

Therefore, if we obtain a value for the terms b and c fitting the curve in Equation (5.17), we can end up building a system of 2 equations with 2 unknowns: $B_{back.,x}$ and $\nabla_x B_{back.,x}$.

$$b = \left(\frac{M_{r,x}}{\kappa} + \frac{\chi V}{\mu_0} \left[\nabla_x B_{back.,x} + \frac{B_{back.,x}}{\kappa} \right] \right) \tag{5.18a}$$

$$c = \Bigg(\langle M_{r,x} \cdot \nabla_x B_{back.,x} \rangle + \frac{\chi V}{\mu_0} \left[\langle B_{back.,x} \cdot \nabla_x B_{back.,x} \rangle + \frac{1}{2} \langle B^{AC}_{i,x} \cdot \nabla_x B^{AC}_{i,x} \rangle \right] \Bigg) \tag{5.18b}$$

With this method we are able to extract the values of the background magnetic field and its gradient without directly measuring them, but instead thanks to the precision with which we are able to measure the forces applied on the TMs and the precision with which we have estimated the magnetic parameters of the TMs, χ and $M_{r,x}$. This solves an important problem in the magnetic diagnostics system, that is our inability to measure the magnetic field and its gradient close to the TM position, since our magnetometers had to be placed far from the TMs due to their magnetic active core. Nevertheless, is important to notice that we can only estimate the background terms in this way when we are injecting a signal through the coils, and that we are not estimating the background magnetic field and its gradient continuously.

5.4 COILS CALIBRATION

The very first thing we should do before we start extracting results from the magnetic injections is calibrate our model of the magnetic field created by our coils and explained in Appendix A. This model can not be totally accurate for several reasons: small tilt between the coil and the TM, their centres are not totally aligned in y and z, the distance x between them may have some errors, etc. In order to calibrate our model, we can take advantage of the fact that we have a pair of magnetometers aligned with the centre of the coils, just as the TMs, but in the opposite direction. We show this configuration in Figure 36.

In Figure 37 we show which is the magnetic field measured by magnetometer PX during the injections in coil 1 performed on June 18th, 2016 (DOY 170). Superposed to it, we show which is the magnetic field we would create at the magnetometer according to our model. As can be seen just by a simple look, there is a small difference between both values. For each injection performed on June 18th, 2016 (DOY 170) we will measure which is the DC and amplitude of the applied sinusoid. In order to measure the amplitude with high precision, we will use an heterodyne demodulation, which is explained deeply in Section B.2.

After measuring the values for the DC and amplitude, we find that there is a 4% discrepancy between our model and the magnetometer data, for all the different injections we performed. Even though this is a systematic error, and we can not say that it is all the systematic error present in our system, from here on we will

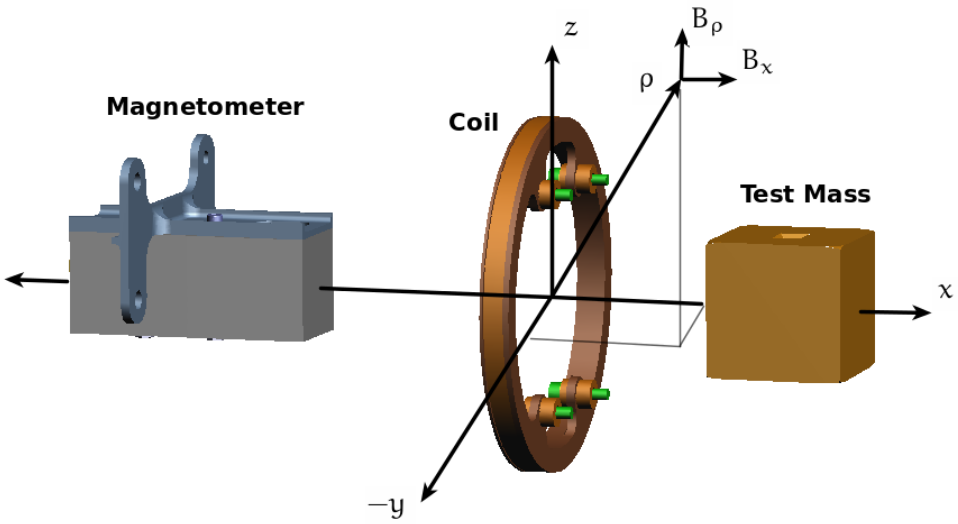

Figure 36: Scheme of the system: magnetometer, coil and TM inside the LTP. The different axis are indicated in the figure for orientation and to see that the 3 items are aligned in the x-direction, but bear in mind that the origin of the LTP reference frame is between the two TMs, and not in the middle of the coil, like the figure shows.

correct it for all our injections and we will check in the last chapter how the results we obtain when fitting the data are better thanks to this correction.

5.5 RESULTS FROM THE EXPERIMENTS AND EXTRACTION OF MAGNETIC PARAMETERS

Now that we have explained how to extract the magnetic susceptibility $\chi(\omega)$, the remanent magnetic moment $\mathbf{M_r}$, the background magnetic field in the x-direction $B_{back.,x}$ and its gradient $\nabla_x B_{back.,x}$ through the analysis of the different components of the forces in the different experiments performed with the magnetic coils, we will proceed to show the results for the estimation of these parameters and discuss them.

5.5.1 *Remanent magnetic moment*

5.5.1.1 *Remanent magnetic moment in the x-direction*

In the following, we will follow the method explained in Section 5.3.2 to obtain an estimate for the remanent magnetic moment in the x-direction $M_{r,x}$. First, we have to select the magnetic injections that allow us to build the straight lines from Equation(5.10). To do so, we will select injections performed in coil 1 from April 28th (DOY 119) and June 18th (DOY 170) 2016. The selected injections should have a constant offset $B^{DC}_{i,x}$ and should have been performed at different amplitudes $B^{AC}_{i,x}$. For these injections, we measure very precisely which is the force $F_{1\omega,x}$ and the amplitude of the magnetic field produced at the TM $B^{AC}_{i,x}$ using the heterodyne method. If we plot the results we obtain the straight lines shown in Figure 38.

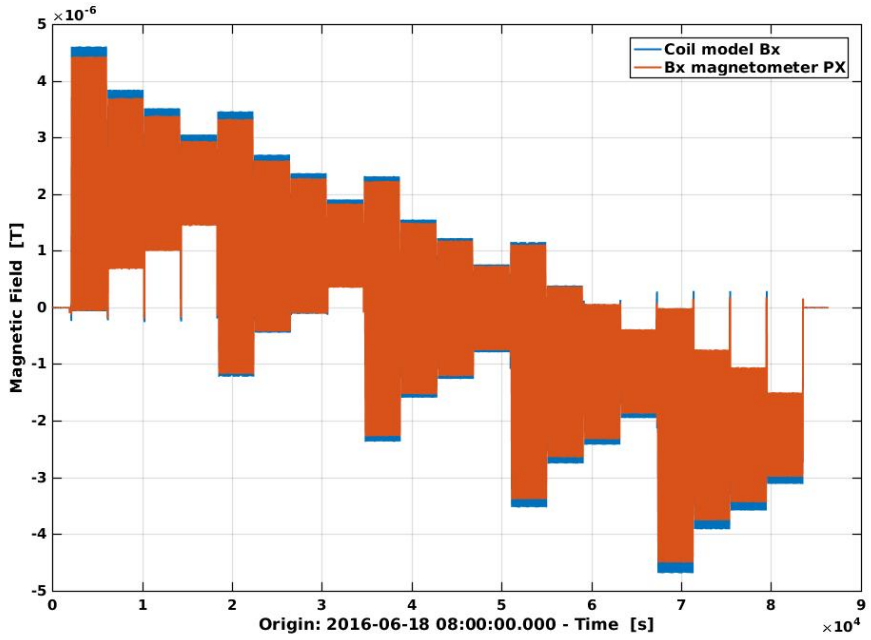

Figure 37: Comparison of the magnetic field in the x-axis measured in magnetometer PX with the coil model explained in Appendix A for the injections performed in coil 1 on June 18th, 2016.

We can now fit the lines shown in Figure 38 to straight lines of the type $y = a + bx$. We show the results of the fits in Table 10. On the one hand, parameters 'a' are close to zero, since if we do not apply any sinusoid in the coil there is no force at 1ω. On the other hand, the slopes 'b' are well fitted except for the $\pm$ 0.1 and 0.2 mA offsets. We only have two points for those lines, so there can be no errors on the fit.

I_{DC} [mA]	offset (a)	slope (b)
DC=+1.50	$(-2 \pm 30) \times 10^{-15}$	$(-2.98 \pm 0.02) \times 10^{-8}$
DC=+0.75	$(-6 \pm 18) \times 10^{-15}$	$(-1.51 \pm 0.02) \times 10^{-8}$
DC=+0.2	$(5 \pm 0) \times 10^{-15}$	$(-4.56 \pm 0) \times 10^{-9}$
DC=+0.1	$(-2 \pm 0) \times 10^{-15}$	$(-2.54 \pm 0) \times 10^{-9}$
DC=-0.1	$(-2 \pm 0) \times 10^{-15}$	$(1.35 \pm 0) \times 10^{-8}$
DC=-0.2	$(-4 \pm 0) \times 10^{-15}$	$(3.31 \pm 0) \times 10^{-8}$
AC=-0.75	$(4 \pm 16) \times 10^{-15}$	$(1.41 \pm 0.02) \times 10^{-8}$
AC=-1.50	$(-7 \pm 26) \times 10^{-15}$	$(2.87 \pm 0.02) \times 10^{-8}$

Table 10: Result of the fits to a straight line of the type $y = a + bx$ of the lines shown in Figure 38.

In Figure 38 can be seen how the force at 1ω changes depending on the intensity of the injected magnetic field, for fixed DCs. The slopes of these lines

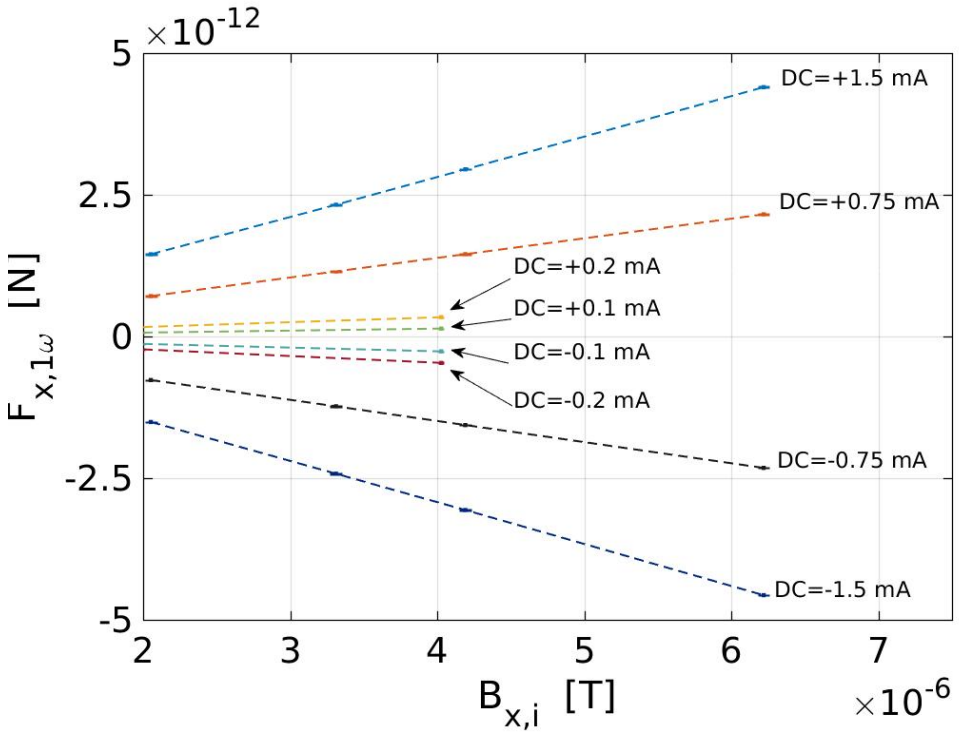

Figure 38: $F_{1\omega}$ applied on TM1 as a function of the amplitude of the applied magnetic field $B^{AC}_{i,x}$. The different colours correspond to the different offsets $B^{DC}_{i,x}$ of the injected current in coil 1, and are indicated in the figure.

(the values of the term 'b' in Table 10) correspond to the effective magnetic moment $M_{eff.,x}$ we have defined in Equation (5.11). If we now plot the effective magnetic moments in front of the injected DC magnetic field, as described in Equation (5.12), we obtain another straight line, which we show in Figure 39. This straight line contains the information we are looking about the remanent magnetic moment. The slope of the line will give us the value of χ at 1ω, and the offset will be directly the value of the remanent magnetic moment in the x-direction $M_{r,x}$. If we fit this line through to a line of the type $y = a + bx$ we obtain that $a = (-0.57 \pm 0.02) \times 10^{-9}$ [A m^2] and $b = -2.907 \pm 0.004) \times 10^{-5}$ []. Therefore, the remanent magnetic moment in the x-direction is measured to be:

$$M_x = -0.57 \pm 0.02 \text{ [nA m}^2\text{]}.$$

5.5.1.2 *Remanent magnetic moment in y and z directions*

Regarding the value of the remanent magnetic moment in the y and z directions, we can get its value analysing the torque of the TM around the y and z axis, i.e. the rotations in θ and ϕ. In Section 3.5 we saw how, due to the symmetry of our system, the torques exerted on the TMs could be simplified a lot and ended up being:

$$N_{1\omega,\eta} = V \sin(\omega t) \left\langle M_{r,z} B^{AC}_{i,x} \right\rangle \tag{5.19a}$$

$$N_{1\omega,\phi} = V \sin(\omega t) \left\langle -M_{r,y} B^{AC}_{i,x} \right\rangle \tag{5.19b}$$

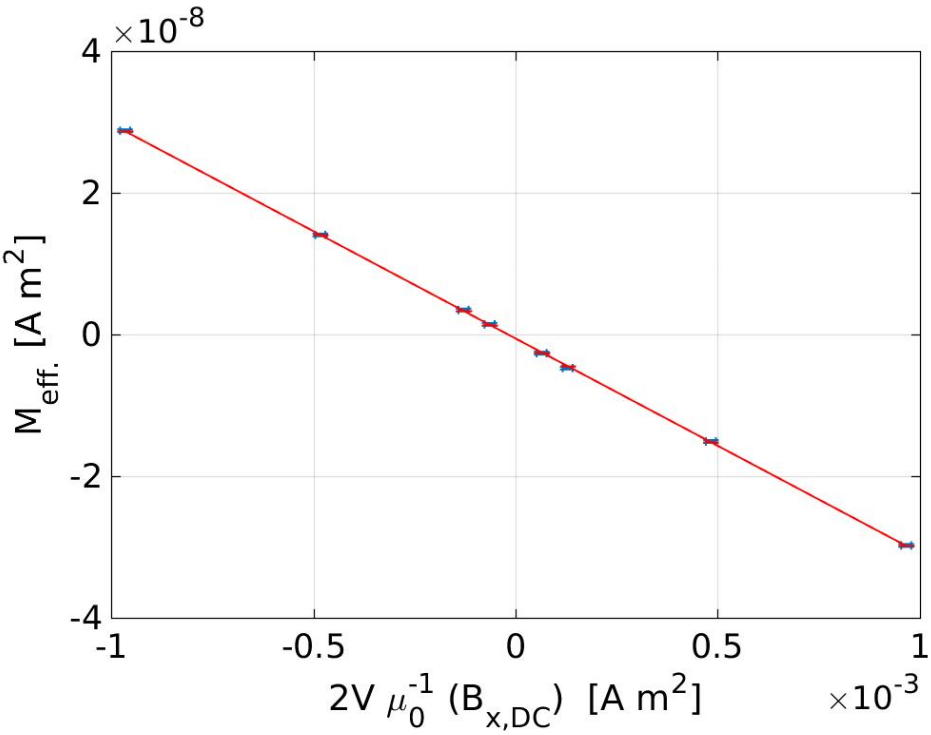

Figure 39: Lineal fit (red line) of the effective magnetic moments as a function of the applied DC magnetic field. The slope of the line is directly χ, and its offset corresponds to $M_{r,x}$.

We will use the injections done on June 18th 2016 (DOY 170) to perform the analysis. The torque of those injections are shown in Figure 33. Heterodyning the torque generated and the magnetic field we are producing, the following values of the magnetic moment are obtained:

$$M_y = -0.33 \pm 0.03 \text{ [nA m}^2\text{]}$$
$$M_z = 0.54 \pm 0.03 \text{ [nA m}^2\text{]}$$

5.5.2 *Background magnetic field*

Now that we have obtained the values of the remanent magnetic moment $\mathbf{M_r}$, we will follow the method explained in Section 5.3.4 to compute the background magnetic field along the x-axis $B_{x,back.}$ and its gradient $\nabla_x B_{x,back.}$. We will need to select the magnetic injections that allow us to build the parabolas from Equation (5.17).We will use the injections performed on June 18th (DOY 170), 2016. We will use those because we can use four different constant ACs while we variate the DC part of the injection. This way, we will obtain four curves with five points on each one. In these injections we will measure which is the DC force that was produced during the injection on the TM and compute using Equation A.6 from Appendix A which is the DC magnetic field created at the TM position. The parabolas obtained using this method can be seen in Figure 40.

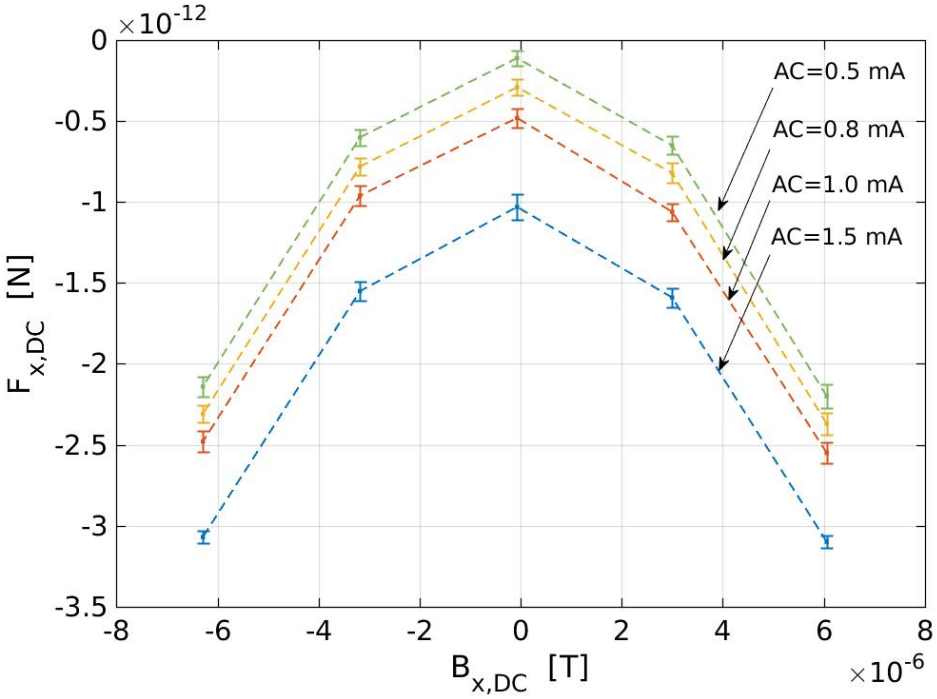

Figure 40: F_{DC} applied on TM1 as a function of the applied DC magnetic field $B^{DC}_{i,x}$. The different colours correspond to the different amplitudes $B^{AC}_{i,x}$ of the injected sinusoidal current in coil 1, and are indicated in the figure.

If we now fit those parabolas to a equation of the type $y = a + bx + cx^2$ we will obtain the different coefficients 'a', 'b' and 'c' from Equation (5.17). We show the results of the fit in Table 11.

I_{AC} [mA]	coeff. a	coeff. b	coeff. c
AC=1.5	$(-1.05 \pm 0.05) \times 10^{-12}$	$(-1.5 \pm 0.4) \times 10^{-8}$	$(-5.3 \pm 0.2) \times 10^{-2}$
AC=1.0	$(-0.50 \pm 0.04) \times 10^{-12}$	$(-2.0 \pm 0.6) \times 10^{-8}$	$(-5.3 \pm 0.2) \times 10^{-2}$
AC=0.8	$(-0.29 \pm 0.04) \times 10^{-12}$	$(-1.7 \pm 0.6) \times 10^{-8}$	$(-5.4 \pm 0.2) \times 10^{-2}$
AC=0.5	$(-0.11 \pm 0.04) \times 10^{-12}$	$(-1.7 \pm 0.7) \times 10^{-8}$	$(-5.4 \pm 0.2) \times 10^{-2}$

Table 11: Result of the fits to a curve of the type $y = a + bx + cx^2$ of the parabolas shown in Figure 40.

Once we have those parabolas fitted, the first thing we can obtain is a value of the magnetic susceptibility χ from the coefficient 'a'. This is a DC value for the magnetic susceptibility, and we will go into more detail about it in the following section. It is computed to be: $\chi_{DC} = (-2.99 \pm 0.08) \times 10^{-5}$.

Next, remember we can build the following system of equations:

$$b = \left(\frac{M_{r,x}}{\kappa} + \frac{\chi V}{\mu_0} \left[\nabla_x B_{back.,x} + \frac{B_{back.,x}}{\kappa} \right] \right) \tag{5.20a}$$

$$c = \left(\langle M_{r,x} \cdot \nabla_x B_{back.,x} \rangle + \frac{\chi V}{\mu_0} \left[\langle B_{back.,x} \cdot \nabla_x B_{back.,x} \rangle + \frac{1}{2} \langle B_{i,x}^{AC} \cdot \nabla_x B_{i,x}^{AC} \rangle \right] \right) \tag{5.20b}$$

Notice that the only unknown parameters here will be $B_{x,back}$ and $\nabla_x B_{back,x}$, since we have obtained the coefficients 'b' and 'c' fitting the parabolas, we computed χ in a non-oscillating magnetic field (DC value) through the parameter 'a' from the parabolas, and we can use the value for $M_{r,x}$ obtained in Section 5.5.1 because this parameter for the TM is independent of the surrounding magnetic field. If we solve the system of equations we obtain the following pair of solutions for $B_{x,back}$ and $\nabla B_{back,x}$:

$$B_{back,x} = 150 \pm 80 \text{ [nT]} \quad \& \quad \nabla B_{back,x} = -3700 \pm 2600 \text{ [nT/m]}$$
$$B_{back,x} = -270 \pm 80 \text{ [nT]} \quad \& \quad \nabla B_{back,x} = 7700 \pm 2600 \text{ [nT/m]}$$

5.5.3 *Magnetic Susceptibility*

The only magnetic parameter left we have to assign a value is the magnetic susceptibility. If we remember the explanation from Section 3.3, the magnetic susceptibility is not a constant value, it changes as a function of the frequency and has two components, one real and another one imaginary. In the previous sections we already got some values for the magnetic susceptibility from the 1ω $F_{1\omega}$ and DC F_{DC} terms. The only term left we can analyse to obtain more values from the magnetic susceptibility is the 2ω term $F_{2\omega}$. We will analyse all the injections performed at different frequencies listed in Section 5.2. This includes injections from: April 28 & 29, 2016 (DOYs 118 & 119; June 18, 2016 (DOY 170) and 14-16 March, 2017 (DOYs 73-75).

5.5.3.1 *Real component*

In Table 12 we show the values obtained for the magnetic susceptibility demodulating the signals at 2ω as explained in Section 5.3.1 for the previously listed injections. Moreover, Table 12 also includes the values obtained for the magnetic susceptibility in the previous sections from the 1ω $F_{1\omega}$ and DC F_{DC} terms. All these values will correspond to the real part of the magnetic susceptibility.

Notice that for TM2 we only performed injections on April 29, 2016 (DOY 119). On that day we did not perform injections varying alternatively the DC and AC of the injections, as we did with the injections of June 18, 2016 (DOY 170). Hence, we can not obtain any information about the magnetic susceptibility from the 1ω $F_{1\omega}$ and DC F_{DC} terms, and the only values shown in Table 12 come from the 2ω term $F_{2\omega}$.

frequency [mHz]	χ_r (TM1)	χ_r (TM2)
DC	$(-2.99 \pm 0.08) \times 10^{-5}$	–
2	$(-3.07 \pm 0.02) \times 10^{-5}$	$(-3.1 \pm 0.6) \times 10^{-5}$
5	$(-3.03 \pm 0.01) \times 10^{-5}$	–
6	$(-3.13 \pm 0.02) \times 10^{-5}$	$(-3.20 \pm 0.01) \times 10^{-5}$
10	$(-3.30 \pm 0.01) \times 10^{-5}$	$(-3.31 \pm 0.01) \times 10^{-5}$
30	$(-4.38 \pm 0.01) \times 10^{-5}$	–

Table 12: Calculated magnetic susceptibility for different frequencies for TMs 1 & 2.

After gathering values for χ at all the possible frequencies, we will proceed to plot the different values together on top of our model, the one shown in Equation (3.17) and Figure 23. We show the results in Figure 41.

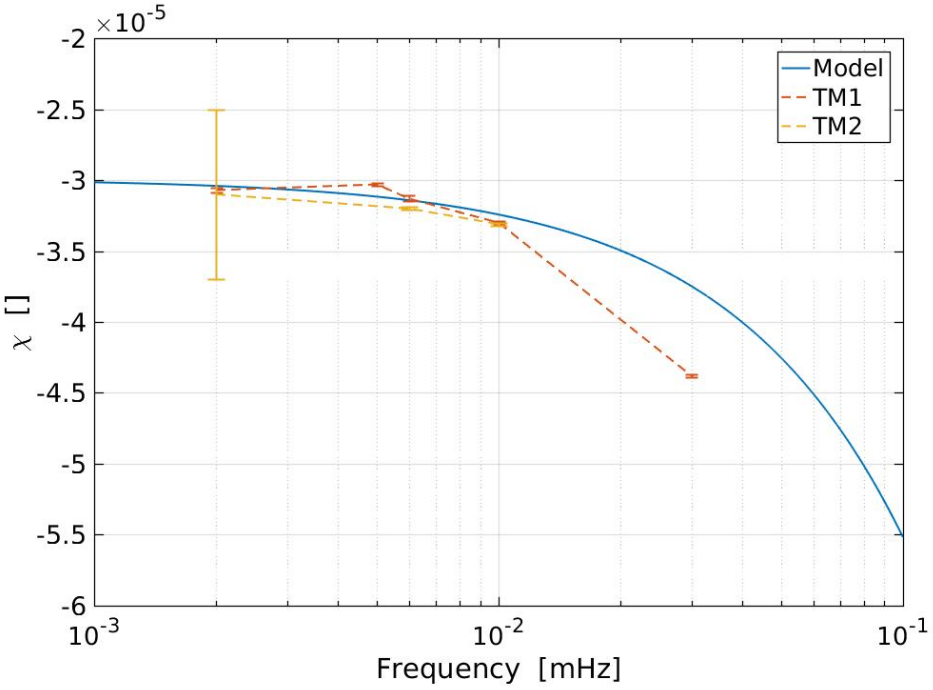

Figure 41: Computed values of χ plotted in top of our model of how the magnetic susceptibility changes with frequency.

5.5.3.2 *Imaginary component*

In terms of computing results and the contribution from magnetic noise later on, we can use the values from Table 12 and Figure 41, which would correspond to the real part of the magnetic susceptibility. However, we will disentangle here which is the contribution coming from the imaginary term to the magnetic susceptibility. In order to do so, we will follow the method explained in Section 5.3.1. We will demodulate $F_{2\omega}$ from the injections at $I^{AC} = 1.5$ mA from June 18, 2016 (DOY 170). We were only able to measure it in this set of injections, since the in-

jections with a smaller amplitude I^{AC} were not powerful enough to measure the tiny effect produced by the imaginary susceptibility.

We show the forces measured in Table 13. There, we can check the measured forces for the previously mentioned set of injections at a $+\pi/2$ and a $+3\pi/2$ delay.

[mA]	$I_{DC} = 1.5$	$I_{DC} = 0.75$	$I_{DC} = 0$	$I_{DC} = -0.75$	$I_{DC} = -1.5$
			$F_{2\omega,+\pi/2}$ [fN]		
$I_{AC} = 1.5$	-0.04 ± 0.11	-0.16 ± 0.06	0.02 ± 0.06	-0.21 ± 0.08	-0.07 ± 0.13
			$F_{2\omega,+3\pi/2}$ [fN]		
$I_{AC} = 1.5$	-0.11 ± 0.15	-0.12 ± 0.08	0.09 ± 0.10	-0.16 ± 0.08	-0.18 ± 0.16

Table 13: Measured forces coming from the 1ω term of the imaginary susceptibility for the injections of $I^{AC} = 1.5$ mA of June 18th, 2016 (DOY 170).

Using Equation (5.5) with the measured values from Table 13 we can obtain the different values for $\chi_i|_{2\omega}$ shown in Figure 42. An important point to notice here is that there appears to be a significant difference between the injections at 0 DC and the injections at DC $\pm$ 0.75 mA and $\pm$ 1.5 mA. Although we are not sure from which effects this difference may be coming from, it is somehow expected, since when we are not injecting any DC different systematic errors may apply.

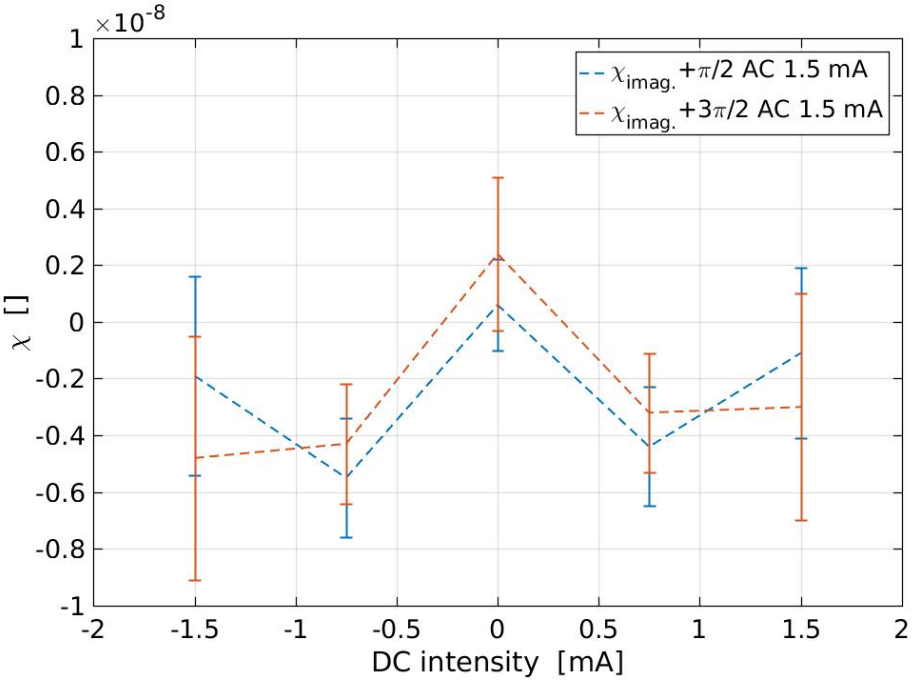

Figure 42: Computed χ_i at 10 mHZ for the measured forces of Table 13 for the injections of $I^{AC} = 1.5$ mA of June 18th, 2016 (DOY 170).

If we now compute the mean value for $\chi_i|_{2\omega}$ from the values obtained with the different injections, we finally obtain that at 10 mHz the imaginary magnetic susceptibility has a value of:

$$\chi_i = -0.24 \pm 0.08 \times 10^{-8} \text{ []}.$$

5.6 CONCLUSIONS

In this chapter we have analysed the magnetic experiments carried away on-board LPF during mission operations and, with the analysis performed, we could estimate the values of the remanent magnetic moment and magnetic susceptibility of the TMs, as well as calculating the x-component of the background magnetic field and its gradient along x.

We were able to estimate the magnetic susceptibility of both TMs. We have also seen how the magnetic susceptibility depends on the frequency of the oscillating magnetic field, adjusting to the model shown in Equation (3.17). The adjustment is not perfect, and this may come from several facts:

- The model corresponds to the polarizability of a sphere, as explained in Vitale [109], while our TM is a cube.
- We lack measurements at more frequencies, for example we do not have values at less than 2 mHz, while the magnetic contribution to the TMs noise acceleration is expected to be imporatant below the mHz. Therefore, we do not have many points to adjust to the curve of Equation (3.17).
- The ideal way of measuring χ is through the 2ω term, since this term only contains χ as unknown parameter and it does not depend on the DC of the magnetic field. However, not all the measurements are performed this way.
- For some of the values shown for TM1, χ_r is obtained through different methods, coming from the DC, 1ω and 2ω terms. This is positive but has some drawbacks. On the one hand, it is good to obtain similar values through different methods, since it strengthens the robustness of the results. On the other hand, using different methods may carry some small systematic errors or assumptions that can cause some small discrepancies to appear.

Nevertheless, the values obtained for χ_r make sense with the on-ground estimations, which predicted a DC diamagnetic magnetic susceptibility with values around -2.5×10^{-5} [133].

Regarding the imaginary component of the magnetic susceptibility, the results obtained are quite good. Even though the effect it produces is so small, producing a force smaller than one fN, thanks to the precision of the method we used to measure it (heterodyning the 2ω force of the most energetic injections in coil 1), having a lot of cycles on each injection for better statistics and measuring it for different injections, we have been able to measure a non-zero value for it. Moreover, the measured values are close to estimations from previous studies, being at least three orders of magnitude smaller than its real counterpart for the frequency range around 1-10 mHz [134, 135]. Indeed, the proportion between them is:

$$\frac{\chi_r|_{10\text{ mHz}}}{\chi_i|_{10\text{ mHz}}} = \frac{-3.03 \times 10^{-5}}{-2.4 \times 10^{-9}} \simeq 14000 \tag{5.21}$$

which is four orders of magnitude smaller than its real counterpart. Although this effect is so small at this frequency range than we can safely neglect it for any magnetic noise contribution calculation, is good to have proven that we can really measure it and that, as supposed from beforehand, it is much smaller than its real counterpart.

Regarding the remanent magnetic moment, the values of its three components are very similar, all within the same order of magnitude and without any privileged direction, which confirms the fact that the TM is isotropic. We can compute the modulus of it, which is:

$$|M_r| = 0.85 \pm 0.02 \text{ [nA m}^2\text{]}$$

This value is measured with better precision than any tests performed on-ground to try to measure the magnetic moment, which in [136] was measured to have an upper limit of $|M_r| < 4 \pm 1$ [nA m^2]. It also confirms that, even after the transport, montage inside the spacecraft, launch and travel to L1, the TM keeps a remanent moment below the requirements, which asked for $|M_r| < 10$ [nA m^2].

Finally, regarding the x-component of the background magnetic field and its gradient along x, with the calculations shown in this chapter, we have been able to obtain a measurement of the background magnetic field and its gradient in the x-direction at the TM1 position. Even though we could not measure it directly, thanks to the precision with which we can measure the forces through the optical system, we have been able to measure these values. Nevertheless, the errors in the estimation are quite high, since we do not have a direct instrument measuring the magnetic field and we had to go through several approximations and manipulation of the forces. Also, since measuring DC forces is not as precise as measuring the amplitude of an oscillation, this also results in higher errors. However, even with the high errors, the obtained values make sense, since we expected a magnetic field a factor 2-10 smaller at the TMs than at the magnetometers, and a gradient of around the 1000-10000 [nT/m] [137–139]. It is worth noticing that this was not a continuous way of measuring the background, we could only measure it during the injections and only in the axis joining the system coil-TM. This was one of the biggest downsides of the magnetic diagnostics system, not being able to directly measure the background magnetic field and its gradient (in all the directions) close to the TMs, and is a thing to improve towards LISA.

6 MAGNETIC NOISE CONTRIBUTION TO Δg

In the previous chapters we have been gathering all the necessary ingredients to be able to compute which is the contribution coming from magnetic effects to the relative acceleration (or Δg) between both TMs. In Chapter 3, we showed which were the forces disturbing the TMs movement, and that these forces appeared due to the coupling of the magnetic field and magnetic field gradient surrounding the TMs with their remanent magnetic moment and magnetic susceptibility. In Chapter 4, we studied in depth which is the magnetic field (and magnetic field gradient) present in the spacecraft and its fluctuations. We also found how the fluctuations of the IMF are not stationary at low frequencies, and how they are related to solar weather parameters like the solar wind speed. In Chapter 5, we analysed the data from the magnetic experiments performed on-board and estimated the value of the remanent magnetic moment and magnetic susceptibility, as well as the background magnetic field (and gradient) at the position of the TMs. In this chapter, we will gather all the previously mentioned information from the past three chapters to build a model which will give the contribution from magnetic effects to Δg.

This chapter is organised as follows. We will start explaining which is the aim of computing the magnetic contribution to the acceleration between the TMs and the problems behind it. Second, we will show which is the model we use for computing the magnetic contribution to Δg and the equations that rule it. We will continue the analysis estimating some of the parameters we need for computing the magnetic contribution, like the ASD of the IMF fluctuations and the magnetic field gradients of B_x. Afterwards, we will show how the values we are using for the model fit the Δg time-series. We will then show which is the contribution from the magnetic effects to Δg ASD. We will end this section discussing the possible contribution from other different magnetic effects from which we had no on-board measurements to the low-frequency ASD of Δg.

6.1 MAGNETIC MODEL

In Chapter 3 we described which were the magnetic forces acting on a magnetic dipole inside a magnetic field, and explained that for the LPF case, we could consider the TMs as a magnetic dipole. To calculate the magnetic contribution to the fluctuations of Δg, we will start from Equation (3.5), which showed which was the magnetic force along the x-axis. Let's write it down again:

$$F_x = \left\langle (\mathbf{M_r} \cdot \boldsymbol{\nabla} B_x) + \frac{\chi}{\mu_0} [\mathbf{B} \cdot \boldsymbol{\nabla} B_x] \right\rangle V \tag{6.1}$$

If we now compute the fluctuations in time of this force:

$$\begin{aligned}\delta F_x &= \delta \left\langle (\mathbf{M_r} \cdot \boldsymbol{\nabla} B_x) + \frac{\chi}{\mu_0} [\mathbf{B} \cdot \boldsymbol{\nabla} B_x] \right\rangle V \\ &= \left\langle (\mathbf{M_r} \cdot \delta\boldsymbol{\nabla} B_x) + \frac{\chi}{\mu_0} [\delta\mathbf{B} \cdot \boldsymbol{\nabla} B_x + \mathbf{B} \cdot \delta\boldsymbol{\nabla} B_x] \right\rangle V \end{aligned} \tag{6.2}$$

where δ means the fluctuations of the corresponding term, i. e., the ASD of the term. Here we are assuming $\mathbf{M_r}$ is constant in time, as well as chi, for a given frequency. If we now expand the terms:

$$\delta F_x = V[M_{r,x} \cdot \delta\nabla_x B_x + M_{r,y} \cdot \delta\nabla_y B_x + M_{r,z} \cdot \delta\nabla_y B_x] \tag{6.3}$$

$$+ \frac{\chi V}{\mu_0} [\delta B_x \cdot \nabla_x B_x + \delta B_y \cdot \nabla_y B_x + \delta B_z \cdot \nabla_z B_x] \tag{6.4}$$

$$+ \frac{\chi V}{\mu_0} [B_x \cdot \delta\nabla_x B_x + B_y \cdot \delta\nabla_y B_x + B_z \cdot \delta\nabla_z B_x] \tag{6.5}$$

$$= \underbrace{V(\mathbf{M_r} \cdot \delta\boldsymbol{\nabla} B_x)}_{term1} + \underbrace{\frac{\chi V}{\mu_0} (\delta\mathbf{B} \cdot \boldsymbol{\nabla} B_x)}_{term2} + \underbrace{\frac{\chi V}{\mu_0} (\mathbf{B} \cdot \delta\boldsymbol{\nabla} B_x)}_{term3} \tag{6.6}$$

To give the magnetic contribution to Δg, we will use Equation (6.6) to build our magnetic model. In Chapter 5 we have estimated the values for the TM magnetic parameters and the background magnetic field. What is left to estimate is the fluctuations of the magnetic field $\delta\mathbf{B}$ and of the gradient $\delta\boldsymbol{\nabla} B$. In Chapter 4 we calculated these fluctuations, but in the following section we will see how we have to modify them a little bit to adjust to the real magnetic field present on the spacecraft.

6.2 FITS TO THE MAGNETIC SPECTRUM

As we saw in Equation (6.6), we need an estimation of the fluctuations of the magnetic field $\delta\mathbf{B}$ and of the gradient $\delta\boldsymbol{\nabla} B_x$ to build the magnetic model that calculates the contribution coming from the magnetic field fluctuations to Δg fluctuations. In Chapter 4 we computed the fluctuations of the magnetic field and its gradient (see Figure 26), but this ASDs included the noise from electronics. To correctly give an estimation of the magnetic contribution to the acceleration between both TMs, we have to only take into account the real magnetic field and gradient, and eliminate the noise coming from electronics (which does not correspond to a real magnetic field). In order to do so, we will fit the ASDs from Figure 26 to try to get rid of the contribution from electronics.

As explained in Chapter 4, when we compute the ASD of the magnetic field, it shows two differentiated components. First, below 1 mHz, the magnetic field ASD is dominated by an approximately f^{-1} behaviour which is coherent between all magnetometers, since this contribution comes from the IMF. Second, above 1 mHz the magnetic field flattens and the plateau is different depending on which magnetometer we are looking at, since this contribution comes from the electronics and is not a real magnetic field measurement.

In order to differentiate these contributions, we will fit the ASD of the magnetic field to a curve of the form $a + b(2\pi f)^c$ for the February 2017 noise run (from 13 Feb'17 to 2 Mar'17). We show the results of the fit in Table 14 and Figure 43. The data used for the three contributions of **B** has been obtained averaging the contribution from the 4 magnetometers for better statistics. This is not a problem, since we will use only the low frequency part of the function, which is coherent within all magnetometers for the same axis.

Parameter	a	b	c
B_x	$(4.06 \pm 0.06) \times 10^{-9}$	$(7.23 \pm 0.01) \times 10^{-10}$	-1.1 ± 0.3
B_y	$(3.73 \pm 0.01) \times 10^{-9}$	$(7.78 \pm 0.01) \times 10^{-10}$	-1.0 ± 0.1
B_z	$(4.62 \pm 0.13) \times 10^{-9}$	$(5.50 \pm 0.01) \times 10^{-10}$	-1.3 ± 0.3
$\partial_x B_x$	$(1.73 \pm 0.05) \times 10^{-8}$	$(-9.657 \pm 0.001) \times 10^{-9}$	–
$\partial_y B_x$	$(1.70 \pm 0.05) \times 10^{-8}$	$(-5.472 \pm 0.001) \times 10^{-9}$	–
$\partial_z B_x$	–	–	–

Table 14: Values of the fits of the ASD of the magnetic field components to a function of the type $a + b(2\pi f)^c$, and to a function of the type $a + b(2\pi f)$ for the case of the gradient of the x-component of the magnetic field.

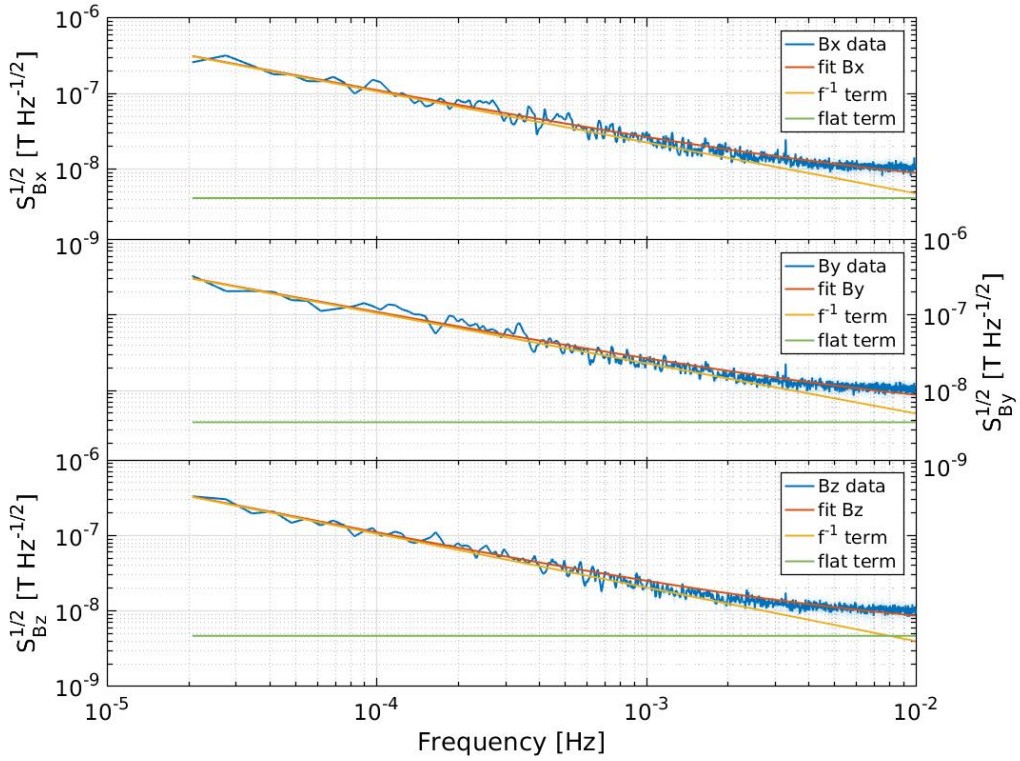

Figure 43: Fits of the ASD of the magnetic field components (from top to bottom, x, y and z axis respectively) to a function of the type $a + b(2\pi f)^c$. The results from the fits are shown in Table 14. In blue we show the ASD of the magnetic field, and in red, the fit to it. The yellow line corresponds to the f^{-1} part of the function, and the green line to the flat part of the function.

Once we have these fits, to build our magnetic model we will only use the f^{-1} term, which comes from the IMF fluctuations, since the flat term contains the readout noise from electronics. Moreover, since this term comes from the IMF, it is completely correct to use it as the fluctuations of the magnetic field in the TM position, even if the measurements are taken at the magnetometers position. This is because over the small distances that can happen within the spacecraft, the IMF fluctuations can be considered not to change. This was proven in Figure 26 (bottom right), where we saw that all the magnetometers measurements for the same component are coherent at low frequencies.

Now it is the turn of the magnetic field gradient fluctuations. We will use the same data, the one from the February 2017 noise run (from 13 Feb'17 to 2 Mar'17), and fit it to a curve of the form $a + b(2\pi f)$. In this case, the relevant contribution for our model is the independent term, which gives us the flat line that would correspond to the IMF gradient fluctuations. Nevertheless, the values we are measuring are probably from the readout of the magnetometers, which are masking the magnetic field gradient fluctuations, which were expected to be an order of magnitude smaller. Therefore, from here on we will use this value as an upper limit of the interplanetary magnetic gradient fluctuations. In this contribution we get rid of the small increase that starts to happen below 0.1 mHz, which is probably coming from the readout noise. The results of the fit are shown in Figure 44 and again in Table 14. As mentioned in previous chapters, we have no way of building a gradient along z since all the magnetometers are in the same x-y plane. For posterior calculations, we will use the results from the gradient along y also for the gradient along z. Since the IMF gradient is very small and our magnetometers are only giving us upper limits for this value, this assumption is not completely crazy.

We can follow the same reasoning as with the magnetic field fluctuations, an use these fluctuations of the interplanetary magnetic field gradient at the TMs position even if they were taken between magnetometers. The only problem left here is that since we do not have magnetometers at different positions in the z-axis, we can not build a gradient of B_x along z. We will simply use the gradient along y also as the gradient along z, and since the gradient fluctuations are smaller than our readout simply continue saying that this will be their upper limit.

6.3 THE THERMISTORS MAGNETIC FIELD GRADIENT CONTRIBUTION

There is only one problem left to solve before we can give the contribution coming from magnetic field fluctuations to the fluctuations of Δg. Although using the magnetic experiments we estimated the gradient along x of B_x, for computing term 2 of Equation (6.6) we also need an estimation along y and z.

The principal contribution to the magnetic field gradient along the faces of the TMs is assumed to come (although we lack local measurements close to the TMs) from the Negative Temperature Coefficient (NTC) thermistors placed in the EH, which have a small remanent magnetic moment. The reader can see their dis-

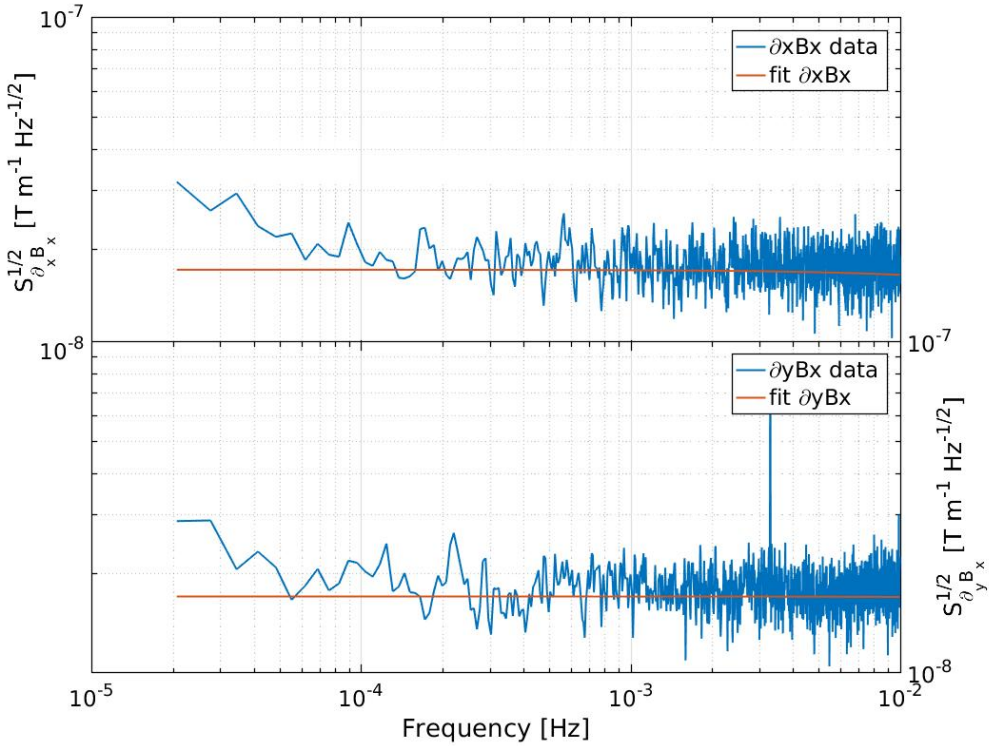

Figure 44: Fits of the ASD of the gradient of the magnetic field along x (top figure) and along y (bottom figure) to a function of the type $a + b(2\pi f)$. The results from the fits are shown in Table 14. In blue we show the ASD of the magnetic field, and in red, the fit to it.

tribution in Figure 45. Although producing a smaller magnetic field than many other components within the spacecraft, the proximity to the TMs makes them specially relevant. Their impact has been deeply analysed in several studies [137, 138, 140].

The main problem with these sensors is that the magnetic field gradient they produce depends heavily on the orientation of the parallel and transverse contributions of the magnetic dipole they form, and we do not know their exact orientation. As we show in Figure 46, the magnetic field gradient of B_x along x is maximised when the NTC transverse magnetic moments are aligned in opposite directions, with a potential value of -11300 nT m^{-1}. On the other side, the magnetic field gradient of B_x along z is maximised when the NTC parallel magnetic moments are aligned in opposite directions, with a potential value of 14500 nT m^{-1}. Anyway, these values are worst cases, and are highly unlikely to be so big. The sensors went into a degaussing procedure and an exact alignment like the ones shown in Figure 46 is highly unlikely as well.

The value we will use for for $\nabla_x B_{x,\text{back.}}$ is -3700 ± 2600 nT m^{-1}, which was estimated in Chapter 5. In the next section we will discuss more in depth why we choose this solution over the other coming from the solution of the 2nd order equation, but for now let's continue with the analysis. This value represents a 32.7% of the worst case shown in the right part of Figure 46. Since we have

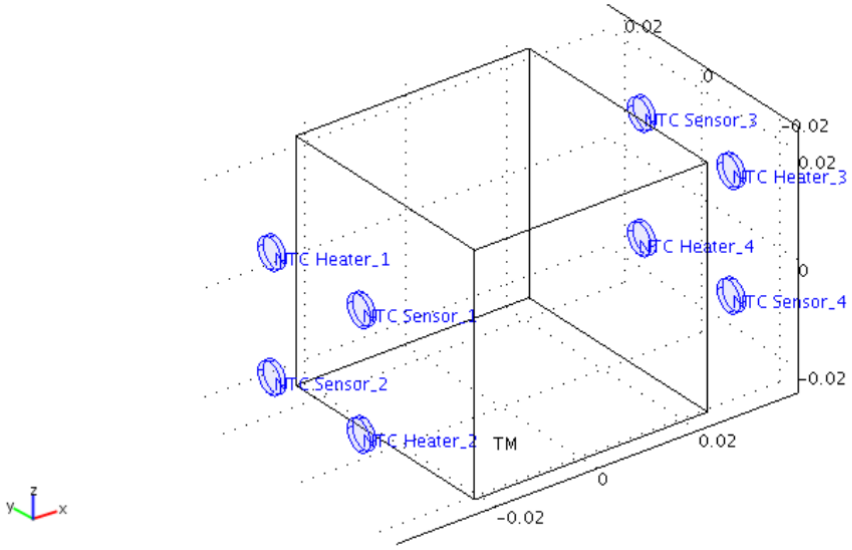

Figure 45: Layout of the different NTC thermistors around the TMs Credits: [140].

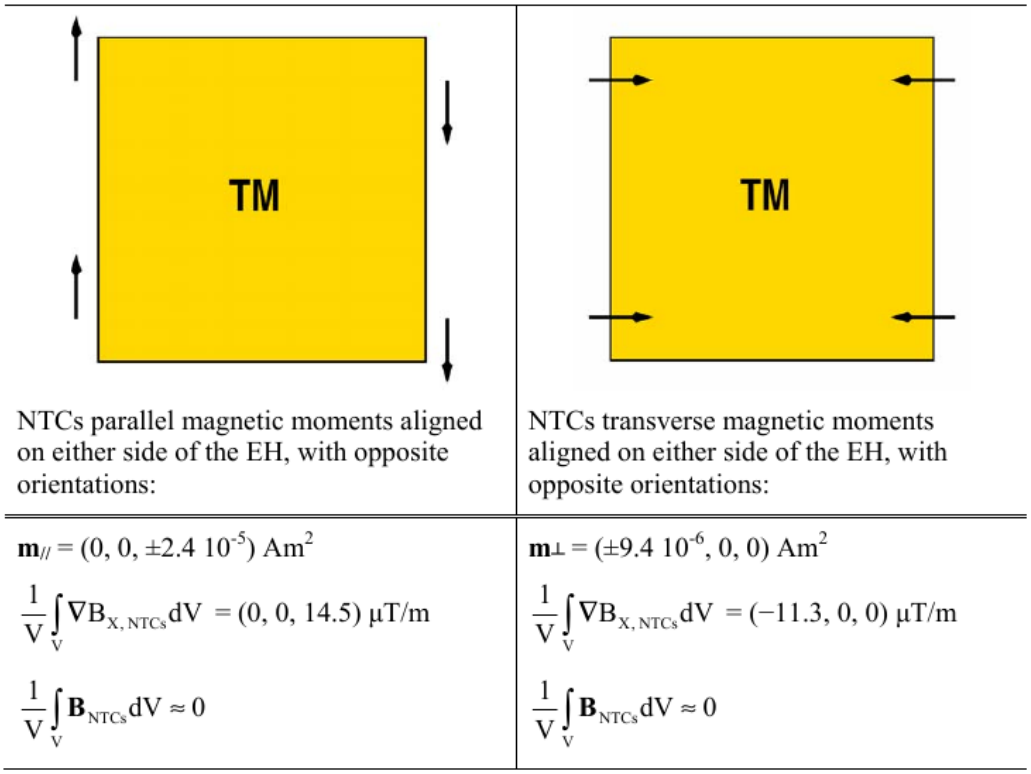

Figure 46: Scheme showing the configuration of maximum x-component magnetic field gradient along x (left figure) and along z (right figure). The figure also shows the respective magnetic moment of the thermistor in each case, as well as the values of the gradient for each configuration. Notice that in the case of maximum magnetic field gradient, the magnetic field is zero (Credits: [138]).

no idea of what $\nabla_z B_{x,\mathrm{back.}}$ can be, only the worst case shown in the left part of Figure 46, we will do a guess here and say this value will represent a 32.7% of the worst case too, like in the gradient along x. If we assume that, the value of

$\nabla_z B_{x,back.}$ will be 4742 nT m^{-1}. We will also assign the same error of $\nabla_x B_{x,back.}$ to this value, which was ± 2600 nT m^{-1}.

Regarding the gradient along y of B_x, the thermistors have no contribution to it (see [137, 138, 140] for more information about this), so we will simply use the gradient of B_x calculated between magnetometers PY-MY during February 2017 noise run (from 13 Feb'17 to 2 Mar'17). Therefore, the values we will use for the magnetic gradient of B_x are:

$\nabla_x B_{x,back.}$ [nT m^{-1}]	$\nabla_y B_{x,back.}$ [nT m^{-1}]
-3700 ± 2600	-29.880 ± 0.006
$\nabla_z B_{x,back.}$ [nT m^{-1}]	$\lvert\boldsymbol{\nabla} B_{x,back.}\rvert$ [nT m^{-1}]
4742 ± 2600	6015 ± 3700

Table 15: Values that will be used for $\boldsymbol{\nabla} B_{x,back.}$ for posterior calculations.

6.4 MAGNETIC CONTRIBUTION TO LPF TEST MASSES RELATIVE ACCELERATION

Before moving to compute the contribution of the magnetic field (and its gradient) fluctuations to the Δg ASD we can do a first check and see how accurate are the values we estimated in Chapter 5. We will do so by adjusting the Δg time-series to the computed force during a magnetic injection with the coil.

The force exerted along the x-axis on a TM during an applied AC magnetic field was given by Equation (3.24a). Let's write it down here again, directly not considering the 2nd order terms that can be neglected due to the axial symmetry of the system (if the reader does not remember why we could neglect those terms, see again Section 5.3):

$$F_x = F_{DC,x} + F_{1\omega,x} + F_{2\omega,x} = \tag{6.7a}$$

$$= V\left[\langle M_{r,x} \cdot \nabla_x B_{o,x}\rangle + \frac{\chi}{\mu_0}\left(\langle B_{o,x} \cdot \nabla_x B_{o,x}\rangle + \frac{1}{2}\langle B^{AC}_{i,x} \cdot \nabla_x B^{AC}_{i,x}\rangle\right)\right] \tag{6.7b}$$

$$+ V\sin(\omega t)\left[\langle M_{r,x} \cdot \nabla_x B^{AC}_{i,x}\rangle + \right.$$

$$\left. + \frac{\chi}{\mu_0}\left(\langle B_{o,x} \cdot \nabla_x B^{AC}_{i,x}\rangle + \frac{1}{2}\langle B^{AC}_{i,x} \cdot \nabla_x B_{o,x}\rangle\right)\right] \tag{6.7c}$$

$$- \frac{V\cos(2\omega t)}{2}\left[\frac{\chi}{\mu_0}\langle B^{AC}_{i,x} \cdot \nabla_x B^{AC}_{i,x}\rangle\right] \tag{6.7d}$$

where, remember that $B_{o,x} = B_{x,back.} + B^{DC}_{i,x}$ and $\nabla_x B_{o,x} = \nabla_x B_{x,back.} + \nabla_x B^{DC}_{i,x}$. The parameters we estimated in Chapter 5 are: χ, $M_{r,x}$, $B_{x,back.}$ and $\nabla_x B_{x,back.}$. The parameters V and μ_0 are constants, and we can estimate the magnetic field (and its gradient) created by the coils at the TM position following Equation A.6 shown in Appendix A (parameters $B^{DC}_{i,x}$, $B^{AC}_{i,x}$, $\nabla_x B^{DC}_{i,x}$, $\nabla_x B^{AC}_{i,x}$). Therefore, we

already have all the terms needed to compute the magnetic force during a coil injection and plot it over the time-series of the force between the masses ($\Delta g.m_{TM}$). The values we used are gathered in Table 16 for an easier comparison, and the results shown in Figure 47.

Parameter	Value	Parameter	Value
$\chi_{r,DC}$	$(-2.99 \pm 0.08) \times 10^{-5}$	$B_{x,back.}$	150 ± 80 [nT]
$\chi_{r,1\omega}$	$(-3.03 \pm 0.01) \times 10^{-5}$	$\nabla_x B_{x,back.}$	-3700 ± 2600 [nT m^{-1}]
$\chi_{i,1\omega}$	$(-0.24 \pm 0.08) \times 10^{-8}$	$M_{r,x}$	-0.57 ± 0.02 [nA m^2]
$\chi_{r,2\omega}$	$(-3.30 \pm 0.01) \times 10^{-5}$		

Table 16: Values that will be used for the calculation of the Δg disturbances by magnetic forces. They were all obtained in Chapter 5.

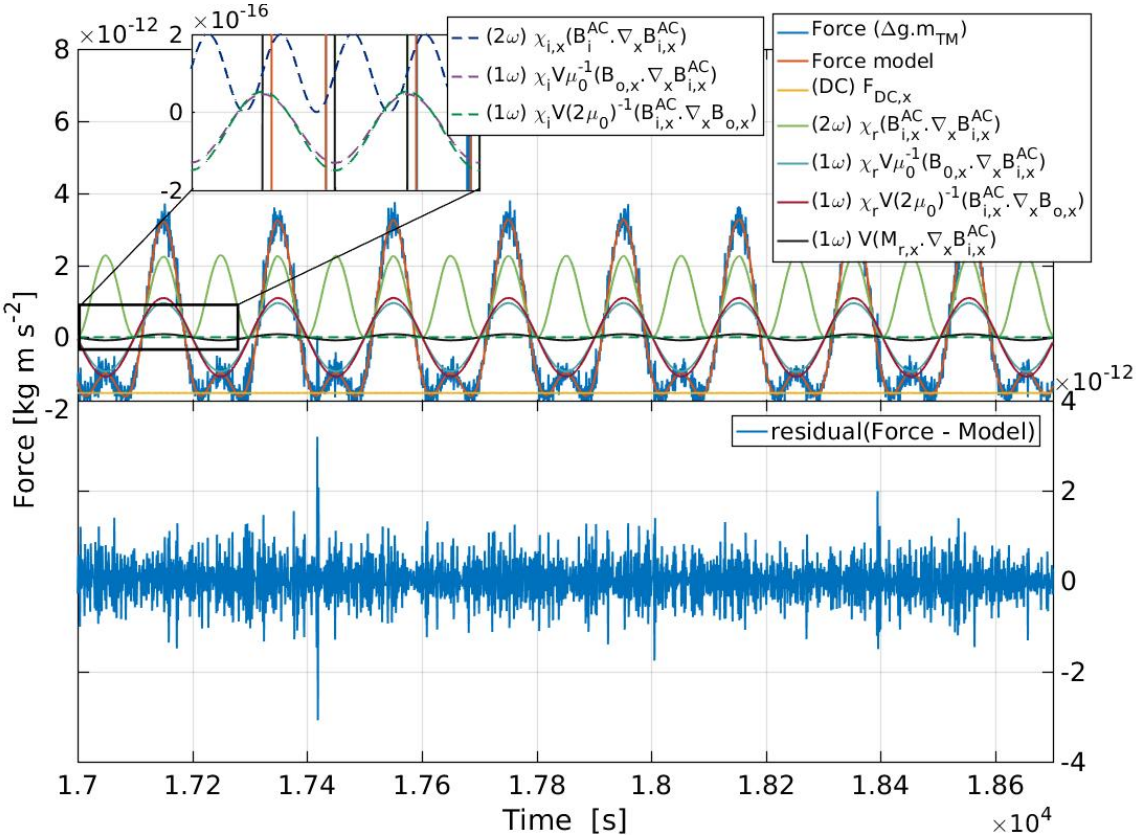

Figure 47: Magnetic model force plotted over the measured force ($\Delta g.m_{TM}$) during the magnetic injection on DOY 170 corresponding to I^{DC}=0.75 mA and I^{AC}=1.5 mA. In the upper figure, in blue, we show the data corresponding to the force time-series, while in red, we show the model of the force produced over the TMs by magnetic effects. In different colours we show the different terms of the model. In a zoomed area we show the contribution coming from the imaginary component of the magnetic susceptibility. In the lower figure, we show the residual resulting from subtracting our model to the data. See the text for more details about this figure.

Figure 47 contains a lot of information, so let's explain its contents in depth. In the upper figure, in blue we can see a portion of the time-series of the force exerted on the TM during the coil injection on June'18, 2016 (DOY170), with I^{DC}=0.75 mA and I^{AC}=1.5 mA. This contains the standard Δg plus the force caused due to the magnetic injection. Over it, in red, is our model built from Equation (6.7a). In different colours are shown the different contributions to the model, and for each, indicated in the legend between brackets, is indicated if the terms belongs to the DC, 1ω or 2ω term, for an easier comparison. In a smaller subplot, there is a zoomed area to distinguish the contribution of the terms coming from the 1ω imaginary susceptibility term, with its corresponding legend. Finally, in the lower figure, we can see the residual from the upper figure, i. e., the result of subtracting the model from the data.

Figure 47 yields very interesting results. Even without being a fit, the model adjusts well to the data, giving a white noise residual. This indicates that the values we estimated in Chapter 5 should be quite accurate, and that our model works nicely. Here we have checked that by applying the correction explained in Section 5.4 the model adjusts better to the data, so this is a reason of why we have applied that calibration correction. Another important result we can see here, is that the contribution of the imaginary susceptibility is totally irrelevant when we want to compute contributions from magnetic effects to Δg, but we have included it in the plot to show how small it is compared to the other terms.

Finally, we have decided to use the pair of solutions shown in Table 16 for $B_{x,back.}$ and $\nabla_x B_{x,back.}$, and not the other pair (remember they come from a 2nd order equation solutions, so we had two pairs, check Section 5.5.2). The reasons to prioritise this pair of solutions over the other pair are:

- The value for the x component of the magnetic field estimated at TM1, 150 ± 80 [nT], is positive, as the measurements of magnetometer PX (around 800-900 nT), which is the closest magnetometer to this TM.
- The value chosen for $\nabla_x B_{x,back.}$ is -3700 nT m^{-1}, which is smaller and has the same sign as the worst case of -11400 nT m^{-1} predicted in [138].
- In a study made by industry before launch [139], after analysing all the possible sources of magnetic field within the spacecraft, the x component of the magnetic field predicted at TM1 was of 267 nT, and its gradient of -7575 nT m^{-1}. The selected pair of solutions are relatively close to these values.
- In a work also performed before launch [141], a value of 130 ± 20 nT for B_x at TM1 was predicted. In this study a Monte Carlo Markov Chain (MCMC) analysis was done using the information from all the magnetic field sources within the spacecraft. Although the model used was not very realistic for the gradient, it was better for the magnetic field, and the similitude between both results strengthens our estimations.

These four reasons made us select the mentioned pair of solutions over the other pair, and we will keep using them for the estimation of the magnetic contribution to Δg fluctuations.

6.5 MAGNETIC CONTRIBUTION TO LPF TMS RELATIVE ACCELERATION FLUCTUATIONS

We are finally ready to give the magnetic contribution to the fluctuations of Δg, which is the principal aim of this work. In Equation (6.6) we showed which was the model we are going to use to compute the contribution, and in Section 6.2, Section 6.3 & Section 6.4 we computed/indicated all the different terms we are going to use in the model. Let's write it down here again the abbreviated version of the model:

$$\delta F_x = \underbrace{V(\mathbf{M_r}\cdot\delta\boldsymbol{\nabla}B_x)}_{\text{term1}} + \underbrace{\frac{\chi V}{\mu_0}(\delta\mathbf{B}\cdot\boldsymbol{\nabla}B_x)}_{\text{term2}} + \underbrace{\frac{\chi V}{\mu_0}(\mathbf{B}\cdot\delta\boldsymbol{\nabla}B_x)}_{\text{term3}} \tag{6.8}$$

The three terms in Equation (6.8) will form the magnetic contribution to Δg fluctuations. On the one hand, terms 1 and 3 will be flat, since they are based in the fluctuations of the IMF gradient. On the other hand, term 2 will follow a f^{-1} curve, since it follows the fluctuations of the interplanetary magnetic field. In Figure 48 we show the three contributions of the model. We can clearly observe that the most important contribution comes from term 2, and for the frequency range we are interested in (below the mHz), the contributions from terms 1 & 3 can be neglected.

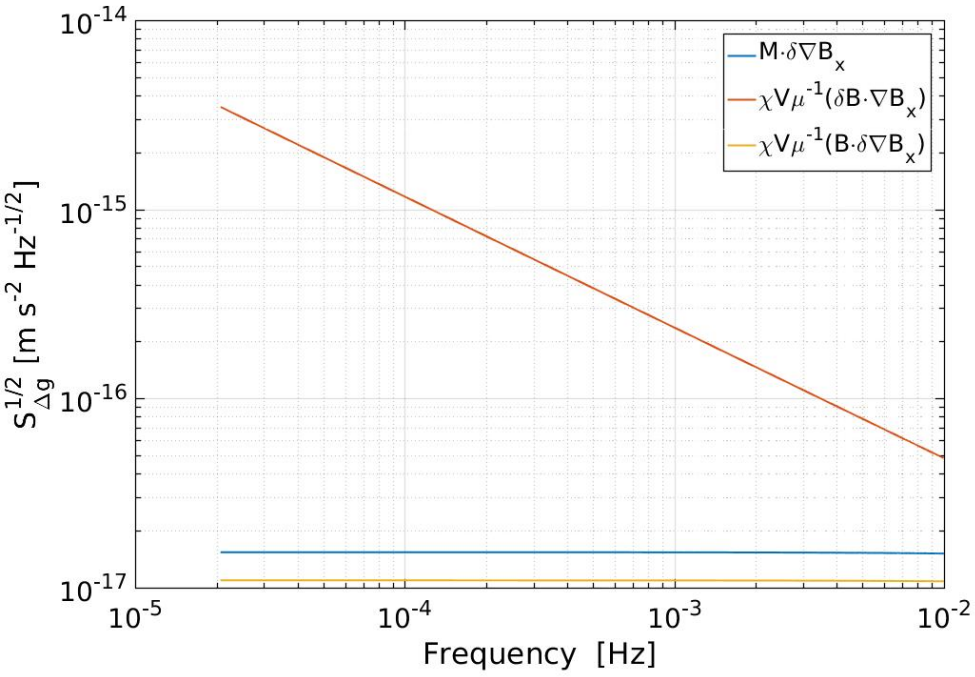

Figure 48: Comparison of the different terms of the magnetic effects contribution to Δg fluctuations. The terms correspond to Equation 6.8 terms: term 1 is shown in blue, term 2 in red and term 3 in yellow.

We will now plot the combination from all, i.e., our magnetic model, in front of the Δg from February 2017 noise run (from 13 Feb'17 to 2 Mar'17). The result

is shown in Figure 49. In blue, we show the fluctuations of Δg, which has been computed using the methods (for the solid line and for the dots) explained in Section B.1. The red line corresponds to the magnetic fluctuations contribution to Δg fluctuations, according to the model that Equation (6.8) describes. The red shadowed areas account for the uncertainty in the estimation, in a 68% (1σ), 95% (2σ) and 99.7% (3σ) confidence intervals. These intervals are built combining the uncertainty in the estimation of the magnetic field gradient along x $\boldsymbol{\nabla} B_x$ with the low frequency fluctuations of the IMF PSD. The uncertainty in the estimation of other parameters like χ or $\mathbf{M_r}$ are not comparable to the uncertainty in the estimation of the gradients. Besides, from Equation (6.8) and Figure 48 it is clear they do not have such a high impact, so we can safely neglect it.

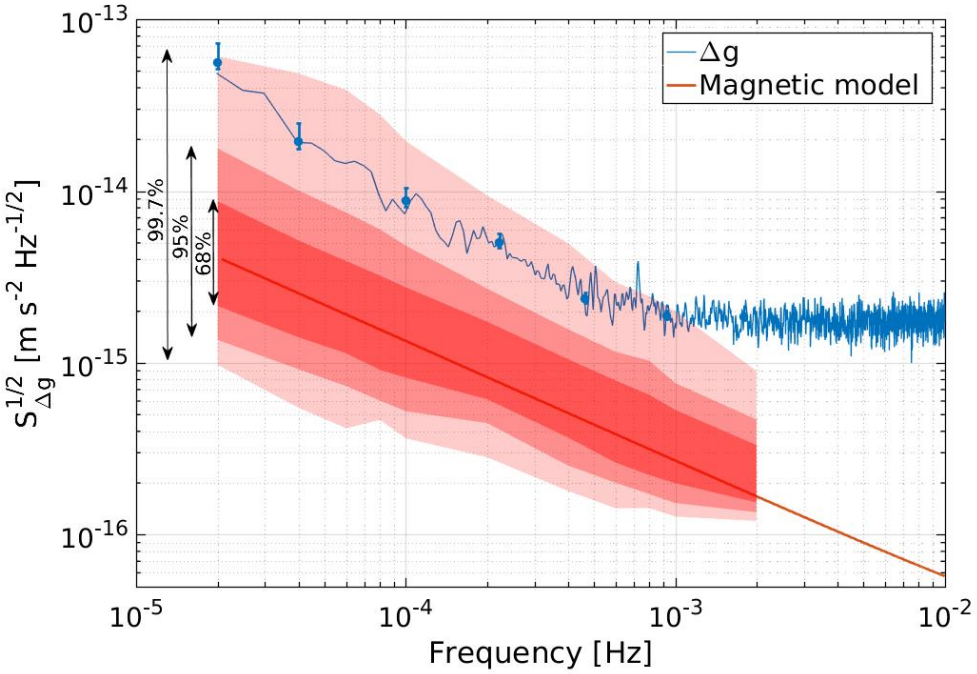

Figure 49: Contribution coming from magnetic field and magnetic field gradient fluctuations to Δg fluctuations. In blue, we show the ASD of Δg for February 2017 noise run. In the red solid line, we show the model estimating the contribution from magnetics to the blue curve. During mission operations, the red solid line moves within the red shadowed area due to the non-stationarity of the low-frequency IMF. There are three red shadowed areas, corresponding to 68% (1σ), 95% (2σ) and 99.7% (3σ) confidence intervals. See text for more details about this plot, like which errors carry the shadowed areas and how they are built.

In Section 4.4, we saw how the IMF fluctuations are not stationary, and how they relate to solar weather parameters like the solar wind speed. To account for this effect in the estimation of the magnetic contribution to Δg fluctuations, we have performed the following analysis. We have taken the time-series of the magnetometers for the whole mission. Next, we divide it in segments of 16 hours, and for each of these windows, we compute the ASD of the IMF at some selected

frequency bins. We start in the bin between 10-30 μHz, so we get a point at 20 μHz, then in the bin between 30-50 μHz, so we get a point at 40 μHz, and so on until we arrive to 20 mHz. We do not go above this frequency because at this point the readout noise from the magnetometers starts to dominate the spectrum, and we are not seeing the IMF fluctuations anymore. After this analysis, we end up having, for each of these frequency bins, a series of values of how the IMF ASD evolved during the mission lifetime. If we plot them, we would get similar results to the ones shown in Figure 28, but for more frequency bins. Instead, for the series of each frequency bin, we will compute the 0.15th, 2.3th, 16th, 50th, 84th, 97.7th and 99.85th percentiles. This way, with the 50th percentile we are obtaining the median of the IMF ASD observations, which matches the red solid line in Figure 49.

Since we want to account for the variability of the IMF at low frequencies, we will use the other computed percentiles to that end. From the 16th & 84th percentiles we get a 68% (or 1σ) confidence interval, which means that 68% of the time during mission operations the magnetic contribution coming from the magnetic field and gradient fluctuations are in this range (remember these confidence intervals also include the uncertainty in the estimation of the gradient of the magnetic field along x ∇B_x). From the 2.3th & 97.7th percentiles we get a 95% (or 2σ) confidence interval, while from the 0.15th & 99.85th percentiles we get a 99.7% (or 3σ) confidence interval.

68% (1σ) confidence interval			
[fm s^{-2} $Hz^{-1/2}$]	20 μHz	0.1 mHz	1 mHz
Upper bound	8.73	2.75	0.53
Median	4.03	1.31	0.27
Lower bound	2.15	0.82	0.20
95% (2σ) confidence interval			
[fm s^{-2} $Hz^{-1/2}$]	20 μHz	0.1 mHz	1 mHz
Upper bound	17.76	4.81	0.76
Median	4.03	1.31	0.27
Lower bound	1.36	0.52	0.15
99.7% (3σ) confidence interval			
[fm s^{-2} $Hz^{-1/2}$]	20 μHz	0.1 mHz	1 mHz
Upper bound	69.92	19.54	2.18
Median	4.03	1.31	0.27
Lower bound	0.98	0.36	0.13

Table 17: Selected values at some key frequencies from Figure 49. Here we show the most recurrent value (median) and the upper and lower bounds from the magnetic model, for three different confidence intervals.

With the previously explained method, we have accounted for the variability of the IMF fluctuations in the estimation of the magnetic contribution to Δg fluctuations. This gives an idea of how this contribution does not stay fixed, but instead varies in time within the shadowed areas (for bigger confidence intervals, the shadowed area widens, while it narrows for smaller confidence intervals) depending on the solar weather parameters.

The results obtained in Figure 49 are quite consistent with on-ground expectations. In Table 17 the reader can check the exact values of the magnetic contribution to Δg fluctuations for some key frequencies, with the corresponding upper and lower bounds and for the three confidence intervals shown in Figure 49. These results show that due to the fluctuations of the IMF, the magnetic contribution to Δg does not stay fixed. We created the red solid line in Figure 49 with the most recurrent values (the median) of the IMF ASD, but it is important to remember that this contribution is not stationary, it fluctuates within the red shadowed region (for bigger confidence intervals, it widens). Also, it is worth stressing that these shadowed areas (or confidence intervals) include the uncertainty in the estimation of the gradient of the magnetic field along x $\boldsymbol{\nabla} B_x$. If we had very precise measurements of them, the confidence intervals would narrow quite a lot, but there would still be an interval, since we can not get rid of the variability of the IMF ASD, it is an effect related to solar physics.

In LPF first results [4], an upper limit of 3 fm s^{-2} $Hz^{-1/2}$ at 0.1 mHz was established for the magnetic field contribution, which is above the median value from our model, and between the 1σ and 2σ confidence intervals for a situation of a high contribution from the interplanetary magnetic field ASD. Our median results are also well below the requirements established before launch, which placed a limit of 12 fm s^{-2} $Hz^{-1/2}$ at 1 mHz. Previous on-ground studies established that at 1 mHz the contribution from magnetic effects would be of 2.8 fm s^{-2} $Hz^{-1/2}$ at 1 mHz and 16 fm s^{-2} $Hz^{-1/2}$ at 0.1 mHz [91], and in a study made by industry [139], the contribution at 1 mHz was estimated at 4 fm s^{-2} $Hz^{-1/2}$. Notice the difficulty of comparing our results at low frequencies (at 0.1 mHz and below) with previous studies. This is mainly because before obtaining LPF first results, it was not expected that the satellite would perform so well at low frequencies.

6.6 OTHER POSSIBLE SOURCES OF MAGNETIC NOISE

In this section we will perform a short assessment of other possible magnetically induced noise sources appearing within the measurement bandwith. Apart from the forces described in Chapter 3, here we will include other possible noise sources as the Lorentz Force, down-converted AC magnetic fields or the appearance of discrete AC magnetic field lines.

6.6.1 *Lorentz Force*

A charged particle q moving through an electro-magnetic field with velocity v experiences a force given by [101]:

$$\mathbf{F}_{\text{lorentz}} = q(\mathbf{E} + \beta \times \mathbf{B}) \tag{6.9}$$

where $\beta = v/c$, and **E** & **B** are the electric and magnetic field, respectively. In the LPF case, the satellite is moving through the IMF. First, we should obtain the electromagnetic field in the rest frame. To this end, we will use the Lorentz transformation in order to translate the interplanetary fields to the spacecraft frame. The general transformation stands that to transform the fields from a system S to S′, which moves at a velocity v relative to S, we can write [101]:

$$\mathbf{E}' = \gamma(\mathbf{E} + \beta \times \mathbf{B}) - \frac{\gamma^2}{\gamma^2 + 1}\beta(\beta \cdot \mathbf{E}) \tag{6.10a}$$

$$\mathbf{B}' = \gamma(\mathbf{B} - \beta \times \mathbf{E}) - \frac{\gamma^2}{\gamma^2 + 1}\beta(\beta \cdot \mathbf{B}) \tag{6.10b}$$

where $\gamma = 1/\sqrt{1 - |\beta|^2}$. The speed of LPF satellite is around 30 km/s, and thus, $\beta \sim 10^{-4}$. Therefore, γ is very close to 1, and we can approximate that:

$$\mathbf{E}' \simeq \gamma(\beta \times \mathbf{B}) \tag{6.11a}$$

$$\mathbf{B}' \simeq \gamma(\mathbf{B}) \tag{6.11b}$$

Hence, the Lorentz force ends up being:

$$\mathbf{F}_{\text{lorentz}} = q(\mathbf{E}' + \beta \times \mathbf{B}') \simeq \gamma\beta \times \mathbf{B} \tag{6.12}$$

The IMF fluctuations causes a fluctuating force on the TM. However, now the IMF is seen as an electric field, which is shielded by the EH and inertial sensors surrounding the masses, and represented by α_S, which has a value of $\alpha_S \simeq 10^{-2}$ [139]. The magnetic fluctuations affect both TMs at the same time, however, a different differential acceleration will appear due to the different charge on each TM. If we assume the charge has the same sign on each TM, the maximum differential acceleration will be obtained when one mass has zero charge and the other one maximum charge Q. In this worst case scenario, the acceleration noise produced by this effect can be computed as:

$$\delta a_{\text{Lorentz}} = \frac{\gamma Q \beta S^{1/2}_{B_{\text{IMF}}}}{m_{\text{TM}} \alpha_S} \tag{6.13}$$

At the end of the section we will give numbers to this contribution using the previous equation and compare it to the other noise sources.

6.6.2 *Down-converted AC magnetic fields*

As we saw in Section 6.1, the force fluctuations on the TM (on the x-axis) due to the coupling of the TMs remanent magnetic moment $\mathbf{M_r}$ and magnetic susceptibility χ with the magnetic field and magnetic field gradient is given by:

$$\delta F_x = V(\mathbf{M_r} \cdot \delta\boldsymbol{\nabla} B_x) + \frac{\chi V}{\mu_0}(\delta\mathbf{B} \cdot \boldsymbol{\nabla} B_x) + \frac{\chi V}{\mu_0}(\mathbf{B} \cdot \delta\boldsymbol{\nabla} B_x) \tag{6.14}$$

From the previous equation, it can be seen that if the time dependent part of the magnetic field has a sinusoidal form, a low-frequency magnetic field can be generated if we mix two or more higher-frequency AC magnetic fields that have frequencies close together. Unfortunately, in LPF the magnetometers measurement bandwidth was limited to low frequencies, and they were not capable of measuring high-frequency magnetic fields above the Hz, so there was no way of estimating them on-board, although some studies are on-going for the design of a high-frequency magnetic field sensor for LISA using magnetic coils similar to the ones in LPF [142]. Therefore, we will only use the measurements performed on on-ground testings and reported in [139] in order to assess this contribution to the budget.

In Figure 50 we show the on-ground estimated magnetic field at high frequencies after the measurements of the high frequency magnetic field emitted by different units in the spacecraft and reported in [139]. In [143], it was calculated that for the down-conversion calculations, a magnetic field linear spectral density was modelled as the following filter:

$$B(\omega) = B_0 \left(\frac{(1 + i\omega\tau_i)}{i\omega\tau_i(1 + i\omega\tau_0)} \right) \tag{6.15}$$

which corresponds to a field PSD of:

$$PSD_B(\omega) = B_0^2 \left(\frac{(1 + \omega^2\tau_i^2)}{\omega^2\tau_i^2(1 + \omega^2\tau_0^2)} \right) \tag{6.16}$$

where τ_i and τ_0 correspond to the breakpoints of the magnetic field spectrum at high frequencies. If we follow the predicted high-frequency magnetic field shown in Figure 50, the spectrum can be described as a f^{-1} spectrum below a first break point $f_i = 20$ Hz, a short plateau of magnitude $B_0 = 0.25$ nT $Hz^{-1/2}$ from 20 Hz to the second break-point $f_0 = 250$ Hz, and then rolling off as f^{-1} above f_0. Therefore, τ_i & τ_0 will correspond to f_i & f_0, respectively.

Taking all the above considerations, the low-frequency tail of this acceleration noise on a TM is constant and can be shown to be [143]:

$$\delta a_{\text{down-AC}} = \left(\frac{V}{\mu_0 l_0 m_{TM}} \right) B_0^2 \sqrt{\frac{\tau_0\tau_e(\tau_0^2 + 3\tau_0\tau_e + \tau_e^2) + \tau_i^2(2\tau_0\tau_e + \tau_i^2)}{2\tau_0(1 + (\frac{\tau_0}{\tau_e}))^3\tau_i^4}} \tag{6.17}$$

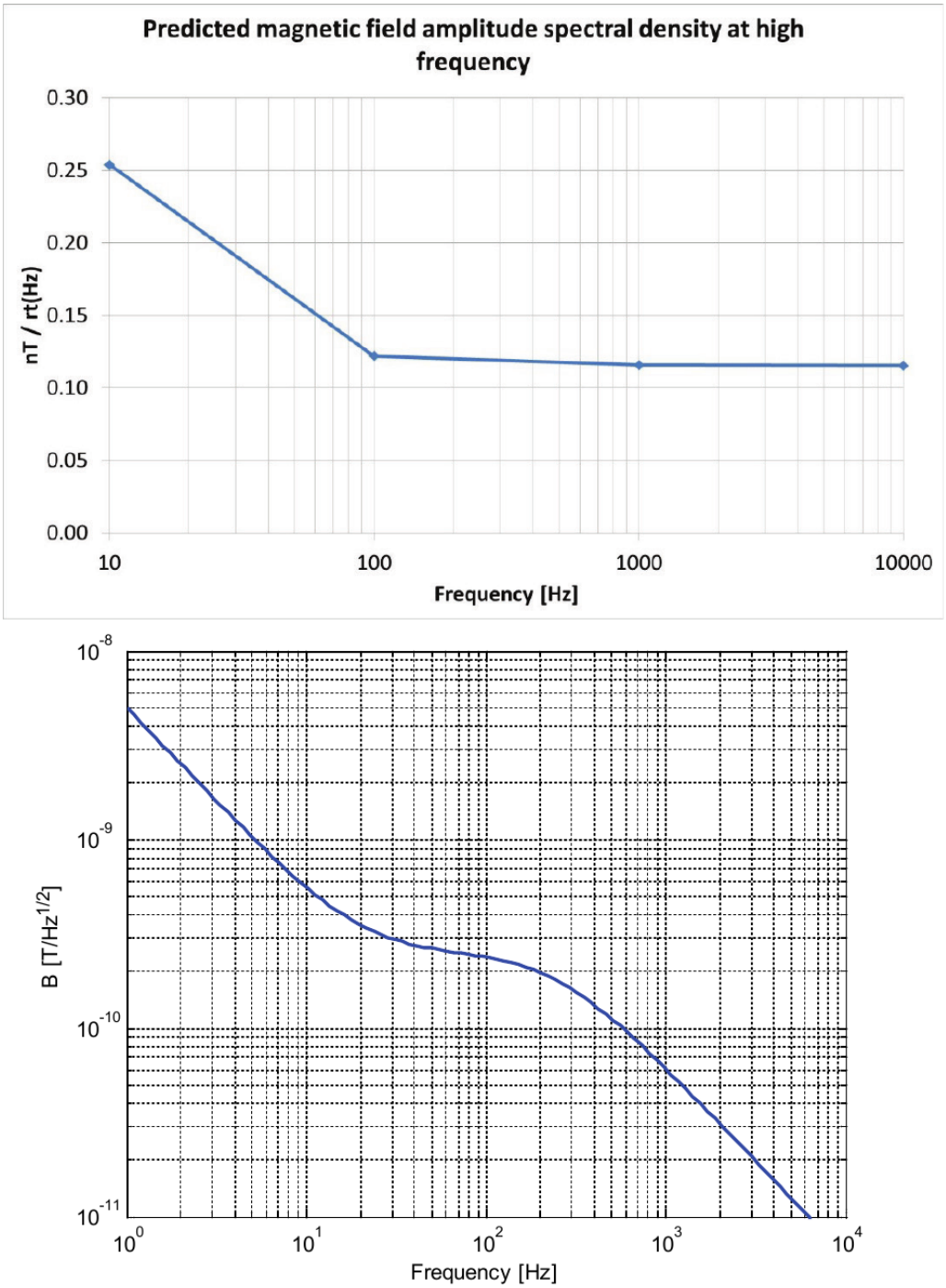

Figure 50: *Top:* On-ground estimations for the high-frequency magnetic field on LPF .*Bottom:* Same predictions as in upper figure, but taking into account the attenuation of the magnetic field due to the shielding of the EH and vacuum enclosure at high frequencies. (Credits: [139])

where $l_0 = 3.5$ m is the characteristic length, which is the length used to convert magnetic field values into magnetic field gradients when the source of field and gradient are correlated. τ_e corresponds to the roll-off frequency of the TMs, which was measured on-ground [110] to be $\tau_e = (2\pi\, 630)^{-1}\text{Hz}^{-1}$.

6.6.3 *AC Discrete Lines*

In practice, the operation of most units within the spacecraft resulted in discrete spectral lines, rather than a continuous noise spectral density. The low frequency amplitude modulation of high frequency discrete lines could result in acceleration noise at low frequencies.

Like we just explained in the previous section, since LPF magnetometers could not measure high frequency magnetic fields, the numbers shown in this section are coming from [139]. In [144], the following expression was derived (and later modified in [139]) for the low frequency acceleration noise along x, induced by the worst case amplitude modulation of a single discrete magnetic field line on a single TM:

$$\delta a_{\text{AC-lines}} = \frac{2}{m_{TM}} \frac{3|\chi_r| V B_o^2}{\mu_0 r} 8 \tag{6.18}$$

where $m_{TM} = 1.96$ kg is the mass of the TM, r is the distance from the TM to the emitting source, χ is the frequency dependent magnetic susceptibility, V the TM volume and B_0 the Root Mean Squared (RMS) amplitude of the magnetic field line. Here, a series of assumptions have been made:

- The distance between the TM and the emitting source is taken as $r = 0.3$ m, which is the minimum possible distance between the TM and a source.
- The offending sinusoidal field is at a frequency where $|\chi_r| \sim 1$.
- There is no shielding effect from the EH and vacuum enclosure.

Taking into account the above expression and assumptions, it was possible to estimate the acceleration noise from high frequency AC lines from test results where these lines were measured. These measurements were performed in an on-ground study and reported in [139].

6.6.4 *Other noise sources summary*

In Table 18 we show a summary of the contribution from the effects explained in Section 6.6 to Δg at 1 mHz. None of the values are too important to the contribution, with maybe the exception of AC discrete lines, that with 0.78 fm s^{-2} $Hz^{-1/2}$ is close to the upper bound of 0.76 fm s^{-2} $Hz^{-1/2}$ at the 2σ confidence interval shown in Table 17. Nevertheless, that value for AC discrete lines is based on worst case expectations and on-ground measurements, while the upper bounds of our model are quite high due to the uncertainty in the estimation of the magnetic field gradients. Therefore, this contribution was probably not as high during mission operations, but since we had no high frequency magnetic field measurements we can not be completely sure.

	[fm s^{-2} $Hz^{-1/2}$]
Lorentz Force	0.01
Down converted AC fields	0.10
AC discrete lines	0.78

Table 18: Contribution at 1 mHz from the noise sources described in Section 6.6. The data used to obtain these values is coming from [139].

7 CONCLUSIONS

In this work, we have studied in depth the magnetic field on-board LPF and its effects on the TMs. More specifically, we have analysed the evolution of the magnetic field and its fluctuations, we have analysed the magnetic experiments carried on-board to estimate the magnetic properties of the TMs, and combining all the information gathered, we have given a contribution from magnetic effects to the differential force per unit mass (or Δg) fluctuations.

In Chapter 4 we provided a complete description on the magnetic field on-board the satellite during the mission duration thanks to the measurements of the magnetometers on-board. They provided very valuable measurements for the mission and achieved all the requirements. Regarding the magnetometers measurements, we saw how their DC measurement was dominated by the magnetic field created by the different satellite components, which created a magnetic field between $2-3$ orders of magnitude higher than the IMF. We have also seen how the magnetic field evolved during the mission lifetime, and how it was affected by the change in the propulsion system that happened between the switches from LTP to ST7-DRS operations. In terms of magnetic field stability, we observed that the magnetic field ASD measured by our magnetometers was dominated by two contributions. On the one hand, below the mHz, the IMF dominates the ASD, since all the magnetometers fluctuate coherently along the same axis and the values coincide with measurements from other space missions like ACE, which are also orbiting around L1. On the other hand, above the mHz, the readout noise from the electronics masked the contribution from the IMF, and did not allow us to measure anything above the mHz. Finally, we observed the non-stationarity of the low frequency magnetic field fluctuations, which was related to the dynamics of the solar wind. This effect implied that, at 20 μHz, the ASD of the magnetic field affecting the TMs could change from 170 nT $Hz^{-1/2}$ (for a slow wind situation) to 750 nT $Hz^{-1/2}$ (for a fast wind situation).

Following the analysis, in Chapter 5 we performed a deep study of the magnetic experiments carried on-board the satellite. We saw how coil #2 showed a malfunctioning, and therefore, most of the experiments were carried out with coil #1. That means that most of the results obtained from the analysis of the experiments are for TM1 only. The magnetic experiments consisted in injecting an electric current through the coil to induce a controlled and known magnetic field in the TMs position. Since the magnetic field and its gradient couple with the remanent magnetic moment and magnetic susceptibility of the TMs, this created a force on the TMs. This way, analysing the resulting movement of the TMs, we could extract the magnetic parameters that rule their dynamics. As explained in Chapter 3, three different forces appeared in the presence of an AC magnetic field – like the ones we generated in the experiments with the coils. A force that oscillates at 2 times the frequency of the injected field $F_{2\omega}$, that gave us informa-

tion about the magnetic susceptibility. A force oscillating at the frequency of the injected field $F_{1\omega}$, which gave us information about the magnetic susceptibility and the remanent magnetic moment. And finally, a DC force F_{DC}, which gave us information about the two previous parameters too but also about the background magnetic field and magnetic field gradient along the x-axis.

The results from the experiments gave us estimations about the remanent magnetic moment $\mathbf{M_r}$, the magnetic susceptibility χ, the background magnetic field along x $B_{x,back.}$ and its gradient $\nabla_x B_{x,back.}$. Regarding the estimation of the remanent magnetic moment, we obtained a value of $|M_r| = 0.85 \pm 0.02$ [nA m^2], which is below the on-ground estimations [136], which established a limit of $|M_r| < 4 \pm 1$[nA m^2]. Moreover, we could estimate its three components, and confirmed that the remament magnetic moment is isotropic, i.e., there was no preferred orientation. Regarding the magnetic susceptibility χ, we could measure its real component at different frequencies, saw its frequency dependence, and adjusted the measured values to the model based on the polarizability of a sphere coming from Vitale [109]. The measured values were around the -2.5×10^{-5} expected from on-ground estimations [133]. Moreover, we could measure the imaginary part of the magnetic susceptibility, which created forces of the order of tenths of fN. This was one the tiniest effects measured by LPF, and we were able to measure it thanks to the incredible precision of the system and from the analysis techniques used. At 1 mHz, its value was of -2.4×10^{-9}, around a factor 10^4 smaller than its real counterpart. Even though its effect is negligible compared to its real counterpart when computing the magnetic contribution to Δg fluctuations, it was a good achievement to measure such a tiny effect and confirm that it has a negligible effect on Δg. A downside about the results of the magnetic susceptibility is that we did not perform experiments at any frequency lower than 1 mHz, which is precisely the frequency band in which we are interested for potential magnetic disturbances in LISA. Finally, thanks to the DC force created by the magnetic injections, we could also estimate the background magnetic field and its gradient along x thanks to the knowledge we had from the system and from the other parameters. The estimated values were $B_{back,x} = 150 \pm 80$ [nT] & $\nabla B_{back.,x} = -3700 \pm 2600$ [nT/m]. These values agree with on-ground estimations and previous studies [139, 141], and specially, gave some insight about the problem with the magnetic field gradient created by the NTC thermistors [137, 138, 140]. The previous studies predicted a potential maximum value of -11300 nT m^{-1} for $\nabla_x B_{back.,x}$, but we had no clue about which value this parameter had between 0 and this upper limit. Nevertheless, there were several downsides. These estimations have high errors, since we are measuring the background magnetic field in a very indirect way, measuring DC forces, which is less accurate than measuring oscillating forces. Also, trough this method we can only estimate the background components in the axis joining the coil and the TM, i.e. along the x-axis. Finally, this method only give us the value of the background components during the magnetic injections, and is in no way a form of continuously monitoring it.

Although the magnetometers on-board provided valuable measurements that helped us in determining the contribution from the magnetic effects to Δg fluctu-

ations, we saw how their placement inside the satellite had some drawbacks. Due to their magnetic active core, they had to be placed far enough from the TMs in order for their own generated magnetic field to not interfere with the TMs geodesic motion. This prevented us from directly measuring the magnetic field at the TM position, and forced us to think of alternative methods. An even worse problem was not being able to measure the magnetic field gradient across the faces of the TMs. Due to the placement of the magnetometers, we could measure gradients between them along the x and y axis, but no along z, since they were all placed along the same x-y plane. However, these gradients were not representative of the magnetic field gradient along the faces of the TMs, which were likely to be dominated by the contribution of the NTC thermistors. These gradients, however, are a key input to the magnetic contribution to Δg, as we saw in Chapter 6. All the previous reasons arise the importance of designing and improved magnetic diagnostics system for LISA, which should be capable of measuring the magnetic field closer to the TM and to measure magnetic field gradients, which is a key contribution to the magnetic effects affecting Δg.

In Chapter 6, we gathered the information and the values estimated in the previous two chapters to create a model which calculates the contribution from magnetic effects to Δg. We first used the estimated values from Chapter 5 to calculate the magnetic force created during a magnetic injection and plot it over the time-series of Δg. The result was very good, the model adjusted well to the oscillations created by the coil injections in Δg, and the residual of subtracting the model from the data gave a white noise. With all the previous ingredients, we finally gave an estimation of the magnetic effects to the ASD of Δg, which is the principal aim of this work. The results, which included the error of the estimation in the magnetic field gradient and the non-stationarity of the IMF, gave a contribution of 4.03 fm s^{-2} $Hz^{-1/2}$ at 20 μHz, which could increase to a total of 8.73 fm s^{-2} $Hz^{-1/2}$ in a high solar wind speed situation (1σ confidence interval). At 0.1 mHz, the contribution is of 1.31 fm s^{-2} $Hz^{-1/2}$ and could increase to a total of 2.75 fm s^{-2} $Hz^{-1/2}$ in a for high solar wind speed situations (1σ confidence interval). Finally, at 1 mHz it accounts for 0.27 fm s^{-2} $Hz^{-1/2}$, which increases to a total of 0.53 fm s^{-2} $Hz^{-1/2}$ in a high solar wind speed situation (1σ confidence interval). These upper bounds increase if we take bigger confidence intervals (check Table 17 for the exact values). For the 1σ confidence interval, these results are below the upper limit of 3 fm s^{-2} $Hz^{-1/2}$ at 0.1 μHz, established at Armano et al. [4], and are well below the requirements, which putted a limit of 12 fm s^{-2} $Hz^{-1/2}$ at 1 mHz.

All the analysis and results obtained in this thesis are not only of great importance for understanding LPF, but can also be transferred to LISA. LISA is expected to perform an order of magnitude better than LPF, since LPF was a technology readiness mission, and therefore, the requirements were relaxed. As we saw in Chapter 6, the most important contribution from magnetics to Δg fluctuations comes from the coupling of the IMF fluctuations with the magnetic field gradient $\delta\mathbf{B} \cdot \boldsymbol{\nabla} B_x$. We have seen how, in LPF, the estimation of the magnetic field gradient was a very difficult task, since we could not directly measure it. It is therefore very important to design an improved magnetic diagnostics system that can esti-

mate directly the magnetic field gradient across the TM, for example by placing magnetometers in both sides of the GRS. Regarding the IMF fluctuations, we have to take into account that for LPF, we were measuring them at L1, which is a quite populated place by other satellites, and where the IMF has been well studied. Nevertheless, for LISA, we do not have information of how the IMF will behave in the orbits the satellites will follow. Considering also its non-stationarity at the frequency band at which LISA will work, it will be very important to keep a rigorous monitoring of the IMF fluctuations to be sure the magnetic effects do not disturb the LISA measurements. We should not forget that, in LPF, the "noise runs" were a couple of weeks long at most, while LISA will need to be in a similar configuration during months. This implies that the changes in the IMF could be of great importance for the success of the mission.

APPENDIXES

A

MAGNETIC FIELD PRODUCED BY LPF COILS

In this appendix we will explain in detail the calculations for computing the magnetic field and magnetic field gradient generated by the LTP coils from the DDS. Let's consider a circular coil of radius a and N loops of metallic wire through which an electric current I is flowing. The coordinate system can be seen in Figure 51. In cartesian coordinates, they would be written as:

$$x = x \quad , \quad y = \rho \cos\theta \quad , \quad z = \rho \sin\theta \tag{A.1}$$

so that the relation $\rho^2 = x^2 + y^2$ is fulfilled. The angle θ is an azimuthal angle around x.

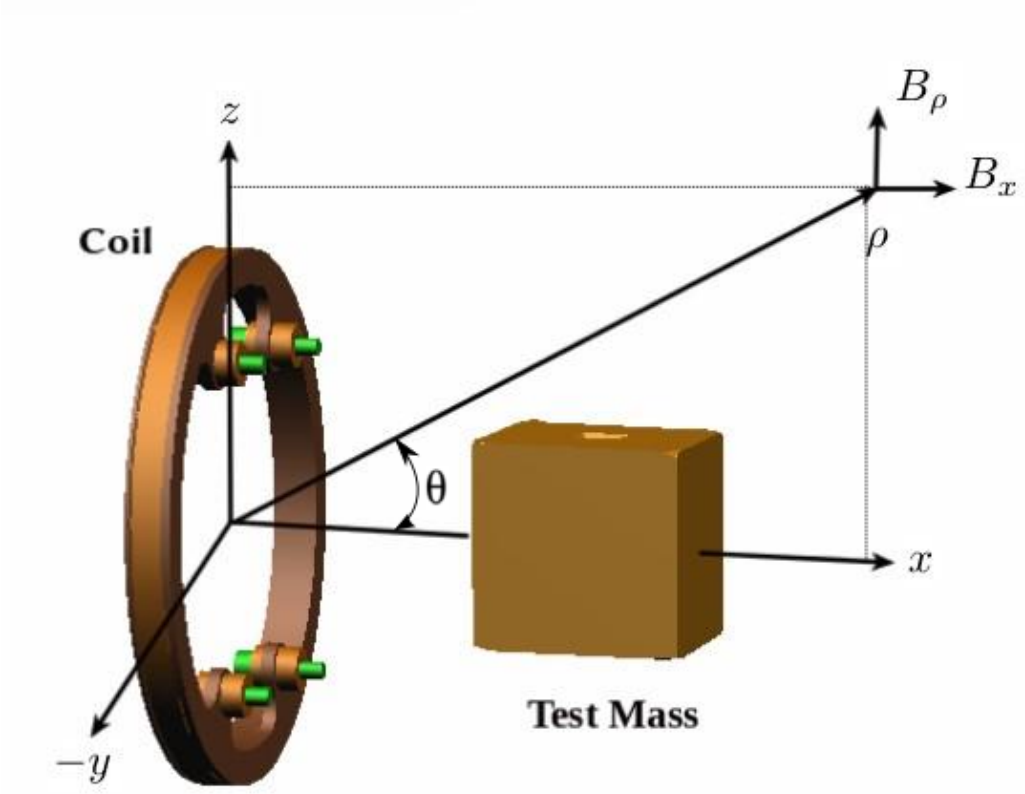

Figure 51: Coordinate reference frame system for the computation of the magnetic field generated by the coil.

The magnetic field **B** generated by the coils will have axial symmetry, i.e., only the x and ρ components will be different from zero, and they will not depend on the angle θ. The magnetic field of these components will be given by:

$$B_\rho(x,\rho) = \frac{\mu_0}{4\pi}\frac{N\pi a^2 I}{(a\rho)^{3/2}}\frac{k}{\pi}\frac{x}{a}\left[-K(k) + \frac{1-k^2/2}{1-k^2}E(k)\right] \tag{A.2a}$$

$$B_x(x,\rho) = \frac{\mu_0}{4\pi}\frac{N\pi a^2 I}{(a\rho)^{3/2}}\frac{k}{\pi}\left[\frac{1}{2}\frac{k^2}{1-k^2}E(k)\right] - \frac{\rho}{x}B_\rho(x,\rho) \tag{A.2b}$$

where:

$$k^2 = \frac{4a\rho}{x^2+(a+\rho)^2} \tag{A.3}$$

and:

$$K(k) = \int_0^{\pi/2}(1-k^2\sin^2\phi)^{-1/2}d\phi \;\;,\;\; E(k) = \int_0^{\pi/2}(1-k^2\sin^2\phi)^{+1/2}d\phi \tag{A.4}$$

are elliptic integrals of the first and second kind, respectively [145]. In cartesian coordinates, the field will be given by:

$$B_x(x,\rho) = B_x(x,\rho) \;\;,\;\; B_y(x,\rho) = \frac{y}{\rho}B_\rho(x,\rho) \;\;,\;\; B_z(x,\rho) = \frac{z}{\rho}B_\rho(x,\rho) \tag{A.5}$$

The simplest (and most frequent) case we will face during LPF coils experiments is to compute the magnetic field created by the coil in the x direction on the centre of the TM. This point is directly over the x axis, and the y or z components would only appear due to missalignments or tilts between the coil and the TM. Therefore, the y and z components can be considered negligible in front of the x component. In this case, the magnetic field will be simply given by:

$$B_x(x,I) = \frac{\mu_0}{4\pi}\frac{N\pi a^2 I}{(x^2+a^2)^{1/2}} \tag{A.6}$$

B

DATA ANALYSIS TOOLS

B.1 SPECTRAL DENSITY

The noise measured on-board the satellite by the different sensors can be approximated to random stationary processes. Such processes can be characterised by their PSD. The PSD of a stationary random process $x(t)$ is defined by the Fourier transform of its autocorrelation function $R_x(\tau) =< x(t)x(t+\tau) >$:

$$S_x(\omega) = \int_{-\infty}^{+\infty} R_x(\tau) e^{-j\omega\tau} d\tau \tag{B.1}$$

which is for the continuous case. For a discrete measurement x_n, the equivalent Discrete-Time Fourier transform is:

$$S_x(\omega) = \sum_{n=-\infty}^{n=+\infty} R_x(n) e^{-j\omega n} \ , \ -\frac{1}{2} \leqslant \frac{\omega}{2\pi} \leqslant \frac{1}{2} \tag{B.2}$$

Sometimes it is useful to compare two signals $x(t)$ and $y(t)$ in the frequency domain. This can be done by computing the Cross-Power Spectral Density (CPSD):

$$S_{xy}(\omega) = \int_{-\infty}^{+\infty} R_{xy}(\tau) e^{-j\omega\tau} d\tau \tag{B.3}$$

where $R_{xy}(\tau)$ is the cross-correlation function defined as $R_{xy}(\tau) =< x(t)y(t+\tau) >$. As in the previous case, the discrete case corresponding to signals x_n and y_n is defined as:

$$S_{xy}(\omega) = \sum_{n=-\infty}^{n=+\infty} R_{xy}(n) e^{-j\omega n} \ , \ -\frac{1}{2} \leqslant \frac{\omega}{2\pi} \leqslant \frac{1}{2} \tag{B.4}$$

Throughout this work, the PSD calculation (or ASD, which is simply the square root of the PSD) has been a common tool to study the fluctuations of several signals. Its implementation in the LTPDA toolbox is based in the Welch's averaged periodogram method [99, 146], using 50% overlapping data stretches and a Blackman-Harris spectral window. The first four frequency bins of the averaged periodogram are discarded, since they are biased by the spectral leakage from very low-frequency noise.

Another way of computing the PSD that has been used in this work, is through bayesian inference. An example of this are the black dots in Figure 21. This method uses bayesian inference to estimate the $1-\sigma$, that is, the 68.3% confidence interval for the value of the PSD (or ASD) at some selected frequencies.

These frequencies are chosen so that the estimates at adjoining frequencies are not significantly correlated. At each of the selected frequencies, the length of the periodograms is adjusted to achieve the maximum averaging and resolution. More details about this method are described at [117].

B.2 HETERODYNE DEMODULATION

The heterodyne demodulation is a tool implemented in the LTPDA Toolbox [96] that allow us to obtain the amplitude and phase of a sinusoidal signal if we know their frequency. It is based in the modulation and demodulation principles of signal processing. Let's consider that we have a sinusoidal signal of the type:

$$A(t) = A\sin(\omega t + \varphi) \tag{B.5}$$

where A is the amplitude of the signal, ω is its frequency and φ its phase. We know the frequency ω of the signal, while the amplitude A and phase φ are unknown. To find them, we will multiply our signal by a sinus and cosinus of the same frequency:

$$\begin{aligned} A\sin(\omega t+\varphi).\sin(\omega t) =& A\Big[\sin(\omega t)\cos(\varphi)+\cos(\omega t)\sin(\varphi)\Big]\sin(\omega t)\\ =& A\Big[\sin^2(\omega t)\cos(\varphi)+\sin(\omega t)\cos(\omega t)\sin(\varphi)\Big]\\ =& A\left[\frac{1-\cos(2\omega t)}{2}\cos(\varphi)+\frac{1}{2}\sin(2\omega t)\sin(\varphi)\right]\\ \underbrace{=}_{\text{lp}}& \frac{A}{2}\cos(\varphi) \end{aligned} \tag{B.6a}$$

where we have used the trigonometric identities: $\sin^2(a) = (1-\cos(2a))/2$ and $\sin(a)\cos(a) = \sin(2a)/2$. In the last step we have applied a lowpass to the function. That means that we only keep the low frequencies, i.e., we get rid of the 2ω terms. If now, instead of multiplying by the sinus, we do it by the cosinus:

$$\begin{aligned} A\sin(\omega t+\varphi).\cos(\omega t) =& A\Big[\sin(\omega t)\cos(\varphi)+\cos(\omega t)\sin(\varphi)\Big]\cos(\omega t)\\ =& A\Big[\sin(\omega t)\cos(\omega t)\cos(\varphi)+\cos^2(\omega t)\sin(\varphi)\Big]\\ =& A\left[\frac{1}{2}\sin(2\omega t)\cos(\varphi)+\frac{1-\sin(2\omega t)}{2}\sin(\varphi)\right]\\ \underbrace{=}_{\text{lp}}& \frac{A}{2}\sin(\varphi) \end{aligned} \tag{B.7a}$$

and now, to determine the phase φ, we can simply divide Equation B.6a by Equation B.7a:

$$\frac{(1/2)A\sin(\varphi)}{(1/2)A\cos(\varphi)} = \frac{\sin(\omega t+\varphi)\cos(\omega t)}{\sin(\omega t+\varphi)\sin(\omega t)} \Rightarrow \tan(\varphi) = \frac{\cos(\omega t)}{\sin(\omega t)}$$

Once we know the phase, we can easily obtain the amplitude A multiplying by the sinus, but this time applying the phase we just calculated:

$$A\sin(\omega t+\varphi).\sin(\omega t+\varphi) = A\sin^2(\omega t+\varphi) \underbrace{=}_{\text{lp}} \frac{A}{2} \tag{B.9a}$$

and if we multiply by the cosinus the terms disappear after the low pass:

$$A\sin(\omega t+\varphi).\cos(\omega t+\varphi) = \frac{A\sin(2\omega t)}{2} \underbrace{=}_{\text{lp}} 0 \tag{B.10a}$$

where again, we have used that $\sin^2(a) = (1-\cos(2a))/2$ and applied a lowpass filter afterwards to get rid of the 2ω frequencies.

This procedure is fully implemented in the LTPDA toolbox [96]. There, we indicate which is the signal we want to analyse and its frequency ω. We multiply a first time by the sinus and cosinus and get which is the phase delay of the signal. Then, with this delay, we multiply again by the sinus and the cosinus. The cosinus should go to zero, and the sinus will indicate us the amplitude A of the signal.

It is worth noticing that this implementation also allows us to measure with an incredible accuracy the frequency of the signal. This is because in our signal we typically have a lot of cycles, and if the frequency we indicate for the heterodyne analysis does not match exactly the one from the signal, when we multiply by the sinus, after each cycle the signal will ramp up or down, depending if the frequency we indicated is bigger or smaller than the one from the signal.

B.3 COHERENCE FUNCTION

The coherence (or magnitude squared coherence) between two signals $x(t)$ and $y(t)$ is defined as:

$$\gamma_{xy}(\omega) = \frac{|S_{xy}(\omega)|^2}{S_x(\omega)S_y(\omega)} \tag{B.11}$$

where $S_{xy}(\omega)$ is the CPSD between x and y, and $S_x(\omega)$ & $S_y(\omega)$ the PSD of $x(t)$ and $y(t)$, respectively, as defined in Section B.1. $S_x(\omega)$ & $S_y(\omega)$ should be different from zero, and the coherence will range between $0 < \gamma_{xy}(\omega) < 1$. A zero value means the signals are totally independent, while a value of one means they are totally correlated. This is true as long as the signals are ergodic and behave linearly.

C

HETERODYNE DEMODULATION MEASUREMENTS

In this section we collect the values of all the heterodyne demodulations performed using the LTPDA toolbox algorithm and based on the method explained in Section B.2. The demodulations correspond to values of magnetic field, which are obtained demodulating the injected current in the coil and applying Equation (A.6), or to values of forces caused by the magnetic injections, which are obtained through the measurements of LPF's interferometric system.

C.1 DOYS 119 & 120 INJECTIONS

C.1.1 *Measured forces*

[mA]	$I_{AC} = 1.0$	$I_{AC} = 0.5$	$I_{AC} = 0.1$
TEST MASS 1			
$F_{2\omega,x}$ force [pN]			
$I_{DC} = -0.2$	0.508 ± 0.001	0.118 ± 0.004	-
$I_{DC} = -0.1$	0.507 ± 0.001	0.118 ± 0.006	-
$I_{DC} = 0$	0.508 ± 0.001	0.119 ± 0.003	0.006 ± 0.002
$I_{DC} = +0.1$	0.507 ± 0.001	0.119 ± 0.003	-
$I_{DC} = +0.2$	0.508 ± 0.001	0.118 ± 0.003	-
$F_{1\omega,x}$ force [pN]			
$I_{DC} = -0.2$	0.373 ± 0.001	0.179 ± 0.003	-
$I_{DC} = -0.1$	0.169 ± 0.001	0.080 ± 0.003	-
$I_{DC} = 0$	-0.041 ± 0.002	-0.023 ± 0.004	-0.005 ± 0.002
$I_{DC} = +0.1$	-0.237 ± 0.001	-0.122 ± 0.005	-
$I_{DC} = +0.2$	-0.440 ± 0.001	-0.219 ± 0.004	-
TEST MASS 2			
$F_{2\omega,x}$ force [pN]			
$I_{DC} = -0.2$	[1]	[1]	-
$I_{DC} = -0.1$	[1]	[1]	-
$I_{DC} = 0$	[1]	[1]	[1]
$I_{DC} = +0.1$	[1]	[1]	-
$I_{DC} = +0.2$	[1]	[1]	-
$F_{1\omega,x}$ force [fN]			
$I_{DC} = -0.2$	89.2 ± 0.3	[1]	-
$I_{DC} = -0.1$	66.6 ± 0.4	[1]	-
$I_{DC} = 0$	43.7 ± 0.3	[1]	[1]
$I_{DC} = +0.1$	20.6 ± 0.4	[1]	-
$I_{DC} = +0.2$	20.6 ± 0.4	[1]	-

Table 19: Results of heterodynining $F_{2\omega,x}$ & $F_{1\omega,x}$ for the injections in coils 1 & 2 performed April 28-29, 2016 (DOYs 119-120). I_{DC} & I_{AC} corresponds to the offset and the amplitude of the injected current in the coil, respectively. Check Tables 6 & 7, and Figures 31 & 32 for more details about these injections. Each error corresponds to the standard deviation from the mean $\sigma/\sqrt{N}$, where the number of observations N corresponds to the number of cycles in the sinusoidal signal.

1 The values corresponding to these injections are not listed because due to the malfunctioning of coil 2 the corresponding signal was very noisy and difficult to demodulate.

C.1.2 *AC & DC of injected magnetic fields*

TEST MASS 1

[mA]	$\mathbf{I_{AC} = 1.0}$	$\mathbf{I_{AC} = 1.0}$	$\mathbf{I_{AC} = 0.1}$
	$B^{DC}_{i,x}$ [μT]		
$\mathbf{I_{DC} = -0.2}$	-0.95 ± 0.05	-0.94 ± 0.02	-
$\mathbf{I_{DC} = -0.1}$	-0.50 ± 0.05	-0.49 ± 0.02	-
$\mathbf{I_{DC} = 0}$	-0.06 ± 0.05	-0.04 ± 0.02	-0.028 ± 0.002
$\mathbf{I_{DC} = +0.1}$	0.38 ± 0.05	0.40 ± 0.02	-
$\mathbf{I_{DC} = +0.2}$	0.82 ± 0.05	0.84 ± 0.02	-
	$\nabla_x B^{DC}_{i,x}$ [μT m^{-1}]		
$\mathbf{I_{DC} = -0.2}$	-23.3 ± 1.2	-23.1 ± 0.4	-
$\mathbf{I_{DC} = -0.1}$	-12.4 ± 1.2	-12.1 ± 0.4	-
$\mathbf{I_{DC} = 0}$	-1.4 ± 1.2	-1.0 ± 0.4	-0.69 ± 0.05
$\mathbf{I_{DC} = +0.1}$	9.4 ± 1.2	9.8 ± 0.4	-
$\mathbf{I_{DC} = +0.2}$	20.3 ± 1.2	20.7 ± 0.4	-
	$B^{AC}_{i,x}$ [μT]		
$\mathbf{I_{DC} = -0.2}$	4.196 ± 0.009	2.072 ± 0.003	-
$\mathbf{I_{DC} = -0.1}$	4.192 ± 0.009	2.074 ± 0.003	-
$\mathbf{I_{DC} = 0}$	4.196 ± 0.009	2.078 ± 0.003	0.458 ± 0.003
$\mathbf{I_{DC} = +0.1}$	4.192 ± 0.009	2.078 ± 0.003	-
$\mathbf{I_{DC} = +0.2}$	4.195 ± 0.009	2.071 ± 0.003	-
	$\nabla_x B^{AC}_{i,x}$ [μT m^{-1}]		
$\mathbf{I_{DC} = -0.2}$	103.7 ± 0.2	51.04 ± 0.08	-
$\mathbf{I_{DC} = -0.1}$	103.6 ± 0.1	51.09 ± 0.10	-
$\mathbf{I_{DC} = 0}$	103.7 ± 0.2	51.21 ± 0.11	11.28 ± 0.03
$\mathbf{I_{DC} = +0.1}$	103.6 ± 0.2	51.09 ± 0.10	-
$\mathbf{I_{DC} = +0.2}$	103.7 ± 0.2	51.04 ± 0.13	-

Table 20: Produced magnetic field and gradient at the TM position by the injections in coil 1 on April 28, 2016 (DOY 119). The measurement has been performed through heterodyne demodulation, using the measurement of the electric current through the coil and using Equation A.6 to convert it to magnetic field at the position of the TM. Check Table 6 for more details about these injections. Each error corresponds to the standard deviation from the mean $\sigma/\sqrt{N}$, where the number of observations N corresponds to the number of cycles in the sinusoidal signal.

TEST MASS 2

[mA]	$I_{AC} = 1.0$	$I_{AC} = 1.0$	$I_{AC} = 0.1$
	$B^{DC}_{i,x}$ [μT]		
$I_{DC} = -0.2$	-0.30 ± 0.02	-0.308 ± 0.006	-
$I_{DC} = -0.1$	-0.15 ± 0.02	-0.159 ± 0.006	-
$I_{DC} = 0$	-0.0058 ± 0.02	-0.010 ± 0.006	-0.01 ± 0.01
$I_{DC} = +0.1$	0.14 ± 0.02	0.140 ± 0.006	-
$I_{DC} = +0.2$	0.29 ± 0.02	0.291 ± 0.006	-
	$\nabla_x B^{DC}_{i,x}$ [μT m^{-1}]		
$I_{DC} = -0.2$	-7.4 ± 0.4	-7.6 ± 0.1	-
$I_{DC} = -0.1$	-3.8 ± 0.4	-3.9 ± 0.1	-
$I_{DC} = 0$	-0.1 ± 0.4	-0.3 ± 0.1	-0.31 ± 0.02
$I_{DC} = +0.1$	3.5 ± 0.4	3.5 ± 0.1	-
$I_{DC} = +0.2$	7.2 ± 0.4	7.2 ± 0.1	-
	$B^{AC}_{i,x}$ [μT]		
$I_{DC} = -0.2$	1.412 ± 0.003	0.703 ± 0.001	-
$I_{DC} = -0.1$	1.414 ± 0.003	0.702 ± 0.001	-
$I_{DC} = 0$	1.416 ± 0.003	0.704 ± 0.001	0.1556 ± 0.0004
$I_{DC} = +0.1$	1.413 ± 0.003	0.703 ± 0.001	-
$I_{DC} = +0.2$	1.413 ± 0.003	0.702 ± 0.001	-
	$\nabla_x B^{AC}_{i,x}$ [μT m^{-1}]		
$I_{DC} = -0.2$	34.96 ± 0.04	17.30 ± 0.03	-
$I_{DC} = -0.1$	34.97 ± 0.07	17.32 ± 0.03	-
$I_{DC} = 0$	35.01 ± 0.07	17.36 ± 0.03	3.839 ± 0.006
$I_{DC} = +0.1$	34.94 ± 0.07	17.32 ± 0.03	-
$I_{DC} = +0.2$	34.92 ± 0.04	17.30 ± 0.02	-

Table 21: Produced magnetic field and gradient at the TM position by the injections in coil 2 on April 29, 2016 (DOY 120). The measurement has been performed through heterodyne demodulation, using the measurement of the electric current through the coil and using Equation A.6 to convert it to magnetic field at the position of the TM. Check Table 7 for more details about these injections. Each error corresponds to the standard deviation from the mean $\sigma/\sqrt{N}$, where the number of observations N corresponds to the number of cycles in the sinusoidal signal.

C.2 DOY 170 INJECTIONS

C.2.1 *Measured forces*

TEST MASS 1

[mA]	$I_{AC} = 1.5$	$I_{AC} = 1.0$	$I_{AC} = 0.8$	$I_{AC} = 0.5$
		$F_{2\omega,x}$ force [pN]		
$I_{DC} = +1.5$	1.129 ± 0.002	0.509 ± 0.003	0.313 ± 0.002	0.123 ± 0.001
$I_{DC} = +0.75$	1.122 ± 0.003	0.507 ± 0.002	0.316 ± 0.001	0.123 ± 0.002
$I_{DC} = 0$	1.128 ± 0.003	0.508 ± 0.001	0.318 ± 0.001	0.124 ± 0.001
$I_{DC} = -0.75$	1.124 ± 0.003	0.509 ± 0.003	0.317 ± 0.001	0.122 ± 0.001
$I_{DC} = -1.5$	1.123 ± 0.004	0.508 ± 0.001	0.317 ± 0.002	0.122 ± 0.001
		$F_{1\omega,x}$ force [pN]		
$I_{DC} = +1.5$	4.193 ± 0.005	2.820 ± 0.004	2.238 ± 0.003	1.395 ± 0.001
$I_{DC} = +0.75$	2.110 ± 0.003	1.432 ± 0.002	1.130 ± 0.001	0.708 ± 0.001
$I_{DC} = 0$	0.0433 ± 0.0003	0.0332 ± 0.0004	0.0287 ± 0.0005	0.0197 ± 0.0004
$I_{DC} = -0.75$	2.073 ± 0.003	1.392 ± 0.002	1.099 ± 0.001	0.680 ± 0.001
$I_{DC} = -1.5$	4.184 ± 0.006	2.799 ± 0.004	2.204 ± 0.003	1.375 ± 0.002
		$F_{DC,x}$ force [pN]		
$I_{DC} = +1.5$	3.10 ± 0.07	2.55 ± 0.06	2.37 ± 0.07	2.20 ± 0.07
$I_{DC} = +0.75$	1.59 ± 0.08	1.06 ± 0.05	0.82 ± 0.06	0.65 ± 0.06
$I_{DC} = 0$	1.03 ± 0.07	0.48 ± 0.06	0.29 ± 0.05	0.11 ± 0.05
$I_{DC} = -0.75$	1.55 ± 0.06	0.96 ± 0.06	0.78 ± 0.06	0.60 ± 0.05
$I_{DC} = -1.5$	3.07 ± 0.06	2.48 ± 0.06	2.31 ± 0.05	2.14 ± 0.06

[mA]	$I_{AC} = 1.5$	$I_{AC} = 1.0$	$I_{AC} = 1.5$	$I_{AC} = 1.0$
	$F_{im,x}$ $\pi/2$ force [fN]		$F_{im,x}$ $+3\pi/2$ force [fN]	
$I_{DC} = +1.5$	-0.04 ± 0.11	-0.19 ± 0.09	-0.11 ± 0.15	-0.35 ± 0.11
$I_{DC} = +0.75$	-0.16 ± 0.06	-0.03 ± 0.09	-0.12 ± 0.08	-0.02 ± 0.09
$I_{DC} = 0$	0.02 ± 0.06	-0.27 ± 0.08	0.09 ± 0.10	-0.31 ± 0.07
$I_{DC} = -0.75$	-0.21 ± 0.08	-0.09 ± 0.07	-0.16 ± 0.08	0.03 ± 0.09
$I_{DC} = -1.5$	-0.07 ± 0.13	-0.08 ± 0.10	-0.18 ± 0.16	-0.01 ± 0.10

Table 22: Results of heterodynining $F_{2\omega,x}$, $F_{1\omega,x}$ & $F_{im,x}$, and measuring the DC force caused by the injections in coil 1 on June 18, 2016 (DOY 170). I_{DC} & I_{AC} corresponds to the offset and the amplitude of the injected current in the coil, respectively. Check Table 8 & Figure 33 for more details about these injections. Each error corresponds to the standard deviation from the mean $\sigma/\sqrt{N}$, where the number of observations N corresponds to the number of cycles in the sinusoidal signal.

C.2.2 *AC & DC of injected magnetic fields*

TEST MASS 1

[mA]	$I_{AC} = 1.5$	$I_{AC} = 1.0$	$I_{AC} = 0.8$	$I_{AC} = 0.5$
		$B^{DC}_{i,x}$ [μT]		
$I_{DC} = +1.5$	6.06 ± 0.07	6.08 ± 0.05	6.08 ± 0.04	6.10 ± 0.02
$I_{DC} = +0.75$	3.00 ± 0.07	3.01 ± 0.05	3.02 ± 0.04	3.03 ± 0.02
$I_{DC} = 0$	-0.07 ± 0.07	-0.06 ± 0.05	-0.05 ± 0.04	0.04 ± 0.04
$I_{DC} = -0.75$	-3.18 ± 0.07	-3.17 ± 0.05	-3.16 ± 0.04	-3.16 ± 0.02
$I_{DC} = -1.5$	-6.29 ± 0.07	-6.27 ± 0.05	-6.27 ± 0.04	-6.27 ± 0.02
		$\nabla_x B^{DC}_{i,x}$ [μT m^{-1}]		
$I_{DC} = +1.5$	149 ± 2	150 ± 1	150 ± 1	150 ± 1
$I_{DC} = +0.75$	74 ± 2	74 ± 1	74 ± 1	75 ± 1
$I_{DC} = 0$	-2 ± 2	-2 ± 1	-1 ± 1	-1 ± 1
$I_{DC} = -0.75$	-78 ± 2	-78 ± 1	-78 ± 1	-78 ± 1
$I_{DC} = -1.5$	-155 ± 2	-155 ± 1	-155 ± 1	-154 ± 1
		$B^{AC}_{i,x}$ [μT]		
$I_{DC} = +1.5$	6.23 ± 0.01	4.18 ± 0.01	3.2 ± 0.3	2.056 ± 0.005
$I_{DC} = +0.75$	6.21 ± 0.08	4.1 ± 0.2	3.31 ± 0.01	2.059 ± 0.005
$I_{DC} = 0$	6.2 ± 0.1	4.19 ± 0.01	3.31 ± 0.01	2.05 ± 0.07
$I_{DC} = -0.75$	6.22 ± 0.08	4.18 ± 0.01	3.31 ± 0.02	2.06 ± 0.03
$I_{DC} = -1.5$	6.24 ± 0.04	4.20 ± 0.09	3.3 ± 0.1	2.056 ± 0.006
		$\nabla_x B^{AC}_{i,x}$ [μT m^{-1}]		
$I_{DC} = +1.5$	153.7 ± 0.4	103.1 ± 0.3	80 ± 7	50.7 ± 0.1
$I_{DC} = +0.75$	153 ± 2	102 ± 5	81.5 ± 0.2	50.8 ± 0.1
$I_{DC} = 0$	153 ± 4	103.3 ± 0.2	81.7 ± 2	51 ± 2
$I_{DC} = -0.75$	153 ± 6	101 ± 5	81.5 ± 0.2	50.8 ± 0.1
$I_{DC} = -1.5$	154 ± 1	103 ± 2	82 ± 2	50.7 ± 0.1

Table 23: Produced magnetic field and gradient at the TM position by the injections in coil 1 on June 18, 2016 (DOY 170). The measurement has been performed through heterodyne demodulation, using the measurement of the electric current through the coil and using Equation A.6 to convert it to magnetic field at the position of the TM. Check Table 8 for more details about these injections. Each error corresponds to the standard deviation from the mean $\sigma/\sqrt{N}$, where the number of observations N corresponds to the number of cycles in the sinusoidal signal.

BIBLIOGRAPHY

[1] P. Amaro-Seoane et al. "Laser Interferometer Space Antenna." In: *Arxiv* (2017). URL: http://arxiv.org/abs/1702.00786 (cit. on pp. 1, 7, 14, 15, 19, 75).

[2] S. Anza et al. "The LTP experiment on the LISA Pathfinder mission." In: *Class. Quant. Grav.* 22 (2005), S125–S138. DOI: 10.1088/0264-9381/22/10/001 (cit. on p. 1).

[3] F Antonucci et al. "The LISA Pathfinder mission." In: *Classical and Quantum Gravity* 29.12 (2012), p. 124014. URL: http://stacks.iop.org/0264-9381/29/i=12/a=124014 (cit. on p. 1).

[4] M. Armano et al. "Sub-Femto-g Free Fall for Space-Based Gravitational Wave Observatories: LISA Pathfinder Results." In: *Phys. Rev. Lett.* 116 (23 June 2016), p. 231101. DOI: 10.1103/PhysRevLett.116.231101 (cit. on pp. 1, 14, 32, 33, 37–40, 69, 74, 77, 113, 121).

[5] B. P. Abbott et al. "Observation of Gravitational Waves from a Binary Black Hole Merger." In: *Phys. Rev. Lett.* 116 (6 Feb. 2016), p. 061102. DOI: 10.1103/PhysRevLett.116.061102 (cit. on pp. 2, 6, 11, 14).

[6] R. A. Hulse and J. H. Taylor. "Discovery of a Pulsar in a binary system." In: *The Astrophysical Journal* 195 (Jan. 1975), pp. L51–L53. URL: http://adsabs.harvard.edu/full/1975ApJ...195L..51H (cit. on p. 2).

[7] Benjamin P Abbott et al. "Multi-messenger observations of a binary neutron star merger." In: (2017) (cit. on p. 3).

[8] MR Drout et al. "Light curves of the neutron star merger GW170817/SSS17a: Implications for r-process nucleosynthesis." In: *Science* 358.6370 (2017), pp. 1570–1574 (cit. on p. 3).

[9] A. Einstein. "The foundation of the general theory of relativity." In: *Annalen Phys. 49* 7 (1916), pp. 769–822. URL: https://doi.org/10.1002/andp.200590044 (cit. on p. 3).

[10] Charles W Misner, Kip S Thorne, John Archibald Wheeler, et al. *Gravitation*. Macmillan, 1973 (cit. on p. 4).

[11] Bernard Schutz. *A first course in general relativity*. Cambridge university press, 2009 (cit. on pp. 4, 6).

[12] Giles Hammond, Stefan Hild, and Matthew Pitkin. "Advanced technologies for future laser-interferometric gravitational wave detectors." In: *Journal of Modern Optics* 61 (Feb. 2014). DOI: 10.1080/09500340.2014.920934 (cit. on p. 5).

[13] Junaid Aasi et al. "Advanced ligo." In: *Classical and quantum gravity* 32.7 (2015), p. 074001 (cit. on pp. 7, 11).

[14] Thimothée Accadia et al. "Virgo: a laser interferometer to detect gravitational waves." In: *Journal of Instrumentation* 7.03 (2012), p. 03012 (cit. on pp. 7, 11).

[15] AM Cruise and Richard MJ Ingley. "A correlation detector for very high frequency gravitational waves." In: *Classical and Quantum Gravity* 22.10 (2005), S479 (cit. on p. 7).

[16] George Hobbs et al. "The international pulsar timing array project: using pulsars as a gravitational wave detector." In: *Classical and Quantum Gravity* 27.8 (2010), p. 084013 (cit. on pp. 7, 12).

[17] R Taylor and R Braun. "Science with the Square Kilometer Array: Motivation, Key Science Projects, Standards and Assumptions." In: *arXiv preprint astro-ph/0409274* (2004) (cit. on p. 7).

[18] STEVEN Detweiler. "Pulsar timing measurements and the search for gravitational waves." In: *The Astrophysical Journal* 234 (1979), pp. 1100–1104 (cit. on p. 7).

[19] Francesco Lucchin, Sabino Matarrese, and Silvia Mollerach. "The Gravitational wave contribution to CMB anisotropies and the amplitude of mass fluctuations from COBE results." In: *arXiv preprint hep-ph/9208214* (1992) (cit. on p. 8).

[20] D Barkats et al. "Degree-scale cosmic microwave background polarization measurements from three years of BICEP1 data." In: *The Astrophysical Journal* 783.2 (2014), p. 67 (cit. on pp. 8, 13).

[21] JA Brevik et al. "Initial performance of the BICEP2 antenna-coupled superconducting bolometers at the South Pole." In: *Millimeter, Submillimeter, and Far-Infrared Detectors and Instrumentation for Astronomy V*. Vol. 7741. International Society for Optics and Photonics. 2010, 77411H (cit. on pp. 8, 13).

[22] CD Sheehy et al. "The Keck Array: a pulse tube cooled CMB polarimeter." In: *Millimeter, Submillimeter, and Far-Infrared Detectors and Instrumentation for Astronomy V*. Vol. 7741. International Society for Optics and Photonics. 2010, 77411R (cit. on pp. 8, 13).

[23] J. Weber. "Detection and Generation of Gravitational Waves." In: *Phys. Rev.* 117 (1 Jan. 1960), pp. 306–313. DOI: 10.1103/PhysRev.117.306 (cit. on p. 8).

[24] J. Weber. "Evidence for Discovery of Gravitational Radiation." In: *Phys. Rev. Lett.* 22 (24 June 1969), pp. 1320–1324. DOI: 10.1103/PhysRevLett.22.1320 (cit. on p. 9).

[25] James L. Levine and Richard L. Garwin. "Absence of Gravity-Wave Signals in a Bar at 1695 Hz." In: *Phys. Rev. Lett.* 31 (3 July 1973), pp. 173–176. DOI: 10.1103/PhysRevLett.31.173 (cit. on p. 9).

[26] James L. Levine and Richard L. Garwin. "New Negative Result for Gravitational Wave Detection, and Comparison with Reported Detection." In: *Phys. Rev. Lett.* 33 (13 Sept. 1974), pp. 794–797. DOI: 10.1103/PhysRevLett.33.794 (cit. on p. 9).

[27] E. Mauceli et al. "The Allegro gravitational wave detector: Data acquisition and analysis." In: *Phys. Rev. D* 54 (2 July 1996), pp. 1264–1275. DOI: 10.1103/PhysRevD.54.1264 (cit. on p. 10).

[28] Massimo Cerdonio et al. "The ultracryogenic gravitational-wave detector AURIGA." In: *Classical and Quantum Gravity* 14.6 (1997), p. 1491 (cit. on p. 10).

[29] Pia Astone et al. "Long-term operation of the Rome" Explorer" cryogenic gravitational wave detector." In: *Physical Review D* 47.2 (1993), p. 362 (cit. on p. 10).

[30] D. G. Blair et al. "High Sensitivity Gravitational Wave Antenna with Parametric Transducer Readout." In: *Phys. Rev. Lett.* 74 (11 Mar. 1995), pp. 1908–1911. DOI: 10.1103/PhysRevLett.74.1908 (cit. on p. 10).

[31] Pia Astone et al. "The gravitational wave detector NAUTILUS operating at T= 0.1 K." In: *Astroparticle Physics* 7.3 (1997), pp. 231–243 (cit. on p. 10).

[32] JA Lobo. "Effect of a weak plane GW on a light beam." In: *Classical and Quantum Gravity* 9.5 (1992), p. 1385 (cit. on p. 10).

[33] Ulrik L Andersen. "Quantum optics: Squeezing more out of LIGO." In: *Nature Photonics* 7.8 (2013), pp. 589–590. URL: https://doi.org/10.1038/nphoton.2013.182 (cit. on p. 11).

[34] Harald Lück, GEO600 Team, et al. "The GEO600 project." In: *Classical and quantum gravity* 14.6 (1997), p. 1471 (cit. on p. 11).

[35] T Akutsu et al. "KAGRA: 2.5 generation interferometric gravitational wave detector." In: *arXiv preprint arXiv:1811.08079* (2018) (cit. on p. 12).

[36] CS Unnikrishnan. "IndIGO and LIGO-India: Scope and plans for gravitational wave research and precision metrology in India." In: *International Journal of Modern Physics D* 22.01 (2013), p. 1341010 (cit. on p. 12).

[37] M Punturo et al. "The Einstein Telescope: a third-generation gravitational wave observatory." In: *Classical and Quantum Gravity* 27.19 (2010), p. 194002 (cit. on p. 12).

[38] David Reitze et al. "Cosmic explorer: the US Contribution to gravitational-wave astronomy beyond LIGO." In: *arXiv preprint arXiv:1907.04833* (2019) (cit. on p. 12).

[39] RN Manchester et al. "The parkes pulsar timing array project." In: *Publications of the Astronomical Society of Australia* 30 (2013) (cit. on p. 12).

[40] Michael Kramer and David J Champion. "The European pulsar timing array and the large European array for pulsars." In: *Classical and Quantum Gravity* 30.22 (2013), p. 224009 (cit. on p. 12).

[41] Maura A McLaughlin. "The North American nanohertz observatory for gravitational waves." In: *Classical and Quantum Gravity* 30.22 (2013), p. 224008 (cit. on p. 12).

[42] Peter E Dewdney et al. "The square kilometre array." In: *Proceedings of the IEEE* 97.8 (2009), pp. 1482–1496 (cit. on p. 12).

[43] SR Taylor et al. "Are we there yet? Time to detection of nanohertz gravitational waves based on pulsar-timing array limits." In: *The Astrophysical Journal Letters* 819.1 (2016), p. L6 (cit. on p. 12).

[44] Peter AR Ade et al. "Detection of B-mode polarization at degree angular scales by BICEP2." In: *Physical Review Letters* 112.24 (2014), p. 241101 (cit. on p. 13).

[45] Planck Collaboration, PAR Ade, and N Aghanim. "Planck 2015 results." In: *XVI. Cosmological parameters* 1303 (2015), p. v1 (cit. on p. 13).

[46] Peter AR Ade et al. "Joint analysis of BICEP2/Keck Array and Planck data." In: *Physical review letters* 114.10 (2015), p. 101301 (cit. on p. 13).

[47] Z Ahmed et al. "BICEP3: a 95GHz refracting telescope for degree-scale CMB polarization." In: *Millimeter, Submillimeter, and Far-Infrared Detectors and Instrumentation for Astronomy VII*. Vol. 9153. International Society for Optics and Photonics. 2014, 91531N (cit. on p. 13).

[48] Keck Array et al. "Constraints on Primordial Gravitational Waves Using Planck, WMAP, and New BICEP2/Keck Observations through the 2015 Season." In: *Physical Review Letters* 121.22 (2018), p. 221301 (cit. on p. 13).

[49] Howard Hui et al. "BICEP Array: a multi-frequency degree-scale CMB polarimeter." In: *Millimeter, Submillimeter, and Far-Infrared Detectors and Instrumentation for Astronomy IX*. Vol. 10708. International Society for Optics and Photonics. 2018, p. 1070807 (cit. on p. 13).

[50] JE Faller et al. "Space antenna for gravitational wave astronomy." In: *Proceedings of the Colloquium on Kilometric Optical Arrays in Space, Cargese (Corsica)*. 1984, pp. 23–25 (cit. on p. 13).

[51] Faller J.E. et al. "An antenna for laser gravitational-wave observations in space." In: *Advances in Space Research* 9 (9 1989), pp. 107–111 (cit. on p. 13).

[52] Karsten Danzmann and the LISA study team. "LISA: laser interferometer space antenna for gravitational wave measurements." In: *Classical and Quantum Gravity* 13.11A (Nov. 1996), A247–A250. DOI: 10.1088/0264-9381/13/11a/033 (cit. on p. 13).

[53] European Space Agency. "NGO assessment study report." In: *ESA/SRE(2011)19* (2012). URL: http://sci.esa.int/ngo/49839-ngo-assessment-study-report-yellow-book (cit. on p. 14).

[54] P Amaro Seoane et al. "The gravitational universe." In: *arXiv preprint arXiv:1305.5720* (2013) (cit. on p. 14).

[55] Benjamin Lange. "The drag-free satellite." In: *AIAA journal* 2.9 (1964), pp. 1590–1606 (cit. on pp. 15, 16).

[56] Massimo Tinto and Sanjeev V Dhurandhar. "Time-delay interferometry." In: *Living Reviews in Relativity* 17.1 (2014), p. 6 (cit. on p. 16).

[57] Frank Flechtner et al. "Status of the GRACE follow-on mission." In: *Gravity, geoid and height systems*. Springer, 2014, pp. 117–121. DOI: https://doi.org/10.1007/978-3-319-10837-7_15 (cit. on pp. 17, 19).

[58] L Carbone et al. "Characterization of disturbance sources for LISA: torsion pendulum results." In: *Classical and Quantum Gravity* 22.10 (2005), S509 (cit. on p. 19).

[59] A Cavalleri et al. "A new torsion pendulum for testing the limits of free-fall for LISA test masses." In: *Classical and Quantum Gravity* 26.9 (2009), p. 094017 (cit. on p. 19).

[60] S Anza et al. "The LTP experiment on the LISA Pathfinder mission." In: *Classical and Quantum Gravity* 22.10 (2005), S125 (cit. on pp. 20, 21).

[61] A Carmain et al. "Space Technology 7 disturbance reduction system-precision control flight validation." In: *2006 IEEE Aerospace Conference*. IEEE. 2006, 7–pp (cit. on p. 20).

[62] G. Anderson et al. "Experimental results from the ST7 mission on LISA Pathfinder." In: *Phys. Rev. D* 98 (10 Nov. 2018), p. 102005. DOI: 10.1103/PhysRevD.98.102005 (cit. on p. 21).

[63] M. Armano et al. "Capacitive sensing of test mass motion with nanometer precision over millimeter-wide sensing gaps for space-borne gravitational reference sensors." In: *Phys. Rev. D* 96 (6 2017), p. 062004. DOI: 10.1103/PhysRevD.96.062004 (cit. on p. 23).

[64] Weber J. *Sensors:ISS-FEE. Slides for the LPF school in ESTEC*. Tech. rep. 2012 (cit. on p. 24).

[65] A. Cavalleri et al. "Increased Brownian Force Noise from Molecular Impacts in a Constrained Volume." In: *Phys. Rev. Lett.* 103 (14 2009), p. 140601. DOI: 10.1103/PhysRevLett.103.140601 (cit. on pp. 24, 40).

[66] M. Armano et al. "Beyond the Required LISA Free-Fall Performance: New LISA Pathfinder Results down to 20 μHz." In: *Phys. Rev. Lett.* 120 (6 2018), p. 061101. DOI: 10.1103/PhysRevLett.120.061101 (cit. on pp. 24, 33–35, 37, 40, 41, 43, 74, 77, 85, 145).

[67] M. Armano et al. "Charge-Induced Force Noise on Free-Falling Test Masses: Results from LISA Pathfinder." In: *Phys. Rev. Lett.* 118 (17 2017), p. 171101. DOI: 10.1103/PhysRevLett.118.171101 (cit. on pp. 25, 30, 38).

[68] M. Armano et al. "Precision charge control for isolated free-falling test masses: LISA pathfinder results." In: *Phys. Rev. D* 98 (6 2018), p. 062001. DOI: 10.1103/PhysRevD.98.062001 (cit. on pp. 25, 38).

[69] C Zanoni et al. "Summary of the results of the LISA-Pathfinder Test Mass release." In: *JPhCS* 610.1 (2015), p. 012022 (cit. on p. 25).

[70] B Zahnd, MM Zimmermann, and R Spörri. "LISA-Pathfinder cage and vent mechanism—Development and qualification." In: *Proceedings 15th European Space Mechanism and Tribology Symposium (ESMATS)*. 2013 (cit. on p. 25).

[71] Gerhard Heinzel et al. "The LTP interferometer and phasemeter." In: *Classical and Quantum Gravity* 21.5 (2004), S581 (cit. on pp. 25, 26, 39).

[72] David Robertson et al. "LTP interferometer—noise sources and performance." In: *Classical and Quantum Gravity* 22.10 (2005), S155 (cit. on p. 25).

[73] EJ Elliffe et al. "Hydroxide-catalysis bonding for stable optical systems for space." In: *Classical and Quantum Gravity* 22.10 (2005), S257 (cit. on p. 26).

[74] DI Robertson et al. "Construction and testing of the optical bench for LISA Pathfinder." In: *Classical and quantum gravity* 30.8 (2013), p. 085006 (cit. on p. 26).

[75] Antonio F. García-Marín. "Minimisation of optical pathlength noise for the detection of gravitational waves with the spaceborne laser interferometer LISA and LISA Pathfinder." Gotfried Wilhelm Leibniz Universiät Hannover, 2007 (cit. on pp. 26, 38).

[76] Gudrun Wanner et al. "Methods for simulating the readout of lengths and angles in laser interferometers with Gaussian beams." In: *Optics communications* 285.24 (2012), pp. 4831–4839 (cit. on p. 26).

[77] P Canizares et al. "The LISA Pathfinder DMU and Radiation Monitor." In: *Classical and Quantum Gravity* 28.9 (2011), p. 094004. URL: http://stacks.iop.org/0264-9381/28/i=9/a=094004 (cit. on pp. 27, 30, 66, 68).

[78] Walter Fichter et al. "LISA Pathfinder drag-free control and system implications." In: *Classical and Quantum Gravity* 22.10 (2005), S139 (cit. on p. 27).

[79] George E Morris and Clive Edwards. "Design of a Cold-Gas Micropropulsion system for LISA Pathfinder." In: *49th AIAA/ASME/SAE/ASEE Joint PropulsionConference*. 2013, p. 3854 (cit. on p. 28).

[80] M. Armano et al. "LISA Pathfinder micronewton cold gas thrusters: In-flight characterization." In: *Phys. Rev. D* 99 (12 2019), p. 122003. DOI: 10.1103/PhysRevD.99.122003 (cit. on pp. 29, 60).

[81] P Canizares et al. "The diagnostics subsystem on board LISA Pathfinder and LISA." In: *Classical and Quantum Gravity* 26.9 (2009), p. 094005 (cit. on p. 29).

[82] I Mateos et al. "LISA PathFinder radiation monitor proton irradiation test results." In: *Journal of Physics: Conference Series* 363 (2012), p. 012050. DOI: 10.1088/1742-6596/363/1/012050 (cit. on p. 30).

[83] M. Armano et al. "Characteristics and Energy Dependence of Recurrent Galactic Cosmic-Ray Flux Depressions and of a Forbush Decrease with LISA Pathfinder." In: *The Astrophysical Journal* 854.2 (Feb. 2018), p. 113. DOI: 10.3847/1538-4357/aaa774 (cit. on pp. 30, 68).

[84] M. Armano et al. "Forbush Decreases and <2 Day GCR Flux Non-recurrent Variations Studied with LISA Pathfinder." In: *The Astrophysical Journal* 874.2 (Apr. 2019), p. 167. DOI: 10.3847/1538-4357/ab0c99 (cit. on pp. 30, 68, 73, 74).

[85] M Armano et al. "Temperature stability in the sub-milliHertz band with LISA Pathfinder." In: *Monthly Notices of the Royal Astronomical Society* 486.3 (Apr. 2019), pp. 3368–3379. ISSN: 0035-8711. eprint: http://oup.prod.sis.lan/mnras/article-pdf/486/3/3368/28536406/stz1017.pdf. DOI: 10.1093/mnras/stz1017 (cit. on pp. 30, 75).

[86] F Rivas. "Thermo-Optical and thermo-elastic effects onboard the LISA Pathfinder mission." 2019. URL: https://www.educacion.gob.es/teseo/imprimirFicheroTesis.do?idFichero=6ZP0VS1oXcI%3D (cit. on pp. 30, 35, 38).

[87] Marc Diaz-Aguiló et al. "Design of the magnetic diagnostics unit onboard LISA Pathfinder." In: *Aerospace science and technology* 26.1 (2013), pp. 53–59 (cit. on p. 30).

[88] M Armano et al. "Spacecraft and interplanetary contributions to the magnetic environment on-board LISA Pathfinder." In: *Monthly Notices of the Royal Astronomical Society* 494.2 (Apr. 2020), pp. 3014–3027. ISSN: 0035-8711. eprint: https://academic.oup.com/mnras/article-pdf/494/2/3014/33129159/staa830.pdf. DOI: 10.1093/mnras/staa830 (cit. on p. 30).

[89] M. Armano et al. "Calibrating the system dynamics of LISA Pathfinder." In: *Phys. Rev. D* 97 (12 2018), p. 122002. DOI: 10.1103/PhysRevD.97.122002 (cit. on pp. 32, 33, 37).

[90] Gudrun Wanner and Nikolaos Karnesis. "Preliminary results on the suppression of sensing cross-talk in LISA Pathfinder." In: *Journal of Physics: Conference Series 840 (2017), Nr. 1*. Vol. 840. 1. Bristol: Institute of Physics Publishing. 2017, p. 12043 (cit. on p. 33).

[91] F Antonucci et al. "From laboratory experiments to LISA Pathfinder: achieving LISA geodesic motion." In: *Classical and Quantum Gravity* 28.9 (2011), p. 094002 (cit. on pp. 34, 113).

[92] F Gibert. "Thermal diagnostics experiments for LISA Pathfinder." 2015 (cit. on pp. 35, 38).

[93] *LPF legacy archive*. URL: http://lpf.esac.esa.int/lpfsa/ (cit. on p. 35).

[94] Hewitson M. "Mission Operations for LISA Pathfinder." In: Moscow, 2014 (cit. on p. 35).

[95] Paul McNamara and Giuseppe Racca. "Introduction to lisa pathfinder." In: *ESA Ref: LISA-LPF-RP-002-Iss1-Rev1* (2009) (cit. on p. 36).

[96] *LISA Technology Package Data Analysis Toolbox*. URL: https://www.lisamission.org/ltpda/ (cit. on pp. 36, 128, 129).

[97] M. Armano et al. "LISA Pathfinder Performance Confirmed in an Open-Loop Configuration: Results from the Free-Fall Actuation Mode." In: *Phys. Rev. Lett.* 123 (11 2019), p. 111101. DOI: 10.1103/PhysRevLett.123.111101 (cit. on p. 37).

[98] Sarah Paczkowski, LPF Collaboration, et al. "Laser Frequency Noise Stabilisation and Interferometer Path Length Differences on LISA Pathfinder." In: *Journal of Physics: Conference Series 840 (2017), Nr. 1*. Vol. 840. 1. Bristol: Institute of Physics Publishing. 2017, p. 12004 (cit. on p. 38).

[99] Stefano Vitale et al. "Data series subtraction with unknown and unmodeled background noise." In: *Phys. Rev. D* 90 (4 2014), p. 042003. DOI: 10.1103/PhysRevD.90.042003 (cit. on pp. 38, 40, 127).

[100] Gerhard Heinzel et al. "Interferometry for the LISA technology package (LTP) aboard SMART-2." In: *Classical and Quantum Gravity* 20.10 (2003), S153 (cit. on p. 39).

[101] John David Jackson. *Classical electrodynamics*. John Wiley & Sons, 2007 (cit. on pp. 43, 46, 114).

[102] Marc Diaz-Aguiló et al. "Design of the magnetic diagnostics unit onboard LISA Pathfinder." In: *Aerospace science and technology* 26.1 (2013), pp. 53–59 (cit. on p. 43).

[103] L. Néel. "Théorie du traînage magnétique des ferromagnétiques en grains fins avec application aux terres cuites"." In: *Annales de Géophysique* 5 (1949), pp. 99–136 (cit. on p. 49).

[104] H.-U. Worm, D. Clark, and M. J. Dekkers. "Magnetic susceptibility of pyrrhotite: grain size, field and frequency dependence." In: *Geophysical Journal International* 114.1 (1993), pp. 127–137. DOI: 10.1111/j.1365-246X.1993.tb01472.x (cit. on p. 49).

[105] Mike Jackson et al. "Field-dependence of AC susceptibility in titanomagnetites." In: *Earth and Planetary Science Letters* 157.3 (1998), pp. 129 –139. ISSN: 0012-821X. DOI: https://doi.org/10.1016/S0012-821X(98)00032-6 (cit. on p. 49).

[106] František Hrouda et al. "Out-of-phase magnetic susceptibility of rocks and soils: a rapid tool for magnetic granulometry." In: *Geophysical Journal International* 194.1 (2013), pp. 170–181. DOI: 10.1093/gji/ggt097 (cit. on p. 49).

[107] Josef Ježek and František Hrouda. "Eddy currents in the measurement of magnetic susceptibility of rocks." In: *Physics of the Earth and Planetary Interiors* 274 (2018), pp. 138 –147. ISSN: 0031-9201. DOI: https://doi.org/10.1016/j.pepi.2017.11.008 (cit. on p. 49).

[108] M. Jackson. "Imaginary susceptibility, a primer." In: *The IRM Quarterly* 13 (2003), pp. 10–11 (cit. on p. 49).

[109] S Vitale. *Effect of Eddy currents on down-conversion of magnetic noise.* Tech. rep. Memo LTP package. University of Trento, 2007 (cit. on pp. 49, 98, 120).

[110] L Trougnou. *AC magnetic susceptibility of LPF TMs, issue 2*. Tech. rep. TEC-EEE/2007149/LT. ESA, 2007 (cit. on pp. 49, 116).

[111] *ISH/CVM FM01 Alignment Verification Report*. Tech. rep. S2-CGS-TR-3119. OHB CGS, 2014 (cit. on p. 53).

[112] Moroni. A. *ISH/CVM FM02 Alignment Verification Report*. Tech. rep. S2-CGS-TR-3120. OHB CGS, 2014 (cit. on p. 53).

[113] J Sanjuan et al. "Magnetic polarisation effects of temperature sensors and heaters in LISA Pathfinder." In: *Journal of Physics: Conference Series* 154 (2009), 012001 (7pp). URL: http://stacks.iop.org/1742-6596/154/012001 (cit. on p. 56).

[114] M Armano et al. "Disentangling the magnetic force noise contribution in LISA Pathfinder." In: *Journal of Physics: Conference Series* 610 (2015), p. 012024. DOI: 10.1088/1742-6596/610/1/012024 (cit. on p. 57).

[115] John K. Ziemer et al. "Colloid Microthrust Propulsion for the Space Technology 7 (ST7) and LISA Missions." In: *AIP Conference Proceedings* 873.1 (2006), pp. 548–555. eprint: https://aip.scitation.org/doi/pdf/10.1063/1.2405097. DOI: 10.1063/1.2405097 (cit. on p. 60).

[116] P Welch. "The use of fast Fourier transform for the estimation of power spectra: A method based on time averaging over short, modified periodograms." In: *IEEE Trans. Audio and Electroacoust.* 15.2 (1967), pp. 70–73 (cit. on p. 63).

[117] *Supplemental material of [66] about Bayesian ASD estimate*. URL: https://journals.aps.org/prl/supplemental/10.1103/PhysRevLett.120.061101/LPF_UltimateSupplementalMaterial_4_1.pdf (cit. on pp. 63, 128).

[118] Martin Hewitson et al. "Data analysis for the LISA Technology Package." In: *Class. Quant. Grav.* 26 (2009), p. 094003. DOI: 10.1088/0264-9381/26/9/094003 (cit. on p. 63).

[119] Andrey Nikolaevich Kolmogorov. "The local structure of turbulence in incompressible viscous fluid for very large Reynolds numbers." In: *Cr Acad. Sci. URSS* 30 (1941), pp. 301–305 (cit. on p. 64).

[120] R Bruno et al. "Coordinated study on solar wind turbulence during the Venus-express, ace and ulysses alignment of August 2007." In: *Earth, Moon, and Planets* 104.1-4 (2009), pp. 101–104 (cit. on p. 64).

[121] R Bruno et al. "The low-frequency break observed in the slow solar wind magnetic spectra." In: *arXiv preprint arXiv:1906.11767* (2019) (cit. on p. 64).

[122] Roberto Bruno and Vincenzo Carbone. "The solar wind as a turbulence laboratory." In: *Living Reviews in Solar Physics* 10.1 (2013), p. 2 (cit. on pp. 64, 70).

[123] Fouad Sahraoui et al. "Evidence of a cascade and dissipation of solar-wind turbulence at the electron gyroscale." In: *Physical review letters* 102.23 (2009), p. 231102 (cit. on p. 64).

[124] Olga Alexandrova et al. "Solar wind turbulent spectrum at plasma kinetic scales." In: *The Astrophysical Journal* 760.2 (2012), p. 121 (cit. on p. 64).

[125] ML Goldstein et al. "Kinetic scale turbulence and dissipation in the solar wind: key observational results and future outlook." In: *Philosophical Transactions of the Royal Society A: Mathematical, Physical and Engineering Sciences* 373.2041 (2015), p. 20140147 (cit. on p. 64).

[126] Khurom H Kiyani, Kareem T Osman, and Sandra C Chapman. *Dissipation and heating in solar wind turbulence: from the macro to the micro and back again*. 2015 (cit. on p. 65).

[127] C. W. Smith et al. "The ACE Magnetic Fields Experiment." In: *Space Science Reviews* 86 (1998), pp. 613–632. URL: https://doi.org/10.1023/A:1005092216668 (cit. on pp. 65, 68).

[128] Emilia Kilpua, Hannu EJ Koskinen, and Tuija I Pulkkinen. "Coronal mass ejections and their sheath regions in interplanetary space." In: *Living Reviews in Solar Physics* 14.1 (2017), p. 5 (cit. on p. 68).

[129] Ian G Richardson. "Solar wind stream interaction regions throughout the heliosphere." In: *Living reviews in solar physics* 15.1 (2018), p. 1 (cit. on p. 68).

[130] R.P. Lepping et al. "The WIND Magnetic Field Investigation." In: *Space Science Reviews* 71 (1995), pp. 207–229. URL: https://doi.org/10.1007/BF00751330 (cit. on p. 68).

[131] R D'Amicis and R Bruno. "On the origin of highly Alfvénic slow solar wind." In: *The Astrophysical Journal* 805.1 (2015), p. 84 (cit. on p. 70).

[132] Roberto Bruno et al. "Solar wind magnetic field background spectrum from fluid to kinetic scales." In: *Monthly Notices of the Royal Astronomical Society* 472.1 (2017), pp. 1052–1059 (cit. on pp. 70, 71).

[133] H. Fang. *Magnetic susceptibility (d.c.) measurement of FM Test Mass 4 submitted for test by CGS S.p.A.* Tech. rep. Bureau International des Poids et Mesures, 2012 (cit. on pp. 98, 120).

[134] S. Vitale. *Effect of Eddy currents on down-conversion of magnetic noise.* Tech. rep. University of Trento, 2007 (cit. on p. 98).

[135] D. Fertin and L. Trougnou. *LisaPF Test Masses Acceleration Noise due to Eddy Currents.* Tech. rep. S2-EST-TN-2016. European Space Agency, 2007 (cit. on p. 98).

[136] LTP Team. *TM FM4 Magnetic Moment Measurement Report.* Tech. rep. S2-CGS-TR-3031. OHB CGS, 2012 (cit. on pp. 99, 120).

[137] M. Nofrarias. *Magnetic characterisation of thermal diagnostic items.* Tech. rep. S2-IEC-TN-3026. IEEC, 2007 (cit. on pp. 99, 105, 107, 120).

[138] L. Trougnou. *Impact of LTP thermal diagnostics on magnetic acceleration noise budget.* Tech. rep. S2-EST-TN-2026. ESA, 2008 (cit. on pp. 99, 105–107, 109, 120).

[139] C. Trenkel. *Prediction of spacecraft magnetic field.* Tech. rep. S2-ASU-TN-2523. Airbus, 2015 (cit. on pp. 99, 109, 113–118, 120).

[140] P. Cañizares et al. *Assessment of the effect of EH NTCs magnetism on LTP acceleration noise.* Tech. rep. S2-IEC-TN-3037. IEEC, 2007 (cit. on pp. 105–107, 120).

[141] J P López-Zaragoza. "Magnetic environment in LISA Pathfinder." MA thesis. IEEC, 2015 (cit. on pp. 109, 120).

[142] J J Ho Zhang. "Design of an antenna for the detection of kHz electromagnetic disturbances on-board LISA." 2019 (cit. on p. 115).

[143] Trougnou L. Fertin D. *AC magnetic analysis*. Tech. rep. S2-ASU-TN-2362. ESA, 2009 (cit. on p. 115).

[144] Trougnou L. Fertin D. *Low-frequency force due to amplitude modulated AC magnetic field*. Tech. rep. S2-EST-TN-3044. ESA, 2010 (cit. on p. 117).

[145] Abramowitz M. *Handbook of mathematical functions*. NBS Applied Mathematics Series 55, 1972 (cit. on p. 126).

[146] P. Welch. "The use of fast Fourier transform for the estimation of power spectra: A method based on time averaging over short, modified periodograms." In: *IEEE Transactions on Audio and Electroacoustics* 15.2 (1967), pp. 70–73. URL: https://ieeexplore.ieee.org/document/1161901 (cit. on p. 127).